Low-dose ion-based transmission radiography and tomography for optimization of carbon ion-beam therapy

Lorena Magallanes Hernández

München 2017

Low-dose ion-based transmission radiography and tomography for optimization of carbon ion-beam therapy

Lorena Magallanes Hernández

Dissertation
an der Fakultät für Physik
der Ludwig-Maximilians-Universität
München

vorgelegt von

Lorena Magallanes Hernández
aus Mexico Stadt

München, 25. Januar 2017

Erstgutachter: Prof. Dr. Katia Parodi

Zweitgutachter: Prof. Dr. Oliver Jäkel

Tag der mündlichen Prüfung: 21.02.2017

Contents

Abbreviations and Acronyms

1D one-dimensional. 169–171
2D two-dimensional. 8, 50, 64, 78, 79, 96, 97, 99, 113, 153, 154, 169–171, 174, 177, 178
3D three-dimensional. 4, 8, 27, 32, 35, 50, 80, 92, 97, 113, 118, 149

ACS Accelerator Control System. 28, 29, 52
ADC Analog-to-Digital-Converter. 58, 65, 67
APS Active Pixel Sensor. 43
ART Algebraic Reconstruction Technique. 113, 114, 116
ART Adaptive Radiation Therapy. 36, 186

BAMS Beam Application and Monitoring System. 14, 16, 27–29, 50, 52–63, 71, 81, 94, 106, 173, 182
BC Bragg curve. 5, 7, 9, 11, 16, 21, 24, 38, 51, 56, 58–60, 62, 64, 73, 74, 76–80, 83, 86–88, 91, 96, 97, 99–101, 105, 108, 110–113, 118, 119, 123, 127–130, 133, 135–137, 140, 141, 145, 149, 150, 156, 162, 168, 185
BEV Beam's Eye View. 7, 36
BP Bragg peak. 6, 12–14, 16, 17, 19, 29, 30, 32, 35, 50, 51, 54, 59, 63, 64, 73, 75–80, 83, 84, 87, 88, 96–101, 107–113, 118, 119, 123–126, 128, 129, 133, 135–137, 140, 141, 145, 149, 150, 152–156, 159, 163, 167, 176, 183, 186
BPD Bragg Peak Decomposition. 111–113, 116, 124, 131–140, 142–147, 149–152, 154–158, 160–162, 183
BPIC Bragg-Peak Ionization Chamber. 58–63
BPS Bragg-peak Steepness. 77, 79, 99

CBCT Cone-Beam Computed Tomography. 39
CCD Charge-Coupled Device. 39, 40
CHO Chinese Hamster Ovary. 21, 22
CMOS Complementary Metal Oxide Semi-conductor. 43, 44
CNAO Centro Nazionale di Adroterapia Oncologica. 42
CSDA Continuous Slowing-Down Approximation. 12
CT Computer Tomography. 30–36, 38–41, 113, 114, 181
CTV Clinical Target Volume. 30, 33

DAQ Data Acquisition. 8, 27, 39, 42, 50, 55–57, 65, 67, 68, 71, 164, 183
DECT Dual Energy Computed Tomography. 33
DFG Deutsche Forschungsgemeinschaft. 8, 182, 187

DFT Discrete Fourier Transform. 89–95
DNA Deoxyribonucleic Acid. 19–21
DRR Digitally-Reconstructed Radiography. 34

EDA Exploratory Data Analysis. 74

FBP Filtered Back Projection. 39, 40, 42
FLUKA FLUktuierende KAskade. 58, 59, 106, 107, 184
FOV Field-Of-View. 27, 41–44, 51, 52, 54–57, 71–76, 78–80, 83–85, 87, 88, 90, 97–101, 106, 108, 109, 116, 117, 124, 125, 134, 140, 143–146, 150, 156, 171–179
FWHM Full Width at Half Maximum. 18, 26, 42, 51, 55, 57, 71, 111, 124, 125, 127, 128, 130, 132–136, 139, 172–179

GEANT4 GEometry ANd Tracking. 184–186
GEM Gas Electron Multipliers. 42
GSI Gesellschaft für Schwerionenforschung. 18, 33, 184
Gy Gray. 18, 63, 73

HEBT High-Energy Beam Transport. 25
HIT Heidelberg Ion Beam Therapy Center. 7, 8, 14, 16, 18, 23, 25–27, 31, 33–35, 39, 40, 49–53, 56–58, 60, 61, 63, 71, 72, 80, 90, 93–95, 103, 104, 106–108, 140, 141, 168, 169, 172, 174–176, 182, 184, 187
HLUT Hounsfield-Units Look-up Table. 32–34, 39
HU Hounsfield Units. 30, 32–34, 40, 41, 123, 181, 186
HV High Voltage. 66, 81–84, 86, 88, 91, 93, 94, 96, 98, 124, 127–130, 132, 168, 170, 172

I/O input/output. 64
IAEA International Atomic Energy Agency. 3, 58
IARC International Agency for Research on Cancer. 3
IC Ionization Chamber. 58–63, 65, 76, 77, 80–82, 84, 86, 96, 107, 129, 162, 173
ICRU International Commission on Radiation Units and Measurements. 18
iCT ion Computed Tomography. 7, 8, 36–39, 49, 105, 106, 116–118, 123, 125, 146, 149–160, 162–164, 167, 182–184
IES Iso-Energy Slice. 26, 27, 29, 52, 63, 66
IGRT Image Guided Radiotherapy. 186
IQR Interquartile Range. 117, 118, 125, 126, 129, 131, 133, 137, 138, 140–143, 151, 153–155, 158, 160–162
iRAD ion Radiography. 7, 8, 36–39, 49, 105, 106, 112, 113, 117, 123–147, 149, 164, 167, 169, 182–185
IVI Interaction Vertex Imaging. 35

LEM Local Effect Model. 23, 24, 32
LET Linear Energy Transfer. 19–24, 83
LIBC List of Ion Beam Characteristics. 26, 28, 52, 53, 57, 59, 61, 71, 72, 100, 108, 172, 174, 176

LINAC Linear Accelerator. 4, 25, 26
LMU Ludwig-Maximilians Universität. 186, 187
LQ Linear-quadratic. 23
LUT Look-Up Table. 111–113, 123

MBP Machine Beam Plan. 29, 53, 54, 57, 71, 75
MBR Machine Beam Records. 29
MC Monte Carlo. 7, 8, 20, 24, 33, 34, 36, 44, 58, 86, 87, 98, 100–102, 105–113, 118, 124, 132, 133, 135, 142, 144–147, 151, 152, 157–159, 161, 162, 182, 184
MCS Multiple Coulomb Scattering. 9, 14, 15, 39, 40, 43, 44, 167, 168, 174, 177, 184
Micromegas MICRO-MEsh GASeous. 40, 41, 167–172, 174–179, 183, 186
MLP Most Likely Path. 36, 40, 42, 167
MRI Magnetic Resonance Imaging. 32, 35, 36
MWPC Multi-Wire Proportional Chamber. 27, 29, 37, 41, 52

NIRS National Institute of Radiological Sciences. 40
NRMSD Normalized Root Mean Squared Deviation. 117, 118, 124–126, 129–131, 133, 135, 140–146, 182, 183
NTCP Normal Tissue Complication Probability. 5, 22, 35

OAR Organ at Risk. 4–6, 30, 33

PACT Programme of Action for Cancer Therapy. 3
PBP Physical Beam Plan. 29, 50, 52, 53, 57–59, 75
PBR Physical Beam Records. 29, 58–61
pCT proton Computed Tomography. 36–44
PDF Probability Density Function. 55, 56
PDG Process Data Generation. 29, 52, 53, 55, 59–62, 85, 94
PET Positron Emission Tomography. 32, 34, 35, 38, 106
PGI Prompt Gamma Imaging. 35
PMMA Polymethyl Methacrylate. 7, 42, 50, 58, 79, 80, 89, 91, 97–105, 107, 108, 110, 111, 118, 123, 124, 127, 131–134, 158, 159, 178, 183–185
PPIC Parallel-Plate Ionization Chamber. 7, 27, 29, 38, 50, 51, 53, 54, 57, 63, 64, 66, 68, 69, 71–73, 75, 80–90, 93, 94, 97, 99, 101, 107–109, 129, 130, 150, 156, 182, 185, 186
PPR Peak-to-Plateau Ratio. 16
pps particles per second. 24, 26, 52–57, 59–62, 71, 83, 85, 90, 173
pRAD proton Radiography. 37, 41, 42, 44
PSS Personnel Safety System. 28
PTCOG Particle Therapy Co-Operative Group. 6
PTV Planned Target Volume. 30

QA Quality Assurance. 25, 29, 42, 59

R&D Research and Development. 33, 44
RAM Random-Access Memory. 28

RBE Relative Biological Effectiveness. 21–24, 32

RE Relative Error. 117, 118, 125, 126, 129, 131–133, 136–138, 140–143, 149, 151, 153–156, 158–163, 182, 183

RI Realibility Index. 73–77, 98

RMS Root-Mean-Square. 92–94, 97

RMSD Root Mean Squared Deviation. 117

ROI Region of Interest. 79, 117, 118, 125–129, 131, 133, 135–138, 140, 143, 146, 151, 155, 159, 167

RP Raster Point. 9, 18, 19, 24, 27, 29, 38, 39, 45, 50–57, 61–79, 81–90, 94–98, 101, 105, 106, 108–113, 116–118, 123, 124, 127–130, 132–137, 139–147, 150, 156, 161, 163, 164, 167, 168, 170–179, 183–185

RRD Residual Range Detector. 8, 14, 15, 49, 50, 53, 54, 63, 65, 66, 71–73, 76, 77, 79–84, 86–94, 96–103, 105, 107–111, 113, 123, 124, 126, 129, 130, 132, 133, 135–137, 140, 141, 149, 150, 156, 159, 163, 167–170, 174, 182–186

RSP Relative Stopping Power. 97

rWEPL relative Water Equivalent Path Length. 6–8, 16, 17, 30, 32–34, 38, 39, 41, 42, 44, 45, 80, 102–104, 107, 108, 111, 113, 114, 117, 118, 123, 133, 134, 146, 149–163, 181–183, 186

SART Simultaneous Algebraic Reconstruction Technique. 113, 116, 149, 157, 161

SFR Signal-to-Fluctuation Ratio. 77–79, 83–86, 99, 100, 127, 128, 130

SNR Signal-to-Noise Ratio. 16, 45, 66, 67, 70, 88, 182, 185

SOBP Spread Out Bragg Peak. 5, 6, 12, 27

SPECT Single Photon Emission Computed Tomography. 32

SPR Stopping Power Ratio. 6, 16, 17, 32, 36

SSD Silicon-Strip Detector. 41–43

TCP Tumor Control Probability. 4, 5, 22, 35

TCS Therapy Control System. 28, 29, 50, 52, 53, 58, 59, 63, 67–69

TCU Therapy Control Unit. 28, 53

TOF Time-Of-Flight. 35

TPS Treatment Planning System. 7, 30, 32, 33, 36, 39–41, 44, 106

TTL Transistor-Transistor Logic. 29, 63, 67, 72, 89

WE Water Equivalent. 16, 17, 50, 59, 80, 81, 118, 124, 127, 132, 134, 135, 140

WET Water Equivalent Thickness. 7, 8, 16, 17, 32–34, 38–42, 44, 45, 49, 63, 73, 75, 80, 88, 97–100, 105, 107–111, 113, 117–119, 123–127, 129–138, 140–145, 149, 150, 154–156, 158, 159, 162, 169, 182–184

WHO World Health Organization. 3

List of Figures

List of Tables

Niedrig-Dosis Transmissions-Radiographie und -Tomographie mit Ionenstrahlen zur Optimierung der Strahlentherapie mit Kohlenstoffionen

Zusammenfassung

In den letzten Jahrzehnten hat sich die Ionenstrahl-Therapie als hoch effizientes Behandlungsverfahren gegen Krebs herausgestellt. Der Erfolg dieser Methode beruht auf der Möglichkeit die angeordnete Dosis präzise auf das Zielvolumen zu beschränken. Dies wiederum wird durch die inverse Tiefendosiskurve und die endliche Reichweite von geladenen Teilchenstrahlen ermöglicht. Jedoch benötigt die Ausschöpfung sämtlicher physikalischer und biologischer Vorteile der Nutzung von Ionen die Entwicklung innovativer Bildgebungsverfahren, um die Reichweite des Ionenstrahls im Patienten zu überwachen. Eine wesentliche Reichweitenunsicherheit resultiert aus der Kalibrierung der relativen wasseräquivalenten Pfadlänge (relative Water Equivalent Path Length, rWEPL), welche auf Röntgen Computertomographie Aufnahmen basiert. Weitere Unsicherheiten ergeben sich aus möglichen Veränderungen der Anatomie oder der Lagerung des Patienten im Verlauf der Behandlung.

In dieser Arbeit wird die Kohlenstoffionen niedrig-Dosis Transmissions-Bildgebung mit einem Reichweiten-Detektor (Residual Range Detector, RRD) als bildgebendes Verfahren für Therapiezentren mit aktiver Strahlführung vorgeschlagen. Diese Art der Bildgebung ermöglicht die Verifikation der Reichweite des Ionenstrahls und der Patientenlagerung anhand von Ionenradiographie (ion-radiography, iRAD) Aufnahmen. Des Weiteren kann die Ionencomputertomographie (ion computed tomography, iCT) genutzt werden, um das Bremsvermögen der Ionen im durchquerten Gewebe direkt zu bestimmen und für die Bestrahlungsplanung zu nutzen. Im Rahmen dieser Arbeit werden erste experimentelle Untersuchungen zur Minimierung der im abzubildenden Objekt absorbierten Dosis vorgestellt.

Das verwendete Detektor System besteht aus einem Array aus 61 Parallelplatten Ionisationskammern (parallel-plate ionization chambers, PPICs) zwischen welchen sich jeweils 3 mm dicke PMMA Platten befinden. Die Leistungsfähigkeit dieses im Integrations-Modus genutzten Vielkanal-Arrays wurde für Bestrahlungen mit niedriger Teilchenfluenz sorgfältig untersucht. Die Charakterisierung erfolgte hinsichtlich folgender Aspekte: Betriebsverhalten der Strahl-Kontrolle am Heidelberger Ionenstrahl-Therapiezentrum (HIT, Heidelberg, Deutschland), RRD Signal-Rausch-Verhältnis (signal-to-noise ratio, SNR), generelle Effizienz sowie der PPIC Driftspannung. Metriken zur Analyse der Signalqualität, welche auf dem Ladungsansprechverhalten der individuellen Kanäle beruht, wurden entwickelt. Diese unterstützen die visuelle Bewertung der Aufnahmen. iRADs von Phantomen unterschiedlicher Komplexität und gewebeähnlicher Zusammensetzung wurden für drei verschiedene Aufnahme-Dosen erstellt: Mittels hoher (5000 Primärionen pro Rasterpunkt (raster-scanning point, RP)), mittlerer (1000

Primärionen pro RP) und niedriger Dosis (500 Primärionen pro RP). Experimentelle Computertomographien wurden nur mit hoher Dosis aufgenommen.

Spezielle Methoden zur Nachbearbeitung der Daten, welche auf Monte Carlo (MC) Simulationen beruhen, sind an der Ludwig-Maximilians-Universität München (München, Deutschland) entwickelt worden und wurden im Rahmen dieser Arbeit angewandt. Sie zielen darauf ab, die Bestimmung der wasseräquivalenten Dicke (Water Equivalent Thickness, WET) in lateraler (räumliches Auflösungsvermögen) und longitudinaler (Auflösungsvermögen der Ionenreichweite) Richtung für iRADs und iCTs zu verbessern. Umfangreiche quantitative und qualitative Auswertungen der Aufnahmen wurden vorgenommen und mit simulierten Daten sowie den analytisch berechneten Idealbildern verglichen. Ausgewertet wurde hierzu die physikalische Dosis [Gy], die Genauigkeit [% des relativen Fehlers (Relative Error, RE)] und die gesamte Bildqualität. iRADs, welche mit einer Dosis von 0.5 bis 1 mGy aufgenommen wurden, zeigten einen mittleren WET-RE von unter 1.5%. iCTs von zwei heterogenen Phantomen wurden in der Konfiguration mit hoher Dosis aufgenommen. Dies entspricht einer Dosis von 4 Gy für das gesamte iCT. Der entsprechende rWEPL-RE für diese geometrische Anordnung, welche ein anatomischen Szenario nachbildet, war unter 1%. Gleichwohl deuten die Ergebnisse aus der Untersuchung von Projektionen mit niedriger Dosis an, dass die Dosis für eine komplette Tomographie mit dem derzeitigen experimentellen Aufbau auf 0.2 Gy reduziert werden kann. Des Weiteren begründen Experimente mit einer verbesserten Auslese-Elektronik und Untersuchungen mit MC Simulationen die Annahme, dass die Dosis um rund eine Größenordnung auf einen klinisch akzeptablen Wert verringert werden kann ($\sim$0.03 Gy).

Zum Abschluss der Arbeit werden die derzeit durchgeführten Verbesserungen des Bildgebungssystems sowie die mögliche Kombination mit Detektoren zur Einzel-Ionen-Messung behandelt. Die erzielten Ergebnisse verdeutlichen die Stärken und Schwächen der Transmissions-Bildgebung mit dem untersuchten Integrations-Modus RRD. Sie ebnen den Weg für weitere Verbesserungen und die mögliche Anwendung im klinischen Arbeitsablauf in der Ionenstrahl-Therapie. Obwohl weitere Optimierungen benötigt werden um die klinische Anwendbarkeit zu ermöglichen, zeigt die Transmissions-Bildgebung mit Ionenstrahlen das Potenzial, direkt im Behandlungsraum akkurate iRADs und iCTs bei niedriger Dosis aufzunehmen. Dies wird es ermöglichen, die Qualität der Ionenstrahl-Therapie zu optimieren.

Schlagwörter: *Ionenstrahl-Therapie; niedrig-Dosis Transmissions-Bildgebung mit Ionenstrahlen; Integrations-Modus Reichweiten-Detektor; Ionenradiographie; Ionentomographie*

Low-dose ion-based transmission radiography and tomography for optimization of carbon ion-beam therapy

Abstract

In the last few decades, ion-beam radiotherapy has emerged as a highly effective tumor treatment modality. Its success relies on the capability to precisely confine the prescribed dose within the target volume, due to the inverted depth-dose profile and the finite range featured by charged particles. However, to fully exploit the physical and biological advantages of ion-beams, it is necessary to prioritize on innovative imaging techniques to monitor the ion-range inside the patient. Main range uncertainties result from X-ray-based calibration of the ion relative Water Equivalent Path Length (rWEPL) during the planning phase, and patient anatomical or positioning variation during the treatment. In this thesis, low-dose carbon-ion transmission-imaging performed with a Residual Range Detector (RRD) is proposed as imaging strategy for actively scanned beam delivery facilities. It enables the verification of the beam range and the patient positioning with ion-radiographies (iRAD), and ion computed tomographies (iCT) can directly provide the ion stopping-power of the traversed tissue for treatment planning purposes. First experimental investigations aiming to minimize the imaging dose to the object are presented. The performance of the integration-mode multi-channel array of 61 parallel-plate ionization chambers (PPICs), interleaved with 3 mm thickness PMMA slabs, was thoroughly investigated for low-fluence irradiation. This characterization has been pursued in terms of beam-monitoring performance at the Heidelberg Ion-beam Therapy Center (HIT, Heidelberg, Germany), RRD signal-to-noise ratio (SNR), RRD charge-collection efficiency and drift voltage applied to the PPICs. Pixel-wise metrics for signal quality evaluation based on specific channel-charge features have been developed to support the visual assessment of the acquired images. Phantoms of different complexity and tissue-equivalent composition were imaged with high (5000 primaries per raster-scanning point (RP)), middle (1000 primaries per RP) and low imaging dose (500 primaries per RP) in the radiographic domain, whereas only high dose tomographic acquisitions were experimentally performed. Dedicated Monte Carlo (MC)-based post-processing methods, developed at the Ludwig-Maximilians-Universität München (Munich, Germany), were applied to improve the retrieval of Water Equivalent Thickness (WET) variations in lateral (spatial resolution) and longitudinal (ion range resolution) directions, for iRADs, and rWEPL in the tomographic case. An exhaustive quantitative and qualitative evaluation of the acquired images was made in comparison with the ground-truth and simulated data in terms of physical-dose to the object [Gy], accuracy [% of Relative Error (RE)] and overall image quality [NRMSD]. iRADs were produced with 0.5 to 1 mGy imaging dose and an absolute mean WET-RE within 1.5%. Tomographies of two heterogeneous phantoms were acquired in the high dose regime, yielding 4 Gy imaging dose and a RE in rWEPL below 1%, for a geometry that resembles an anatomical scenario. Nonetheless, the findings in the low dose projection studies indicate that the dose of tomographic acquisitions with the current experimental setup can be reduced down to 0.2 Gy. Furthermore, the improved readout system tests and MC simulations establish the possibility to decrease the dose received by the imaged object by about one order of magnitude down ($\sim$0.03 Gy), which lies in the clinically accepted

range.

Finally, the ongoing imaging system upgrade and the potential integration with single-ion tracking detectors is outlined. The outcome of this thesis highlights the strengths and weaknesses of ion transmission-imaging with the investigated integration-mode RRD, paving the way to future improvements towards eventual application to the ion-beam therapy clinical work-flow. Although further optimization is still required for clinical application, ion-based transmission-imaging has demonstrated its potentiality to generate accurate low-dose iRADs and iCTs at the treatment site, bringing together the required features to optimize the quality of the ion-beam therapy.

Key words: *ion-beam therapy; low-dose ion-based transmission-imaging; integration-mode range detector; ion radiography; ion tomography*

Part I.
Generalities

Serendipity: Making discoveries, by accidents and sagacity, of things which they were not in quest of...

Horace Walpole

1 Introduction

1.1 Scientific context

Cancer is a diverse group of diseases that develop into malignant tumors in any part of the body due to the uncontrolled growth and proliferation of abnormal cells. The spreading process of tumor cells towards other organs than those where original tumor growth started is referred to as metastasizing. Worldwide, one in seven deaths is due to cancer; cancer causes more deaths than AIDS, tuberculosis, and malaria combined. According to the different countries economic ranking, cancer is the second prevailing cause of death in high-income countries (following cardiovascular diseases) and the third most common reason of death in low- and middle-income countries (after cardiovascular diseases and infectious or parasitic diseases) [American Cancer Society 2015].

The fight against cancer has become a high-priority global problem to be solved. According to the statistics and predictions of the cancer morbidity and mortality of the World Cancer Report [Stewart and Wild 2014], by 2030, over 13 million people will die from cancer every year (Table 1). International joint efforts to overcome this pandemic disease are carried out by the Programme of Action for Cancer Therapy (PACT). For this enterprise, the International Atomic Energy Agency (IAEA) combines its expertise in radiation medicine with the experience of the World Health Organization (WHO) and its specialized cancer agency, the International Agency for Research on Cancer (IARC).

Many cancers have a high probability to be cured if they are detected at early stages and treated appropriately. Every cancer type requires a treatment tailored to the individual patient, which includes one or more modalities among surgery, chemotherapy, immunotherapy and/or radiotherapy. Over 50% of all patients in developed countries, who have localized malignant tumors, receive radiotherapy as part of their treatment course, either alone or in combination with surgery and chemotherapy [Loeffler and Durante 2013].

Table 1.1: Estimated and projected numbers (millions) of cancer cases (morbidity (morb.)) and deaths (mortality (mort.)), including all types of cancers and both sexes worldwide [Stewart and Wild 2014].

		prediction				new prediction	
2008		2030		2014		2030	
morb.	mort.	morb.	mort.	morb.	mort.	morb.	mort.
12.4	7.6	20.0	12.9	14.1	8.2	22.0	13.0

Conventional radiotherapy comprises the internal (*brachytherapy*) and external (*teletherapy*) use of γ–rays, high-energy photons (X-rays) or electrons to deliver lethal dose to the tumor cells and prevent them from further dispersion. Teletherapy refers to the use of a radiation source distant to the tumor location in the patient body. To this aim, Linear Accelerators (LINACs) are used to accelerate electrons or produce Megavoltage X-rays. Specially in developing countries, Cobalt-60 units are still used to produce γ-radiation. Radiotherapy technology has increasingly improved over the past decades [Thariat et al. 2012]; nowadays, modern LINACs provide a great versatility, the beam shape and intensity can be modified to offer three-dimensional (3D)-conformal, intensity-modulated and stereotactic radiotherapy.

The potential of X-rays for oncological purposes was exploited very shortly after their *serendipitous* discovery by Röntgen in 1895 [Roentgen 1959; Thariat et al. 2012]. Two months after the first detection of X-rays, they found their clinical application by Emil Grubbé, who treated an advanced ulcerated breast cancer [Grubbé 1933] in January 1896 [Bernier et al. 2004]. Cobalt-60 paved the way towards the usage of Megavoltage energies for treatment of deep seated tumors, shortly before the start of the LINAC era. Interestingly, the first ion-beam therapy landmark was not distant from this date. In 1946, Robert R. Wilson proposed that accelerated protons could be used to treat localized tumors, owing to their characteristic inverse depth–dose distribution [Wilson 1946]. The use of ion-beams as anticancer therapy was only adopted a couple of years later, by the Lawrence Berkeley Laboratory (LBL) in California. The first patient treatment for pituitary irradiation was treated in 1954 [Tobias 1958], after gaining experience in animal biological studies using protons, deuterons and helium beams [Tobias et al. 1952]. By this time, charged particle therapy was performed at nuclear physics facilities. It was only until late 80's that the first hospital-based proton treatment center opened in Clatterbridge, UK [PTCOG], followed by Loma Linda, California, where the first ocular melanoma patient was treated in October 1991 [Schulte and Wroe 2012]. Many factors have contributed to this relatively slow development, but the lack of appropriate 3D-imaging and accurate planning techniques were among the major reasons [Schulte and Penfold 2012].

When using external ionizing radiation for cancer treatment, healthy surrounding tissues are unavoidably exposed to the radiation dose, too. To minimize this collateral effect, external beam radiotherapy aims for:

- Confining the radiation dose to the target volume.
- Sparing the healthy surrounding tissues, particularly if they involve Organ at Risks (OARs).
- Widening the *therapeutic window*, i.e. the difference between the Tumor Control Prob-

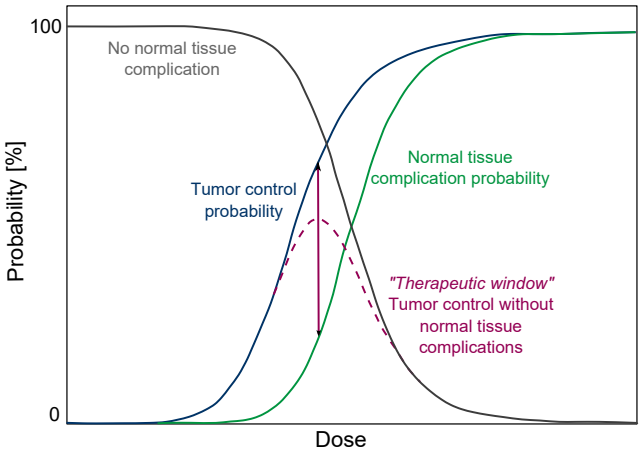

Figure 1.1: The main goal of radiotherapy is to irradiate the tumor with sufficient dose to achieve local control while minimizing the dose to adjacent OARs and thus avoiding complication in healthy tissues. TCP and NTCP increase with increasing dose, however, there is a dose range (*"therapeutic window"*) where the probability for tumor control with complication-free treatment finds its maximum.

ability (TCP) and the Normal Tissue Complication Probability (NTCP) curves as a function of the radiation dose. These probabilities are biologically-based predictions which are highly complex due to the multi-faceted dependencies of their clinical outcomes (clonogenesis, tumor response, radiosensitivity, etcetera). Their expectation relies upon statistical and biological principles as well as clinical endpoints. The TCP and the NTCP steeply increase with increasing dose and their separation is highly correlated to the treatment plan and margin selection. However, within the therapeutic window, the probability for tumor control without long-term complications reaches its maximum (cf. Figure 1.1).

- Rapid recovery and improved quality of life of the patient during and after the treatment.

Photons are attenuated in tissue, leading to an exponential decay of the radiation dose after an initial, energy-dependent build-up region. In contrast, heavy charged particles (protons and heavier ions) deposit little energy at the entrance to the body, when their velocity is higher, and most of their energy is released towards the end of their course, just before they come to rest in the tumor site (cf. Figure 1.2a). This distinct and favorable energy deposition was named as Bragg curve (BC) after W. H. Bragg, who investigated the slowing down process of α particles in air [Bragg and Kleeman 1905; Brown and Suit 2004]. In order to cover the whole tumor volume, several beam-energies have to be superimposed as it is shown in Figure 1.2b. This extended treatment area is known as Spread Out Bragg Peak (SOBP).

The favorable physical and biological properties of heavy charged particle interaction in tissue (cf. Chapter 2 for more details) encourage the use of ions to achieve optimal target dose distribution in localized tumors that are in the proximity of OARs, such as the spinal cord, in head and neck anatomical districts [Levin et al. 2005]. However, as technology moves forward, tumors in other body sites are also being treated, including those in the gastrointestinal area, prostate and lung. Ion-beam radiotherapy, especially with proton beams, is also often indicated for pediatric cases, since it might be associated with a reduced risk of radiation-induced secondary malignancies and neurocognitive damage due to the less dose exposure in

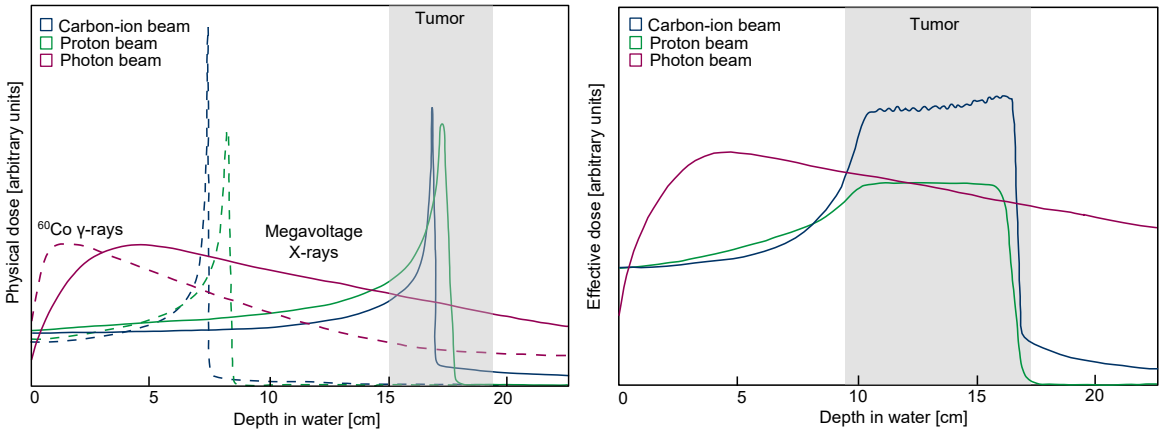

Figure 1.2: Comparison of the depth-dose distribution of conventional photons (X-rays and ^{60}Co $\gamma-$rays) and ion beams (protons and ^{12}C) of different energies in water. Photons show an exponentially decreasing dose with increasing depth after an initial maximum, whereas ions dispose of an inverse dose profile, increasing the dose in depth (left panel). The Bragg peak can be shifted by energy variation to cover the whole target volume (SOBP), leading to a much higher dose deposition inside the tumor and sparing of surrounding healthy tissue compared to photons (right panel). Adapted from Parodi [2014]; Durante and Loeffler [2009]; Schardt and Elsässer [2010].

OARs and healthy tissue. In the case of ions heavier than protons, the selective enhancement of the ionization density in the tumor area (cf. Section 2.2) holds a great potential to treat radioresistant and hypoxic tumors, which are more resistant to conventional sparsely ionizing radiation.

The recent Particle Therapy Co-Operative Group (PTCOG) statistics [Jermann 2015] reports that more than 137,000 patients have been treated with particle therapy worldwide from 1954 to 2014. These include 15,000 cases in 2014, 86% of which were treated with protons and 14% with carbon ions in 48 facilities that are currently in clinical operation. Nevertheless, the number of candidates for ion-beam therapy treatment might increase considerably when more positive evidence arises from ongoing clinical trials.

Full therapeutic exploitation of ion-beams demands a precise determination of the ion penetration depth (*range*) inside the patient, determining the Bragg peak (BP) position. Unwanted consequences of range uncertainties are possible longitudinal shifts of the BP, which might lead to significant underdosages of the tumor or overdosages of surrounding OARs. (cf. Section 2.3.5). Therefore, image guidance is essential in ion-beam radiotherapy to guarantee the accuracy of the ion-range in the patient, likely resulting in improved quality of the treatment results (cf. Section 2.4.1).

1.2 Aim and structure of this work

The aim of this thesis is to investigate ion-based transmission imaging as an innovative imaging method to tackle the uncertainties faced nowadays in ion-beam radiotherapy.

The use of ion based transmission imaging could enable full clinical exploitation of the advantages of ion beams for cancer treatment, since it promises to overcome several major delivery inaccuracies at different stages of the treatment work-flow. During the planning phase, the distribution of the Stopping Power Ratio (SPR) relative to water, also defined as the relative

Water Equivalent Path Length (rWEPL), of the patient anatomy could be reconstructed and introduced as input for the Treatment Planning System (TPS). Using this information directly deduced from ion interaction in tissue, the uncertainties arising from the current use of a X-ray-based empirical calibration method could be avoided. Furthermore, at the treatment site, transmitted planar or reconstructed volumetric images can be used before and in-between the treatment to monitor the patient positioning and anatomical changes as well as for Beam's Eye View (BEV) verification of the integral rWEPL relative to water.

Ion-based radiographies and tomographies rely on lower doses to the patient than those usually reached with conventional X-rays diagnostic images, as shown by some of the state-of-the-art investigations (cf. Section 2.4.3). This advantage is owed to the high-energetic and low-fluence ion-beams used, which guarantee the patient to be exposed only to the reduced radiation dose at the entrance region of the BC.

To this end, ion Radiography (iRAD) and ion Computed Tomography (iCT), by means of the direct measurement of the ion residual range, has started being investigated at the Heidelberg Ion Beam Therapy Center (HIT). This research was performed with various phantoms of different complexity and tissue-equivalent composition, which were imaged using an integration-mode multi-channel detector. The range telescope, consisting of 61 air-filled Parallel-Plate Ionization Chambers (PPICs) interleaved with Polymethyl Methacrylate (PMMA) absorber slabs of 3 mm thickness, already demonstrated the transmission imaging proof-of-principle of carbon ion transmission imaging at very high doses [Rinaldi 2011; Rinaldi et al. 2013]. Therefore this thesis work addresses a comprehensive characterization of the detector performance with new electronics under low-dose irradiation conditions.

The investigations of this work revealed the sensitivity to noise of the charge signal integrated in the PPIC-stack in the low-dose regime. In consequence, part of this work aimed at proposing *ad-hoc* data-acquisition parameters of the transmission-imaging prototype to achieve optimal signal quality. Moreover, in order to obtain the maximum radiographic and tomographic information in lateral *(spatial resolution)* and longitudinal *(ion range resolution)* directions, signal-feature assessment strategies and advanced data pre- and post-processing techniques supported by Monte Carlo (MC) simulations [Marcelos 2014; Meyer 2015] were developed. Making use of these dedicated data-analysis methods, reduced-dose carbon iRADs and iCTs could be experimentally demonstrated within the scope of this work.

Finally, the ultimate goal of this work is to pave the way towards the clinical application of ion-based transmission imaging, by improving the next generation of the actual prototype. The results provided in this work demonstrate the potential to obtain reliable iRADs and iCTs with the optimal trade-off between the minimal dose to the patient and a precise retrieve of the patient Water Equivalent Thickness (WET) and rWEPL, respectively.

This thesis is divided in four parts and organized as follows: The first part contains two chapters. In the first chapter, the ion-beam therapy and the topic of this study are introduced in the context of the current situation of cancer malignancies and conventional therapy worldwide. The second chapter, establishes the physical and biological foundations of ion-beam radiotherapy and how they influence ion-based transmission imaging. Besides, the technical and clinical implementation at the HIT facility is covered in detail. The sources of uncertainties present in

the clinical application of particle therapy are discussed and the different approaches of medical imaging to overcome them are reviewed in this chapter, too. Special focus is dedicated to the historical development of ion-based transmission-imaging techniques to know the state-of-the-art of the studied topic. The second part of the thesis contains Chapter 3 and 4 and it delves into the materials and methods involved in the performed investigations. These include the experimental acquisition process (cf. Chapter 3), which requires the synchronization of the Data Acquisition (DAQ) system of the new electronics with the active scanning beam delivery available at HIT, and a comprehensive characterization of the experimental setup in the low-dose regime. Moreover, single-spot signal assessment maps are developed and implemented to visually evaluate the detector performance. The irradiated phantoms are also presented in the third chapter.

Chapter 4 describes the two-dimensional (2D)-radiographic and 3D-tomographic image reconstruction strategies, as well as the underlying MC simulations. Then, the MC-based advanced post-processing methods applied in this work, are also described.

Part III of this thesis is dedicated to the carbon ion-based imaging results and discussion. It is subdivided in two chapters, where Chapter 5 presents low-dose iRADs of three phantoms of different geometry and material composition. In this chapter, the WET achieved with the Residual Range Detector (RRD) under various experimental acquisition-conditions is determined and compared to reference MC *in-silico* [Meyer 2015] and *ground-truth* radiographies. The core topic of this thesis, iCT, is addressed in Chapter 6, where the carbon-iCTs of two different tissue-equivalent phantoms are shown and evaluated also in comparison to the rWEPL obtained from the geometry-based calculation (ground-truth) and the MC simulations.

Finally, the Part IV wraps up the the final remarks of this thesis work. Chapter 7 outlines the use of proton beams for transmission imaging as future prospect of these investigations, together with the possibility to couple single-particle position-tracking detectors to the RRD for these purposes. The conclusions of this thesis work are discussed in Chapter 8, followed by the forthcoming perspectives and the identified necessary improvements to accomplish the desired clinical application of iRAD and iCT to improve ion-beam radiotherapy in the not too distant future.

This thesis work has been pursued on the frame of the German Research Fundation (Deutsche Forschungsgemeinschaft (DFG)) project: *"A novel imaging technique for ion beam therapy: Ion Computed Tomography"*, which aims for the development of a fully integrated transmission imaging system for range monitoring and planar and volumetric medical images reconstructed from actively scanned ion beams.

The best scientist is open to experience and begins with romance: the idea that anything is possible.

Ray Bradbury

2

Foundations of ion-beam therapy and ion-based transmission-imaging

Ion-based transmission images, similar to other imaging modalities, rely on the attainable image-quality at a given patient dose. Planar and volumetric images are reconstructed from highly-energetic, low-fluence, ion-beams traversing the patient and being detected afterwards (see Figure 2.1). The detection method exploited in this work is grounded on the integration-mode detector technology. The signal revealed by this type of detector systems encodes information about the energy deposition of the ion beam traversing and interacting with the material of the object being imaged and the detector. Many physical parameters influence the quality of the transmitted images, since the signal attributes depend upon the distinct Bragg curve (BC) shape, also affected by the lateral and longitudinal beam distortion.

A comprehensive understanding of the physical interactions influencing the BC profile shape is of great importance to accurately interpret the discrete experimental data points and determine image-quality indicators, such as (a) *the radiography spatial resolution*, which relies upon the finite beam size and irradiation steps (also known as Raster Points (RPs)) and the (b) *the range accuracy*, which is inherently limited by the detector granularity and it is connected to the *the density resolution or contrast*. These metrics ultimately determine the quality of the radiography, and, together with the angular sampling of the tomographic image reconstruction, the image-quality of the tomography.

2.1 The physics of ion-beam therapy and its implications in ion-based imaging

In principle, any material encountered along the beam path can potentially modify the shape and trajectory of the beam due to the atomic and/or nuclear interactions. Besides slowing down the beam, the irradiated material might lead to scatter (*Multiple Coulomb Scattering (MCS)*), smear its energy (*range straggling*) and fragment part of it (*nuclear fragmentation*)

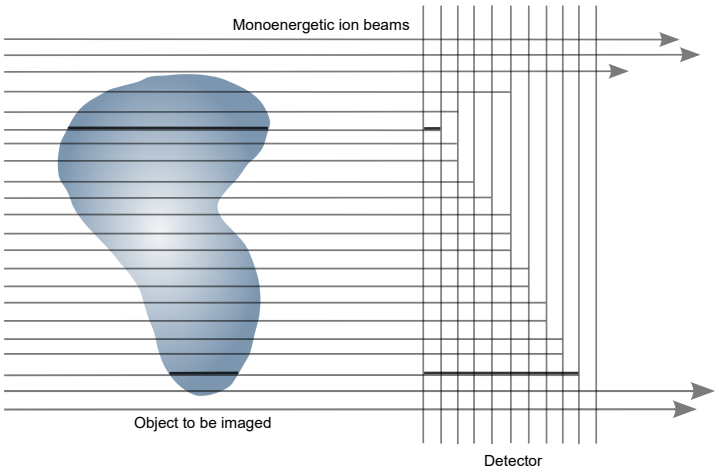

Figure 2.1: Ion-beam radiotherapy requires that the ion beams stop within the tumor to be treated, ion-based transmission imaging, conversely, needs that the ion beams pass through the patient and reach the detector. To this aim, the initial beam energy must be higher than the energy range used for clinical purposes. Adapted from Tobias et al. [1977].

[Chu 1993]. These physical processes that are relevant for our imaging purposes are described as follows.

2.1.1 Stopping power and range of ions in matter: The Bragg peak

Therapeutic ion beams to treat deep-seated tumors (∼30 cm) require maximum energies up to ∼220 MeV for protons and ∼430 MeV/u for carbon ions, which corresponds to particle velocities β of $\beta_p \approx 0.6$ and $\beta_C \approx 0.7$, i.e. a (semi-)relativistic approach should be taken into consideration.

In the therapeutic energy range, ions moving at these velocities through an absorbing tissue decelerate while losing energy mainly due to two stopping processes: (1) *Collisional interactions*, S_{col}, which can be either inelastic Coulomb collisions with the orbital electrons of the target atoms, S_{elec}, or interactions by repulsive elastic Coulomb scattering with the target atomic nuclei, S_{nuc} and (2) *radiative interactions*, S_{rad}, due to Bremsstrahlung radiation emission [Leo 1990]. The total stopping power of a charged particle is therefore expressed as:

$$S = S_{col} + S_{rad} = (S_{elec} + S_{nuc}) + S_{rad}. \tag{2.1}$$

The radiative stopping power, S_{rad}, is inversely proportional to the square of the projectile mass. Hence, Bremmstrahlung generation by heavy charged particles is negligible [Attix 1986; Newhauser and Zhang 2015; Leo 1990]. For radiotherapy applications, the amount of energy loss resulting from Coulomb interactions with the material nuclei contributes less than the 0.1% to the total stopping power [Ziegler 1999]. This contribution is only relevant to the energy loss process for very low projectile energies below 10 keV/u and in the last few μm of the ion trajectory as it is shown in Figure 2.2 [Ziegler 1999; Schardt and Elsässer 2010; Kraan 2015]. In consequence, the slowing-down process is dominated by the electronic interaction, $S \approx S_{elec}$, which is highest at the end of the ion range, causing the maximum energy release within the aimed volume (cf. Figure 1.2). For ions moving faster than the orbital electron velocity, with charged number Z_p impinging to a target material of atomic number Z_t, the

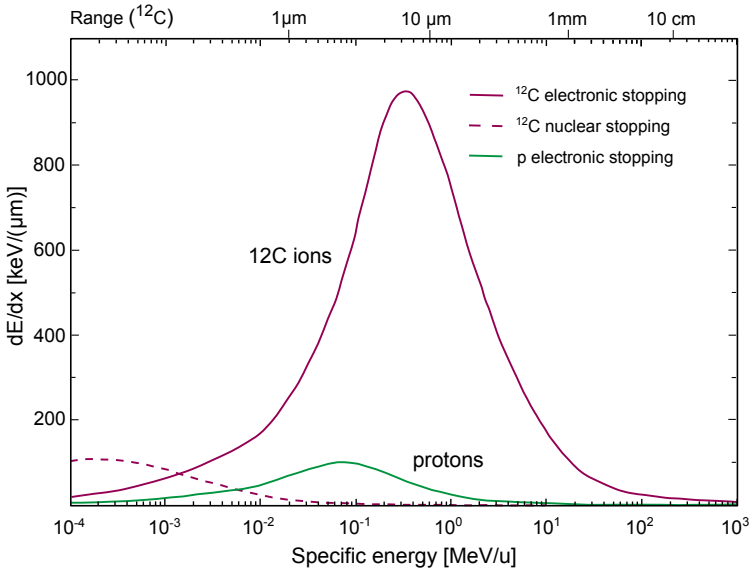

Figure 2.2: Electronic and nuclear energy loss of proton and carbon ion beams per unit path length in water, S. The ^{12}C beam range is indicated on the top scale. Redrawn from Schardt and Elsässer [2010].

rate of the mean energy loss per unit path length, $S_{elec} = {}^{dE}/_{dx}$, is well described by the Bethe-Bloch equation [Bethe 1930; Bloch 1933; Ziegler 1999]:

$$S = -\frac{dE}{dx} = \frac{4\pi e^4 Z_t Z_p^2}{m_e v^2}\Big[ln\frac{2m_e v^2}{< I >} - ln(1-\beta^2) - \beta^2 - \frac{C}{Z_t} - \frac{\delta}{2}\Big], \tag{2.2}$$

where e and m_e are the electron charge and mass, respectively. $< I >$ is the mean ionization energy of the target material, which may vary from about 19 eV for hydrogen to about 820 eV for lead [Newhauser and Zhang 2015].

At extreme energy regimes, Fano [1963] included the last two corrective terms of the equation 2.2: the *density effect* (${}^{\delta}/_{2}$) and the *shell correction* term (${}^{C}/_{Z_t}$). In case of ultra-relativistic particles, a density correction is needed to account for polarization effects in the target material, which causes a slight reduction of energy loss in denser materials [Ziegler 1999]. On the other hand, C is a non-relativistic shell adjustment that corrects the assumption that the ion velocity is much larger than the target electrons velocity [Ziegler 1999]. In the low-energy regime (below ~10 MeV/u), when the particle velocity is similar to the one of the target electrons (≈0.0073 c), partial ion neutralization (recombination) due to electronic capture plays a role in the overall stopping process and shall be considered by replacing Z_p in equation 2.2 by the effective charge (Z_{eff}) derived empirically from experimental data by Barkas [1963]:

$$Z_{eff} = Z_p[1 - exp(125\ \beta\ Z_p^{-2/3})]. \tag{2.3}$$

From the Bethe-Bloch formula, it follows that the inverse dependency of the electronic stopping power on the squared particle velocity, together with energy straggling and nuclear-reactions effects, which are introduced later, cause the distinctive BC profiles shown in Figure 2.3 for proton and carbon ion beams at energies of therapeutic interest.

The stopping power formula described so far applies for pure elements. Body tissue materials are compounds of different elements and the ion beam encounters several of them along its

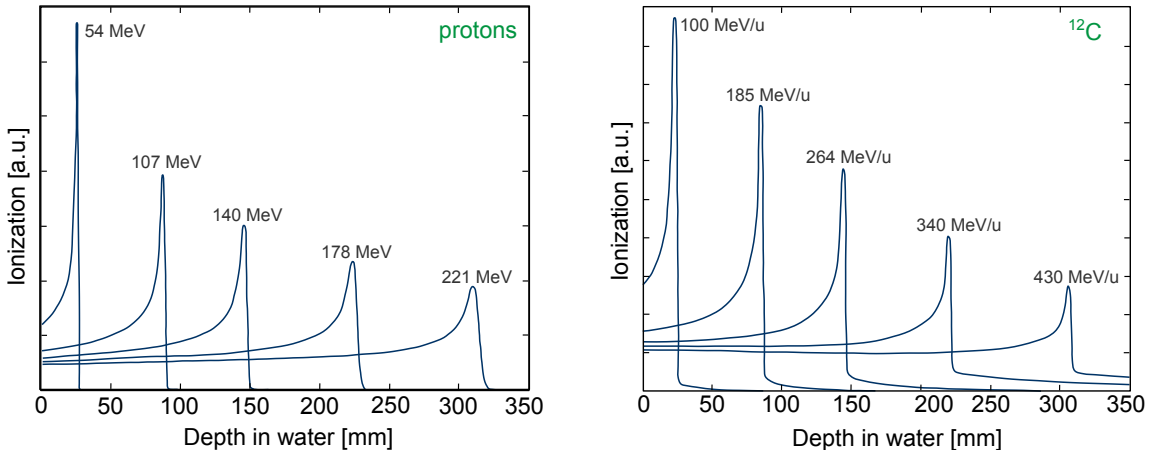

Figure 2.3: Simulated ^{1}H (*left*) and ^{12}C ions (*right*) integral depth-dose profiles at different energies in the therapeutic regime corresponding to the same penetration depth in water.

trajectory. In most of the cases, the so-called Bragg's rule [Bragg and Kleeman 1905] is a good approximation of the S for composite materials. It considers that different atoms contribute nearly independently to the overall stopping power, and hence the effect of S of each element in the compound is additive, counterweighted by the fraction of weight of the different elements present in the mixture [Leo 1990], thus

$$S_{composite} = \sum_i w_i S_i, \tag{2.4}$$

where w_i are the mass fraction of each element in the compound.

2.1.2 Energy and range straggling

Clinical ion-beams are composed by millions (or more) of accelerated ions experiencing different amount of interactions with the medium, therefore most of the physical features that describe them are inherently statistical. The effect of these statistical fluctuations are discussed as follows. It is commonly considered that the energy loss rate occurs by ions slowing down smoothly and continuously, i.e. in a Continuous Slowing-Down Approximation (CSDA) [Berger and Seltzer 1964]. Under this assumption, neglecting any stochastic variation, the total ion penetration depth within the absorber may be calculated as:

$$R(E)_{CSDA} = \int_0^{E_0} \frac{dE}{S} = \int_0^{E_0} -\left(\frac{dE}{dx}\right)^{-1} dE, \tag{2.5}$$

where E_0 is the initial kinetic energy of the particle. The mean range, R_{mean}, is defined as the depth at which half of the primary particles have come to rest [Newhauser and Zhang 2015] as it is depicted in the range-transmission curve in Figure 2.4 [Leo 1990]. In terms of dose distribution, the mean range coincides with the position where the dose has decreased to 80% at the distal dose fall-off of pristine BPs, d_{80} [Paganetti 2012; Gottschalk 2012]. However, in most of the ion beam therapy facilities, the clinically prescribed range is taken at the 90% SOBP distal-edge position in water. Especially in the case of heavy ions, $R(E)_{CSDA} \approx R_{mean}$, due to the minimal deviations along its trajectory (cf. Sections 2.1.2 and 2.1.3).

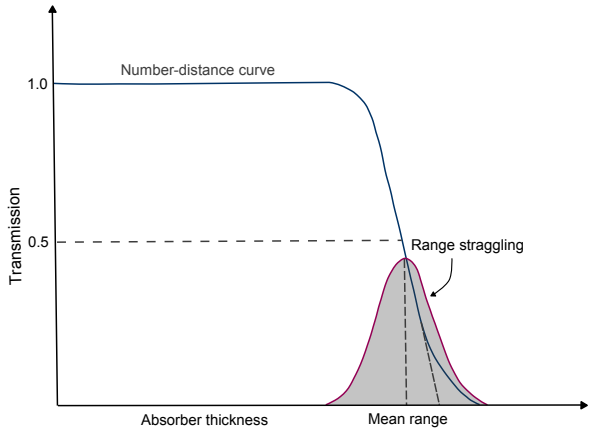

Figure 2.4: Range transmission curve showing the transmitted fraction of incident ions in a beam as a function of the absorber thickness. For short traversed thicknesses, almost all the particles pass through, however as the range is approached, less primary ions survive due to stochastic fluctuations in the energy loss of individual ions yielding a Gaussian distribution of ranges. Adapted from Leo [1990].

The statistical fluctuations of the energy-loss process result in a broadening of the BP of the incident ion beam (*energy-loss straggling*) and, in consequence, a smearing of its range. This phenomenon is known as *range straggling* (cf. Figure 2.4) and it is responsible for the limited density resolution of ion-based radiographies and tomographies.

Different models describe the straggling effect according to the target thickness. For most applications in ion therapy, Bohr's theory for thick layers of matter provides adequate accuracy. This principle states that in the limit of many collisions (i.e. when the central limit theorem holds), the energy or range distributions become Gaussian [Bohr 1940; Lewis 1952]:

$$f(\Delta(E,R)) = \frac{1}{\sqrt{2\pi\sigma^2_{(E,R)}}} \quad exp - \Big(\frac{(\Delta(E,R) - \overline{\Delta(E,R)})^2}{2\sigma^2_{(E,R)}}\Big), \tag{2.6}$$

where the variance of the range straggling, σ^2_R, and the variance of the energy loss, σ^2_E are related by [Schardt and Elsässer 2010]:

$$\sigma^2_R = \int_0^{E_i} \Big(\frac{d\sigma_E}{dx}\Big)\Big(\frac{dE}{dx}\Big)^{-3} dE. \tag{2.7}$$

The width of the range straggling can be also expressed by:

$$\sigma_R = \frac{R}{\sqrt{m}} f\Big(\frac{E}{mc^2}\Big), \tag{2.8}$$

where m and E are the projectile mass and energy, and f is a function that varies slowly and includes the medium dependence [Rossi 1952]. The $1/\sqrt{m}$ factor is the cause that protons show a higher range-straggling than heavier ions. For instance, the range-straggling for ^{12}C ion beams is about 3.5 times smaller than for proton beams for the same range in water [Schardt and Elsässer 2010].

It is common to use power law approximations to estimate the width of the range straggling distribution, σ_R, as a function of the ion beam range and the mass number [Chu 1993; Bortfeld

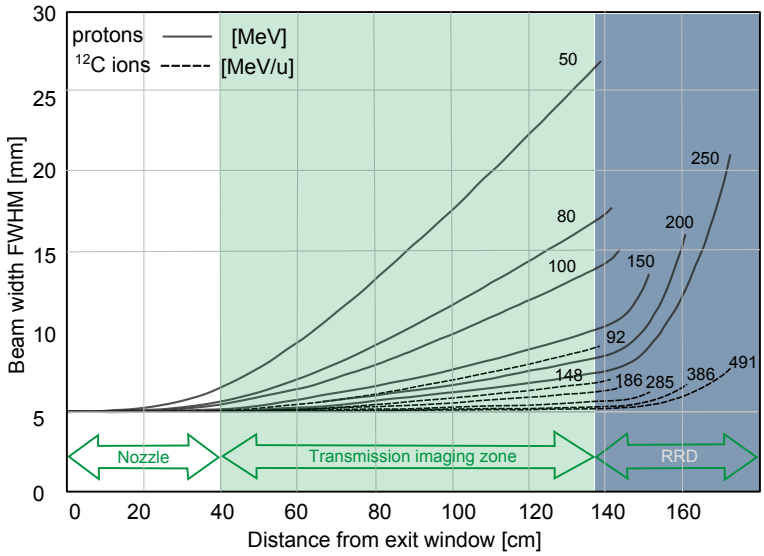

Figure 2.5: Multi Coulomb scattering beam spread effect. Lateral scatterings calculated for a nozzle based on the GSI therapy facility, which is pretty similar to the scanning-therapy setup at the HIT. The beam penetrates through the vacuum windows and the Beam Application and Monitoring System (BAMS) to finally reach the object to be imaged at about 1 m distance (*isocenter*) from the nozzle. After the beam goes through the target, it is detected by a RRD. Adapted from Weber and Kraft [2009].

1997; Newhauser and Zhang 2015]:

$$\sigma_R[cm] = k_w R_w^m = 0.012 \quad R_w^{0.935} A^{-0.5}, \tag{2.9}$$

where R_w is the range in water in centimeters, k is a target-dependent constant of proportionality and m is empirically determined. σ_R almost proportional to the range R and inversely proportional to the square root of the particle mass number A. This difference in range straggling leads to sharper BPs for heavier ions while it reduces the height and increases the width of proton BPs, which in turn, it potentially results in ^{12}C ion-based images of superior depth resolution.

2.1.3 Multiple coulomb scattering and lateral beam straggling

Other consequences of the stochastic nature of charged particle interactions are small deflections of the ions from its original beam path, which are predominantly caused by elastic Coulomb interactions due to repulsive forces from the target nuclei, the so-called Multi Coulomb Scattering (MCS). As it was explained in Section 2.1.1, the contribution of Coulomb interactions with atomic nuclei to the overall energy-loss process is negligible (cf. Figure 2.2), nevertheless, it has important implications in dosimetry and transmission imaging since it causes a considerable lateral broadening of the pencil beam especially for protons. An analytic derivation of the probability distribution of the net scattering angle of emerging ions ($F(\theta, L)$), after traversing some material of thickness L, was well described by Molière. For small deflection angles ($< 10°$), the higher-order terms in Molière's solution can be neglected and an ideal Gaussian shaped spread can be considered [Moliere 1947]:

$$F(\theta, L) \approx \frac{1}{\sqrt{2\pi\sigma^2_{(\theta,L)}}} exp - \left(\frac{\theta^2}{2\sigma^2_{(\theta,L)}}\right). \tag{2.10}$$

The width of the Gaussian function, σ_θ, in equation 2.10 is given by the Highland's formula as [Highland 1975; Schardt and Elsässer 2010]:

$$\sigma_\theta[rad] = \frac{14.1[MeV]}{\beta pc} Z_p \sqrt{\frac{L}{L_{rad}}}\Big[1 + \frac{1}{9} log_{10}\Big(\frac{L}{L_{rad}}\Big)\Big], \tag{2.11}$$

where L_{rad} is the radiation length defined as the distance over which the electrons energy is reduced by a factor of $1/e$ only due to radiation loss within a specific material [Leo 1990]. The term βpc in the denominator of equation 2.11 determines the extent of the angular beam spread at the end of the range, according to its initial energy and momentum. For heavy charged particles, like ^{12}C ions, the beam may diverge few millimeters, whereas protons scatter about three times more when comparing beams with similar range in water. Figure 2.5 shows the lateral beam widening of proton and carbon-ion beams at energies and distances relevant for therapeutic applications.

Analogous to the energy-range straggling, MCS of charged particles in water can be approximated by a power law in terms of the charge Z, and mass A of the incident ions [Chu 1993]:

$$\sigma = 0.0294 R_w^{0.896} Z^{-0.207} A^{-0.396}. \tag{2.12}$$

In transmission imaging, particularly with light ions, the scattering along the beam monitoring system, the phantom thickness and the detector materials becomes a significant limitation for spatial resolution. In order to overcome it, additional position information such as exit coordinates and angles, as well as probabilistic path reconstructions are required. On the contrary, as rendered in Figure 2.5, for the highly energetic carbon-ion beams that we mostly use in this work, the beam lateral spread is minimal. Hence, assuming straight carbon ion trajectories is sufficiently accurate to identify them within the RRD.

Overall, the reduced straggling and scattering offered by heavy ions in contrast to protons, allows for a better depth and lateral resolution for transmission imaging applications. Additionally, the detection of soft-tissue abnormalities and tumors that have similar densities and composition from the surrounding media supports the use of heavy-ions in diagnostic radiology, where enhanced image contrast is required to detect subtle density changes [Benton et al. 1975].

2.1.4 Nuclear interactions and fragmentation

So far, the main electromagnetic processes that contribute to the energy losses of the primary projectiles have been described. However, therapeutic ion beams can also undergo nuclear reactions with the nuclei of the target material. Owing to their mass difference, protons and carbon ions interact differently to the nuclei that they encounter along its trajectory. The proton reaction is at nucleon level and it is modeled according to the so-called *exciton* formalism [Griffin 1966], where protons, neutrons and light fragments are emitted while the residual nucleus reaches the equilibrium state with certain remaining excitation energy [Kraan 2015]. The nuclear interactions experienced by heavy ions are well described by the *abrasion-*

ablation model [Serber 1974]. During the first stage of the interaction, the projectile and target nucleons overlap, creating a reaction zone which is normally referred as *fireball*. During the ablation stage, the remaining projectile and fragments come to rest by evaporating lighter nuclei or fragments. The secondaries from the primary beam hold approximately the same velocities and direction as their originator but lower charges. Therefore, since their range is proportional to A/Z^2 (c.f equations 2.2 and 2.5), they continue traveling and interacting further than the mother particle. On the contrary, the fragments resulting from the target have shorter ranges and both yield to the distinctive BC tail.

In the clinical context, the main consequence of the aforementioned interactions is the exponential reduction of the beam fluence, which is relevant for the design of beam models used by treatment planning systems as well as for range verification methods. As example, considering proton and carbon ion beams with ∼16 cm range in water, roughly 80% of the impinging protons and 50% of the carbons reach the final BP [Cussol et al. 2011], i.e. by increasing the penetration depth and the interaction zone, the Peak-to-Plateau Ratio (PPR) is gradually scaled down as displayed in Figure 2.3. For transmission imaging purposes, it is crucial to keep the detection system noise at low level so that the Signal-to-Noise Ratio (SNR) is large enough to allow the maximum signal identification, which will be associated to the residual range of the primary ions.

2.1.5 Water equivalence

Water is routinely used as a tissue surrogate in ion beam therapy, mainly because of its similar density and Z_{eff} values to most of the body constituents. Hence, the physical behavior of ions in tissue resembles the one in water. Water Equivalent (WE) values serve to *translate* the body heterogeneities and beam path elements (absorbers, BAMS, etcetera) into a well known composition. In a WE system, high-density matter corresponds to ion path lengths larger than that for water, low-density matter to shorter WE ion path lengths. This has two advantages; first, the dose deposition to elaborate treatment plans is calculated or simulated in a homogeneous material, including the inherent density variations of the body; and second, the impact on the residual range of elements used before the patient can be easily accounted as fixed offsets. For instance, at HIT, the beam path length of the BAMS plus 1 m of air matches 2.89 mm of water. In the same sense, water equivalence is also extensively used for imaging as it will be recapitulated in the following sections.

Given a slab of material with thickness t_m and mass density ρ_m, the WET of the material is the thickness of water t_w that results in the same ion range. In consequence, the dimensionless rWEPL also known as SPR_w^m is the stopping power of the material relative to water and corresponds to the ratio t_w/t_m. The concepts of rWEPL and WET are schematically depicted in Figure 2.6.

At HIT, the rWEPL of relevant tissue-equivalent materials is determined experimentally with 0.01 mm maximum resolution by using an adjustable-thickness water column [Sánchez Parcerisa 2012], which measures the range shift in water of the desired material in relation to the reference BP obtained without it.

The WET is often used to characterize the beam penetration range of materials of known

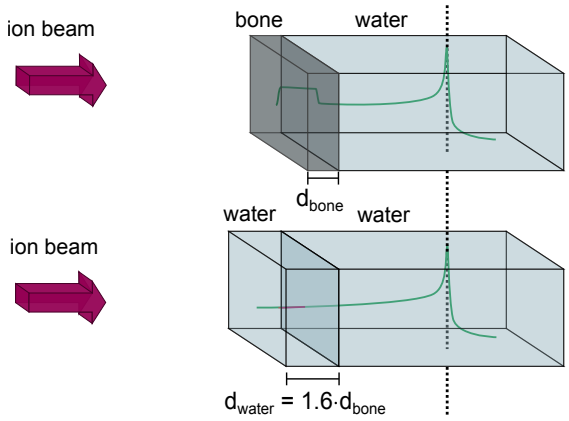

Figure 2.6: Schematic representation of the relative Water Equivalent Path Length (rWEPL) concept. The shifts of the measured BPs for different tissues give their corresponding rWEPL values, when the beam impinges from vacuum into the target, neglecting the displacement due to the air thickness. The denser bony tissue, d_{bone}, is converted to its longer water equivalent, d_{water}, via $d_{water} = 1.6 \cdot d_{bone}$ where $rWEPL_{bone} = 1.6$. Courtesy of S. Meyer in Meyer [2015].

length. According to Zhang et al. [2010], the WE of *radiologically thin* materials[A] can be calculated in terms of the non-corrected Bethe-Bloch equation as:

$$rWEPL = SPR_w^m = \frac{t_w}{t_m} = \frac{\rho_m}{\rho_w} \cdot \frac{\hat{S}_m}{\hat{S}_w} = \frac{\rho_m}{\rho_w} \cdot \frac{(Z/A)_m}{(Z/A)_w} \cdot \left[ln \frac{2m_e c^2 \gamma^2 \beta^2}{< I >} - \beta^2 \right]_w^m, \tag{2.13}$$

where $\hat{S}_m$ and $\hat{S}_w$ stand for the mass stopping power of the material and water, respectively.

Since for typical tissue-like materials the ionization potential does not vary much, it is common to use $< I >= I_{water}$. Especially for materials whose Z differs a lot from water, such as cortical bone, implanted fiducial markers or metal implants [Zhang and Newhauser 2009; Zhang et al. 2010], and at energies lower than 10 MeV [Warren et al. 2015], the SPR of a material displays an energy dependence, which must be taken into consideration for the clinical applicability.

For transmission imaging goals, an accurate WE conversion is relevant for the reconstruction of WET and rWEPL distributions of the phantom and/or patient, which can potentially benefit different stages of the treatment as it will be deepened later. To this aim, the WET of the detector, measured experimentally, is used to calibrate the integrated energy loss in terms of water. Thus, the WET equates the line integral of the rWEPL along the ion path length l, including all the material heterogeneities encountered, i.e.:

$$WET_{object} = \int_0^l rWEPL \; dl. \tag{2.14}$$

[A] A thin target is defined in Zhang and Newhauser [2009] as a medium in which the ion beam loses only a small fraction of its energy. In contrast, a thick target is a material in which the ion energy loss is sufficiently large. This classification depends on the initial beam energy, the material composition, density and physical thickness.

2.1.6 Physical absorbed dose

The physical absorbed dose, D, in a certain volume stands for the statistical average of the energy absorbed per unit target mass at certain point. It is defined by the International Commission on Radiation Units and Measurements (ICRU) as the mean energy (of several energy deposition events from electronic and nuclear interactions), $d\epsilon$, imparted by ionizing radiation in a mass element dm, in SI units [ICRU85 2011]:

$$D = \frac{d\epsilon}{dm} \left[\frac{J}{kg} = Gray(Gy)\right]. \tag{2.15}$$

However, the fundamental physical relationship which is relevant in radiotherapy is the association between the physical absorbed dose, the primary beam fluence and mass stopping power, $\hat{S} = {}^{S}/_{\rho}$ $[{}^{MeV}/_{(g/cm^2)}]$. In this regard, for a mono-energetic parallel beam with particle fluence Φ passing through a thin slice of material of density ρ, the absorbed dose is expressed as:

$$D[Gy] = \Phi\frac{S}{\rho} = 1.6 \cdot 10^{-10} \times \Phi\left[\frac{1}{cm^2}\right] \times \frac{dE}{dx}\left[\frac{MeV}{cm}\right] \times \frac{1}{\rho}\left[\frac{cm^3}{g}\right]. \tag{2.16}$$

In ion beam therapy facilities with active beam delivery system, the dose must be calculated and optimized for each beam to cover the full target volume. This is accomplished by segmenting the target laterally and longitudinally in a three-dimensional scanning grid. To account for the scanning path following the predefined grid, the fluence is expressed as:

$$\Phi(x, y) = \frac{N_{RP}(x, y)}{\Delta x \Delta y}, \tag{2.17}$$

where the Δx and Δy are the scanner step sizes in x and y transversal directions. In order to impart a homogeneous dose distribution to the target scanned area, a trade-off between the approximated Gaussian beam profile and the Δx has to be found by a even overlapping of neighboring beam positions.

This approach is accurate enough when the lateral scanning steps are chosen as a small fraction of the beam width, i.e.,

$$\Delta x = \Delta y \leqslant f_F \times FWHM_{beam}, \tag{2.18}$$

for the Full Width at Half Maximum (FWHM) of the beam at isocenter and f_F being facility-specific, selected empirically according to the beam widths available and the treatment plan complexity. A typical value that fulfills the above-mentioned requirement at Gesellschaft für Schwerionenforschung (GSI) is $f_F = {}^{1}/_{3}$ [Krämer et al. 2000], the HIT facility generally adopts this value, too.

Finally, using the fluence definition, the dose deposited per individual RP by mono-energetic beams yields:

$$D[Gy]_{RP} = \frac{N_{RP}(x, y)}{\Delta x \Delta y} \cdot \frac{S}{\rho}. \tag{2.19}$$

When a high-energy carbon-ion beam traverses the body, it produces fragmentation of some

of the projectiles into lighter species with a broad energy distribution. Hence, a realistic ion-beam will create a mixed, poly-energetic radiation field inside the patient. Therefore, the particle fluence and energy must be replaced by their spectra, the distribution $d(E_{beam}, z)$ should then include the energy spectrum not only of the single-particle energy-loss, but also the energy-loss straggling and the projectile fragmentation [Krämer et al. 2000]:

$$d(E_{beam}, z) = \sum_{T} \int_{E} dE \frac{dN}{dE}(E_{beam}, z, T, E) \frac{1}{\rho} \frac{dE}{dx}(T, E), \tag{2.20}$$

where T represents the secondary particle species formed during the stopping process and $dN(E_{beam}, z, T, E)/dE$ stands for the energy spectra. Under these assumptions, Equation 2.19 can be written as:

$$D(E_{beam}, x)[Gy] = (1.6 \times 10^{-10}) d(E_{beam}, z) \left[\frac{MeV}{g\ cm^{-2}}\right] \cdot \frac{N(E_{beam}, x, y)}{\Delta x \Delta y}[cm^{-2}]. \tag{2.21}$$

In other words, the dose at each RP is a superposition of many elementary beams:

$$D(x) = \sum_{E_{beam}} d(E_{beam}, x). \tag{2.22}$$

2.2 The biology of ion-beam therapy and its implications in ion-based imaging

2.2.1 Ion-beam Linear Energy Transfer and microscopic track structure

What makes a remarkable distinction between proton and carbon ion-beam irradiation is their microscopic spatial energy distribution along the particle tracks, which turns into a different biological effect as it will be presented as follows. The elastic and inelastic electronic interactions described previously cause the excitation and ionization which is responsible for energy deposition in the medium. Those radial ionizations result from target electrons (known as δ-electrons) that are ejected away from their atoms. If they are energetic enough, they might ionize further. These δ-electrons form the striking track structure surrounding the original path of the primary particle. Their kinetic energy varies from tens to hundreds of eV as can be seen from the color classification in Figure 2.7. At the BP region their energy drops usually below 100 eV, which corresponds to a mean free path of few nm [Schardt and Elsässer 2010]. Considering that the Deoxyribonucleic Acid (DNA) strands are separated roughly by 2 nm [Laczko et al. 2004; Amaldi and Kraft 2005], it is very likely that an ionization event occurs exactly there. This also means that the radial dose is confined at the track core and falls off when the radial distance r becomes larger, showing a $1/r^2$ dependence.

Figure 2.7 renders the ionization patterns caused by the halo of secondary electrons around carbon ion tracks compared to the proton ones at different energies in relation to the actual dimension of a DNA double-strand [Krämer and Durante 2010].

There can be, however, few of these δ-rays with a sufficient kinetic energy to travel farther away from the track of the primary ion. In order to establish a limit of the deposited energy prompted by these electrons, the Linear Energy Transfer (LET) concept is introduced. It basically refers to a *restricted electronic stopping power* (based on the equation 2.2) including

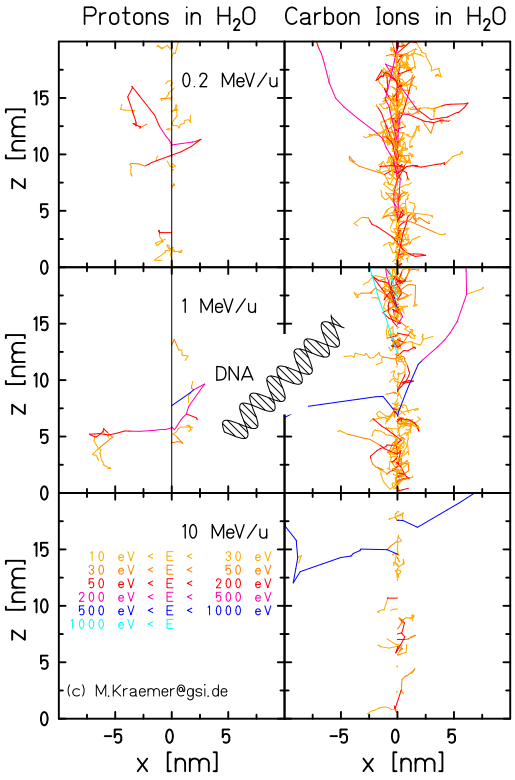

Figure 2.7: Comparison of MC simulated track structure of protons (*left*) and ^{12}C ion-beams (*right*) in water. The lines represent the individual paths of δ-electrons colored according the energy code. The DNA schematics in the middle highlights the nanometric scale of the beam halo [Krämer and Durante 2010].

only the collisions whose transferred energy to the target is lower than certain threshold Δ, i.e. *locally*. The $LET_{\Delta} = \frac{dE_{\Delta}}{dx}$ [ICRU85 2011], expressed in $\left[\frac{keV}{\mu m}\right]$ is usually used in regard to dose delivery and local biological effect, as it will be addressed in the following section.

2.2.2 Radiobiological effectiveness and biological dose implementation

DNA damage of exposed tumor tissue leading to cell death is one of the detrimental effects of ionizing radiation that is exploited, with beneficial consequences, for radiotherapy. The pattern of the discrete energy depositions during passage of the ionizing track of radiation defines the spatial distribution of lesions induced in DNA [Lomax et al. 2013].

Tumor cells can be affected by ionizing radiation in different extent. The harm mainly depends on their repair capabilities, the direct or indirect induced damage and the complexity of the DNA fractures. The electrons liberated in the ionization processes can cause single or double-strand breaks directly, by hitting the bio-molecule straightaway, or indirectly, by means of free radicals that are created in the radiation-induced hydrolysis of water molecules surrounding the cell nucleus [Hall and Giaccia 2012]. There is evidence that single-strand breaks are able to repair rather easily, whereas double-strand breaks eventually result in cell mortality [Hall and Giaccia 2012; Lomax et al. 2013]. Therefore, the latter are preferred for tumor eradication [Taksuahiro et al. 2016].

The biological difference between ion species is evident from its variable LET, which depends on the Z_p^2 and $1/\beta^2$ (cf. Equation 2.2) and consequently results in higher ionization density for heavy ions tracks as it is shown in Figure 2.7. High-LET irradiation, as the one from

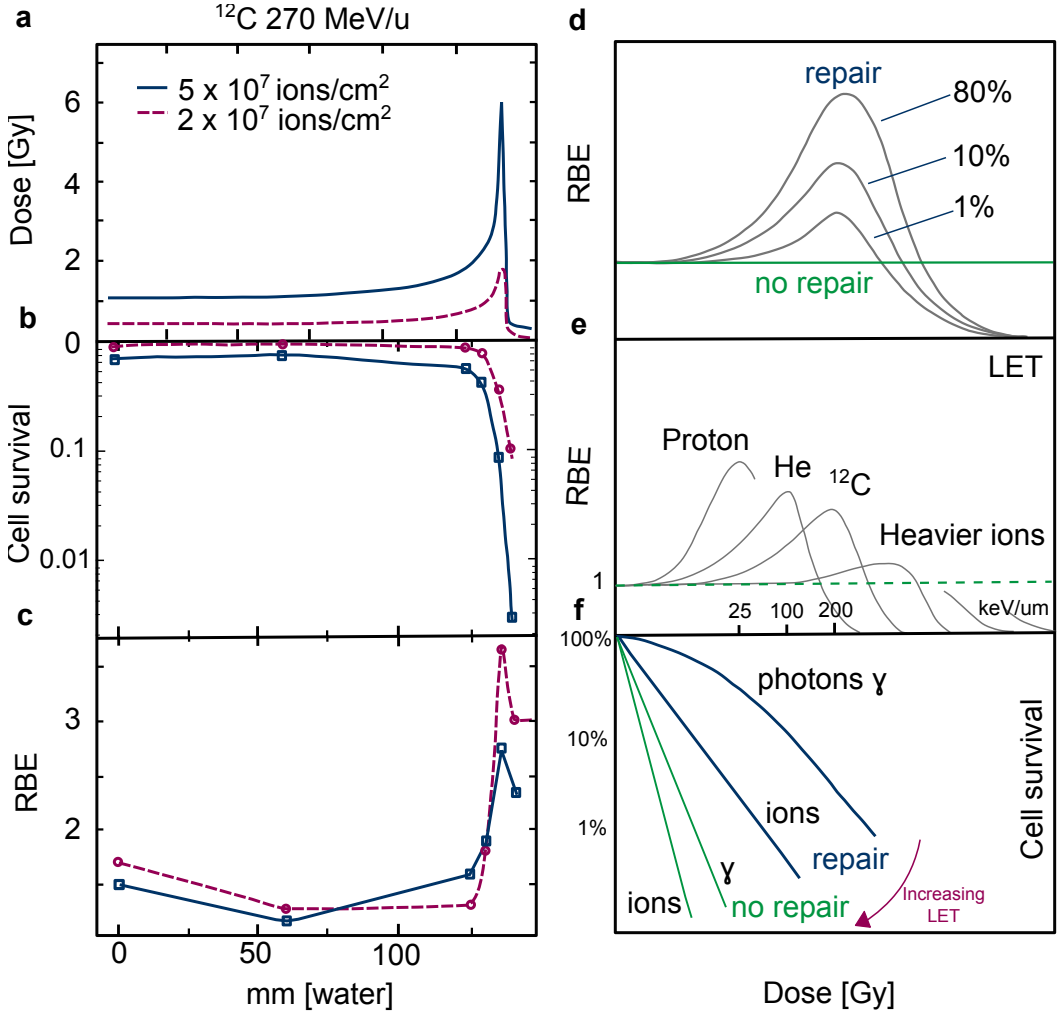

Figure 2.8: Dependencies of radiobiological effectiveness on different factors. (a) Dose profiles (BCs) for $270MeV/u$ carbon ion beams as function of penetration depth in water. (b)Cell survival of Chinese Hamster Ovary (CHO) cells corresponding to the two fluences shown in (a). (c) Calculated RBE relative to photon dose [Kraft 1999]. (d) Variation of the RBE with respect to the LET at 80%, 10% and 1% survival levels according to the different applied dose.(e) Schematic of the RBE-LET relationship for cells exposed to a given dose of different ion types. The difference in RBE associated with increasing atomic number is related to their different microscopic track structure (cf. Section 2.2.1) (f) Survival curves for cultured cells exposed to photons and ions irradiation. As the LET of the radiation increases, the slope of the curves representing the remaining cells gets steeper, and the size of the curve shoulder gets narrower. Adapted from Kraft [1999].

carbon ions, enhances the biological efficacy in the target tumor due to the capability to cause irreparable cell damage by breaking multiple DNA double-strands.

Since most of the actual knowledge about the cell response to ionizing radiation is based on photon radiation exposure, the biological effect of ion radiation is commonly described in relation to a reference photon impact by means of the Relative Biological Effectiveness (RBE) concept. The RBE is defined as the ratio of the dose of X-rays divided by the dose of ion irradiation that results in the same biological effect (*isoeffect*):

$$RBE = \frac{D_{photon}}{D_{ion}}\Big|_{isoeffect}. \tag{2.23}$$

The RBE depends on various parameters such as the biological end point of choice, dose, dose rate, particle type, beam energy, tissue treated and number of radiotherapy fractions, meaning

that the overall biological response of the tumor is highly complex and can vary drastically according to different factors.

As already mentioned in the introductory section (cf. Figure 1.1), the NTCP and TCP are the most relevant biological endpoints to assess the radiotherapy outcome. Among other survival factors, the NTCP reflects the desirable low-risk of normal tissue complications, while the TCP is related to the amount of remaining tumor cells at the end of the treatment. Focusing on the cellular effects, as a particular example, the Figure 2.8 exhibits some of these RBE dependencies by comparing the cell survival of CHO cells (cf. Figure 2.8(b)) along a 270 MeV/u ^{12}C beam dose profile (cf. Figure 2.8(a)) and the RBE (cf. Figure 2.8(c)) for two different particle fluences. At first look, one observes that while the local dose increases with penetration depth, the cell survival decreases from the plateau region where the survival is approximately 60% and 80% till 0.2% and 10% for the two particle fluences respectively. The effectiveness of high-LET doses is apparent in Figure 2.8(c) that shows an $RBE = 3.5$ for the lower fluence and $RBE = 2.5$ for the higher one [Kraft 1999].

The dose association with the RBE as a function of the LET is sketched in Figure 2.8(d), where three different cell killing levels (80%, 10% and 1%) are displayed. Similar to the behavior noticed in Figure 2.8(c), the RBE curve is shallower for higher doses with less tumor cells survive (∼1%). The reduction of the RBE with increasing doses reflects the fact that at high doses the X-ray dose distribution becomes as effective as the localized dose produced by ion beam tracks [Kraft 1999].

The role of the LET in the RBE-dose dependence already suggests that the biological effectiveness is subject to the projectile sort and its initial energy as it is depicted in Figure 2.8(e). As long as the atomic number of the projectiles increases, their RBE maximum location is shifted and shorten towards higher LET irradiation, i.e. heavier ions. In addition, RBE increases with LET up to an ion-dependent maximum value related to the limit of dose deposition, after which any extra LET is considered wasted because it does not provide additional biological benefit.

Figure 2.8(e) also indicates that even at equal LET values, RBE can strongly differ, suggesting that the neither the energy transferred locally to the target nor the range of different ion types are accurate predictors of the resulting RBE [IAEA and ICRU 2008]. Given a high-LET particle track, its radial dose halo is determined by the maximum path length of the δ-electrons (cf. Section 2.2.1), which in turn depends on the primary beam energy. Higher projectile energies therefore correspond to larger pathway diameters, scarce ionization density and lower RBE values.

Finally, typical cell survival curves in Figure 2.8(f) make evident that the RBE and cell lethal effects are correlated with dose and LET changes.

In Figure 2.8(f), a pure exponential survival curve without the characteristic shoulder of the photon dose-effect curve indicates absence of cell repair and does not show a pronounced RBE peak in Figure 2.8(d). On the contrary, radioresistant cells show an apparent RBE maximum. In this regard, the enhanced RBE offered by high-LET radiation is also beneficial to treat poorly oxygenated hypoxic regions in the tumor volume which commonly present radioresistance too [Lomax et al. 2013; Schardt and Elsässer 2010].

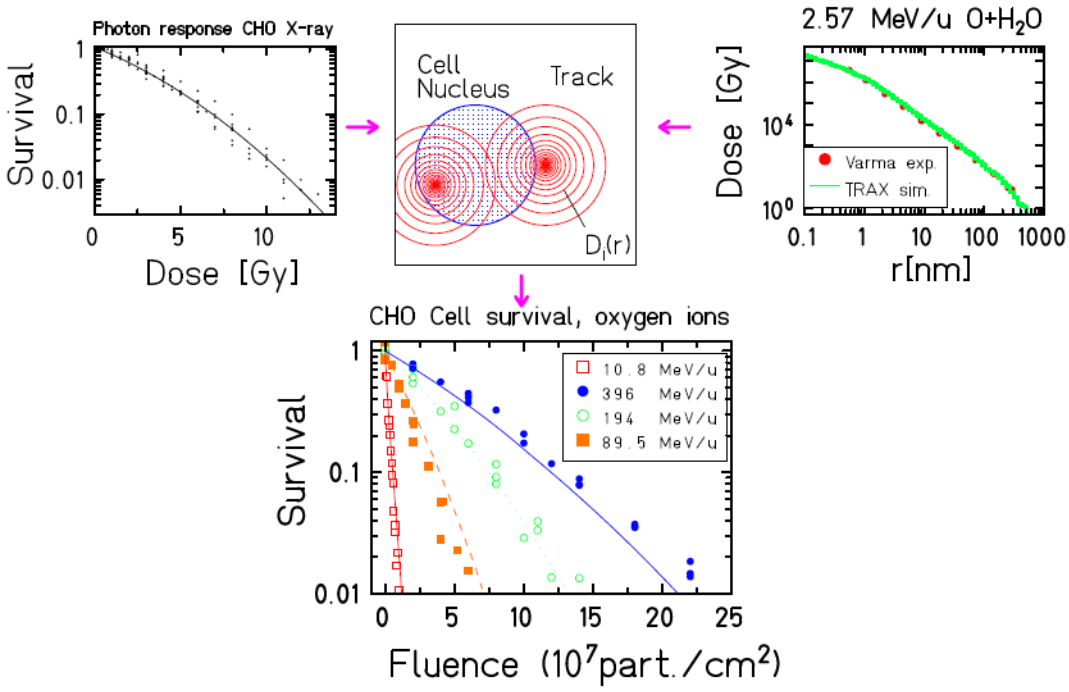

Figure 2.9: Local Effect Model (LEM) principle: experimental photon dose response combined with radial dose distributions around an ion track on a cell nucleus yields survival curves. [Krämer and Durante 2010].

The RBE is a very meaningful quantity in biological treatment planning of heavy-ion therapy, since it determines the biological-effectiveness of ions relative to photons. Weighting factors, W_{ion}, are defined to account for the radiation quality of different ion types, taking into account the ion-track structure and cell response. Hence, the product of the absorbed dose and W_{ion} is often referred as *weighted absorbed dose*, D_{RBE} $[Gy(RBE)]$ *(Gray-equivalent)*.

In the current application of charged particles for radiotherapy, a generic $RBE = 1.1$ for low-LET protons is adopted [Paganetti et al. 2002; ICRU78 2007]. However, given the intricate nature of the RBE, the investigation into variable RBE values also for protons has been increasingly growing towards defining more accurate biological models as has been done for heavier ions [IAEA and ICRU 2008]. The reviews by [Carabe et al. 2012] and [Paganetti 2014] delve into the state-of-the-art models of radiobiological effectiveness of proton irradiation.

Cell survival curves as the ones shown in Figure 2.8(f) are used to experimentally quantify the biological effect of ions compared to classical treatment with photons. In order to parametrize the cell survival s, the Linear-quadratic (LQ) model assumes that two factors determine the cell killing by radiation, one depending linearly to the dose, D, and another quadratically [Hall and Giaccia 2012]. Hence, being α and β tissue-dependent experimentally determined parameters, the cell survival curve is expressed as:

$$s(D) = exp(-\alpha D - \beta D^2). \tag{2.24}$$

The entangled RBE dependencies described previously make the assistance of a track structure-based modeling necessary in order to characterize the biological effect of ion beams in the clinical practice. At the HIT facility, the so-called Local Effect Model (LEM) is applied [Scholz and Kraft 1994; 1996], which determines the RBE of heavy ion irradiation by averaging the

local biological effect for the interaction volume and comparing it with the effect of photons at the same dose, as it is depicted in Figure 2.9. The main physical parameters that provide this information are the nucleus size, the $^{\alpha}/_{\beta}$ photon curve and the radial dose distribution, $D(r)$, where r is the distance from the track core [Laczko et al. 2004]. Simpler biophysical models, relying on linear regression analysis of the RBE-LET relationship, can be found in [Ando and Kase 2009; Jones 2015]. Additionally, upgraded versions of the originally stablished LEM are treated in [Grün et al. 2012].

From the point of view of the transmission imaging principle, the RBE values that are relevant to determine the biological dose received by the patient would be the ones at the plateau BC zone, since this is the region that would be exposed (cf. Figure 2.1). Differently from treatment purposes, the carbon beam fluence used for transmission imaging is lowered at least three orders of magnitude (from $\sim 10^6$ to $\sim 10^3$ ions/RP), thus strongly reducing the physical dose and, in consequence, the track is not heavily ionizing.

Unfortunately, there are no experimental data available on these effects within the dose range involved in these studies, namely in the order of 1 mGy (per single projection). Furthermore, it is unclear whether single cell effects are at all related to the long-term response of complex organisms at these low doses [Hanson et al. 1981]. At clinically applied doses, the radiobiological research available for the plateau region exposure includes the skin as dose-limiting tissue indicator for radiation effect, which might give a hint of the expected biological effects related to the plateau low-dose exposure. Opposite to protons, which do not show apparent RBE variation on fractionation nor location along the BC ($RBE \approx 1.1 - 1.4$), carbon RBE data for skin response show much more dependence on beam location and dose fractionation parameters [Raju and Carpenter 1978; Schulte and Ling 2012], varying in a range of $RBE \approx 1.2 - 2.0$ [Ando et al. 1998; Zacharias et al. 1997; Kagawa et al. 2002]. Nevertheless, skin sensitivity response studies are usually performed in a different time scale than the ion radiographies or tomographies are supposed to take place, which also influences the final RBE prediction. Therefore, this statement should only be considered as a rough consideration to show the need of a deeper investigation regarding normal tissue toxicity under transmission imaging low-dose conditions. This work, nonetheless, includes physical dose approximations based on MC simulations which will be addressed in the part three.

2.3 Technological implementation of ion-beam therapy

2.3.1 The Heidelberg Ion Therapy Center (*HIT*)

Ion beam radiotherapy requires a particle accelerator capable to speed up heavy ions up to about 0.7 c to be able to traverse at least 30 cm of water in order to reach deep-seated target volumes within the human body. To this aim, it requires kinetic energies of several hundreds of MeV/u and beam intensities (particle delivery rate) up to typically 10^8 or 10^9 particles per second (pps), depending on the target treatment [Muramatsu and Kitagawa 2012]. An accelerator dedicated for medical applications must guarantee a reliable machine operation and extreme care in beam control for patient safety [Schardt and Elsässer 2010]. Both synchrotrons and cyclotrons have been used to produce charged particle beams for medical applications; however synchrotrons are specially suitable for ion beam therapy applications since they allow to accelerate ions heavier than protons. Moreover, they allow multiple choice of ions to make

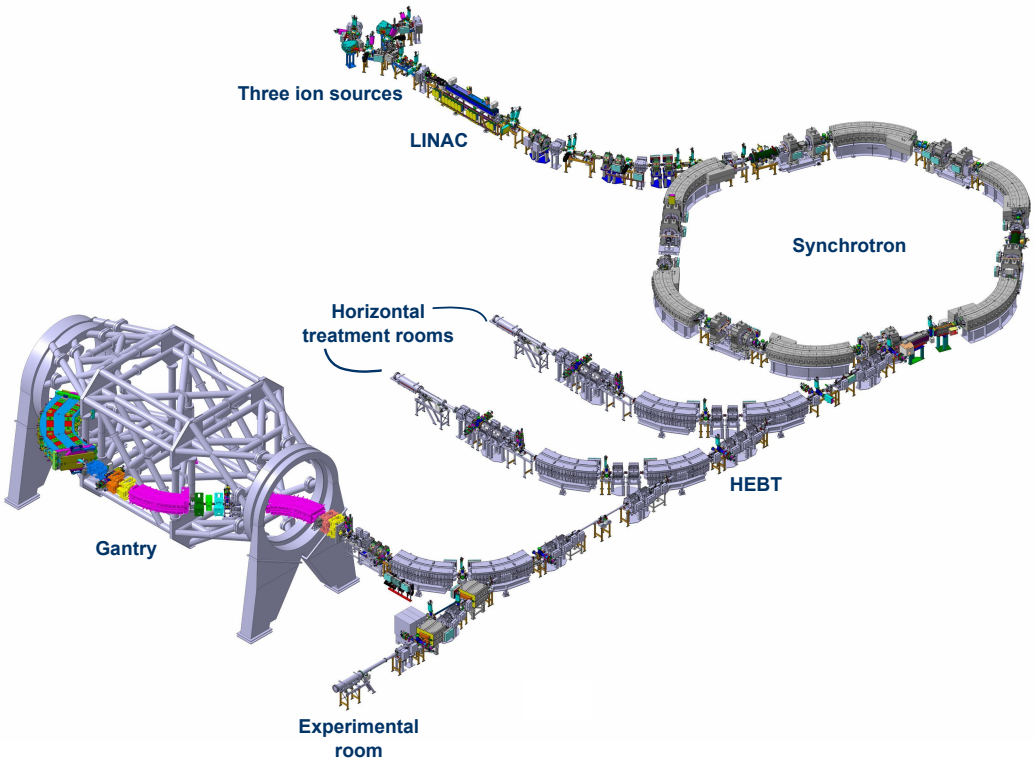

Figure 2.10: Overview of the HIT accelerator complex, where ^{1}H, ^{4}He, ^{16}O and ^{12}C-ions are produced in three different ion sources and then injected into a two-staged LINAC to be accelerated up to 0.1 c [HIT]. Subsequently, the charged particles are driven towards the synchrotron ring. The ion beam is transported along the High-Energy Beam Transport (HEBT) line to the four irradiation stations. Figure courtesy of Christian Schömers in Schoemers et al. [2015].

the most of the physical and biological properties of different charged particles for oncological treatments. For either type of accelerator, the particle species, the beam energy and its spread, the intensity, beam size and divergence as well as the time-structure of the extracted bunch of particles have an impact on the patient treatment [Chu 1993].

The *Heidelberg Ion Beam Therapy Center* (HIT, cf. Figure 2.10) [Haberer et al. 2004] is an outstanding 119-million euros multi-ion therapy facility, actively operating since November 2009. Since then, more than 2500 tumor cases have been treated with protons and carbon-ions using the intensity-modulated raster scanning method (cf. Section 2.3.3) [HIT; Haberer et al. 2004; Combs et al. 2010; Schoemers et al. 2015]. To complement the highest irradiation precision at HIT, the world's first 360° rotating beam delivery system has been established, being operated by a 13 meters diameter gyratory gantry, thus enabling to direct the therapeutic beams at patient-specific optimal angles. Moreover, each treatment is supported with high-precision robots for automated imaging and exact patient positioning [HIT; Nairz et al. 2013]. Nowadays, the routine operation is fully established with up to 60 patients per day [Peters 2016].

As it is shown in Figure 2.10, the HIT complex has three radiotherapy rooms for patient treatment with active scanning (two of them equipped with a fixed horizontal beam line, while the third one is dedicated to the isocentric gantry) and one experimental area reserved for Quality Assurance (QA), technical and scientific research. The experimental campaigns to obtain the ion-based images presented in this work were all performed at the latter.

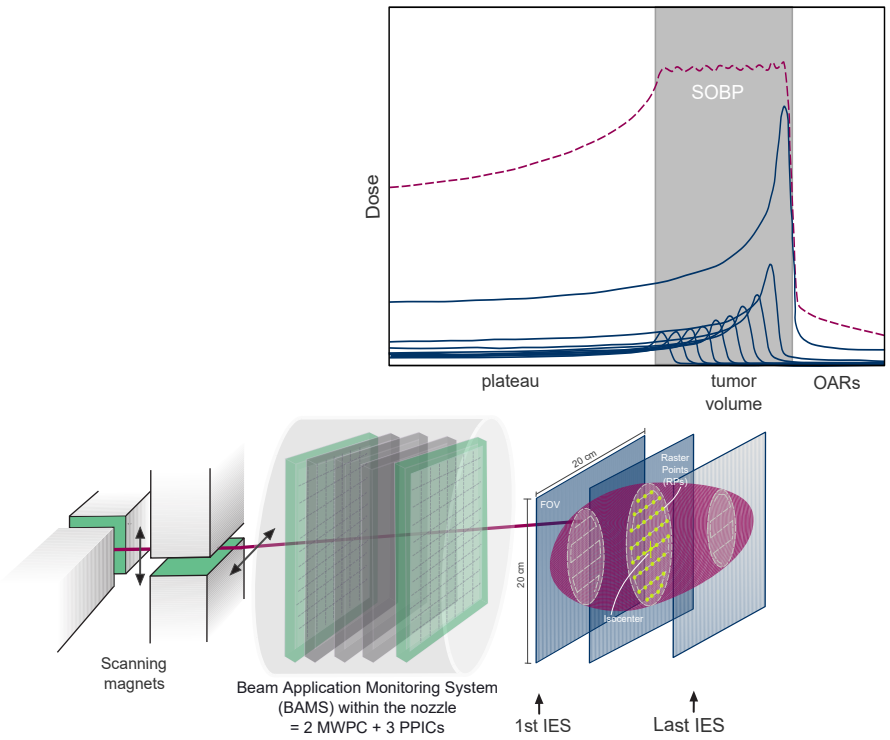

Figure 2.11: Schematic irradiation process for a tumor treatment dose delivery with ion beams. The target volume is virtually dissected in slices of equidistant particle ranges, and it is covered longitudinally from the distal to the frontal Iso-Energy Slice (IES) by varying the beam energy and transversely by displacing the beam with scanning magnets.

2.3.2 The multi-ion synchrotron at the HIT

The HIT facility comprises three ion sources that provide ^{1}H, ^{4}He, ^{12}C and ^{16}O-ion beams, out of which carbon-ions and protons are currently used for therapy, whereas helium and oxygen ions are only used experimentally at the moment. However, commissioning towards their clinical application is ongoing. The ion sources are followed by an injection LINAC of less than 10 m length and finally by a synchrotron ring with a circumference of ∼65 m with maximum magnetic rigidity of Bρ = 6.6 Tm (cf. Figure 2.10).

The fundamental beam properties for all ion types provided by the synchrotron are compiled in the List of Ion Beam Characteristics (LIBC), the accelerator database where 255 initial beam energies per ion sort (48 to 221 MeV for protons and 88 to 430 MeV/u for ^{12}C ions) to cover target depths from 2 to 30 cm are available. These energies are separated by a step width of 1 mm range in water for medium energies and 1.5 mm for higher energies. The LIBC also includes the typical intensity range of protons, which varies from $8 \cdot 10^{7}$ to $4 \cdot 10^{9}$ pps and from $2 \cdot 10^{6}$ to $1 \cdot 10^{8}$ pps for carbon ion beams. In addition, four different foci (i.e., the FWHM of the lateral beam sizes in air, at isocenter) are used in the clinical practice at HIT, diverging from 4 mm to 30 mm [Parodi et al. 2012b]. The discontinuous beam is extracted gradually out of the accelerator ring by 5 seconds interspersed macroscopic pulses (commonly called *spills*) by means of RF-knockout (RF-KO), which allows controllable spills for a precise beam position and intensity monitoring and highly safe dose delivery [Noda et al. 2002; Schoemers et al. 2015].

2.3.3 3D-active scanning beam delivery system

At the HIT facility, a 3D-dose-controlled spot scanning delivery system for each patient treatment is implemented [Haberer et al. 1993]. The clinical target volume is virtually segmented longitudinally and irradiated slice-by-slice from the distal to the frontal edge of the tumor. The beam is magnetically deflected in traversal directions to follow a sequential *zig-zag* path of equally-spaced scanning steps (Δx, Δy) or RPs. The beam remains in each RP until the prescribed dose has been reached individually, thereupon it moves to the next one. The maximum Field-Of-View (FOV) at isocenter is a $20 \times 20\ cm^2$ extended area. The Beam Application and Monitoring System (BAMS) is an ensemble of beam-verification devices in charge of controlling and guiding the beam according to the required treatment plan. The BAMS is located at the end of the beam line already inside of the treatment room; it includes three ionization and two Multi-Wire Proportional Chambers (MWPCs) necessary to monitor the beam intensity, width and location to achieve the prescribed dose distribution within the target with the highest precision (cf. Figure 2.11 and Table 2.1 for ionization chamber properties). The beam information (position and intensity) collected by the BAMS is also the input for the dedicated signal that triggers the DAQ of the transmission imaging system, as it will be detailed in Section 3.4.1.

Table 2.1: Parameters of the PPICs inside the BAMS at HIT

PPIC gas	Ar (80%) and CO_2 (20%)
PPIC gap width	2 cm
PPIC output current	3 - 17,000 nA
PPIC W-value$_{Ar}$	26 eV
PPIC W-value$_{CO_2}$	34 eV

The beam delivery and treatment planning systems must consider that the ion-beam passing through all these devices, including the ∼1 m air drift space between the BAMS and isocenter, undergo an overall shape deformation due to the beam energy straggling and scattering described in Sections 2.1.2 and 2.1.3, respectively.

In a treatment-like scenario, longitudinally homogeneous physical dose distributions (SOBPs) are necessary to cover the tumor volumes (cf. Figure 2.11), for which the beam must be swept through a sequence of Iso-Energy Slices (IESs). Inhomogeneous dose distributions at different IESs are possible and effectively implemented in the clinical work-flow by the recently developed intensity feedback system [Schoemers et al. 2015]. In this respect, transmission imaging requires a much simpler irradiation application, since only one individual IES and a fixed number of ions per RP are needed per projection. Transmission images are then obtained by irradiating the desired FOV with a reduced number of ions per RP, well below the standard values intended for treatments. Aiming at decreasing the dose to the patient as much as achievable, low-dose scenarios were explored in the investigations of this thesis by operating the HIT accelerator in research mode (cf. upcoming section for definition and Section 3.3 for details).

2.3.4 Safety and operation communication

The HIT facility operation chain is a synergy of the accelerator devices and the medical systems. An effective communication between the two parts, by means of software and hardware

interfaces, has to be established in order to assure qualified patient treatments. This system interrelation also ensures that the beam can be redundantly qualified in case of emergencies [Peters 2016]. On the clinical side, the fully-integrated particle therapy solution from *SIEMENS*, known as *IONTRIS* [Rohdjeß 2011], encompasses the DICOM-RT and *Syngo* (*Syngo PT planning; Siemens Oncology Care*) systems, work-flow optimization (irradiation authorization and beam requests), the patient handling through dedicated robotic devices and the Therapy Control System (TCS) that manages the Personnel Safety System (PSS) [Scheloske et al. 2008] and the LIBC available for treatment selection.

On the accelerator side, the Accelerator Control System (ACS) is in charge of the automatized diagnosis, generation, guidance and safety monitoring of the ion beam, according to the more than 100,000 combinations of beam energy, intensity and foci that can be requested by the TCS [Schoemers et al. 2015]. The ACS tasks are performed in time-spans that vary from μs to ms [Mosthaf et al. 2008]. In consequence, the possible accelerator system states are either TCS-mode, ACS-mode or IDLE. Only one of the two control systems is allowed to allocate the beam to only one room at a time.

The information exchange between the TCS and the ACS mainly consists of one digital connection commanded from one of the Therapy Control Units (TCUs) to the ACS master. Each of the control rooms has its own TCU. Through this interface the user can call the beam from the ACS, switch TCU-operation submodes or quit interlocks generated by the TCS itself [Fleck et al. 2008].

With a suitable irradiation plan, the accelerator can be operated from all the treatment rooms in four different modes, which mainly differ on the system memory repository used to render the accelerator features, the interlocks and the robots configuration [B], namely:

- *Treatment mode.* In patient treatment mode, the accelerator settings are ordered from the system flash memory, the interlocks and robots direction is imposed by the TCS for the highest safety constraints. This means that the TCS directly commands the patient positioning and the scanning magnets to deflect the beam across the tumor volume according to the treatment plan, and monitors the scanning course with the BAMS, which works as interlock operator.

- *Technical mode.* When the technical mode is activated the accelerator parameters are allocated in the flash memory of the system, as well. There is a default technical interlocks configuration, which is used for the accelerator maintenance and service.

- *Research mode.* In research mode, the accelerator settings come from the system Random-Access Memory (RAM) and the interlocks configuration is the same as the technical one. However, it may be adjusted by the user, as it was the case for the experiments with under-clinical doses carried out in this work.

- *Remote mode.* As its name indicates, this configuration allows the accelerator to be fully controlled remotely by the ACS.

[B] Private communication with J. Naumann. Heidelberg, 2016

The irradiation plans are requested by loading a customized plan, the so-called Physical Beam Plan (PBP), through the TCS. Each IES is irradiated by following a complex and systematized Transistor-Transistor Logic (TTL) sequence of instructions and/or interlocks that is put in a nutshell in the list below:

1. The TCS requests a certain IES to the ACS. The ACS sends a receipt confirmation back to the TCS.

2. The TCS allows the ACS to start accelerating the ions without extracting them.

3. The TCS resets the BAMS to be ready for the new scanning according to the required parameters. Meanwhile, the ACS verifies the state of the accelerated ions and announces whether it is prepared to deliver them.

4. The TCS authorizes the irradiation and inspects the treatment delivery progress (via the BAMS).

5. The ACS continues the spill(s) extraction until it is notified by the TCS that the last RP has been irradiated. In case that there are some ions left in the accelerator by then, they should be dumped.

6. The cycle is completed and both systems are settled for the next IES request.

The data recording and follow-up of these processes are fundamental for QA as much as for maintenance and research purposes. The Process Data Generation (PDG) underlies the log-file rendering of the accelerator activity. From a PBP, a Machine Beam Plan (MBP) is created by the PDG, to be interpreted by the ACS. Once the MBP is performed, the irradiation is documented in the Machine Beam Records (MBR), relying upon the beam-control data collected by the BAMS. Immediately, the PDG translates the MBR into the isocenter coordinate system, this information comprises the Physical Beam Records (PBR). Later in the course of this thesis, the role of these records on the experiments and data processing will be explained.

These files include individual RP time-stamps, beam coordinates measured by the MWPCs and the charge collected by the BAMS PPICs, among other features related to the most recent irradiation.

2.3.5 Sources of uncertainties in ion-beam therapy

Ion beam radiotherapy can be considered as a *'two-edged sword'*. On one hand, the physical and biological features of ion beams (cf. Sections 2.1 and 2.2) make them extremely favorable to confine the desired dose in complex target volumes. However, on the other hand, the dose gradients at the end of range in the BP are highly steep (cf. Section 2.1.1), which can cause severe cold or hot-spots in the overall dose distribution when they are not correctly applied. In consequence, as stated in Knopf and Lomax [2013], this gradient is rarely used to spare critical normal tissues due to such worries about its exact position in the patient.

The main sources of uncertainties occurring prior to and during treatment are presented as follows:

Pre-treatment uncertainties

Considerable range uncertainties might come already before the treatment delivery during the imaging process, dose calculation and patient positioning.

Imaging-related uncertainties have to do with inherent Computer Tomography (CT) artifacts (e.g. due to metal implants, noise, beam hardening and/or partial volume effects [Barrett and Keat 2004]), as it will described in detail in Section 2.4.1. Image noise can add variations up to $\pm 1\%$ of the CT values. Beam hardening, on the other hand, may have a larger effect; depending on the tissue position, object size and density, the CT calibration procedure might cause uncertainties of the order of $\pm 1.8\%$ of the CT-value assigned to bony structures and $\pm 1.1\%$ in soft tissues (cf. Figure 2.13). These uncertainties may produce errors in the BP fall-off position in the order of 1 to 3 mm [Schaffner and Pedroni 1998]. The Hounsfield Unitss (HUs) of certain materials can vary also according to the CT imaging procedure with different CT scanners [Moyers et al. 2010].

Tomographic reconstruction artifacts due to the presence of metal implants made out of steel or titanium, may underestimate the ion range in the TPS up to 5% and 18% for hip prosthesis [Jäkel and Reiss 2007], while gold implants in prostate cancer may yield 31% difference in the Clinical Target Volume (CTV) dose calculation [Giebeler et al. 2009]. Artifacts from gold teeth fillings have shown range variations in the order of 3% [Jäkel and Reiss 2007].

These imprecisions are directly reflected on the CT-HU to ion rWEPL calibration [Minohara et al. 1993; Schaffner and Pedroni 1998; Jäkel et al. 2001]. Paganetti [2012] reports the pure uncertainty due to rWEPL conversion being on average $\sim 0.5\%$.

Dose calculation uncertainties may also arise from the physical models to define the beam shape and medium ionization potential ($<I>$).

During-treatment uncertainties

Uncertainties in the exact position of the distal dose falloff during the treatment arise mainly from organ motion, patient setup and anatomical variations.

Organ motion includes inter- and and intra-fraction motion. In the case of active delivery, the major effect of the latter is the interplay with respiratory motion, with a frequency similar to that of the scanned beam which can cause severe off-dose in the target volume [Knopf and Lomax 2013]. Moving targets may undergo considerable dose deviations up to 20% in the CTV when the treatment plan is optimized to maximize the OAR sparing and no motion mitigation is used. Moreover, there are cases in which even inter-fraction errors cannot be compensated by using extended Planned Target Volume (PTV) margins, implying that more sophisticated tools are needed for uncertainty management and assessment at the treatment planning level [Lomax 2008]. Patient positioning errors can typically cause range deviations in the order of 0.7 mm [Paganetti 2012]. Patient-specific anatomical variations constitute the major contribution to treatment delivery uncertainties, since changes in the patient weight or cavity fillings could induce beam-range deviations up to few centimeters.

All the uncertainties mentioned above are currently taken into account in clinical practice by the use of target-definition and proper selection of the beam incident directions. Target safety margins accounting for these uncertainties might be as large as 3.5% of the range + 1 mm in depth in certain facilities [Paganetti 2012]. Reducing the uncertainty levels would allow to

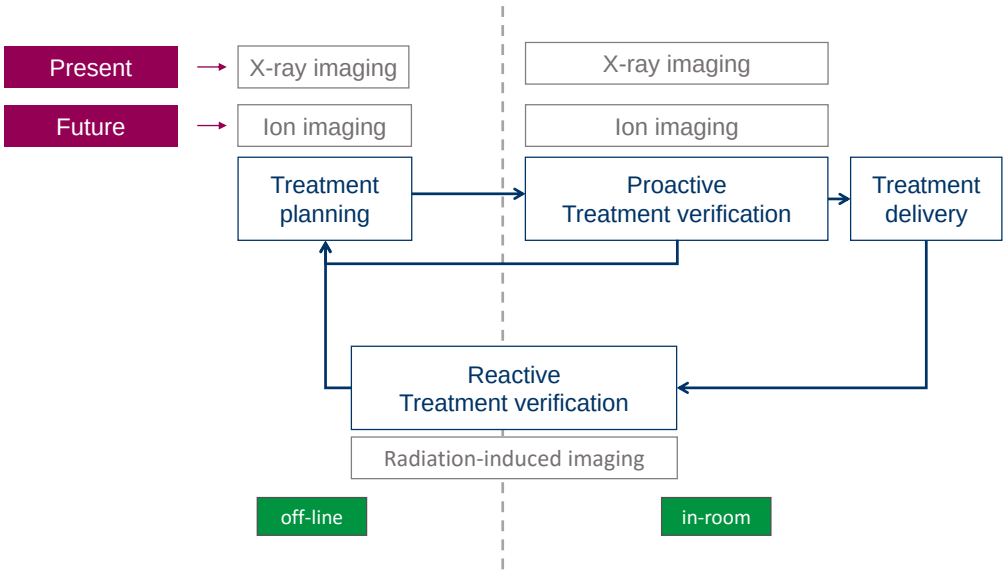

Figure 2.12: Flow-chart of imaging procedures carried out during the clinical work-flow, showing the role of the X-ray-based imaging techniques used nowadays and the perspectives in the application of the proposed ion-based imaging methods. Courtesy of C. Gianoli.

reduce the treatment volume and thus obtain a higher benefit of the advantages of ion beams [Paganetti et al. 2002]. Most of the uncertainties presented so far can be potentially addressed and substantially reduced with an adequate use of novel imaging techniques mentioned already. However, special attention is dedicated in this work to ion-based transmission radiography and tomography.

2.4 Rationale of ion-based transmission imaging in ion-beam radiotherapy

2.4.1 The role of medical imaging in ion-beam radiotherapy

The more precise a radiation therapy is, the more important is the quality control of the patient treatments [Schneider and Pedroni 1995]. Following the classification by Seco and Spadea [2015], the currently available or still under development imaging technologies tailored to ion-beam therapy (cf. Figure 2.12) can be applied at three different stages of the treatment:

- Stage 1: Pre-treatment imaging
- Stage 2: During-treatment imaging
- Stage 3: Post-treatment imaging

Stage 1: Pre-treatment imaging

This treatment phase includes the patient diagnosis, target contouring, margins definition and treatment planning. Helical single-energy X-ray-CT is the current imaging standard used worldwide at this stage of the radiotherapy and the HIT is not an exception. A CT image represents the spatial distribution of photon linear attenuation coefficients, which is typically

described by the HU scale, ranging from air: -1000 to cortical bone: +3000, being by definition 0 for water. Therefore, the HU value of a certain material, m, can be obtained as:

$$HU_m = 1000 \cdot \frac{\mu_m - \mu_{H_20}}{\mu_{H_20} - \mu_{air}}, \tag{2.25}$$

where μ_m, μ_{H_20} and μ_{air} refer to the linear attenuation coefficients of the imaged material, water and air, respectively. Often μ_{air} is neglected from the equation 2.25, since the attenuation coefficient of air is close to zero. In certain cases, CT images are co-registered with images obtained from other imaging modalities, such as Magnetic Resonance Imaging (MRI), Single Photon Emission Computed Tomography (SPECT) or Positron Emission Tomography (PET), that enhance the contrast or metabolic active regions of the structures to be delineated. Hybrid imaging modalities such as PET-CT and PET-MRI also may provide supplemental information for better diagnosis than the conventional anatomical imaging, combining the high spatial resolution of CT or MRI fused together with molecular, functional and physiological information [Schiepers and Dahlbom 2011; Nensa et al. 2014].

For the acquisition of the first treatment planning CT, skin or mask marks are drawn to indirectly localize the target position, which corresponds to the center of the target volume defined by physicians, based on external surrogates [Nairz et al. 2013]. The TPS must determine the biological dose per each voxel on the 3D grid of CT diagnostic images, taking into account the complex dependency of the RBE on several irradiation parameters (cf. Section 2.2.2). A trustworthy TPS for ion-beam radiotherapy strongly relies on accurate and efficiently calculated dose distributions based on the macroscopic physical beam-model inside the body tissue and the biological effect evaluated by the LEM, previously introduced. The accuracy of the dose distribution should be better than 5% on average and the position of single BPs should be reproduced within 0.5 mm (i.e. normally 1/2 CT voxel) [Krämer and Durante 2010].

The rWEPL explained beforehand is a fundamental quantity for the analytical dose calculation carried out by the TPSs used in ion beam therapy, since it assumes that the body is entirely made out of water [Krämer et al. 2000]. The HU values (cf. Equation 2.25) collect photon attenuation information; however, the key feature needed as input for the TPS, considering anatomical heterogeneities, is the stopping power relative to water (rWEPL) of the body tissues when the charged ions pass through the patient. Hence, the patient anatomy has to be *translated* to a rWEPL or SPR map using adequate Hounsfield-Units Look-up Tables (HLUTs) [Chen et al. 1979; Mustafa and Jackson 1983; Jäkel et al. 2001]. The sum over all rWEPL values, times the pixel length (in beam direction), defines the WET traversed, as can be seen in Figure 2.14.

Due to the different underlying physical interaction with the medium experienced by photons and ions, there is no simple direct theoretical correlation between the HU and rWEPL. Therefore, different empirical approaches have been developed to establish a HLUT; one of them consists in defining a piece-wise converting function which is experimentally determined and parametrized by measuring the rWEPL of various materials of well-defined HU with water columns of variable thickness (cf. Figure 2.13), as it is reported in Minohara et al. [1993]; Jäkel et al. [2001]; Rietzel [2007]. The two different line segments result from atomic number dependencies, since elements with large atomic number reduce the rWEPL for ions. This is

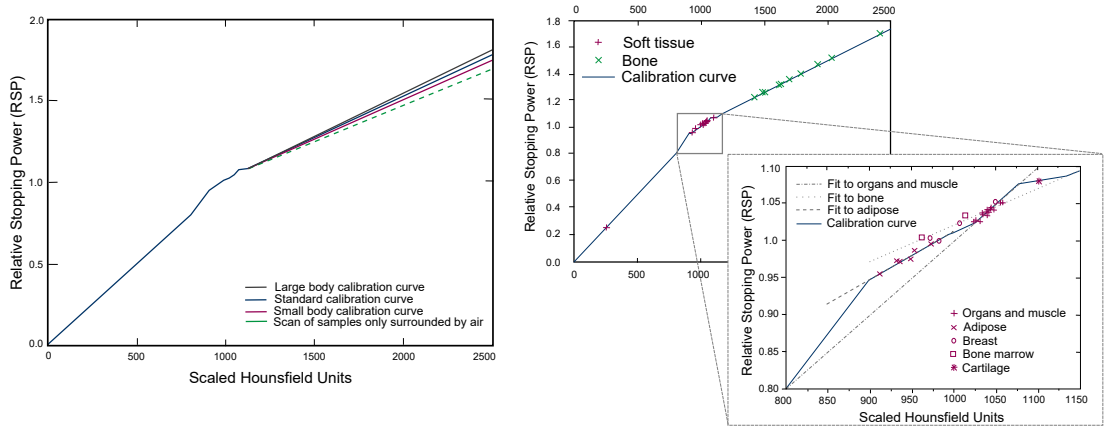

Figure 2.13: Piece-wise HLUTs obtained empirically by measuring the rWEPL of various materials of different sizes. Scaled HUs, $HU_{scaled} = HU + 1000$, are displayed. On the *left*, the beam hardening effect present in X-ray-based CTs and its handling is shown. The standard calibration curve is obtained by averaging between the small and large body corresponding curves. On the *right*, rWEPL values *vs* scaled HU for different biological samples are plotted, enlarging the soft tissue region. The dashed lines indicate the different linear fits to the soft tissue, adipose and bone rWEPL values [Schaffner and Pedroni 1998]. The uncertainties introduced by these variations are explained in detailed in Section 2.3.5.

mainly a consequence of the electron density and slightly due to their higher I-value, thus decreasing the slope of the second half line for materials like bone and metals. A HLUT can be also obtained by means of a stochiometric calibration as it was introduced by Schneider et al. [2000]. In addition, some authors have suggested analytic expressions to calculate WET values, as the one proposed by Zhang and Newhauser [2009].

At the HIT the routine treatment planning procedure is performed with the 3D planning CT and physician-approved CTV and OARs contours by using a commercial TPS (*Syngo PT planning; Siemens Oncology Care Systems*), largely based on the *TRiP98* code developed and validated during the GSI ion therapy pilot project, back in 1998 [Krämer et al. 2000; Krämer 2009]. However, continuous Research and Development (R&D) on treatment planning is simultaneously ongoing to improve the current system capabilities and offer more accurate treatments to the patients. These efforts include, for instance, MC approaches [Boehlen et al. 2013] or the incorporation of motion management by extending the TPS *TRiP* to a full $4D$ functionality, allowing the implementation of motion-mitigation techniques such as tracking, gating or rescanning, and margin optimization through changes of treatment parameters [Bert and Rietzel 2007].

Ion beam therapy at diagnostic and treatment planning stages might benefit from the recent developments of Dual Energy Computed Tomography (DECT). Acquiring X-rays images at two different voltages allows to improve electron density and effective Z maps of the patient tissues, improving the accuracy of the currently used TPS [Landry et al. 2013; Hünemohr et al. 2014].

Stage 2: During-treatment imaging

An inaccurate treatment delivery in ion beam therapy can lead to severe dosimetric implications (under or over target dosages). Therefore, image guidance is extremely important. The role of imaging during treatment involves at least three aspects of the therapy: patient set-up, range verification and plan adaptation [Seco and Spadea 2015].

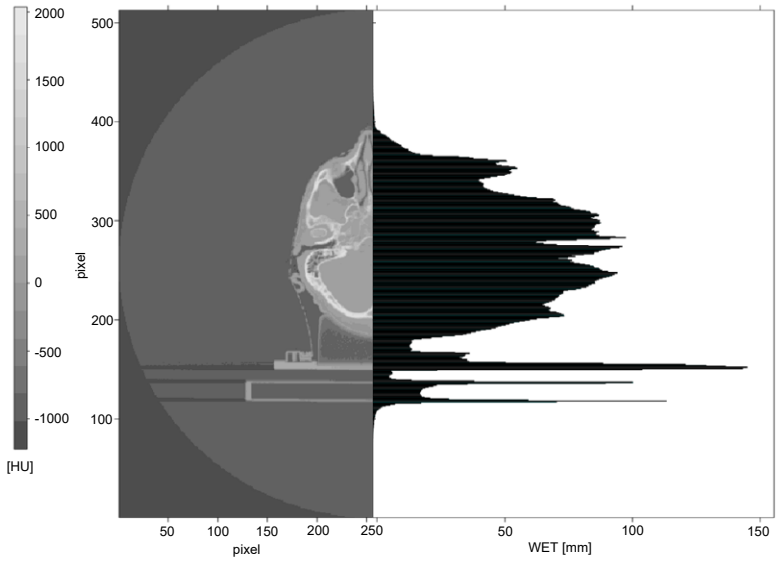

Figure 2.14: Head example of the CT(HU)-rWEPL conversion. On the left hand side the CT number image is shown in correspondence to the WET values determined with the HLUT [Hünemohr 2014].

At the HIT treatment rooms, the patient positioning is settled automatically by a combined adjustment of digital X-ray radiographic systems and treatment tables operated by robotic systems that guarantee sub-millimetric precision in six degrees of freedom. During the first treatment session, the patient position to be applied on the following treatment fractions is defined. In addition, position verification is performed by two orthogonal images obtained with a C-arm X-ray imaging system (*Axiom Artis from Siemens, Germany*). For determining the setup correction vector, an automated $2D-3D$ matching algorithm is employed between Digitally-Reconstructed Radiographys (DRRs) calculated from the treatment planning CT and the newly taken planar images. The algorithm finds the geometric transformation of the treatment planning CT which minimizes the difference between the calculated DRRs and the X-ray images [Nairz et al. 2013] to define a correction shift together with the table offset registered on the first therapy session.

In-vivo range verification techniques rely on the detection of secondary particles emitted as a result of nuclear reactions between the projectile and the patient, or transmitted highly energetic ion-beams. On the first classification, PET is currently the most clinically applied imaging method for verification and monitoring of ion-beam therapy. PET verification relies on the detection of the radioactive decay of positron emitters (^{11}C, ^{15}O and ^{10}C) which are produced within the patient by nuclear fragmentation during the ion treatment irradiation. The activation results in two collinear annihilation photons that can be detected by PET scanners during (on-line [Enghardt et al. 2004; Parodi 2012]) or after (in-room/offline) treatment [Bauer et al. 2013]. *In-vivo* treatment verification at the HIT is approached by means of offline PET-CT, right after the irradiation [Bauer et al. 2013; Combs et al. 2012a]. The treatment assessment results from the comparison of the patient activation measured by a commercial full-ring PET-CT scanner (*SIEMENS Biograph mCT*) with a MC simulated activity prediction based on the patient-specific planned dose distribution, activation and wash-out biological models. This method allows to detect treatment delivery inaccuracies, which potentially indi-

cate the need of treatment plan adaptation for the subsequent irradiation fractions. However, PET, especially in offline implementations, cannot provide millimetric accuracy range verification at every position of the tumor due to its sensitivity to wash-out processes and signal noise [Knopf and Lomax 2013; Kurz 2014].

Prompt Gamma Imaging (PGI) is also being studied as an alternative method for real-time range control for ion-beam therapy. The high energy photon emission results from nuclear products or from excited fragments produced when primary ions impact the body tissues. The deexcitation process occurs almost simultaneously to the treatment delivery, within the first 10^{-11} seconds after the collision. The correlation between the prompt-γ emission profiles along the ion-beam tracks and the BP position can be used to monitor the ion-beam range on-line. Several prompt-γ measurement approaches are discussed in the literature, varying the type of detectors: the parallel-slit collimator to identify γs emitted perpendicular to the beam direction [Polf et al. 2009; Smeets et al. 2012] and the Compton camera, which relies on Compton scattering to detect the γ emission point [Richard et al. 2011]. Additional information as Time-Of-Flight (TOF) [Testa et al. 2009] or prompt-γ-ray spectroscopy [Verburg and Seco 2014] have shown significant gain of accuracy on the prompt-γ range verification method. The so-called prompt-γ-ray timing, based on timing spectroscopy, offers an alternative to the collimated imaging systems [Hueso-González et al. 2016].

Detection of secondary charged particles is also being considered as an imaging method for range verification during treatment. The nuclear interactions along the ion-beam track produce secondary protons that emerge out of the patient. This Interaction Vertex Imaging (IVI) method attempts to detect these emitted particles and reconstruct their trajectories to obtain information about the origin of the reaction vertex. The longitudinal distribution of nuclear emission vertices is directly related to the primary ion range and depth-dose profile [Henriquet et al. 2012; Gwosch et al. 2013]. Another proposed range verification strategy is the detection of thermoacoustic signals that are generated due to localized energy loss of ion beams in tissue (*ionoacoustics*) [Assmann et al. 2015]. Under idealized conditions, the achievable BP position resolution of this technique has been proved to be in a sub-millimeter order.

Beyond this classification, the clinical work-flow can benefit from transmission imaging techniques before and during the treatment, as it is depicted in the Figure 2.12. This innovative method produces planar and 3D images making use of the beams exiting the patient, which have higher initial energy and lower fluence than the therapeutic ones [Parodi 2014]. At the HIT, actively scanned energetic proton and carbon ion-beams provide an ideal environment for the investigation of ion-based radiography and tomography using a range telescope [Magallanes et al. 2014b;a], which is the central study of this thesis and it is deepened in the Section 2.4.

Stage 3: Post-treatment imaging

With continuous increase in tumor control and cure, also side effects of the treatments, especially long-term normal tissue toxicity, have become a growing concern [Combs et al. 2012b]. Treatment follow-up and long-term assessment is as important as the radiotherapy itself since it provides supportive evidence for the current and future treatment, TCP, NTCP; besides, it increases the statistics for valuable clinical trials. The most common imaging modalities used for patient monitoring after the end of the treatment are CT and MRI and the time periods

in which they are scheduled varies between few weeks and years (especially in pediatric cases) depending mainly on the recurrence risks and clinical studies. Some follow-up imaging cases after particle therapy are reported in Krejcarek et al. [2007]; Combs et al. [2012b]. Furthermore, weighted or contrast-enhanced MRI has been proposed as dosimetric verification method to be applied a couple of weeks after the therapy [Seco and Spadea 2015], taking advantage of the radiobiological or histological changes of the treated volume, namely the bone fat, after radiation exposure, which are visible on these type of images [Gensheimer et al. 2010; Yuan et al. 2013].

2.4.2 Ion-based transmission imaging in ion-beam radiotherapy

As any other imaging modality, the reliability of ion-based transmission imaging is threefold [Poludniowski et al. 2015]:

- It must minimize the dose delivered to the patient, as compatible with non-invasive imaging guidelines, to enable periodic treatment verification.
- It must provide anatomical stopping power properties useful for clinical requirements.
- It must be acquired in a time span compatible with clinical work-flow and patient throughput.

In this sense, charged particle radiotherapy can benefit from the application of ion-based transmission imaging during the treatment stages outlined in Section 2.4.1. To this aim, radiographies and tomographies reconstructed from transmitted ion beams count on favorable features such as direct target visualization from the BEV, allowing for a better positioning at the treatment site [Seco and Spadea 2015]. Several MC simulation studies have proposed ion-based radiography to replace the currently used patient set-up images [Depauw and Seco 2011; Huber et al. 2011; Depauw 2013; Spadea et al. 2014].

Moreover, lower dose image guidance compared to conventional X-ray imaging, such as the one provided by iRAD and iCT [Hansen et al. 2014a], would allow to acquire more images and thus increase the patient anatomical information available to facilitate treatment adaptation (Adaptive Radiation Therapy (ART)). Additionally, iRAD and iCT offer a direct retrieving of SPR information without introducing inaccuracies from the calibration process. In consequence, the TPS could calculate the prescribed dose based straight on SPR distributions reducing the related uncertainty. Ion-based imaging resolution has been investigated for different ion types: proton Computed Tomography (pCT) shows inferior spatial resolution than that of conventional X-ray CT, when no entrance/exit coordinates and angles, as well as Most Likely Path (MLP) information is considered [Schneider et al. 2012]. These results coincide when comparing simulated proton and carbon iRADs, the latter showing a better spatial resolution [Seco et al. 2013]. On the other hand, an even higher resolution than the one obtained with carbon-iCT has been demonstrated for helium-iCT [Hansen et al. 2014a]. Nonetheless, several investigations agree on the acceptable density resolution [Schneider et al. 2005; Schulte et al. 2005] of ion-based imaging at relatively low-doses, and the convenient in-room/in-beam orientation has been also suggested to simplify tumor tracking techniques [Depauw 2013].

In the following section, the historical development of the ion-based transmission imaging, the actual investigations and future perspectives are also outlined, focusing on the advancement of detection systems, the dose deposition and image reconstruction algorithms.

2.4.3 Origins, state-of-the-art and future perspectives of ion-based transmission imaging

Origins

Landmark studies on iRAD and iCT date back to more than 50 years ago. Before any experimental or clinical implementation, the theoretical conception of iCT of representing a two-dimensional region given the intersection of its line integrals was proposed by the Nobel Laureate A. M. Cormack [Cormack 1964], to determine density heterogeneities using the energy loss of charged particles in the irradiated body. Back then, he already pointed out the *treatment planning underlying problem of determining the high ionization at just the right place*, as well as highlighted the main challenges on the ion-based imaging applicability [Cormack 1980].

A couple of years later, proton Radiography (pRAD) was first proposed by Koehler [1968] as a potential imaging technique that offers very high-contrast radiographic projections albeit poor spatial resolution. These investigations were based on the use of proton ranges just equal to the object to be imaged, in order to exploit the steeply-falling proton flux-depth curve (cf. Figure 2.4) and considering that the range-straggling is only a minor part of the total proton path length. In this way, it was possible to obtain the highest image contrast of thickness changes on the order of ∼5% of the object total length.

The idea of transmission imaging, based on proton energy loss by extending the dynamic range of protons to be detected after traversing the object, is attributed to Kenneth Hanson [Morris et al. 2006]. Subsequently, studies by Steward and Koehler [Steward and Koehler 1973; A .M. Koehler and V. W. Steward 1973; Steward 1979] and Krämer et al. [1980] showed that the high contrast images obtained by proton radiography provided improved imaging of low contrast lesions in the brain and breast, compared to conventional X-ray-based diagnosis.

The theoretical method proposed in Cormack [1964] was used to perform the first tomographic reconstruction of a distribution of stopping power throughout simulated and experimental transversal projections of different phantoms and biological materials with alpha particle beams [Goitein 1972; Crowe et al. 1975]. In Crowe et al. [1975], density differences smaller than 2% and brain ventricles could be easily distinguished in human trials using a MWPC detector. Comparing with X-ray imaging, the 10 to 50 times lower doses required to obtain images with alpha particles was highlighted.

In 1975, the first pCT was published by Cormack and Koehler [1976]. It was performed with a 158 MeV proton beam detected with an integration-mode *NaI* scintillator-based detector, which can reliably distinguish density differences of 1% in soft tissue. These investigations were followed by Hanson [Hanson et al. 1978; 1981] who started exploiting an imaging set-up configuration combining two types of detectors: (1) a position-sensitive detector, consisting on a MWPC to track protons location and deflection; and (2) a residual energy/range detector. The latter evolved from a hyper-pure germanium *(HPGe)* detector working as a calorimeter, towards a stack of plastic scintillators used as a range-telescope. This double information paved the way to the idea of applying cuts to the proton exit trajectory measurements to improve

spatial resolution [Poludniowski et al. 2015]. Hanson's work reached out the examination of pCT scans of human specimens like brain and heart, thus providing a definite dose advantage over X-ray CT [Hanson et al. 1982].

In the same era, Benton et al. [1975] explored ^{16}O and ^{12}C iRADs in rats as a diagnostic tool to overcome the failure of X-rays imaging on detecting soft tissue abnormalities and subtle density and/or composition variations. Remarkable is their reference to the use of plastic stack detectors and the potential of iRAD to produce blur-free radiographies of moving targets, thanks to their short exposure times. In 1977, Tobias et al. [1977] were able to detect tissue stopping power differences as small as 0.2% with iRADs, by using a stack of plastic nuclear detector foils like Lexan or cellulose nitrate. Carbon iRADs were proven to give superior depth and lateral resolution than images produced with protons or helium ions at low radiation doses. In the same publication, the principle of the modern PET to measure the beam depth penetration is also introduced. Emphasizing the fact that in the future it may be feasible to use pure radioactive heavy-ion-beams for therapy and simultaneous imaging of the treatment. Using the same detector system, Sommer et al. [1978] supported these findings by reporting additional carbon and neon radiographies and tomographies of tissue- and tumor-equivalent phantoms as well as fresh pathologic specimens containing tumors. Except for calcified metastases, most of the tumors were better detectable by imaging with heavy ions than with X-rays [Sommer et al. 1978].

State-of-the-art

The modern era, which in this review spans from the middle 1990's to nowadays, is characterized by a strong focus on the application of iRAD and iCT to range verification and treatment planning in charged particle therapy [Poludniowski et al. 2015]. As aforementioned, the main goal of iRAD and iCT is retrieving trustworthy rWEPL maps of the patient. As pointed out by Schulte et al. [2004], reasonable goals for this purpose are a spatial resolution of 1 mm, a density resolution of 1%, an acquisition time of less than 15 minutes and a maximum dose between 3-5 cGy per scan comparable to the standard X-ray-CTs used nowadays. There are several alternatives to accomplish these requirements, depending on the detector system of choice. The current and most relevant approaches for ion-based transmission imaging applications are briefly explained as follows, emphasizing on the accuracy to retrieve WET or rWEPL values, the CT reconstruction algorithm applied and the imaging dose achieved:

Residual range/energy integration-mode detectors

The BC signal per RP from an integration-mode detector contains averaged information about the beam energy degradation yielded by ionization and excitation of the phantom/patient and detector crossed material. Therefrom, a calibration between the acquired signal and the WET of the material traversed by the beam is needed. The generated BC signal is directly related to the incident beam fluence and energy. This scheme matches with the imaging prototype optimized in this work, a multi-array of air-filled PPICs, which will be thoroughly described in the following chapter. The detector conception emerged from a preceding work dedicated to obtain a 3D-reconstruction of the depth-dose profiles for actively scanned particle

therapy [Brusasco et al. 2000]. The feasibility studies for its usage for ion-based transmission imaging were performed at HIT [Rinaldi et al. 2013]. A depth resolution of 3 mm, limited by the inner slabs thickness, was reported. First radiographic projections were obtained by delivering high number of primaries per scanning spot. Extrapolated dose calculations, however, led to the possibility to acquire planar images with doses of about 0.4 mGy per RP [Rinaldi et al. 2014], that can vary according to the irradiated volume. Several features of the detector are being upgraded [Takechi et al. 2014] in order to achieve a higher image resolution, optimal detector performance, improved DAQ and lower doses to the patient, as it will be tackled on the course of this thesis.

Another integration-scheme was used to obtain carbon-iRADs with a commercial flat-panel detector at HIT: a gadolinium oxysulfide scintillator coupled to an amorphous silicon matrix array. The dynamic range coverage is based on the active energy variation of carbon ion beams. Using this method, a 0.5 mm WET accuracy was obtained at the radiographic level and rWEPL was recovered after reconstructing the carbon-iCT using a Filtered Back Projection (FBP) algorithm with an accuracy of 1%. High spatial resolution of 0.8×0.8 mm^2 is given by the original detector design [Telsemeyer et al. 2012]. As an application of this imaging technique, a measured WET distribution of a patient-like phantom was compared to the WET map calculated by the HLUT of the TPS used during commissioning at HIT. The ratio between the two maps shows a mean of 1.004 ± 0.022 with pronounced differences at high WET values. However, to obtain a single iRAD, the active energy scanning method required the irradiation of 52 equally-spaced energy slices, each of them imposing an imaging dose up to 10 mGy, which is also clinically unacceptable [Telsemeyer et al. 2014].

The exploitation of Charge-Coupled Devices (CCDs) for ion-based imaging purposes using scattered beams is also considered in the integration-type detector classification. The principle of pCT was proven with this technique by Zygmanski et al. [2000] using a cone-shape proton beam detected with a gadolinium oxysulfide ($Gd_2O_2S : Tb$) scintillator viewed by a CCD camera. The tomographic reconstruction was performed using the Felkamp-Davis-Kress FBP algorithm which is commonly used for Cone-Beam Computed Tomography (CBCT). The average total dose to the phantom volume was estimated to be about 0.57 Gy for the 200 CT projections. Although the rWEPL values obtained by the proton-CBCT imaging system are better than those derived from conventional X-ray CT, MCS effects degrade significantly the image-quality causing discrepancies up to 1 cm in WET.

The same scintillator-CCD approach combined with a range modulator wheel has been studied by Ryu et al. [2008] attaining images with high density resolution, however deteriorated in spatial resolution owed to the well-known MCS of proton beams. The average dose to the presented phantom per radiography resulted to be 4.5 mGy.

A similar methodology to the one developed by Zygmanski et al. [2000] was applied to iCT by Abe et al. [2002] and Muraishi et al. [2009]: based on the measurement of residual range distribution using an X-ray intensifying screen and a CCD camera system, they studied the improvement in spatial resolution using heavier ions than protons. Highly energetic helium and carbon scattered beams were used to create a uniform irradiation field of 10 cm diameter. The projection images obtained yielded 3 Gy to the phantom irradiated. The iCT was

reproduced from the full phantom rotation sampled at 1.4° angular sampling, applying a FBP algorithm with Shepp-Logan filter, leading to a overall dose to the phantom up to 40 Gy. Several improvements of the described system are suggested to increase the spatial resolution, including the exploitation of iterative reconstruction algorithms to exploit statistical features of the measurements.

The imaging system developed by Tanaka et al. [2016] integrates the scintillation light along the beam-path, which is photographed by a CCD camera. The light intensity is then converted to a proton-range by means of an appropriate calibration. To demonstrate the functioning principle of the detector, a pCT was acquired using a 70 MeV proton-beam and reconstructed from 416 angular projections by using the FBP method with Shepp–Logan filter. No dose of beam-fluence is reported in this study. The spacial resolution achieved with this imaging setup is at the same level as that of X-rays CTs. A maximum discrepancy of 8.8% for one specific material was found with respect to the HU-to-WET conversion table used for the TPS available at National Institute of Radiological Sciences (NIRS).

Integration-mode detectors are not capable to resolve individual ion tracks. This does not represent a critical drawback in case of heavy ions which minimally scatter along their path (cf. Section 2.1.3). However, in the case of proton-based imaging, MCS is a fundamental issue that limits the overall image-quality. In order to overcome this difficulty, either coupled detector systems which include proton position and angular details, determination of the proton's MLP, post-processing methods relying on the beam spot size and MCS models [Gianoli et al. 2016] or prior X-ray CT information [Hansen et al. 2014b; Spadea et al. 2014] must be considered to enhance the spatial resolution.

In the same integration-mode subgroup, the floating strip MICRO-MEsh GASeous (Micromegas) devices have also found their way to medical imaging applications. They are ionization chambers with a fine micro-structured mesh inside, originally intended for use in high-energy muon spectrometers. In order to prove the principle of ion-transmitted imaging, a 6.4 $\times$ 6.4 cm^2 Micromegas doublet, flushed with an $Ar : CO_2$, was irradiated at the HIT with proton and carbon ion beams at particle rates between 2 MHz and 2 GHz. These investigations demonstrate the suitability of this equipment to identify single particle hits and achieve ion-based radiographic images with a spatial resolution below 200 μm [Bortfeldt et al. 2015].

During later experimental campaigns at the HIT, carbon ion radiographies of a homogeneous and a heterogeneous phantom were obtained with three floating strip Micromegas doublets and a scintillator-based range telescope consisting of 18 plastic scintillator layers of 1 mm thickness. The two dimensional Micromegas provided hit information in x- and y-directions and, different from the previous experiment, they were operated with $Ne : CF_4$ gas. The different tissue-equivalent layers of a heterogeneous phantom could be reconstructed with a spatial resolution in the order of 1 mm and a range resolution within 0.2 mm with $\sim 40 \times 10^3$ single carbon ion tracks detected; approximately 50% were discarded when falling under a quality threshold. Moreover, the dynamic range of the current telescope is foreseen to be augmented, keeping the thickness of the scintillator layers since they are already in the same limits as the particle range straggling [Klitzner et al. 2016; Bortfeldt et al. 2016]. Special attention is drawn to this detector configuration since, as it will be mentioned in the outlook of this thesis, the stack of

ionization chambers investigated in this work was coupled with a pair of Micromegas for proton beam scattering investigations.

Experimental tests using Micromegas chambers for imaging purposes have also been carried out at the Roberts Proton Therapy Center at the University of Pennsylvania. Different beam delivery modalities, such as double-scattered, scanned and pristine proton beams have been explored, reaching image spatial resolution of 1.1 mm with a 1 ms time resolution [Hollebeek et al. 2012; Dolney et al. 2016].

Ion trackers combined with range/energy deposition detection

Early research on pRAD and pCT started at the Paul Scherrer Institute in Switzerland [Schneider and Pedroni 1995]. Proton radiographies of an Alderson head phantom and the head of a sheep were obtained by measuring the protons residual energy and calculating single particle tracks with a detector array consisting of two MWPCs before and after the imaged object, a scintillator counter and a NaI calorimeter to register the ion residual energy. Range uncertainties and precision of the HU-CT calibration were quantified, finding an improvement of range determination by a factor of 2.5 by using information of the measured rWEPL of tissue surrogates. The applied dose of a proton projection of 2.6 cm $\times$ 1.4 cm FOV obtained with about 10^6 events out of which 50% are actually detected, was calculated to be 0.01 mGy. This group also foresaw the possibility to perform faster proton range measurements with a stack of scintillators working as a range telescope.

Later in 1999, the above described imaging system evolved towards a proton-tracking system consisting of two scintillating fibre hodoscopes coupled to a photomultiplier tube and a range telescope consisting of 64 scintillator tiles of 3 mm thickness. The light from each tile was collected by a wavelength fiber coupled to a photomultiplier channel too. This setup was capable to detect position and range at a MHz rate. The spatial resolution achieved for the residual-range images was $\sim$1 mm and the density resolution was 0.3%, when irradiating 200 protons/mm^2 over a FOV of $\sim$22 cm^2 [Pemler et al. 1999]. The feasibility of using *in-vivo* pRAD for the patient-specific optimization of the HU-rWEPL calibration used by the TPS was validated with a pRAD of a dog patient treated for a nasal tumor. As a result, the deviation between WET calculation and measurement could be reduced from 7.9 to 6.7 mm with the optimized calibration [Schneider et al. 2005].

The clinical pursuit for more precise range accuracy encouraged the formation of a scientific collaboration between the Department of Radiation Medicine at the Loma Linda University Medical Center, the University of California Santa Cruz, the Brookhaven National Laboratory and the State University of New York in the United States in 2003, dedicated to investigate pCT [Schulte and Wroe 2012]. Their first pCT scanner prototype, built in 2011 [Hurley et al. 2012], consisted of four up- and down-stream trackers of Silicon-Strip Detectors (SSDs), able to convey position and angular information of single protons, combined with a calorimeter composed by an array of 18 cesium iodine *(CsI:Tl)* crystals to record their final energy lost. With this early design, the proton location could be determined with 100 μm resolution and its energy was resolved within the 2%. In order to obtain pCTs, various phantoms were scanned

with 90 projections in 4° steps over an area of 9 × 18 cm^2. Good agreement with the reference rWEPL values within 1% was achieved. Furthermore, the same first-generation pCT scanner was used to generate proton energy-loss and scattering radiographies of a hand phantom. Both planar images clearly show the anatomical structure, although the former one exhibits better resolution. The estimated dose delivered to the center of the phantom was ∼20 μSv, which is within the same order of magnitude as the dose delivered by a conventional X-ray radiography of a human extremity [Plautz et al. 2014].

The second phase of the primal design aimed at incorporating a hybrid between a range counter and a calorimeter, consisting of a five-stage scintillation device whose signals are read out by optical fibers and silicon photomultipliers [Schulte et al. 2012]. The tomographic images obtained with both devices were already reconstructed with iterative algorithms and include the MLP concept.

Recently, the novel multi-stage detector was calibrated in terms of rWEPL using a tailored polystyrene step phantom. The rWEPL measurement accuracy achieved is ∼3 mm per proton, providing an uniform and WET independent resolution [Bashkirov et al. 2016]. A full 360° pCT scan with 4° angular sampling is completed in less than 10 minutes due to the attained high DAQ rate. rWEPL values of different tissue-equivalent materials are reconstructed accurately with ∼1.5×10^6 protons passing through the phantom per projection angle, corresponding to a dose of the order of 1 mGy. Further improvements of the current version of this device might enable full pCTs with low overall radiological dose in only two to four minutes depending on the FOV, which is acceptable on a daily-basis clinical use [Johnson et al. 2016].

Several Italian projects in the first decade of the 2000's dedicate efforts towards the pRAD and pCT realization. The first one is the project called AQUA *(Advanced Quality Assurance in Hadron Therapy)* under which their *PRR* (Proton Range Radiography) system was built and tested to improve the QA at the Centro Nazionale di Adroterapia Oncologica (CNAO) in Pavia, Italy [Amaldi et al. 2011]. As the previous device, the next generation telescope, *PRR30*, only counts on two high-rate Gas Electron Multipliers (GEM) tracking detectors located after the object. The latter are integrated in a stack of 48 plastic scintillators of 3.2 mm thickness to measure energy loss and range of individual primaries over a scanning surface of 30 × 30 cm^2 [Bucciantonio et al. 2013]. The residual range is determined by digital recognition and fitting of the signal over certain threshold, yielding to a 0.2 mm range accuracy.

The PROton IMAging *(PRIMA)* group [Sipala et al. 2011] proposed an imaging array similar in design to the LLU/UCSC prototype described above, albeit the SSDs are half thinner and the calorimeter used is made out of four YAG:Ce (Yttrium Aluminum Garnet activated by cerium) crystals that might increase the proton rate allowed due to its short decay constant (∼70 ns). The small sensitive FOV is 5×5 cm^2 with the possibility to be extended to 5× 20 cm^2 in the upgraded version [Scaringella et al. 2013]. A full tomographic scan of a PMMA cylindrical phantom has been acquired at 10° angular sampling and reconstructed using individual proton tracking with the MLP technique and a FBP algorithm, applying a Butterworth filter [Vanzi et al. 2013]. By irradiating 1.5 × 10^4 protons/cm^2, the spatial resolution achieved is 0.9 mm at FWHM, being able to resolve electron density within 2.4% accuracy [Scaringella et al. 2013].

The *OFFSET* (Optical Fiber folded scintillating extended tracker) detector, funded by the

Istituto Nazionale di Fisica Nucleare (INFN), Italy, is an alternative residual-range imaging approach which exploits two pairs of perpendicular layers of scintillating fibers as position sensitive planes, extended over a 20 × 20 cm^2 FOV. Their channel reduction strategy would allow a larger detection surface at lower cost and complexity [Lo Presti et al. 2014]. The residual range measurement is performed by a stack of sixty scintillation fiber layers, each of them coupled to a photomultiplier. The goals for the final detector are to achieve real-time images of a large FOVs and a high spatial resolution up to 150 μm. First experimental investigations were evaluated at high doses up to 1.6 Gy, which served to prove the efficiency and performance of the detector.

A collaboration between the Northern Illinois University (NIU) and the Fermilab National Accelerator Laboratory (FNAL) in the United States has proposed an assembly of a eight position tracking planes consisting of scintillating polystyrene fiber hodoscopes (four before and four after the objective) and a stack of 3 mm plastic scintillators, both read out by silicon photodetectors, for proton-based imaging of a ∼20×24 cm^2 extended field [Uzunyan et al. 2014]. The prototype is characterized and has begun collecting data of different phantoms [NIU 2016].

A different approach to accomplish pCTs has emerged from the Proton Radiotherapy Verification and Dosimetry Applications (PRaVDA) consortium in 2013. The group aims to construct a prototype of the first fully solid-state pCT scanner using SSDs for both the tracking and proton range/energy measurements [Taylor et al. 2016]. Their technology resembles the inner detectors developed for the ATLAS experiment at the Large Hadron Collider (LHC). The high-precision directional information is obtained by a pair of anterior and posterior trackers consisting of three rotated (60° to one another) planes, which would compensate resolution issues at high proton rates. The sensitive area expands over 10 × 10 cm^2 to be enlarged. The calorimeter functioning as range telescope is placed afterwards to measure the residual energy of single protons. The tracker is also envisioned to monitor the beam profiles and total dose delivered during the treatmens at high proton fluences by alternating between its two operating modes [Taylor et al. 2015].

Pixelated sensors combined with energy deposition detection

Proton-counting by means of Complementary Metal Oxide Semi-conductor (CMOS) Active Pixel Sensors (APSs) is also a promising technology for light ion-based imaging applications. CMOS devices can be used either in integration-mode, where the signal in a pixel is integrated over many incident protons as it was proven in Seco and Depauw [2011] or in a tracking-mode as it is suggested by Poludniowski et al. [2014], since the pixelated constitution of the CMOS detectors allows several protons to be resolved individually in a single projection.

The former format was used to obtain proton radiographies of metal and tissue-equivalent materials with a double scattered proton beam at the proton therapy unit of the F. H. Burr Proton Center, Massachusetts General Hospital (MGH) [Seco and Depauw 2011]. The proton images were compared to x-ray kVp EBT2 and X-Omat film images. The CMOS detector showed poorer spatial resolution than the X-rays, affected by MCS and depending on the

object-detector gap. In tracking format, besides being able to distinguish isolated proton trajectories, a stack of DynAMITe large-area CMOS sensors has the possibility of inferring the proton range, therefore giving the necessary information to overcome the MCS well-known limitation. The PRaVDA collaboration is investigating the future development of CMOS arrays towards pRAD and pCT applicability [Poludniowski et al. 2014].

Another CMOS-based ion imaging implementation makes use of a Gridpix system of time projection chambers filled with helium and isobutane, whose technology is founded on the Timepix chip evolved from the Medipix2 developed at CERN [Medipix]. These type of detectors also allow to retrieve position and direction information of the impinging protons over an active area of 2 cm^2 with a square pixel size of 55 μm, which defines the reachable spatial resolution. However, the main drawback of this sensor technology is still the lack of a larger FOV coverage. To determine the proton residual energy, a single BaF_2 crystal coupled to a photomultiplier tube is used. 3×3 cm^2 proton radiographies of a tiny 2.5 cm length and 2.5 cm diameter cylindrical phantom with tissue-equivalent insertions were obtained, leading to a good visual agreement with a dose of 0.4 mGy delivered to the phantom [Biegun et al. 2016]. Further improvements of the imaging setup are envisioned as well as small scattering angle cuts are proposed in the data processing to improve the image-quality [Takatsu et al. 2014].

Recently, the single-detector proton radiography proposal has come into view towards an easier implementation of transmitted imaging into the clinical environment. This approach has been investigated experimentally by using CMOS detectors as well, in order to record the dose maps beyond the imaged object at two different energies. The dose ratio map is then converted to a WET map with an accuracy of 1.6 mm WET [Doolan et al. 2015], however the method is currently restricted by a short WET extent.

2.4.4 Limitations and challenges of ion-based imaging techniques

Owing to the contemporary prevalence of proton therapy centers, the ion-based imaging research is mainly focused on the use of protons. Nevertheless, most of the designs covered above are appropriate for other therapeutic ion choices. The particle type and beam shape will also define main detector features, given their behavior throughout the matter.

It is important to mention that MC simulations play a significant supporting role on the development of all the imaging alternatives summarized above. Basically, all these approaches rely on their dedicated MC model for comparative and bench-marking studies.

At the end of the day, the reliance of any of the ion-based imaging methods must be founded on the *visual image-quality*, determined by the image contrast and resolution, as well as the degree of *accuracy to resume the WET and rWEPL* with the *lowest imaging dose* achievable. The aforementioned efforts give a survey of the current attempts to maximize the quality of ion radiotherapy by exploiting the potential of ion-based transmission imaging as mainstream technique or in synergy with conventional X-ray imaging.

Despite the R&D is increasingly approaching the clinical work-flow requirements, there are still technological challenges faced by most of the endeavors. In the first instance, the best trade-off between high image-quality at high speed acquisition and low dose to the patient is necessary; moreover, the most suitable setup for the already operating proton facilities must be able to integrate the existing monitoring, imaging, TPS, hardware and software tools. Some of

the limitations confronted by ion-based transmission imaging attempts to fulfill these demands are listed as follows:

- *Facility related:*
  - Lack of higher beam energies than the therapeutic ones.
  - An available rotational gantry.
  - Accelerator technology able to extract very low beam fluences ($\sim 10^2$ ions/RP) and high precision monitoring systems to handle them accurately.
- *Detector operation related:*
  - In case of calorimeters, the energy resolution within the coverage of the ion range straggling.
  - In case of telescopes, the range resolution particularly owed to discretization issues. Specific challenges of our experimental setup in this regard are addressed in the following chapter.
  - Precise WET calibration and scattering models of all the devices included in the imaging setup to be considered in the final rWEPL maps.
  - Usually, increased number of primaries overcome experimental challenges related to high-rates, ionization gains and SNR, which are directly reflected in the overall image-quality at the severe cost of extra dose to the patient. In this concern, an optimal detector efficiency is crucial to register most of the primaries delivered to the imaged object, leading to the best compromise between deposited dose and signal quality.
- *Software related:* Reconstruction algorithms and data analysis methods inherent to the physics involved in the imaging process, being aware of the computational effort undertaken; the ultimate goal is to acquire *in-vivo* images for guidance and verification within minutes in the clinical work-flow.

Part II.
Materials and methods

Cuando creíamos que teníamos todas las respuestas,
de pronto, cambiaron todas las preguntas.

When we thought we had all the answers, suddenly
all the questions were changed.

Mario Benedetti

3

Materials and experimental methods: Characterization and optimization of the ion-based transmission imaging system in the low-dose regime

3.1 Experimental setup

Low-dose ion-based transmitted images are proposed as a means of improving the underlying uncertainties in the ion therapy treatment delivery and planning procedures at HIT. In fact, the prospective imaging technique can be also put forward in any particle therapy facility with active beam delivery system, which, in addition to the detector, represents the major experimental component to achieve spot-wise image formation. As it was generally introduced in the previous chapter, the HIT complex provides the suitable experimental environment to investigate iRAD and iCT, enabling ion beams to be actively delivered at sufficiently high energies in order to reach the imaging RRD that measures their residual range behind the transmitted object. Even so, exploring the low-dose scenarios to produce clinically-suitable images introduces unprecedented experimental challenges for the limits of the facility control systems and the detector performance, as it will be detailed in the Section 3.3 and 3.4.4, respectively. All the components of the experimental setup adopted in this work are depicted in the Figure 3.1. An exhaustive description on their role in the image formation process, from the irradiation plan design to the detection efficiency under different dose schemes, is given as follows (cf. Figure 3.1 as explanatory guideline of the elements from left to right).

Each ion-based transmitted image should enclose the ion stopping power relative to water of the studied volume. This information is inherently provided by the active scanning system (*transverse coordinates*) and the signal maximum identification within the RRD (*longitudinal coordinate*). iCTs result from the tomographic reconstruction of the stopping power from its angular projections, while iRADs constitute the integral stopping power ratio or WET, i.e., a

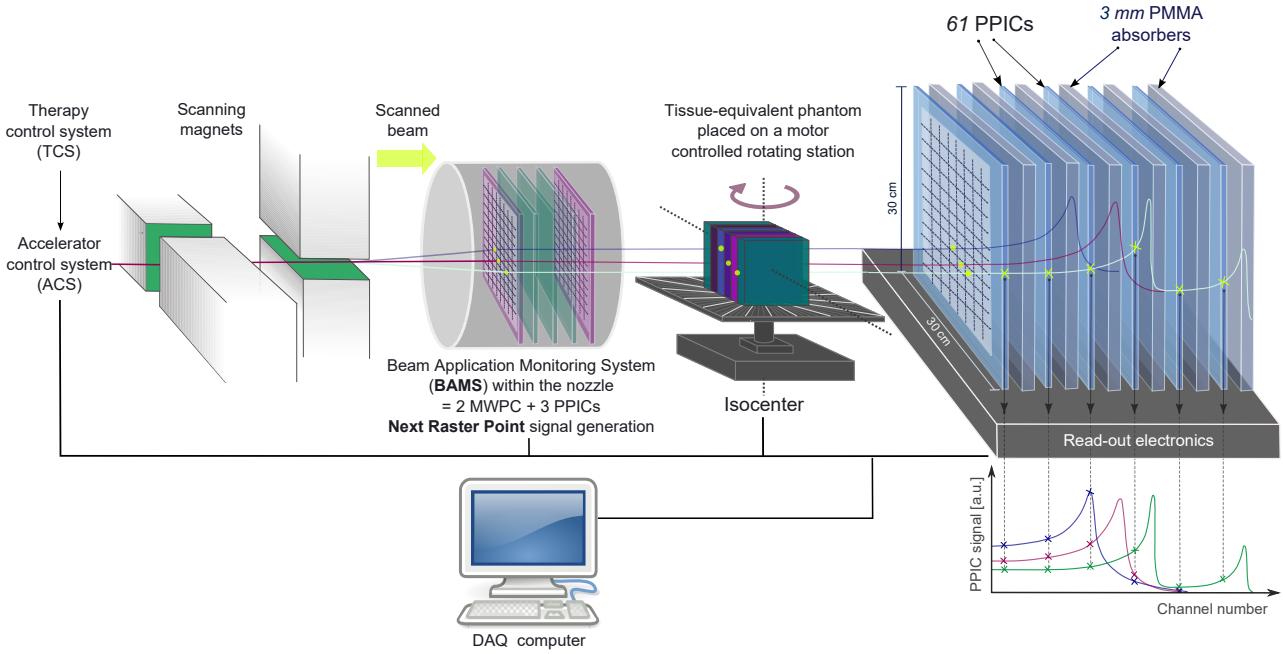

Figure 3.1: Ion-based transmission imaging experimental setup at the HIT facility. The 3D information included in each transmitted projection is produced by means of the HIT's active scanning system (*traverse coordinates*) and the energy selection, which enables a correlation between the measured BP position and the corresponding WE ion range (*longitudinal coordinate*) after the beam passes through the imaged phantom. The beam and scanning parameters are specified in the PBP, previously loaded through the TCS (cf. Section 2.3.4). During the performance of the irradiation, the BAMS keeps track of the beam status and generates a signal indicating the completion of the requested number of primaries per RP and the subsequent beam position (cf. Section 3.4.1). This signal triggers the single-RP charge integration process in the detector PPICs, which is initialized by the read-out electronics (cf. Sections 3.4 and 3.4.2). The RRD consists on an integration-mode multi-channel array of 61 PPICs, interleaved with 3 mm thickness PMMA slabs (cf. Section 3.5).

single projection consists of a 2D-distribution of BP positions disposed on a RP grid.

The description of the experimental constituents necessary to create such low-dose ion range maps is given in four steps: First, the dose scenarios explored in the experimental investigations of this work are specified. Second, the procedure to obtain and monitor low-fluence ion beams from the HIT accelerator is detailed. On the third place, the synchronized DAQ with the active delivery system, using the updated electronics module, is presented in perspective, from the previous imaging-setup to the currently used and the upgraded prototype under construction. Finally, the comprehensive characterization and optimization of the multi-channel range telescope on detecting reduced-fluence beams are brought in context. A close examination of the detector response is performed and assessed, since the reliability of the measurements is intrinsically related to the beam intensity dynamics and the behavior of the DAQ under extreme conditions.

3.2 Physical dose schemes

Equation 2.19 defines the guideline to the different dose levels considered in the experimental part of this work, since it exhibits the dependencies of the dose per RP on the number of delivered primaries and the corresponding separation between them. Generally speaking, typical ^{12}C-ion treatment plans allocate more than 10^5 particles per RP, subject to the prescribed dose per fraction. Hence, the term *low-fluence* is used solely in the context of this thesis when referring to 10^3 or less delivered primaries per RP, since the beam fluence has to be reduced

Figure 3.2: Comparison of typical BC signals produced by deposition of 5000 (*high-dose*), 1000 (*middle-dose*) and 500 (*low-dose*) ions/RP. (a) Absolute-scale discretized ionization curves. The total signal observed by the PPICs might be subject to the detector efficiency on collecting charge under different acquisition frameworks, as it will be discussed in Section 3.4.4. (b) Same discretized BCs compared relatively to their maximum value.

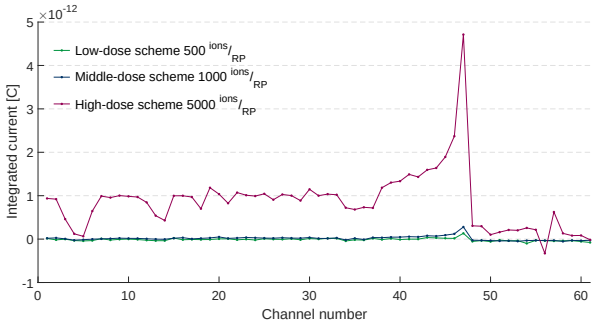

(a) Representative Bragg curves in the different dose scenarios considered for the experimental investigations. The BCs shown correspond to the same RP of a scanned FOV irradiated with a 299.94 MeV/u ^{12}C ion beam of 3.9 mm FWHM without target.

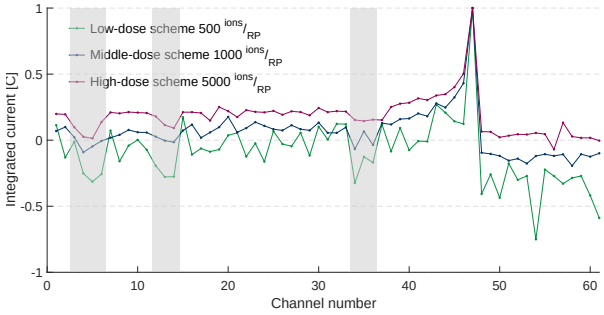

(b) The same curves on the left have been normalized by their maximum value in order to make evident the impact of the noise in each experimental sample, and how this condition reduces significantly the smoothness of the low-dose BCs.

from clinical standards by two to three orders of magnitude for ion-based imaging applications.

With this in mind, six different dose schemes, combining variations of N_{RP} and (Δx, Δy), were used. Images taken with what is referred as *high-dose* scheme consist of depositing 5000 ions per RP, separated by 1 mm. In a preliminary rough approximation, this number of particles leads to doses in the order of few mGy per projection. The particle number applied in the high-dose scheme is further reduced in two steps, to a *middle-dose* regime of 1000 primaries per RP and *low-dose* irradiations performed with 500 ions per scanning spot. Enlarging Δx and Δy to 2 mm would then reduce the dose by a factor of four, this RP separation was also considered in some experimental acquisitions in order to reach the lowest dosimetric level. Figure 3.2a, compares the three main dose schemes in terms of the impact on the single BCs. The curves were randomly selected from a 299.94 MeV/u ^{12}C ion beam scanned irradiation, for each dose scenario. No phantom material is traversed. The BP is found in the channel number 47, according to the maximum signal identification. The sampling time (t_s) is equivalent to the fixed integration-time (t_{int}) times the amount of averaging cycles or conversions per sample ($n \cdot {}^c/_s$) (cf. Section 3.4.3). Then, the $t_s = t_{int} \cdot n \cdot {}^c/_s$ used to acquire each curve has been optimized to correctly detect scanning spots with the maximum charge integrated, in each specific scenario (cf. Section 3.4.4). The real-scale curves intend to show the impact of the number of primaries on the signal amplitude in the PPICs of the detector. Furthermore, it is visible how the minimal signal at low-dose level gets close to the base-line, already in the noise-sensitive region, as it will be explored in detail in Section 3.5.3. Apart from evident under-responsive channels (shaded in light gray, which introduce a systematic lower signal), the noise level in the low-dose acquisitions might affect severely the independent data points of the discretized BC, likely causing wrong identification of the position of the BP (cf. Figure 3.2b). This is especially possible in unfortunate cases where a noise fluctuation appears in a certain channel and predominates over the real BC signal.

Under the accelerator clinical configuration at HIT, with the standard interlock-mask activated, the high-dose irradiation plans are typically completed without safety-errors driven by

the TCS. However, in order to attain the lowest imaging dose, it is necessary to manipulate the beam-delivery default features used for clinical applications as it will be examined in Section 3.3. It is possible to use the research mode of the synchrotron without altering the beam properties determined by the medical standards, which are securely locked. Any machine working mode can only be activated if several global and device-specific checksums and status reports meet specific requirements, being highest for the patient treatment mode [Fleck et al. 2008].

3.3 Low-fluence beam irradiation and monitoring

The process to create an ion-based image begins with the design of a customized PBP. This irradiation plan contains the beam parameters such as the ion-type and IES of choice, beam width and suggested nominal intensity (pps), as well as the FOV geometry including the extension of the surface to be irradiated, the scanning pattern and step separation (Δx, Δy), and the desired number of primaries to be deposited in each RP. The irradiation proposal is then requested via the TCS as detailed in the Section 2.3.4.

One of the major motivation of this research, in view of future clinical application, is to image the studied phantoms with the minimal possible dose, while keeping a reliable image-quality. Since the HIT accelerator is originally designed for clinical usage, owing to the high dosages required in ion treatments, the minimum amount of particles to be deposited per RP never reaches the low-number of ions demanded for imaging applications. The irradiation of low-fluence PBPs, therefore requires technical efforts which are not always standardized in the clinical work-flow. In this regard, the boundaries of the BAMS' capabilities to accurately track few ions per RP were explored to determine the optimal experimental conditions for low-dose radiographic and tomographic acquisitions, as it is discussed in the following.

3.3.1 Determination of the beam intensity for different dose-schemes

The particle delivery rate determines the acquisition time of each projection. Ideally, the fastest irradiation is desirable for both therapeutic and imaging goals. In turn, the preferred dose-scheme also impacts the beam intensity of choice. Hence, a precise knowledge of how the beam intensities are handled by the TCS and ACS is necessary to select the appropriate scanning pace and the corresponding experimental parameters, according to the number of particles to be delivered.

In ordinary clinical conditions, a nominal intensity value from the LIBC is selected by the PDG based on the requested PBP, as long as certain technical requisites established by the BAMS are fulfilled, as it is detailed as follows. The time-span needed by the BAMS to complete the irradiation monitoring measurements delimits the minimum period that the beam must stay in each RP. This means that the irradiation time per spot should not be shorter than 1.7 ms, which is bound by the integration time of the two MWPC (2 cycles·250 μs = 500 μs), the ionization chambers integration time (minimum 50 μs), the offset time (450 μs) dedicated to data processing and reset, plus a safety margin of $\sim$700 μs [A].

This timing chain is also used in complex prescribed PBPs, where the doses may vary from one RP to another, thus allowing to irradiate each spot with the highest possible rate, while minimizing the total treatment time [Schoemers et al. 2015]. Different from intensity-modulated

[A] Private communication with R. Panse, Heidelberg, 2015

treatment plans, transmitted images always require the same number of ions per scanning spot. In this scenario, the highest ion rate achievable is thus accomplished when the mean residence time of the beam in each RP (t_{RP}) is ∼1.7 ms, as it is demonstrated in Section 3.3.3.

Another limitation imposed by the BAMS is the measurement range of their built-in PPICs. It defines the sensitivity of the chambers to the currents that can be detected. There are 4 measurement ranges available at HIT, whose upper limits are 17 nA, 170 nA, 1.7 μA and 17 μA [Schoemers et al. 2015].

Recapping, when loading a high-dose PBP in treatment mode, the TCS would select the maximum available beam intensity from the LIBC that satisfies the aforementioned conditions. However, when aiming at decreasing the number of primaries deposited in each spot (middle-dose scheme or low-dose scheme), while using the nominal beam intensity chosen by the TCS PDG, the PBP is inevitably completed in much less time. In this circumstances, the timing conditions enforced by the treatment mode described above might not be achieved, leading to the activation of safety interlocks, thus preventing the irradiation to be completed. Moreover, there is a time-limitation imposed by the imaging-system read-out electronics when acquiring data synchronized to the RP scanning-sequence at high rates (cf. Section 3.4 for further details). Consequently, the beam intensity must be reduced and the RRD electronics parameters adjusted to accomplish investigations under medium- and low-dose schemes, allowing the electrometer to have enough time elapsed between RPs without risking to miss them out.

In order to overcome these limitations, the research mode in the TCU must be enabled before the irradiation. This configuration allows the user to adjust the beam intensity, BAMS PPICs measurement range and/or integration time, and interlock settings. To deliver middle-dose PBPs it is enough to enforce the lowest nominal intensity of the accelerator ($2{\cdot}10^6$ pps) instead of the one automatically selected by the PDG. The low-dose irradiations, however, require a reference intensity value even lower than the minimal available in the LIBC. Thus, the BAMS current allowance must be customized directly in the MBP, so that the PDG is evaded. Furthermore, in the low-dose regime, the measurement range of the BAMS PPICs is also adapted to the maximum sensitivity to be able to detect the faint charges expected. The irradiation of MBPs is strictly restricted to research and technical TCU working modes.

The parameter to be tuned in the MBP is the threshold current (in amperes) of the first PPIC of the BAMS. The starting point to further reduce the ion delivery rate is the reference current determined when the lowest nominal intensity is selected. When the number of requested ions is known via the MBP generation, the PDG sets the corresponding current values (in amperes) per individual RP, which must not be transgressed.

The conversion from pps to amperes relies upon the calculation of the charge expected in the BAMS PPICs, which, in turn, depends on the design specifications of the ionization chambers (See Table2.1), the filling gas and its stopping power $^{dE}/_{dx_{gas}}$ calculated analytically by the Bethe-Bloch formula. Considering these factors, the charge accumulated (Q) within the PPIC gap equals:

$$Q = N_{prim} \cdot \frac{dE}{dx}_{gas} \frac{\Delta x_{gas}}{W_{gas}/e}, \tag{3.1}$$

where N_{prim} is the number of primaries, Δx_{gas} and W_{gas} stand for the air gap width and the average energy needed by an incident particle to create an ion pair inside the PPIC, respectively.

In this work, the reference value of the ion delivery rate allowed by the BAMS was decreased gradually through the MBP until the best trade-off between the irradiation time to cover the requested FOV and the accurate detection of all the expected RPs was attained. This way, the BAMS will take the new-defined thresholds as reference intensity for the primaries to be delivered at the updated rate, thus enlarging the time-interval between RPs (t_{RP}).

A practical example of this procedure is shown in the Section 3.3.3, namely in Figures 3.6a and 3.6b.

3.3.2 Spill structure and intensity fluctuations

The determination of the intensity as explained in the previous section assumes an ideal beam without fluctuations. In reality, the phase space distribution of ions within the bunched beam is irregular and varies from pulse to pulse of the accelerator, causing the beam intensity to fluctuate around its expected value. To illustrate this effect, the Figure 3.3 shows a typical ^{12}C spill structure of a beam impinging the detector in the center of the FOV (i.e without active scanning) and measured with one of the PPICs of the RRD, when the intensity control system [Schoemers et al. 2015] is activated. The time resolution of this measurement is t_s = 495 μs, which was chosen together with the fifth nominal beam intensity of $1 \cdot 10^7$ pps in order to mimic the typical high-dose scheme (5000 ions/RP) used for a scanned irradiation to obtain a transmitted image. Standard deviations (σ) from the mean charge value might reach up to 20%, while outliers might vary up to a factor of 3.

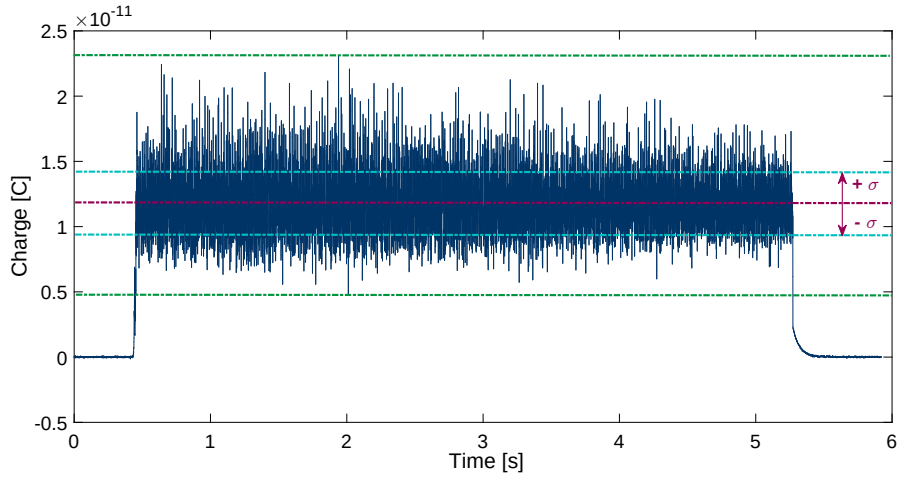

Figure 3.3: Typical spill time-structure of a 299.94 MeV/u ^{12}C ion beam entering the RRD exactly at the isocenter traversal coordinates (i.e., no active scanning is applied). The graphics shows the current (beam intensity) integrated by the 47th PPIC of the imaging detector, where the Bragg peak (BP) is located. In this example, the particle delivery rate was chosen in combination with the PPIC integration time, so that the number of ions registered per sample resembles the high-dose irradiation scheme used for imaging acquisitions. i.e, if the time resolution of the measurement is equal to the sampling interval t_s = 495 μs and the beam intensity is $1 \cdot 10^7$ pps, ~4950 ions are expected per sample. Standard deviations (σ) of the intensity fluctuations easily extend up to 20% of the expected value. The minimum and maximum variations are also indicated with dark green level-lines.

3.3.3 Experimental implications of the intensity fluctuations

The beam intensity (I) instability has important repercussions for the DAQ and processing. If a determined dose (number of ions (N_{ions})) per RP is set, the time spent by the beam in each scanning spot (t_{RP}) will vary accordingly (cf. Figure 3.4):

$$t_{RP} = \frac{N_{ions}}{I}. \tag{3.2}$$

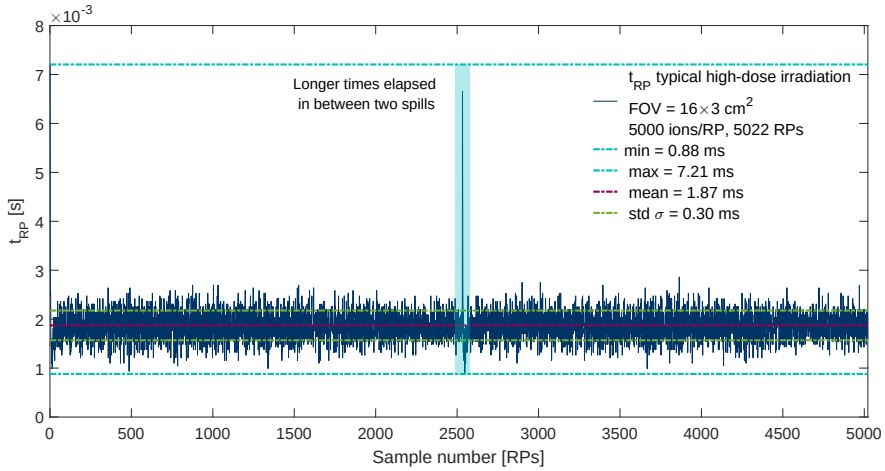

Figure 3.4: Time interval variability between consecutive Raster Points (RPs) in a typical high dose irradiation scheme to obtain an ion-based radiographic projection. In this particular example, an extended FOV of 16.1×3.0 cm^2 was irradiated with a 299.94 MeV/u ^{12}C ion beam of 3.9 mm FWHM. The RPs were separated by 1 mm in horizontal and vertical directions, each of them required to be irradiated with 5000 carbon ions delivered at a nominal rate of $3 \cdot 10^6$ pps, chosen by the PDG. The time in between RPs might deviate up to 7.21 ms from the mean value of 1.87 ms (excluding RPs occurring between the end and beginning of beam spills, which can last up to 5 s). The mean time variability distribution is in agreement with the expected value of 1.7 ms, restricted by the integration time of the BAMS (cf. Section 3.3.1), with a standard deviation of 0.3 ms.

The fluctuations of the t_{RP} are shown in Figure 3.4 as example of the sampling-time variability typically observed in a high-dose radiography irradiation. Although the expected t_{RP} is imposed by the BAMS (cf. Section 3.3.1), extreme periods up to 5 s can occur due to the longer time elapsed for RPs in between spill pauses. These pause outliers have been replaced in the graphic by the mean interval value, remaining only one longest time span of 7.2 ms. To illustrate the variance of the lapses between RPs (t_{RP}), the Figure 3.5 shows the related occurrence histogram. Later in this thesis, data processing methods applied in both, time and frequency domains, will be introduced. Hence, in order to apply the appropriate statistical assumptions, it is important to describe the underlying distribution of the non-uniform sampling-time of the acquired data.

In this attempt, the Scott's rule[B] [Scott 1979] was used to choose the right binning size of the histogram. This method is suggested whenever random samples have a roughly normal distribution, which it was assumed in this case. Applying this binning method to the t_{RP} data plotted in Figure 3.4, the produced histogram consists of 128 bins of $5 \cdot 10^{-5}$ s width (w_{bin}), which are then considered to evaluate the respective Probability Density Function (PDF). In

[B]The Scott's rule uses the bin width $w_{bin} = {}^{3.5\sigma}/_{N_{tot_{RP}}^{1/3}}$, where σ is the sample standard deviation.

this case, the PDF of a Gaussian curve is parametrized in terms of the mean (μ) and the variance (σ^2) of the sample, obtained from the plot 3.4 as:

$$f(x) = \frac{1}{\sqrt{2\sigma^2\pi}} \exp\left[-\frac{(x-\mu)^2}{2\sigma^2}\right]. \tag{3.3}$$

The height (h) of each bar is thus proportional to the fraction of counts ${}^{N_{t_{RP}}}/_{N_{tot_{RP}}}$, scaled by the inverse of the bin-width (w_{bin}) as:

$$h = \frac{N_{t_{RP}}}{N_{tot_{RP}} \cdot w_{bin}} [s^{-1}]. \tag{3.4}$$

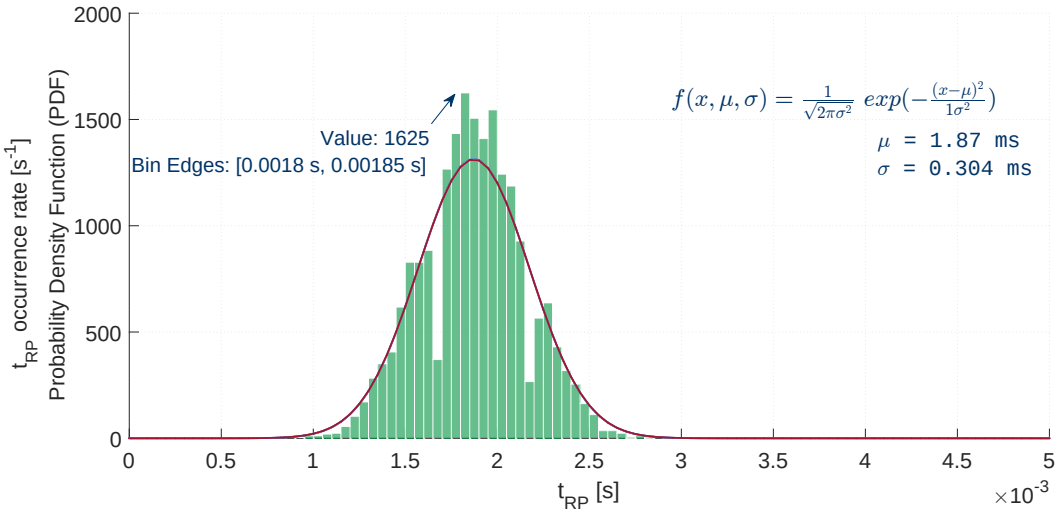

Figure 3.5: Occurrence histogram of the lapses between RPs (t_{RP}). The Scott's rule was implemented to bin the data, yielding 128 bins of $5 \cdot 10^{-5}$ s width. The PDF is then parametrized in terms of the mean (μ) and the variance (σ^2) to produce an integral under the function equal to 1. The area of each bar is relative to the number of occurrences and its height is given by the equation 3.4. For instance, the bin with most number of events, spanning from 1.8 to 1.85 ms is indicated. Its area represents the rate of the fraction of events ${}^{N_{t_{RP}}}/_{N_{tot_{RP}}}$, meaning that only ~8% of the total number of t_{RP} intervals actually falls near to the range delimited by the BAMS. Nonetheless, the lapses between RPs follow a Gaussian distribution.

On the other extreme, the behavior of the t_{RP} in a low-dose scenario (500 ions/RP at 1 mm separation) is examined in Figure 3.6. The lowest nominal delivery rate available at HIT for carbon-ion beams ($2 \cdot 10^6$ pps) was enforced. In this case, the same FOV ($16.1 \times 3.0 cm^2$) as the one used to obtain Figure 3.4 was completed with less than one-full spill in about 1.3 s (as reference, the high-dose irradiation takes 18.2 s and two spills to be done). As mentioned before, the system read-out electronics has limitations on collecting data at these considered fast-rates. Minimum intervals between RPs of 165 μs appeared in ~14% of the samples. The underlying reason of this limit is justified by the DAQ method and how it is synchronized with the scanning delivery system, widely explained in Section 3.4.3. For now, the Figure 3.11 is a visual aid to represent t_{RP}, which in this concrete example comprises $t_{RP} = t_s + t_{gap} = (t_{int} \cdot n \cdot {}^{c}/_{s}) + t_{gap} = 55\ \mu s \cdot 1\ {}^{c}/_{s} + 100 \mu s = 155\ \mu s$. i.e., only a tiny interval of 10 μs prevented these RPs to be missed. Even though, ~6% of the expected number of samples were overlooked, which makes impossible to assign the correct RP to its corresponding BC in the projected image.

Figure 3.6: Typical response of the t_{RP} on low-dose (500 primaries/RP at 1 mm separation) irradiations with the first nominal intensity enforced (a) and when the reference intensity allowed by the BAMS has been modified (b).

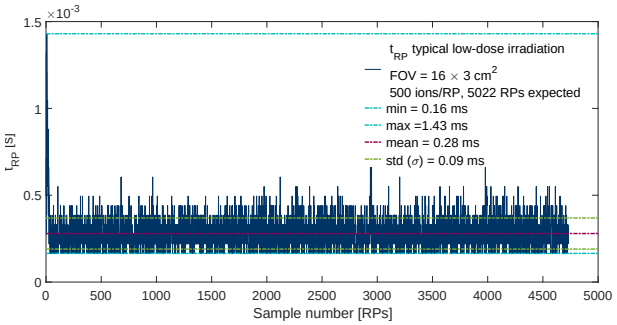

(a) Behavior of the t_{RP} in a low-dose scenario (500 ions/RP at 1 mm separation). A FOV of 16.1 × 3.0 cm^2 was scanned with a 299.94 MeV/u ^{12}C ion beam of 3.9 mm FWHM, using the lowest nominal intensity from the LIBC ($2 \cdot 10^6$ pps) acquired with the shortest integration time ($t_{int} = 55$ μs) allowed by the read-out electronics (cf. Section 3.4). The PBP needed less than one-full spill and about 1.3 s to be concluded, leading to minimum intervals between RPs of 165 μs in ∼14% of the samples. ∼6% of the expected number of samples (5022 RPs counts in this instance) were missed.

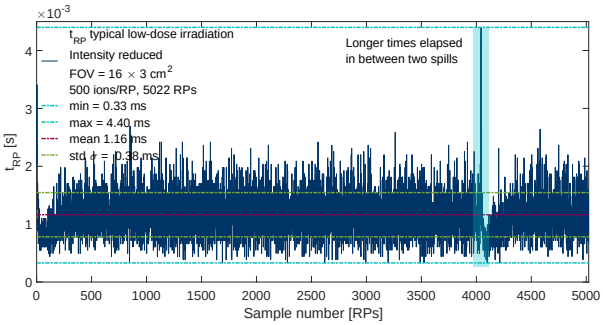

(b) The low-dose-PBP timing showed on the left lies on the border of the electronics capabilities to acquire synchronous data to the active scanning. Therefore the BAMS reference intensity allowance was reduced from 3.65 nA/RP to 0.8 nA/RP in order to slow the irradiation time by about a factor of four, so that t_s is enlarged ($t_s = 165$ μs) and all the RPs are registered. Note that when the beam is requested through the MBP, the dynamic intensity control [Schoemers et al. 2015] is not activated, hence the rising slope of the spill is not as steep as the one in Figure 3.3, which has an impact in the t_{RP} along the irradiation.

The solution to this issue is to slow down the irradiation rate. Based upon the principle described in Section 3.3.1 to determine the reference intensity value allowed by the BAMS via equation 3.1, the low-dose fast-PBP, whose timing is represented in Figure 3.6a, yielded a reference current value of 3.65 nA/RP, corresponding to a reference charge measurement by the first BAMS PPIC of 0.92 pC/RP, since its integration time was also extended to 250 μs to allow longer signal accumulation. The third measurement range was used, which guaranteed reliable current measurements up to 170 nA.

The current allowance in the MBP was then downsized to 0.8 nA/RP in order to slow down the plan by increasing the irradiation time to 5.8 s to be completed with ∼1.3 spills (cf. Figure 3.6b). This configuration assured the detection of the total expected number of RPs with an extended sampling time of $t_s = 55$ μs $\cdot 3$ $^c/_s = 165$ μs.

Consequences of these time fluctuations affecting the DAQ performance, detection efficiency and noise mitigation methods will be addressed in the subsequent sections.

3.3.4 Beam Application and Monitoring System response to low-fluence and low-intensity irradiations

For the sake of obtaining ion-based transmitted images with the lowest achievable dose, the BAMS intensity-threshold is decreased; so that the ionization chambers take longer periods to integrate the charge generated by the delivered primaries (cf. Section 3.6). In the patient treatment dose regime, for which the HIT accelerator and raster scanning system are originally intended, typical doses per RP are expected to be around 1 Gy or higher. In some pre-irradiation cases, the doses can be slightly lower, which, for carbon ions, corresponds to an amount of particles per scanning spot in orders of ∼10^4 to ∼10^7, varying according to the specific treatment plan requirements and fractionation. Lower fluence limits have never been

explored at HIT before, in consequence, the BAMS have never been calibrated for the low number of particles intended for transmission imaging purposes (cf. Section 3.2). In order to give a realistic estimation of the dose deposited in the imaged phantoms, the exact number of ions delivered per scanning step must be known accurately. Therefore, the BAMS response to low-fluence and low-intensity irradiations was investigated by means of a Bragg-Peak Ionization Chamber (BPIC)[C] as external reference device, in order to verify whether the number of irradiated particles registered by the BAMS and recorded in the PBRs coincide with the actual number of particles exiting the nozzle. The experimental description of these investigations are explained after introducing briefly the BAMS Ionization Chambers (ICs) calibration procedure in the clinical scenario at the HIT facility.

As it was described in the Section 2.3.3, the BAMS consists of three ICs committed to monitor and control the beam fluence before and during the delivery of the treatment. The BAMS ICs work in a threshold-mode, which is determined by a pedestal value and its deviation margin, given in terms of Analog-to-Digital-Converter (ADC) counts. Thus, the ICs will provide inexact particle counts whenever the induced charge signals are close to the established threshold in the integrator.

The TCS relies mainly on the feedback from the first IC (IC1), being its charge accumulation constraints the highest for safe clinical applications. In other words, the IC1 reading will show the number of particles which is closest to the requested ions in the PBP, keeping the dose safely bounded. IC2 widens the charge pedestal tolerance to a certain extent, thus showing a more realistic response to be compared with the BPIC measurements, even when the dose security-thresholds are not fulfilled.

The BAMS has its own independent dosimetric calibration method, owing to the active beam delivery system for which it is used. This calibration is based on the code of practice for dosimetry (absorbed dose to water) established by the IAEA, however, the reference conditions are adjusted according to the raster scanning system and facility-specific dynamic energy range. This energy-dependent calibration is experimentally validated by absorbed dose measurements in homogeneous fields at a few representative energies using a Farmer-type ionization chamber[D]. The dose is quantified at the plateau region of the BCs. The full energy range is then obtained by an interpolating fitting function. The agreement between measured and calculated doses is usually better than 1% for square mono-energetic fields. The procedure is very similar to the one described by Jäkel et al. [2004], although at HIT, the fitting curve is based on the Bethe-Bloch formula with two additional free parameters. The collected charge to number of particles conversion for each beam energy and ion species relies on the geometry and parameters of the BAMS ICs (cf. Table 2.1) and stopping power tables obtained both, analytically and by MC (FLUktuierende KAskade (FLUKA)) simulations, including the full HIT beam-line [Parodi et al. 2012b].

The BPIC is a plane parallel IC with disk shaped air-filled sensitive volume of 2.5 cm^3 with an electrode spacing of 2.1 mm. The electrode radius is 40.8 mm. The entrance and exit windows have a respective thickness of ∼3.5 mm and ∼6 mm. The housing of the BPIC is made of PMMA, hence these thicknesses correspond to water equivalent path lengths of ∼4

[C] © Bragg-Peak ionization chamber by PTW Freiburg GmbH (http://www.ptw.de/bragg_peak.html)
[D] Farmer ionization chamber by PTW Freiburg GmbH (http://www.ptw.de/farmer_chambers0.html)

mm and ∼7 mm, respectively.

In the same way as it is regularly done for the above described QA protocols, the measurements with the BPIC were performed at the entrance region of the beam, i.e., at the plateau region of the BC. The BPIC was located at 13 cm downstream of the beam-line nozzle outlet, aligned with the beam direction. This choice is justified by three main reasons; first, to obtain a reasonable comparison between the external device (BPIC) and the BAMS ICs outputs. Second, in transmission imaging applications, the plateau region is the most important zone for dose assessment. And third, owing to the energy dependency of ionization chamber outcomes, measuring in the steady part of the BC allows to fairly extrapolate a similar behavior for other energies. Absolute charge measurements were obtained from the BPIC, adjusting the measurement range according to the charge level expected from each beam irradiation configuration. The performance comparison between the BAMS ICs and the BPIC was done in terms of particle number. The PBRs of the first two ICs of the BAMS provide these numbers for each irradiated PBP, while the number of ions detected by BPIC is estimated as follows:

$$N_{ions_{BPIC}} = \frac{Q \cdot W}{\left(\frac{dE}{dx}\right)_w x_w}, \tag{3.5}$$

where:
$x_w \approx (2.1 \pm 0.1) \cdot 10^{-3}$ mm WE chamber air gap.
W_{carbon} =34.5 ±0.5 J/C (in dry air).
W_{proton} =34.23 ±0.14 J/C (in dry air); W_{proton} =34.8 ±0.5 eV (in humid air).
Q is given in Coulombs as the absolute charge measured by the BPIC with an uncertainty of 1% given by the manufacturer documentation.
$\left({}^{dE}/_{dx}\right)_w$ represents the FLUKA depth dose in water (from vacuum), evaluating the dose per unitary fluence ($^{dE}/_{dx}$ in water for ρ= 1 $^{g}/_{cm^3}$) at the specified depth of 6 mm [3.11mm (BPIC) + 2.89 mm (Vacuum Window, Air and BAMS) WE]. This calculation is based on FLUKA v2011.2c.

Bragg Peak Ionization Chamber (BPIC) energy calibration

In order to rule out any energy dependence of the BPIC on the charge collection and to compare its performance with respect to the BAMS ICs, the BPIC was exposed to proton and carbon-ion beams of six different LIBC energy settings: E255, E209, E157, E104, E58, E21, corresponding to 221.05 MeV, 190.48 MeV, 160.09 MeV, 130.52 MeV, 100.46 MeV and 70.03 MeV for proton beams and to 430.1 MeV/u, 366.78 MeV/u, 305.27 MeV/u, 246.57 MeV/u, 187.97 MeV/u and 129.79 MeV/u for carbon-ion beams, yielding approximately the same ion range in water (cf. Figure 3.7). For both ion types, the TCS irradiation was configured to deliver a fixed high number of particles at the isocenter, thus discarding any BAMS ICs inaccuracy due to low-fluence acquisition. The required number of particles to be delivered at the center of the BPIC was $2 \cdot 10^9$ protons and $5 \cdot 10^7$ carbon-ions. The beam intensity was the one automatically chosen by the TCS PDG, i.e., I10 = $3.2 \cdot 10^9$ pps for protons and $8 \cdot 10^7$ pps for carbon-ion beams, in all the irradiation configurations.

For both ion types, the lowest energies show a slightly larger discrepancy from the originally required number of primaries, due to the proximity of the BP to the chamber. Without

Figure 3.7: Bragg Peak Ionization Chamber (BPIC) energy calibration. A fixed high number of (a) protons ($2 \cdot 10^9$) and (b) carbon-ions ($5 \cdot 10^7$) was requested to be delivered at the isocenter at six representative energies, covering the energy span available at HIT. The number of ions counted by the BPIC was determined with the Equation 3.5 and compared to the readings registered in the PBRs of the first two BAMS ICs, as well as the originally requested number of primaries.

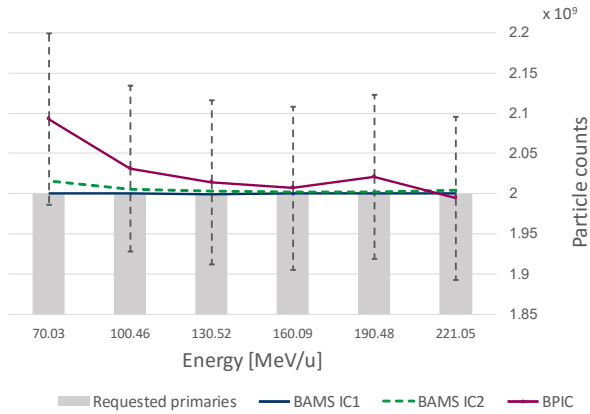

(a) Proton counts comparison between the BPIC outcome and the number of protons registered in the PBR by the BAMS ICs. As reference, the target dose ($2 \cdot 10^9$ protons) is indicated in light gray. Protons were irradiated at the center of the BPIC, located in the plateau region of the BC (13 cm downstream of the nozzle exit-window), at six different beam energies: 221.05 MeV, 190.48 MeV, 160.09 MeV, 130.52 MeV, 100.46 MeV and 70.03 MeV.

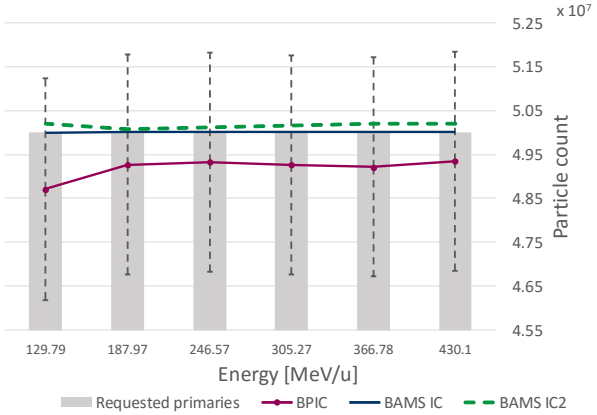

(b) Carbon-ion counts comparison between the BPIC outcome and the number of ions registered by the BAMS ICs. The expected number of carbon-ions ($5 \cdot 10^7$) is represented in gray. Analogously, carbon-ions were irradiated at the center of the BPIC, located in the plateau region of the BC (13 cm downstream of the nozzle exit-window) at six different beam energies: 430.1 MeV/u, 366.78 MeV/u, 305.27 MeV/u, 246.57 MeV/u, 187.97 MeV/u and 129.79 MeV/u.

taking into account the lowest energy, the BPIC estimation of protons and carbon-ions is in agreement to the target fluence within a difference lower than 1% and 1.5%, respectively, and not beyond their corresponding estimated error. Transmission imaging applications usually require energies higher than 200 MeV/u, for which the BPIC exhibits a stable performance with no strong energy-dependence.

BPIC response for typical fluences available at HIT

In order to investigate the response of the BPIC on the application of different typical fluences used in a standard treatment scenario, the highest carbon-beam-energy available at HIT (430.1 MeV/u) was chosen and $2 \cdot 10^6$, $5 \cdot 10^6$, $8 \cdot 10^6$, $1 \cdot 10^7$, $2 \cdot 10^7$, $5 \cdot 10^7$ primaries were requested to be delivered at the nominal intensity chosen by the PDG (I10 = $8 \cdot 10^7$ pps) (cf. Figure 3.8). The BPIC and the BAMS were found to accurately coincide with the target fluences requested. As expected, the IC1 shows the best agreement (−0.18% difference), followed by the IC2 (−0.54% difference). Nonetheless, on average, the BPIC does not exceed the 1.5% uncertainty for this specific energy.

BPIC and BAMS ICs response to reduced beam intensity

Once the BPIC performance is characterized for the standard irradiation conditions, the accelerator procedure to decrease the particle delivery rate (cf. Section 3.3.3) should be tested. To this aim, a mono-energetic 430.1 MeV/u ^{12}C beam was used, the targeted number of particles was settled to be $2{\cdot}10^6$, which is determined by the number of particles delivered by the lowest nominal intensity available at HIT ($2{\cdot}10^6$ delivered in one second), and the particle delivery

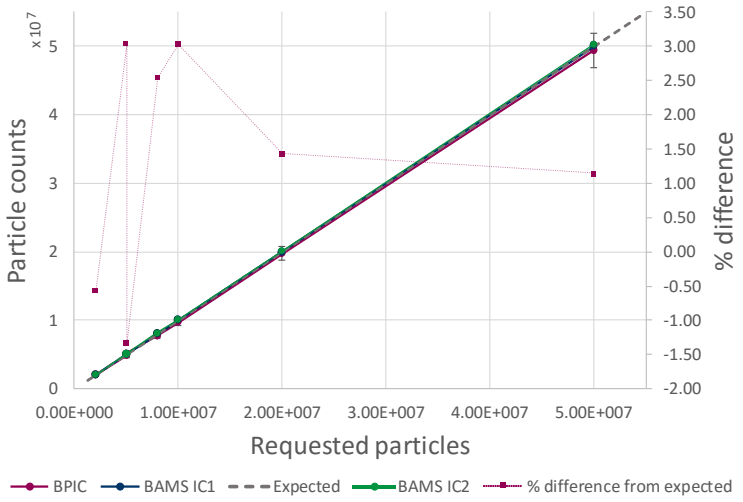

Figure 3.8: BPIC calibration for typical fluences available at HIT. To perform a scan over the usual number of primaries requested by treatment plans, a 430.1 MeV/u ^{12}C beam was used to assess the accuracy of the BPIC to recover the amount of particles requested. The target dose (number of particles) was reduced from $5 \cdot 10^7$ to $2 \cdot 10^6$ and a linear behavior was confirmed among the three ICs compared. On average, the BPIC chamber ion-counts coincides with the expected primaries within 1.5%, although differences up to 3% can be found.

rate was reduced by decreasing the current allowance of the BAMS IC1, starting from the reference current value defined by the PDG (cf. Figure 3.9). Already on the forth reduction step (1 nA), the BPIC shows a difference of ∼20% from the expected particle count, which is not detected by the BAMS IC1. Further reduction of the reference current value allowed by the BAMS (∼fA), might yield discrepancies up to 80% primaries count. This BAMS limitation should be taken into account when low-dose irradiations are performed to determine the optimal and reliable BAMS IC reference current.

BPIC and BAMS ICs response to a fluence reduction under nominal particle rates

The accelerator research working-mode also allows to fix the desired number of particles to be delivered while deciding which beam nominal-intensity should be used, so that the PDG is sidestepped. Under this configuration, a carbon-ion beam of a typical energy used for transmission imaging was chosen (E189 = 339.8 MeV/u) to impinge $2 \cdot 10^6$, $1 \cdot 10^5$, $1 \cdot 10^4$, $1 \cdot 10^3$, $5 \cdot 10^2$ and $1 \cdot 10^2$ ions on the BPIC (cf. Figure 3.10). The higher numbers of primaries requested per RP ($2 \cdot 10^6$ and $1 \cdot 10^5$) were irradiated without inducing safety interlocks at the tenth carbon-beam LIBC intensity, I10 = $8 \cdot 10^7$ pps. In order to deposit $1 \cdot 10^4$ per RP, the beam rate was decreased by one order of magnitude to the I4 = $8 \cdot 10^6$ pps, while the rest of the particle requests demanded the lowest carbon-beam intensity available, I1 = $2 \cdot 10^6$ pps. As it was mentioned in Section 3.2, the dose schemes used in this work fall within the limit of the HIT capabilities to deliver low number of particles and register them accurately by the BAMS records, as it is evident from the percentage of discrepancy between the BPIC and the BAMS IC2 readings indicated on the right axis of Figure 3.10. By extrapolating the curve tendency (due to missing data point), the high-dose scheme might display up to 27% disagreement from the BAMS IC2 readings, while the middle- and low-dose scenarios may differ from the PBRs up to 90% and 142%, respectively.

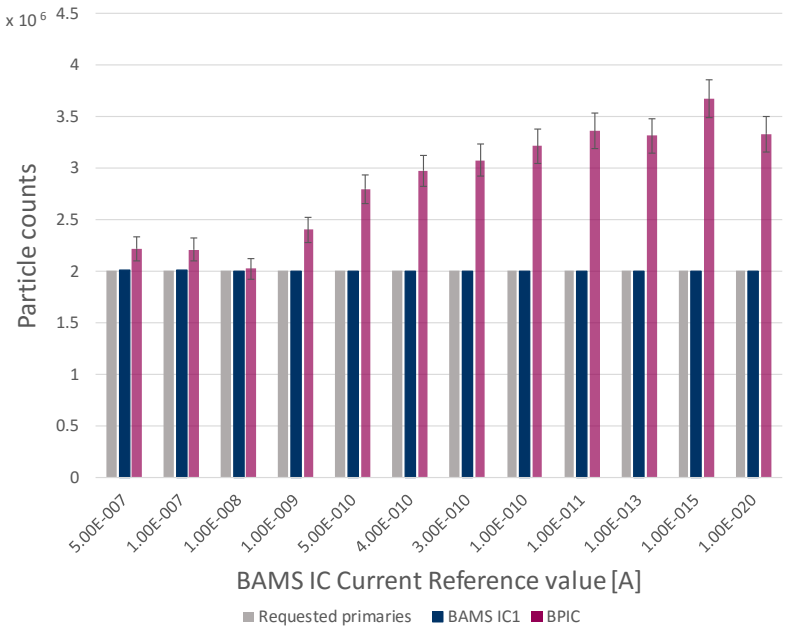

Figure 3.9: BPIC and BAMS IC1 response to reduced beam intensity. $2{\cdot}10^6$ ^{12}C-ions at 430.1 MeV/u were requested for delivery while the reference current accepted by the BAMS IC1 was reduced in 12 steps. When the current allowance by the IC1 is reduced to ∼1 nA the BAMS fails to detect ∼20% ions of the expected particle goal. Further reduction of the BAMS IC1 reference current leads to higher inaccuracies, which should be avoided. Optimally, currents of ∼10 nA should guarantee the best trade-off between the correct detection of RPs by the read-out electronics, long-enough integration times and with reliable dose delivery.

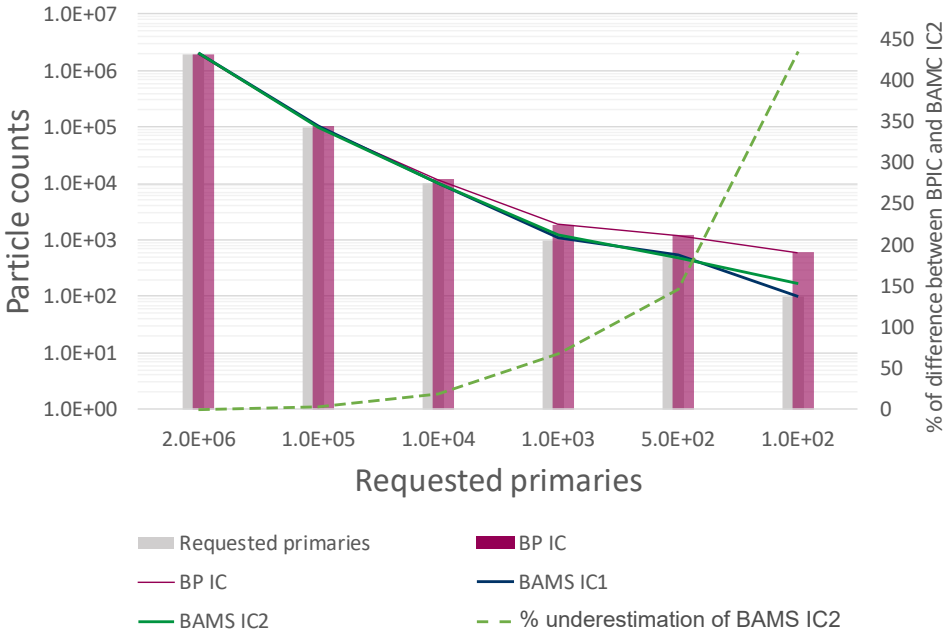

Figure 3.10: BPIC and BAMS ICs response to fluence reduction under nominal particle rates. A 339.8 MeV/u ^{12}C-ion beam, which is in the energy-range used normally for transmission-imaging purposes, was chosen to irradiate $2 \cdot 10^6$, $1 \cdot 10^5$, $1 \cdot 10^4$, $1 \cdot 10^3$, $5 \cdot 10^2$ and $1 \cdot 10^2$ ions at the isocenter, traversing the BPIC in the plateau of the BC. For this investigation, the PDG was evaded by enforcing a certain nominal beam-intensity before the particle delivery. To deposit $2 \cdot 10^6$ and $1 \cdot 10^5$ carbon-ions per RP, I10 $= 8 \cdot 10^7$ pps was used. Requesting $1 \cdot 10^4$ ions per RP already required a reduced beam-intensity by one order of magnitude, while the last three doses ($1 \cdot 10^3$, $5 \cdot 10^2$ and $1 \cdot 10^2$ carbon-ions) were achieved by selecting the I1 $= 2 \cdot 10^6$ pps before the irradiation started.

Dose implications

The dosimetric implications per RP of the particle counting mismatches presented in the former section, at the three different dose-levels investigated in this work, are summarized in the Table

3.1. The dose is estimated by the Equation 2.19, in the plateau region of a 339.8 MeV/u ^{12}C-ion beam. Exemplary scanning steps of 1 mm and the particle fluences obtained with the different ICs are considered for the calculation.

Table 3.1: Dose calculation comparison given by the BAMS ICs and BPIC particle outcome when irradiated at the three different dose-schemes considered in the experimental investigations of this work.

	requested primaries	BAMS IC 1	BAMS IC 2	BPIC	
Low-dose	500	532	477	1208	ions
Dose	0.95	1.01	0.91	2.29	mGy
Middle-dose	1000	1069	1226	1898	ions
Dose	1.90	2.04	2.33	3.61	mGy
High-dose	5000	5166	5759	6348	ions
Dose	9.52	9.83	10.96	12.09	mGy

The results presented in this section show the limitations of the HIT accelerator and monitoring system under the non-clinical dose regime. They provide indicators that must be taken into consideration for accurate image dose estimation when acquiring low-dose transmitted-images.

3.4 Synchronized data acquisition with the active delivery system and updated electronics

Each RP reading must be attributed to a pixel in the transmitted ion-based image. In the context of this work, the term *pixel* or *picture element* refers to the physical point in the image which contains the WET information of the materials of the imaged object and the detector, crossed by the carbon-ion beam. It is associated with the BP position within the RRD for each RP. In further data processing, it represents the smallest element that can be addressed in the displayed projections. To properly obtain a BP signal per RP, the RRD is equipped with a read-out electronics that must acquire and stream data points synchronously with the active scanning delivery system. Two trigger systems are involved in this process: the first one, sent and controlled by the TCS, indicates the RP sequence followed by the beam, discussed in the next section; while the second one is coupled to the latter to initialize the data integration every time that the beam reaches a new RP. The Sections 3.4.2 and 3.4.3 focus on the second triggering system.

3.4.1 Edge-mode *Next-Point* trigger signal to follow the scanning progress

As previously introduced in Sections 2.3.3 and 2.3.4, during the performance of the irradiation, the BAMS keeps track and records the beam intensity and positions. When each RP has received the desired number of primaries, the beam is magnetically deflected to the subsequent position. The scanning progress (RP sequence) per IES is registered by a TTL signal provided by the TCS via the Beckhoff EtherCAT system[E]. This signal indicates that the next point is ready to be irradiated, hence its name *Next-Point* trigger. This is a crucial step in the image formation method, since the logical signal created *on-the-fly* will initialize the charge integration process simultaneously in all the PPICs of the RRD.

[E]Beckhoff Automation GmbH, Frankfurt, Germany. (`www.beckhoff.de`)

The Beckhoff TwinCAT System Manager is a configuration interface for the input/output (I/O) response of the EtherCAT automatic controllers. It allows to shape the *Next-Point* trigger signal in three different modalities (which are later depicted in the Figure 3.11):

- *Pass-by.* The pass-by mode is the original binary signal that switches between two voltage levels (0 to 5 V) to designate the transition between two RPs. Only when the scanning spot underway has been irradiated and the beam has reached the next position, the pass-by signal is set to *high* or *low*, represented by two discrete values 1 and 0, respectively. The pass-by binary signal might randomly start from a high or low state. Such a binary waveform enables external transition detection through rising or falling edges of the signal. In this case, opposite flanks are generated for two consecutive RPs (cf. Figure 3.11 upper panel). The read-out electronics (cf. Section 3.4.2) can be settled to start the charge collection by detecting either rising or falling signal steps. Hence, in order to have the same high (*Pulse*) or low (*Edge*) transition every single RP two additional waveforms were designed (see below).

- *Pulse.* If the pulse-mode is chosen, a fast pulse (100 ns rise-time) of 50 μs minimum width and 100 μs shortest period is generated by the *Next-Point* trigger signal, whenever a new high or low transition of the pass-by signal occurs, i.e., when the irradiation of a new RP has started. Therefore, in contrast to the pass-by signal, each rising edge features the most recent RP (cf. Figure 3.11 middle panel). This trigger modality was adopted in the first implementation of the present imaging system [Rinaldi et al. 2013].

- *Edge.* The edge-mode is the trigger signal shape applied at the moment to acquire transmission images. It consists on an inverted-gap signal produced when the beam has completed the irradiation of an individual RP and has moved to the next point in the irradiation plan. Equivalent to the pulse characteristics, the reaction-time of the edge-mode is 100 ns. The narrowest available gap is also 50 μs width, owing to the fact that pulses and gaps are created in cycles of 50 μs. Due to the finite signal reaction-time, one single cycle might result unreliable to define the initialization of the charge accumulation by the electrometer. Therefore, to guarantee the correct rise identification of a valid RP, a double-cycle gap of 100 μs was preferred (cf. Figure 3.11 lower panels).

The synchronized *modus operandi* of the *Next-Point* trigger signal together with the triggering modes of the charge collectors used in these and previous investigations (cf. section below) is explained in detail in the Section 3.4.3 and exemplified in the Figure 3.11.

3.4.2 Read-out electronics evolution and improvement

The obtained transmitted projections should be a 2D-distribution of BP positions, determined from their corresponding discretized BCs in each delivered RP. In order to retrieve each individual point of the BC, the read-out electronics system simultaneously collects and logs the charge measured by the 61 PPICs.

In a full-performance scenario of the presented imaging setup, all the irradiated particles per scanning step are detected. i.e., the current in each PPICs is integrated by the capacitor in the delivery time t_{RP} of each RP, irrespective of its variable duration (cf. Section 3.3.2 and

Figure 3.4). However, these ideal experimental conditions might be critically affected by various factors, namely the detector and electronics performance, and the electronic and environmental noise influencing the setup, as it will be discussed in greater length in the successive sections. The currently-used read-out electronics is put in perspective by making a comparison between the electrometer utilized previously and the one potentially adopted in the forthcoming imaging prototype, in terms of the most significant acquisition parameters.

The main electronic parameters involved in the DAQ for the image formation method proposed in this work are the RP-wise charge collection, specifically the sample time length (t_s), in addition to the triggering and integration-gating modes that will produce a sample point every time a new RP is encountered.

The I3200-A500

In this regard, the first version of the experimental-setup [Rinaldi et al. 2013] was supplied with two I3200 32-channel digital electrometers[F] controlled by an A500 module necessary to cover the measurements acquired with the 61 channels of the RRD.

The sample generation by the I3200-A500 was achieved by the so-called gated integration, which consists on measuring the total charge (ΔQ) accumulated on a capacitor due to ionization, over a finite measurement period (integration time, t_s). When the ionizing radiation is present in the IC, the capacitor charges-up and the voltage increases by ΔV. By noting the change in the voltage across the capacitance (C), over the integration time, the total integrated ionization current or ionization charge can be deduced as $\Delta Q = C \cdot \Delta V$ or $\Delta I = {}^{C \cdot \Delta V}/_{t_s}$, respectively. Due to the innate voltage-range limit of the ADC, an intermittent charging and discharging of the capacitor is necessary between two consecutive integration periods. Hence the *gated* attribution is given.

The integration time used with this electronic module was chosen to be 100 μs. The integrator also enabled the possibility to adjust other timing sequences involved in the integration process, such as the settle time (25 μs) before switching on the capacitor, the set-up time (20 μs) at the end of the charge collection and a reset time (20 μs) to get the analog circuitry ready to acquire the next measurement. In total, the I3200-A500 needed 165 μs to collect a sample point, out of which only 100 μs were effectively used to gather information about the irradiated tissue at the RP position. Considering averaged intervals between treatment points (t_{RP}) of about 1.8 ms (cf. Figure 3.5), data collecting of $\sim$5% of the total time that the beam remains in each RP must be improved. As reported by Rinaldi [2011], main experimental drawbacks faced with these electronic modules comprise a poor ratio of the detected to delivered primary ions, as well as long logging cycles attributed to a limited number of samples that could be buffered, which causes data-transmission times lagging behind real time. In these cases, a lower beam-intensity should be chosen, which would result in longer irradiation times.

The I128

The transmission imaging system was upgraded by incorporating an I128 128-channel charge integrator[G], aiming at overcoming the deficiencies related to the previous read-out electronics and improve the overall setup performance. First, firmware and host software upgrades helped

[F] Pyramid Technical Consultants (`http://www.ptcusa.com/products/21`)
[G] Pyramid Technical Consultants (`http://www.ptcusa.com/products/22`)

to speed-up the data flow to the host computer and thus minimize the time needed per image acquisition; furthermore, increasing the integration time between RPs to consequently boost the detection efficiency and SNR.

The compact I28 module provides 128 parallel and independent integrator channels to simultaneously accumulate and log the integrated-currents as charge (C), measured by the 61 PPICs of the imaging RRD. The collectors have a dynamic measurement range of 0.1 pC $<$ C $<$ 10 nC, that can be obtained during pre-established sampling times (t_s), from 55 μs to 1 ms. Longer integration periods can be achieved by numerical summing up of up to 255 integrations, i.e by increasing the so-called conversions per sample ($^c/_s$). The latter feature is fundamental to achieve the optimal timing for the various experimental scenarios explored in the course of this work, as explained in the next section. Major improvements of the I128 from the previously used I3200 include a faster Ethernet connection and buffer functionality, which uses its internal memory to store up to 65535 sets of readings [Pyramid Technical Co. 2012], thereby allowing *on-the-flight* data-flow up to 18.2 kHz (when the shortest integration time (t_{int} = 55 μs) and 1 $^c/_s$ are used), thus avoiding buffer overflow. In regard to this work, a typical high-dose irradiation of one IES generates data at a rate of ~2 kHz, obtained by using integration times in the order of 500 μs. Higher data rates may cause sample-streaming issues, as it is addressed in Section 3.4.3. The digital buffer of the electronics is limited to 83 sample blocks, i.e., readings are transmitted to the host computer only when a full block is filled. This number must be kept in mind while setting the expected number of RPs (samples) in the software user-interface before starting each acquisition. When the total number of readings is not properly specified, the acquisition will be terminated after completing the last block of exactly 83 samples, so then missing the rest of RPs if they are not enough to complete the next block.

Regardless of the integration time, the maximum current allowance per channel is up to 500 to 600 nA. In principle, the I128 electrometer is not designed to measure multi-channel inputs of negative currents, nonetheless it has some negative current measurement range to allow for baseline noise fluctuations [Pyramid Technical Co. 2012]. The PPICs are directly connected to the electrometer via banks of 2×32 analog input/output channels, included in the module by using 44-pin connectors, therefore no additional controller is needed as in the previous configuration. The I128 is also equipped with an internal High Voltage (HV) supply (yielding a bias-voltage range from 20 V to 1000 V with a confirmation feedback), which is, in turn, instructed by the *PTC Diagnostic v5.8.0* firmware provided by the same producer.

Similar to the periodic capacitor-charging/discharging method used by the I3200, the I128 also implements a gated integrator, which typically discharges the capacitor once per user-selected sampling period (t_s). However in this model, the settle, set-up and reset times involved in the charge collection are restricted to the manufacturer initial configuration, not enabled for user manipulation. There is, in any case, a typical reset sequence of about 50 μs in which the I128 is prepared for the next accumulation. During this time no current measurement is lost, since the system holds until the next integration recommences.

The I128 can measure continuous data in a auto-running mode, using the buffered internal trigger, or it can wait for an external trigger in its gate input as a flag to start acquiring

data [Pyramid Technical Co. 2012]. For the research carried out in this work, the internal triggering was mainly used to obtain noise-level measurements, prior to every experiment. On the other hand, for imaging goals, it was necessary to trigger the DAQ system externally. The initiation of each integration can be controlled by a external TTL input signal in versatile working modes, i.e., by assigning the edges of such trigger signal to start, hold, pause and/or stop acquisitions, responding either to rising or falling edges. In particular, the so-called *External/Start hold* trigger mode was suitable to assure that one sample period (t_s), consisting on several conversions per sample ($^c/_s$), ($t_s = t_{int} \cdot n \cdot {}^c/_s$) collected the averaged charge corresponding to an individual RP. In this acquisition configuration, the default number of full integrations requested (burst size) is forced to be one. Other customized triggering modes to synchronize the data collection with external events were tested. Nonetheless, the constraints explained in Section 3.4.3 make various edge selection combinations very prone to detection failure.

The Section 3.4.3 goes into details of the merged operation, response and limitations when the external *Next-Point* trigger signal provided by the TCS is implemented in the gate input of the I128.

The I400 towards the I6400

Important improvements were already achieved by equipping the current transmission imaging setup with the I128 electronics. Nevertheless, there is a significant modification in the trigger signal edge-detection allowing optimal variable-length integration in between sequential RPs, resulting in a maximal detected-to-delivered particles ratio and SNR. Ideally, an adaptive gated integration mode would acquire data throughout the time that the *Next-Point* trigger gate is high.

In order to proof this principle, the I6400[H] 64-channel integrator is proposed, based on the external gated trigger capability of the I400[I] charge collector. Relative to the electrometers described before, the I400 consist of only four gated integrator channels but its flexible-triggering feature allows to accurately starts accumulating the charge of each RP with the rising edge of the *Next-Point* trigger signal. The ADC readings are taken at high rate, and when the gate line goes low, the averaged charge between the gate edges is returned [J]. The maximum allowed gate period is 65.5 ms, which is fairly enough to cover even the longest t_{RP} (cf. Figures 3.4 and 3.5).

Prior to experimental investigations, the aforementioned feature was tested on a I400 electrometer in external trigger conditions similar to the ones faced during image acquisitions, and a linear behavior between the expected and measured charge was demonstrated over several sampling rates [K]. As comparative evaluation, the results on merging the integrated current gain of the I400 four gated channels together with the rest of the I128 channels when using the *Next-Point* trigger signal as external input gate are shown in the forthcoming section.

[H] Pyramid Technical Consultants (http://www.ptceurope.com/datasheets/I6400_DS_140304.pdf)
[I] Pyramid Technical Consultants (http://www.ptcusa.com/products/20)
[J] Private communication with J. Gordon. Heidelberg, 2015
[K] Idem.

3.4.3 Synchronization between *Next-Point* trigger and read-out electronics gating system

The two elements that play the major role in the transmission imaging DAQ principle have been introduced as (1) the RP-based scanning system, whose progress is emulated by the *Next-Point* trigger signal, and (2) the electronics system(s) that allows synchronous charge recordings of the 61 PPICs. Figure 3.11 merges these two factors and synthesizes the concepts related. The *Next-Point* analog trigger signal, set by the TCS, is sent from the EtherCAT interface box to the I128 electrometer via a 50 ohm coaxial cable. The latency between the gate input and output is about 25 ns, which is negligible compared to even the shortest integration period available by the I128 [Pyramid Technical Co. 2012].

What follows below is the description of some experimental considerations that might influence the optimal synergy between these two elements, considering that the total sampling length (t_s) equals the user-defined fixed integration time (t_{int}) multiplied by the number of conversions per sample ($^c/_s$).

- *Electronics external trigger response*

  There is a trigger response-time that makes the trigger edge starting-time asynchronous relative to each integration. During experiments, for each projection acquired, the I128 is set to be ready to receive the incoming gate signal before the actual irradiation starts. Then, the I128 integrates continuously the signal present (generally noise), even if the data is not being recorded yet. Whenever the external signal reaches the gate input, there can be a slight variation in the time between its arrival and the recorded sample. In the worst-scenario, the delay is equal to one integration period (t_{int}), although on average, it is less than half of this time [Pyramid Technical Co. 2012]. Therefore, it is recommended to use short integration times (t_{int}) over several conversions per sample ($^c/_s$) in order to restrict any unpredictable delay due to the trigger response.

- *Compatibility between the Next-Point trigger and the I128 External/Start hold triggering performance*

  Transmitted images require equal amount of ions per RP, however beam intensity fluctuations (cf. Section 3.3.2) may cause very irregular *Next-Point*-edge signal high/low transitions, as it is represented in Figures 3.4 and 3.6 for typical experimental scenarios at different dose-schemes. With the I128 configured to start collecting data on the rising edge of the incoming *Next-Point* signal, two alternatives are possible. First, to integrate the current immediately after the rising side is detected (*Next-Point*-pulse mode, Figure 3.11, middle panel). Or second, by using the *Next-Point*-edge mode (cf. Figure 3.11, lower panels) to rather collect the charge after a short lapse (determined by the width of the gap) to prevent extreme intensity fluctuations that might take place when the beam is relocated into a new RP or when, randomly, a RP coincides with the beginning of a new spill. The later arrangement has been adopted in the experiments performed in this work. This choice is also motivated by the need to elongate the integration times in the middle of two scanning spots without introducing another (high-to-low) edge transition,

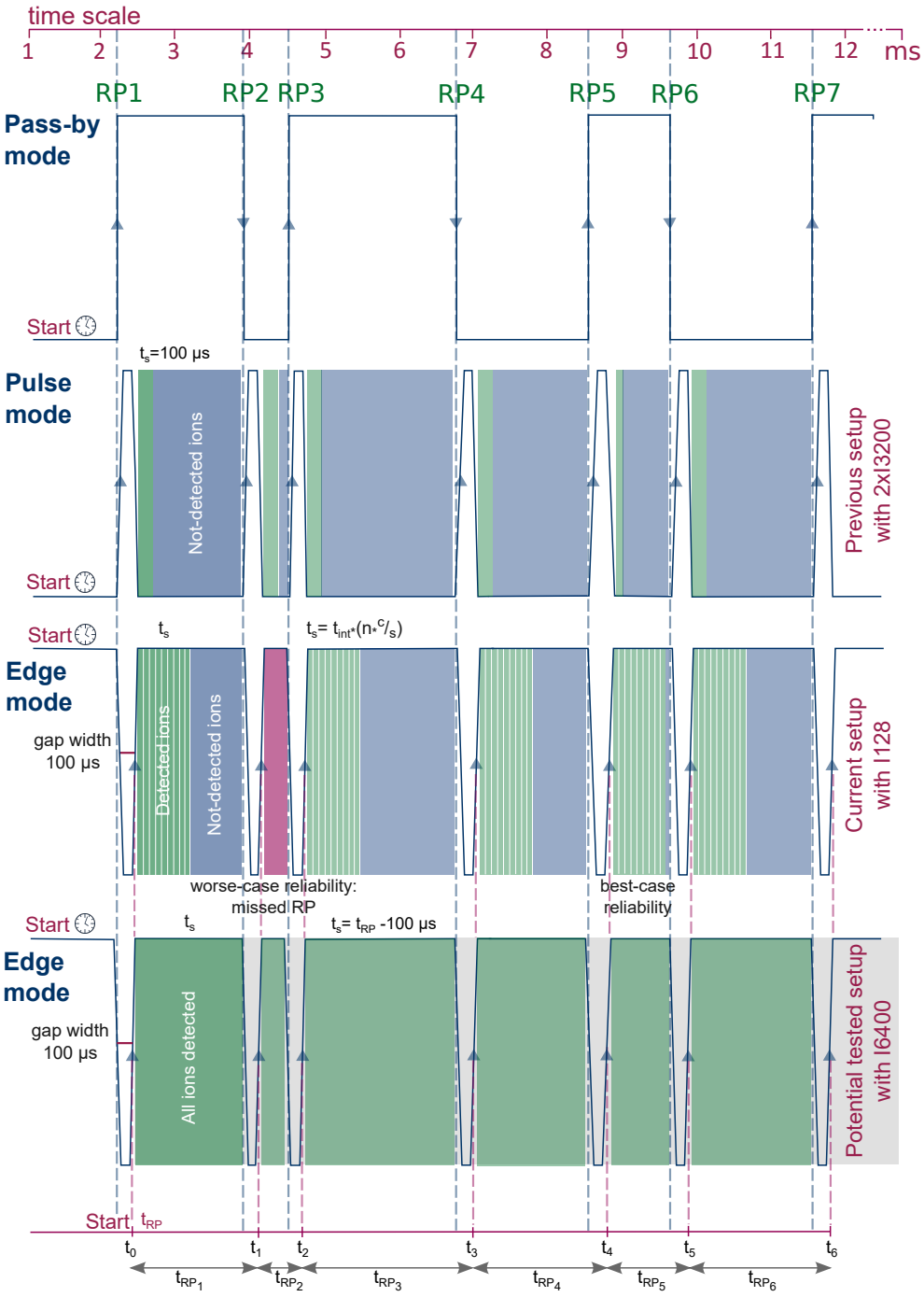

Figure 3.11: Different working modes of the *Next-Point* trigger signal provided by the TwinCAT-EtherCAT system. The original signal is originated from the TCS scanning process feedback, i.e., a high-to-low transition or vice-versa, is created per each irradiated RP. The *pass-by* binary signal (upper panel) is the basis to generate the *pulse* (middle panel) and *edge* (lower panels) sub-signals. The current transmission-imaging system makes use of the edge-mode inverse-gap signal as an input gate to initialize the data streaming, simultaneously in all the PPICs of the detector. Moreover, a comparison between the evolution of the charge collection procedure from the former to the actual and potential envisioned setup is illustrated. The green-shaded areas represent the fraction of ions detected under different integration cases, while the regions colored in blue correspond to the ions which are not detected owing to the rigidity of the integration times. The magenta shade in the second middle panel represents a worse-case scenario in which the RP has been missed. In the last panel, the effect of an adaptive gated integration is depicted, showing the desirable system performance in which the delivered-detected ions ratio is 1. Furthermore, the t_{RP} concept (cf. Section 3.3.2) is sketched at the bottom of the figure.

which may compromise the accurate detection of consecutive RPs. By using the inverse-gap shape, the trigger signal *holds* in the high state during the duration of t_s until the opposite polarity appears. Hence, it is not necessary to specify a pause-response, which has been also related to wrong RP detection [Gordon 2015]. The continuity of the input signal in a high state has been also beneficial for the application of the adaptive gated integration with the I400 electrometer (cf. Sections 3.4.2 and later findings in the current section).

In addition, the external trigger signal shape must be compatible with the basic detection capabilities of the read-out electronics. In the case of the I128, the rising edge of the external trigger input is expected to be fast (∼few ns) and sharp-edged. Otherwise, a noisy border and/or ripple effect may be interpreted by the electronics as multiple trigger entries, rather than a single one. Analog or digital signal acceptance might also cause detection discordances between the gated electronics and the trigger input. The I128 admit digital signals, while the EtherCAT system provides an analog output, which might cause minimal, but likely random detection inaccuracies.

- *Noise trade-off*

  The longer the t_s the more primaries detected and the better the SNR. When there is a noise frequency dominating the experimental system (cf. the noise characterization section), it can be partially suppressed digitally from the acquired data by matching the integration period with the noise period, or an integer multiple number of it [Pyramid Technical Co. 2012]. This way, the noise signal integrates to zero and it is nullified from the main signal.

Based on these experimental variables, the fundamental integration time used in this work for all the experiments was the shortest available period of $t_{int} = 55$ μs, which, relying on the noise trade-off principle explained above, may also remove typical effects from 50 or 60 Hz noise caused by the electrometer power supply. The integration time was then extended by increasing the number of conversions per sample, usually, if possible, in multiples of three. This choice is justified by the presence of a high-frequency noise of ∼6060 Hz in most of the experiments (cf Section 3.5.3): although this resonance is not very dominant, its mitigation would not harm the data acquisition, i.e in order to avoid integrations at this particular frequency, a $t_s = 165$ μs is desired, which can be accomplished by $t_{int} = 55$ μs times 3 $^c/_s$. For standard high-dose irradiations, the mean t_{RP} allows this integration time (t_{int}) to be incremented by a factor of 3, yielding a sampling time of $t_s = 495$ μs, which represents ∼26% of the average time that the beam holds in in each RP, improving the acquisition conditions of the old imaging-setup by a factor of 5. Due to beam variations and according to the number of primaries of choice, the particles detected within RP intervals also fluctuate, as it will be mentioned later when the detector efficiency is discussed. Low-dose acquisitions lead to plans with higher scanning-speed that require the minimum integration times (cf. Section 3.6), which will be specified when the results are presented.

Figure 3.12 illustrates, with a real low-dose example, the zoomed effect of the beam intensity fluctuations (cf. Section 3.3.2) on the *Next-Point* trigger signal shape and its possible conse-

Figure 3.12: Realistic low-dose example showing the augmented effect of the beam intensity fluctuations (cf. Section 3.3.2) on the *Next-Point* trigger signal periodicity and its impact on the DAQ system.

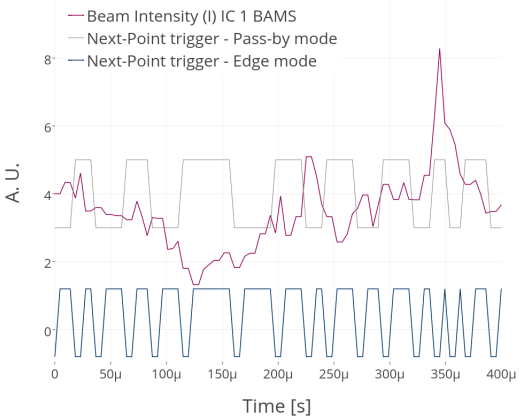

(a) Time span of 0.4 ms of a low-dose MBP irradiation scanned with a 299.94 MeV/u ^{12}C ion beam of 3.9 mm FWHM in 1 mm RPs steps. The lowest intensity from the LIBC ($2 \cdot 10^6$ pps) was enforced. The beam intensity fluctuations (magenta) originate the *Next-Point*-pass-by trigger (gray) dynamics which is the basis to obtain the *Next-Point*-edge trigger (blue). As expected, when the current goes down, the RPs needs more time to deposit the prescribed dose, yielding longer t_{RP} values. On the contrary, a high intensity peak leads to fast transitions of the *Next-Point* logic signal, often preventing that the rising edges are detected by the I128.

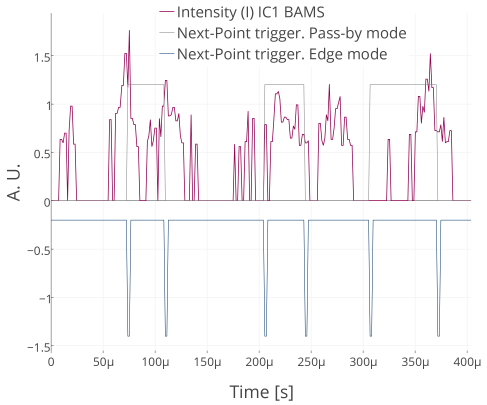

(b) The reference intensity value has been decreased from 3.5 nA to 0.5 nA (cf. Figure 3.6), leading to sparser t_{RP} values in the same time span of 0.4 ms, allowing the read-out electronics to accurately count all the expected RPs. The price to pay is the major reduction of the current detected by the BAMS, which is reduced in the same extent in the PPICs of the RRD. At these dose-levels, the acquired data might be almost overshadowed by the noise that affects the imaging setup. For this reason, the underlying noise sources must be understood (cf. Section 3.5.3) and the dedicated noise-reduction and processing methods presented in Chapter 4 are indispensable.

quences in the DAQ procedure. On the left, a short irradiation interval (0.4 ms) of the MBP is shown. It was scanned with the nominal lowest intensity available for carbon-ion beams at HIT ($2 \cdot 10^6$ pps) to obtain the reference current value measured by the BAMS. The beam intensity fluctuations (magenta) that originate the *Next-Point*-pass-by trigger (gray) are visible, which, in turn, generate the *Next-Point*-edge trigger (blue). The latter signal serves as input for the I128 to initialize the charge collection every RP. On the right, the reference intensity value has been decreased (cf. Figure 3.6), leading to sparser t_{RP} values in the same irradiation time-span. This procedure has the advantage of allowing the read-out electrometer to catch all the occurring RPs, with the drawback, however, that the current level is minimal, sometimes not even registered by the BAMS. This also justifies the fact that at these dose-levels the detected signal in the RRD might be severely affected by noise from different sources, which are inspected in Section 3.5.3. Processing methods for noise mitigation are addressed in the following chapter.

The observed effects in the Figure 3.12 can be reduced by boosting the amount of the charge collected per RP, which is inherently related to the electronics performance on detecting the external trigger input signal. This was proven by connecting four of the RRD channels (19 to 22) to a I400 electrometer, while the rest of the channels remained plugged in the I128. To be able to compare the overall gain effect when the I400 was used, the mean integrated current of the 961 RPs of a small 3×3 cm^2 FOV was considered. The extended field was scanned

with the highest ^{12}C ion beam energy available in the HIT LIBC (430.10 MeV/u). The RPs were separated by 1 mm in horizontal and vertical directions and received 5000 ions each. The energy was selected in such a way that the beam went through all detector channels without being stopped inside. When all the channels are connected to the same electrometer, a flat gain is expected. Figure 3.13 shows the output of the I400 merged with the channel response of the I128 to complete the visualization of all the 61 RRD channels. The four channels that collected data with the I400 integrator showed a highly improved performance owing to its adaptive gated-integration feature, that allows an effective synchronization to the *Next-Point* TTL-signal (cf. Figure 3.11). The charge signal gain is about three orders of magnitude higher as the one obtained with the I128, which fully supports the need to implement in the current transmission-imaging setup a read-out electronics which allows flexible integration intervals adjustable to the variability of t_{RP}.

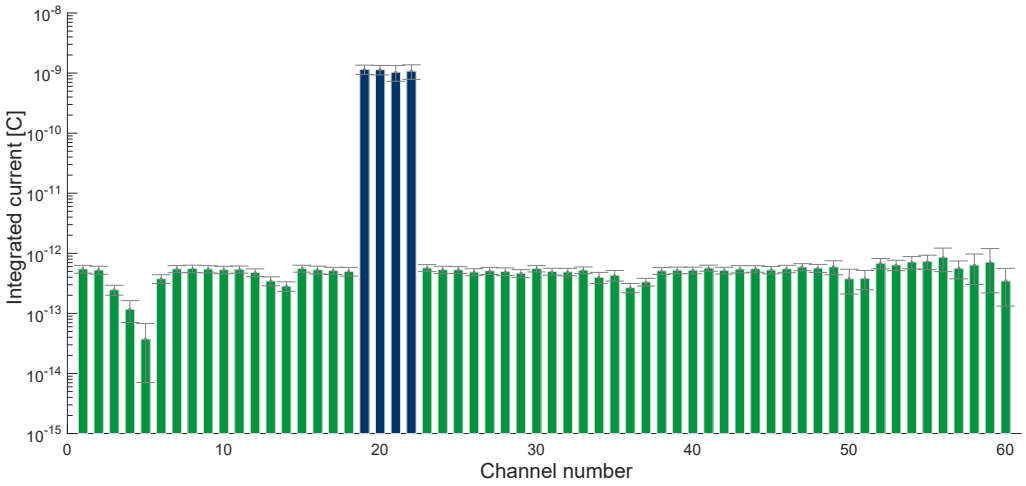

Figure 3.13: Charge signal gain of the I400 electrometer in comparison to the one with the I128 integrator for a high-dose scanned irradiation (5000 ions/RP in 1 mm RP-steps). The I400 electronics module is a charge collector which consists of four gated integrator channels allowing for adaptive integration (cf. Figure 3.11). Four RRD channels (19 to 22 in blue) were connected to a I400 electrometer, while the rest of the channels remained plugged to the I128. A FOV of 3 $\times$ 3 cm^2 was scanned with the highest ^{12}C ion beam energy available in the HIT LIBC (430.10 MeV/u) to assure that the beam did not stop inside the detector and a flat gain was recovered. Indeed, except for three under-responsive channels in the front part of the detector, the channels which remained connected to the I128 show the same signal gain level. The channels 19 to 22 collected signals three orders of magnitude higher due to the I400 variable integration synchronized with the irregular t_{RP} lapses (cf. Figure 3.11).

In the current experimental conditions, meaningful assessment methods are necessary to evaluate the quality of the acquisitions. This evaluation is based on quantification metrics related to the parameters that are most sensitive to errors. To this aim, a *reliability index* is introduced in the following section.

3.4.4 Optimal signal detection efficiency and reliability assessment

The requirement of the minimum deposited ions per RP demands an efficient charge-signal detection in the multi-PPIC RRD. The best performance of the imaging experimental-setup is reached when most of the delivered particles are actually detected. Independently of the intrinsic charge-collection capability of the RRD, addressed in the Section 3.5.2, the ratio between delivered and detected primaries can only be close to one by implementing a gated current integration that allows to collect the whole signal per scanning spot (cf. Figure 3.13).

As explained in Section 3.4.3, a poor synchronization between the triggered data acquisition system coupled to the RRD might limit the optimal collection of the signal corresponding to the initially irradiated primaries (N_{prim}) per RP. Conversely, the detected fraction of primaries (N_{det}) is given by:

$$N_{det} = \frac{t_s \cdot N_{prim}}{t_{RP}}, \tag{3.6}$$

where t_s and t_{RP} stand for the user-defined sampling time ($t_s = t_{int} \cdot n \cdot {}^{c}/_{s}$) and the RP lapse, respectively, i.e., in the case that $t_s = t_{RP}$ (true for versatile integration times), all primaries are detected. When a longer t_{RP} occurs, due to beam-intensity fluctuations (cf. Section 3.3.2), N_{det} is degraded. In such cases, the requested ions are distributed along the whole RP interval, however, only a portion of them are detected during the shorter and fixed t_s, besides more random signal noise is collected.

The BC signal amplitude in relation to the system noise level is crucial in order to correlate its maximum with the BP location. Low-amplitude signals might be severely affected by noise from different sources, which are inspected in section 3.5.3.

A RP-wise *Realibility Index (RI)*, which links the RP duration (t_{RP}) to the fraction of detected particles from the originally irradiated (N_{det}), makes it possible to recognize those BCs which are prone to allocate a maximum signal in an ambiguous channel, potentially leading to a wrong WET value. The RI is equal to the N_{det} normalized to the number of particles detected in the fastest RP ($t_{RP_{min}}$) of the whole FOV. This latter RP contains the largest fraction of detected particles, hence it is the most reliable. Thus, the RI ranges from 1, which stands for the most certain BC of the FOV to lower RI values, corresponding to the BCs that collect less signal information and are more likely to be misinterpreted by the maximum identification criteria.

Table 3.2 condenses the typical acquisition parameters of the three dose-levels investigated in this work, as well as the median RI and N_{det} over a FOV of 5022 RPs.

Table 3.2: Exemplary experimental acquisition parameters of the three dose-schemes investigated in this work together with the median value of the RI distribution and the median N_{det} over a FOV of 16.1×3.0 cm^2 covering 5022 RPs.

Dose-scheme	$t_{RP_{median}}$ [μs]	t_{int} [μs]	${}^{c}/_{s}$	t_s [μs]	$N_{det_{median}}$	RI_{median}	Dose mGy
Low-dose	1155	55	3	165	71	0.29	0.95
Middle-dose	495	55	1	55	111	0.33	1.90
High-dose	1870	55	9	495	1323	0.44	9.52

The 61 PPICs integrate the signal simultaneously during each t_{RP}. Consequently, for every RP, all the signal-points in the discretized Bragg curve are affected in the same extent. This leads to a vertical shift of the whole BC according to its N_{det} or RI, as it is shown in Figure 3.14. In consequence, the detection efficiency, i.e the part of detected primaries (N_{det}) from the originally expected, is not homogeneous over all the RPs of the scanned FOV.

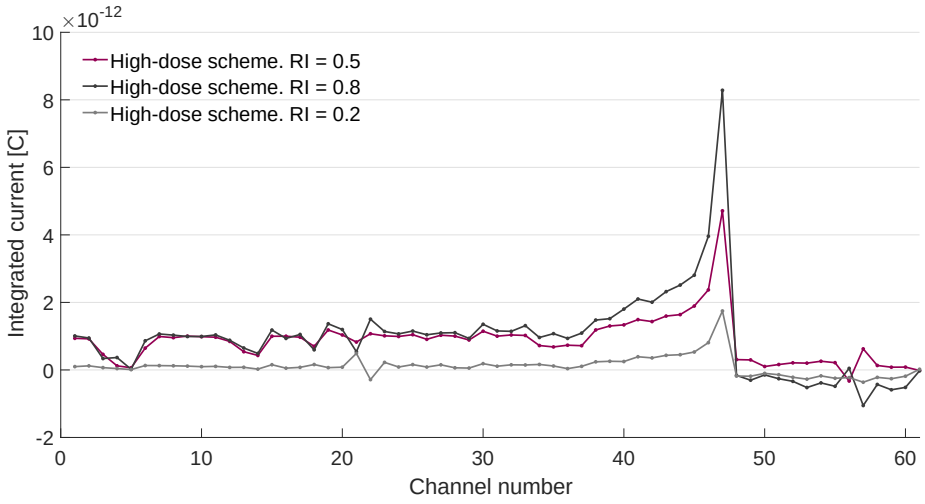

Figure 3.14: Characterization of Bragg curves in terms of the RI. Three different BCs with characteristic RI values are taken from the same FOV irradiated with the high-dose settings, using a scanned 299.94 MeV/u ^{12}C ion-beam. As reference for comparison, the BC with a RI=0.5 corresponds to the one shown in Figure 3.2 for the high-dose level.

Graphical representation of signal-quality metrics

Before proceeding to examine the RI behavior in different experimental scenarios, it will be necessary to briefly justify the use of Exploratory Data Analysis (EDA) techniques to interpret the main descriptive statistics of the signal-quality metrics defined in the course of this thesis. Owing to the RP-based nature of the experimental data acquisition (cf. Section 3.4), each image pixel might be affected in different degree within the overall projection quality.

This statistical strategy allows to visually inspect the overall quality-index distribution over the full collection of RPs, making it easier to determine whether certain RP-signals or image zones potentially have undergone significant distortions during the experimental work-flow. Preliminary conclusions on this first glance may warrant the omission of certain projections for subsequent analysis or provide a basis for further data collection according to passed-failed quality scores. Especially considering that a high-resolution tomographic acquisition requires at least 200 projections covering 180 degrees (cf. Chapter 6), a proper good-quality selecting protocol is important.

In the following, *violin* plots [Hintze and Nelson 1998] are used to provide, visually, exploratory statistical information about the underlying density-distribution estimation of each irradiation example. The density trace mirrors the shape of the (smoothed) histogram[L] and it is plotted symmetrically on the left and right sides of a vertical guideline that spans over the range of the sample.

The ultimate goal of these exploratory-data tools is to provide stand-alone experimental protocols to be used during the tune-up of the detector acquisition-parameters on-the-fly, and in this way obtain the optimal trade-off between the detected signal and the unavoidable noise for each scan.

[L]The density distribution is estimated at each point as $d(y,h) = \sum_{i=1}^{n} \delta_i / nh$, where n and h are the sample size and the interval width, respectively. δ_i is a Heaviside-function equal to 1 when the ith data value is within the interval $[y - h/2, y + h/2]$ and 0 otherwise. h is usually chosen ∼15% of the data range for an acceptable data binning [Hintze and Nelson 1998].

The upper panel of Figure 3.15 shows the density distribution of the detected ions percent for the low-, middle- and high-dose schemes. The wider sections of each violin-shape indicate the most likely amount of ions detected under each acquisition settings (cf. Table 3.2). The median value and the interquartile range of the sample are also indicated with discontinuous lines. This representation is particularly favorable for a better indication of the distribution shape. For instance, the high-dose scheme reveals an almost normal density profile, yielding a symmetric violin with widest point around the median value and equally-separated upper and lower quartiles. The middle-dose level case discloses distinct RP clusters appearing as protuberances in the density estimation, while the low-dose scenario shows a positively-skewed density distribution towards lower detection efficiency.

The violin shapes are extended till the maximum and minimum values of the distribution, making evident that, in this example, for a high-dose irradiation only few RPs reach the 60% of the initially irradiated ions. According to Table 3.2, the middle-dose example has the shortest sampling time of t_s=55 μs, which is reflected in the lowest median value of N_{det} ∼11%. These particular irradiation parameters trace the boundaries of the accelerator capabilities to operate in treatment mode. By using the accelerator research mode, N_{det} could be slightly increased by lengthening t_{RP} and allowing prolonged integrations at the cost of some additional technical effort (cf. Section 3.3.3). In this case, the low-dose irradiation-time per RP has been enlarged by modifying and irradiating the MBP in research working-mode, allowing to detect ∼14% of the originally irradiated ions.

By definition of the RI (cf. Equation 3.4.4), the RI smoothed histograms (or violin distributions) for each dose-scheme are quite similar to the violin shapes of N_{det}, shown in the upper panel of Figure 3.15, hence they are not displayed. However, the RI is an irradiation-specific metric, which quantifies the certainty of the BP determination influenced by the beam-intensity fluctuations in each irradiated PBP, hence its median value might vary in accordance. The lower panel of Figure 3.15 superimposes the RI histograms of the FOV (5022 RPs), for the three dose-scenarios. From the latter graphic, it is evident that the irradiation plans with more primaries requested per RP appear more reliable than low-dose irradiations, even though a partial percentage of particles account for the final residual-range detection. The histogram can be also used to visually determine which proportion of irradiated RPs reached certain pre-set N_{det} threshold, e.g. 50%, used as passed-failed criteria. The RI as visual assessment method for radiographies is presented in Chapter 5.

3.4.5 Additional Raster-Point-based signal quality metrics to assess the experimental setup performance

The correct determination of the BP position in the detector PPICs is fundamental to define the correct ion-range, i.e., the underlying information in the transmitted projections to obtain the WET of the traversed materials. The ultimate image accuracy can be affected by a wide variety of artifacts which are inherent to the experimental-setup functioning principle. Some of these artifacts are not visually obvious in the projection domain, yet can potentially degrade the image-quality. Furthermore, some of these anomalies might seriously reduce the efficiency of quantitative image analysis and reconstruction algorithms used and/or being developed along this research.

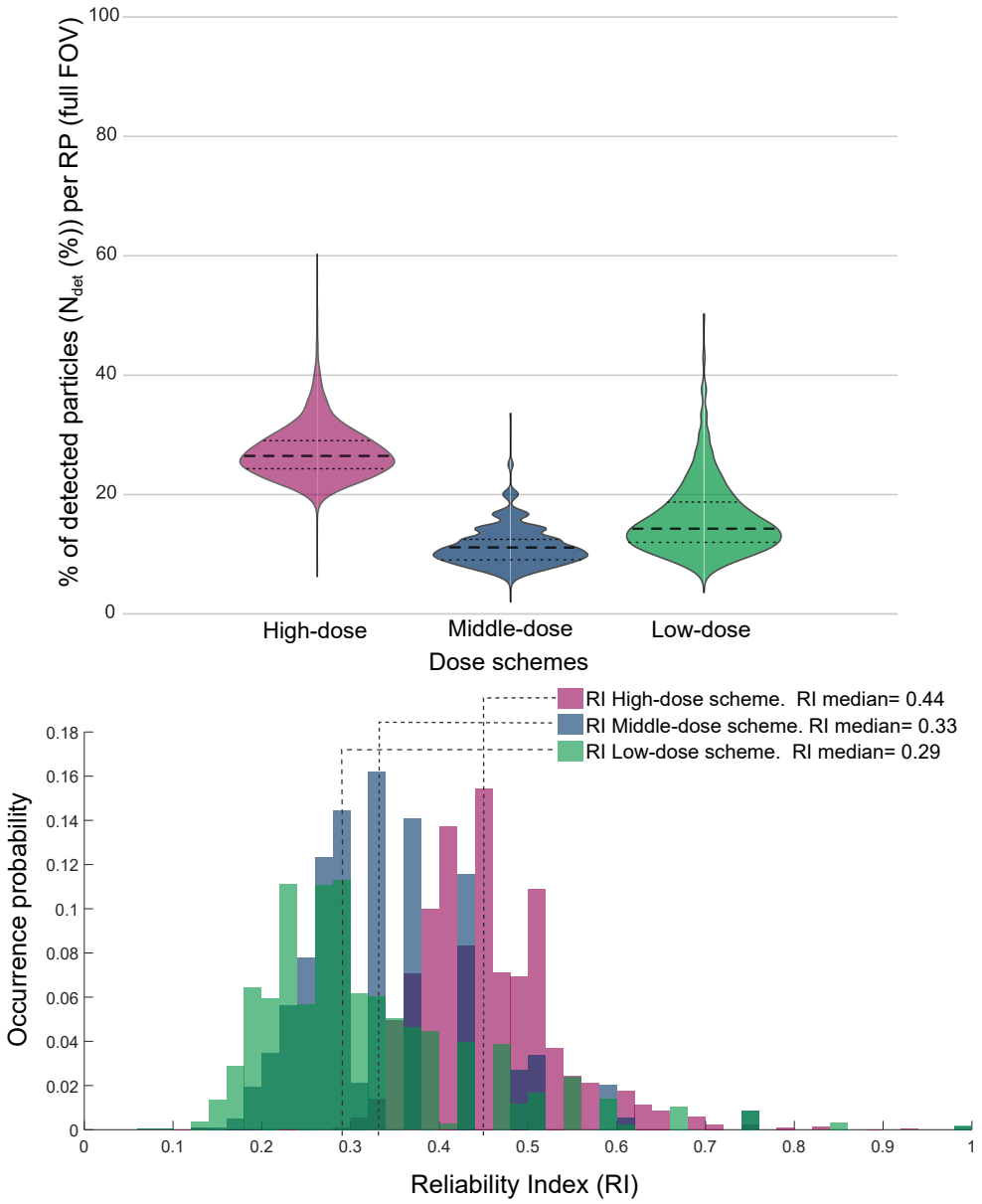

Figure 3.15: Detection efficiency and RI of the three dose-scenarios. For high- (magenta), middle- (blue) and low-dose (green) levels, the RP distribution of the percentage of detected ions in the RRD from the originally delivered primaries is represented with a violin plot. The violin-shape is formed by a mirrored density distribution estimate. The median value and the interquartile range of the sample are pointed out with dashed and dotted lines, respectively (upper panel). In the lower panel, the RI histograms of occurrence over the 5022 RPs FOV are superimposed to visualize the different dose-schemes leading to distinct RI values.

Bearing this in mind, identifying defects in the obtained profile of the BCs becomes indispensable. In order to recognize significant signal corruption due to noise, that might affect the maximum-signal identification, the signal-quality analysis of the BCs is based on its structural features, distinguishing its three main distinct zones: plateau, peak and tail. Figure 3.16 shows how each BC is split into its three features to define the quality-metrics in accordance. The algorithm used to split the BC relies on the maximum-signal identification criteria. Once the RRD channel with the BP is recognized, a window of channel-signals around it (usually 8 to 10 channels before the peak to account for broader peaks, and 1 or 2 channels after) is defined as the peak zone, whereas the rest of ICs are classified into the plateau and tail regions.

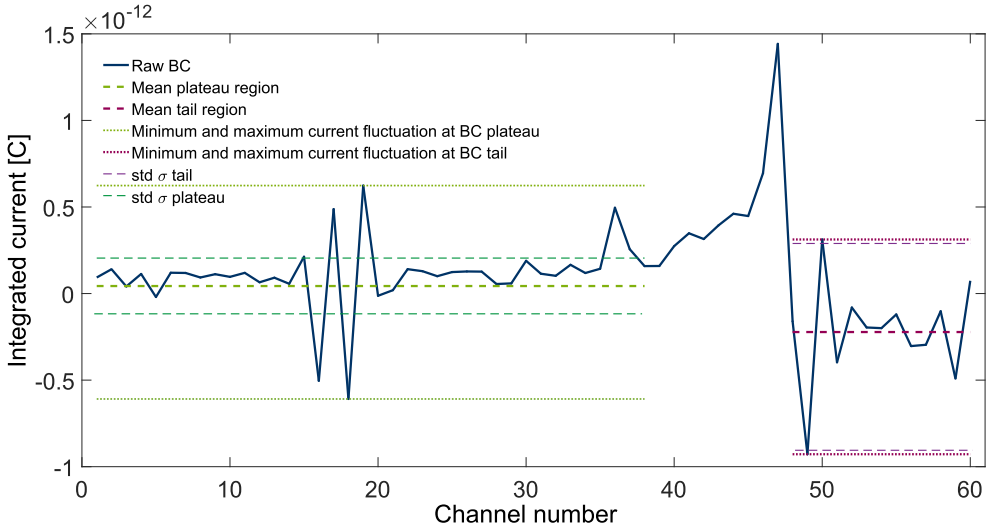

Figure 3.16: Sectioned BC for signal-quality assessment. The split BC corresponds to a high-dose 299.94 MeV/u ^{12}C-beam impinging the RRD detector without traversing any phantom, yielding the signal maximum in the channel 47. Channels ∼15 to 20 show signal-coupling effects due to noise resonances picked-up by those channels (cf. Section 3.5.3). Statistical parameters of the ICs signals such as mean, standard deviation, maximum and minimum are evaluated RP-wise for each part of the curves.

Broad-band noise affects the output signals in different extent (cf. Section 3.5.3). Noise resonances might cause coupled signal fluctuations in two or more consecutive channels, resulting in a zigzagged-signal effect (cf. Figure 3.16, RRD-channels ∼15 to 20). Namely in case of low-dose irradiation plans, these signal oscillations may result in current-amplitudes larger than the BP signal itself, leading to a mislead maximum/range determination.

In the following, dedicated evaluation metrics are established to monitor the detector performance prior to and during the experimental acquisitions and to assess the image-quality *on-the-fly*. The definition of the indices relies on the fundamental factors affecting the image-quality in time and space domains, due to the local and global functioning of the RRD channels. The already defined RI is a time related value which provides information about the electronics operation. Moreover, in space-domain, the Signal-to-Fluctuation Ratio (SFR) estimate the noise influence globally on all the RRD-channels, while the Bragg-peak Steepness (BPS) yields local information, involving only the channels where the BP is located.

The proposed procedures for quality assessment could benefit both research and future routine clinical imaging, improving the acquisition work-flow through the capability to easily rule-out unusable low-quality projections.

Signal-to-fluctuation ratio

The *SFR* is introduced as a metric to assess the overall signal quality respect to the current-signal fluctuations among the channels of the RRD due to multi-origin noise. The SFR is calculated RP-wise as the ratio of the amplitude difference between the maximum charge-signal, expected to be at the BP (Q_{BP}), and the mean charge-signal along the plateau region (Q_{plat}); and the largest fluctuation detected in the plateau and tail zones (Q_{fluc}). The latter parameter is determined by looking for the IC with the maximum signal among the selected

channels. According to the BC division given in Figure 3.16, the SFR is given by:

$$SFR[dB] = 10 \times log_{10}\left[\frac{Q_{BP} - Q_{plat}}{Q_{fluc}}\right] \tag{3.7}$$

The decibel scale is used to widen the window of the resulting values, which will be also useful to enhance the color-bar contrast when the projections are evaluated on 2D-colored maps in the later course of this work (cf. Chapter 5). In such maps, the pixel-wise evaluation of the SFR visually shows the impact of the noise on the whole projection.

Weak signal-fluctuations (with small amplitude) would yield higher SFR values. On the contrary, if large-amplitude fluctuations, with the same order of magnitude as the BP-to-plateau separation, are encountered along the discretized BC, the SFR would have a poor value, indicating that the BP location, determined by the maximum identification procedure, is prone to be ambiguous. By construction, multiple-peak RPs, caused by different-density interfaces, will show a poor SFR-value, since the second peak would be considered as a large noise fluctuation. For the visual purposes for which this metric is designed, this assessment is sufficient to easily recognize where in the FOV there is cluster of RPs affected by a sharp-density boundary (cf. Figure 5.5). To determine the noise-level of those BCs, an iterative application of the same algorithm is needed, so that it discards the first peak found and searches for a second or a third one.

In the worse-case scenario, arbitrary fluctuations may exceed the BP signal-amplitude, causing the BC-segmentation to fail. In such rare incidents, the SFR-value would be meaningless and other assessment method should be applied to those specific pixels.

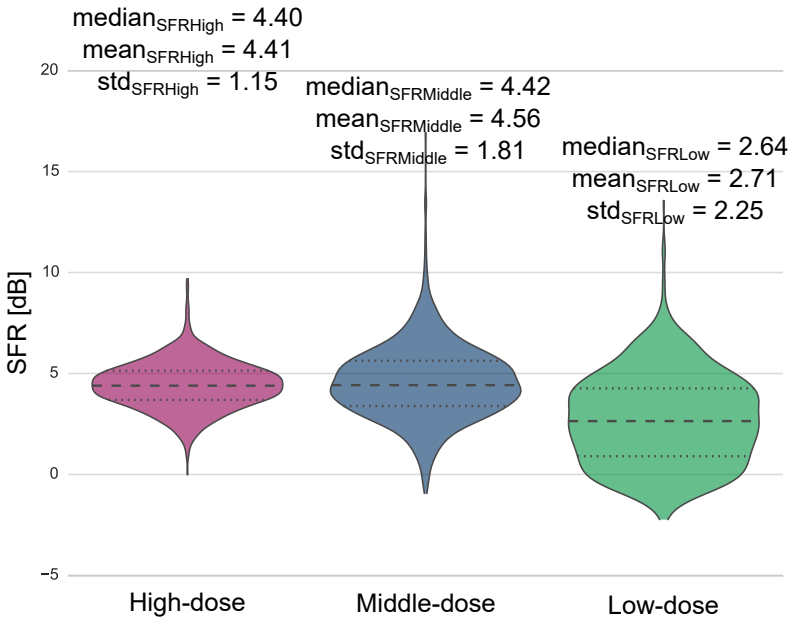

Figure 3.17: Signal-to-fluctuation-ratio (SFR) statistics of three different dose-schemes. The SFR distribution for the high- (magenta), middle- (blue) and low-dose (green) levels, is represented with violin plots, which illustrate an estimation of the probability density distribution of SFR values over the irradiated area. The median value and the interquartile range of the sample are pointed out with dashed and dotted lines, respectively. The three data-sets correspond to the irradiation plan for a FOV of 16.1× 3.0 cm^2 scanned with a 299.94 MeV/u ^{12}C-beam. No phantom is located between the beam-nozzle and the detector.

The violin-shapes in Figure 3.17 aid to judge how noisy is the acquired sample. When the noise-level is steady, i.e., no strong noise oscillations distort the expected BC shape, as it occurs in the high-dose irradiations, the SFR distribution is normal and narrow (cf. Figure 3.17, magenta violin), which can be considered as a good measure. Middle-dose images are more susceptible to noise fluctuations that might overshadow the BPs, this is reflected in the broader range of SFR values occurring all over the projection (cf. Figure 3.17, blue violin). In low-dose irradiations, the signal amplitude and the noise level are of the same magnitude, leading to poor SFR values for most of the RPs of the irradiated FOV. Low-dose image-quality can be classified as a low-quality projection from the deformed shape of its SFR distribution.

This statistical representation can be used to eyeball the overall quality of scans, since unexpected bumps in the violin plots might indicate potential data with significant corruption due to noise, warranting the exclusion of the projection or the need to be acquired again. It is also possible to define cut-off points in order to design a discriminative criteria to classify other scans.

Steepness of the BP fall-off

The maximum-signal criteria to identify the BP position in the RRD is very sensitive to noise and the intrinsic detector granularity (cf. Section 3.5.4). Hence, a shape-sensitive quality measure is defined, based on the second gradient of the spline-interpolation of the discrete BP. The BPS might provide more information about the steepness of the BP distal fall-off indicated by the minimum of the second derivative of the interpolated experimental data and a rough estimation of the BP location within the corresponding PMMA slab. This feature will be illustrated when the detector discretization-issue is addressed in Section 3.5.4

The scarce and noise-corrupted data points complicate any function-based interpolation along the discretized BCs or at the BP (where only 3 to 4 data points are located). To explore the gradients of each BC, a piece-wise cubic spline interpolation was applied. The interpolation curve is biased towards the data points surrounding the maximum signal. Once the maximum signal is found breaking-points are defined around it, thus avoiding over-fitting when noise effects distort the rest of the BC. The robustness of the interpolation procedure was tested by applying different splines orders and various breaking constraints around the peak. Linear interpolation is performed along the data-points where breaks are not specified.

The first and second derivative of the interpolated function are computed and the values at the minimum concavity are recorded (cf. Figure 3.18, solid dots). The absolute value of these points corresponds to an estimation of the rate of change of the original BC slope, i.e., a steep fall-off yields a higher first-gradient change, consequently a larger absolute value (cf. Figure 3.18, left BP).

The visualization of this quality-metric in 2D-maps is potentially helpful to observe the behavior of the corrupted BCs in certain Region of Interest (ROI) of the FOV. A particular application of this index to investigate the image homogeneity affected by potential detector material-heterogeneities in the absorber plates is discussed in Section 3.5.4.

One concern regarding the use of this quality indicator might be its robustness when multiple-peak BCs occur. In such cases, the smaller peak will be omitted. A possibility to overcome this issue suggests the incorporation of additional break-points to enforce the spline interpola-

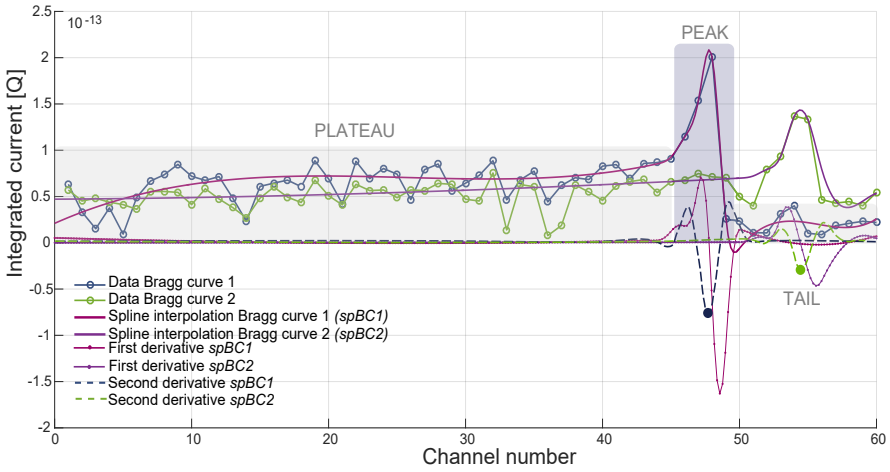

Figure 3.18: Assessment of the BP fall-off steepness. The BCs correspond to a high-dose 330.48 MeV/u ^{12}C-beam BC impinging the RRD detector while traversing two different PMMA thicknesses of a wedge-shape stepped phantom (cf. Section 3.6), yielding the maximum signal in the channels 48 and 54, respectively.

tion to account for most of the data and therefore to extend the algorithm to a second-peak discernment, which was however beyond the scope of this thesis.

3.5 Integration-mode multi-channel range telescope characterization and performance

The multi-channel array used in this work as RRD for ion-based transmission imaging (cf. Figure 3.1) was originally designed as a dose-verification system [Brusasco et al. 2000] to measure quasi-3D dose-distributions with high granularity. For dosimetric applications, the inner PMMA slabs simulate the patient volume, while the depth-dose profiles (BCs) are measured, discretely, by the stack of PPICs.

The gold-standard detection device for direct dose-measurements in photon and ion-beam radiotherapy is the IC [Andreo et al. 2001]. This choice is owing to its simple operation and inherent linearity with respect to the delivered dose (in the ion-chamber region, cf. Figure 3.19, right panel). Moreover, the use of low-density inter-electrode material avoids additional scattering perturbation effects, commonly related to solid-detector components. These reasons also support the use of PPICs as integral part of the imaging prototype presented in this work. As mentioned before, the crucial information to accurately reconstruct the WET of the material traversed is established by the BC shape, namely the discernible definition between the plateau, peak and tail zones. As long as the right BP location is recognized from the output signal measured by the electrometer, no strict ion-recombination correction factors are required as for dosimetric and quality assurance applications.

As it was briefly introduced before, the RRD used to perform the experiments presented in this work consists of a stack of 61 subsequent air-filled PPICs interspersed with PMMA beam absorbers. The rWEPL=1.165 of the PMMA tiles establish the dynamic range of the detector, ~21 WE cm. The large active-area of each IC covers 30×30 cm^2 to enable the maximum irradiation FOV available at HIT, which is 20×20 cm^2 (cf. Figure 3.1). This extended cross-section eliminates any need to consider the potential non-uniformity of the electric field intensity at the ends of the chamber, ensuring that edge-effects are minimal. The PPICs' electrodes are made of low atomic-number conductive plastic, a pair of 25 μm-thick aluminized kapton foils

enclose a collecting air-gap of 6 mm with a capacitance (C) of 80 pF (cf. Figure 3.19, left panel). The WE of each chamber is ∼60 μm.

The charge-collection response of ICs strongly relies upon irradiation features such as the beam energy and the number of primaries, as well as the chamber geometry, gas stopping-power properties and applied voltage. The previously-introduced Equation 3.1 relates these dependencies since the BAMS PPICs share the same working principle as the PPICs of the imaging detector. For typical treatment-doses, similar to the ones used for the proof-of-principle of ion-based imaging with the current prototype detector [Rinaldi et al. 2013], a voltage in the order of 1000 V was necessary for a suitable PPICs functionality [Voss et al. 2010].

As introduced in Section 3.2, transmission images are obtained with two to three orders of magnitude less ions per RP than typical treatment plans, which makes the detected signal extremely noise-sensitive. Thus, the ICs performance has to be properly characterized to establish the drift-voltage operating range of the chambers for an optimal signal acquisition in this non-clinical scenario. Generally, for a low particle-flux, low voltages around hundreds of volts are sufficient to reach current saturation. A high particle-flux would require to increase the voltage to account for non-linearities in the output signal as it is detailed in the next section. In the following, the physical principle of operation of the PPICs of the RRD and the procedure to tune the experimental parameters in accordance is introduced.

3.5.1 Current-voltage characterization

ICs detect the charge accumulated in a gas-gap traversed by ionizing radiation. The parallel-plate chamber-configuration contains the gas volume within a pair of electrodes where an electric field is induced by the application of an external HV. When an ion-beam traverses the detector, it excites and ionizes the gas molecules, creating electron-ion pairs which then drift along the electric field towards the anode and cathode, where they are collected, respectively (cf. Figure 3.19, left panel). The induced charges on the signal electrodes are then measured by the electrometer, which integrates the current over a finite period of time as it was explained in Section 3.4.2.

The PPIC optimal gain relies upon the strength of the electric drift-field between the electrodes. Therefore, the HV must be strong enough to guarantee a linear response, i.e., that all the ions and electrons created by ionization are collected without recombination or diffusion losses within the charge collection volume.

Ionic recombination and operation zones

Recombination of the charges to form neutral molecules can occur within or between tracks. The former is termed initial recombination (also known as columnar recombination) and occurs when ions and electrons are produced and combined within single particle ionizing tracks. Therefore, it depends on the ionization density but it is independent of the beam intensity (particle delivery rate). The second recombination process, known as general or volume recombination, is due to ion-pairs from different ion tracks, which meet and recombine, thus it depends on the beam delivery rate or dose. The larger the ionization density, the higher the probability of recombination. The general recombination is treated separately for different types of beam delivery, namely, continuous, pulsed and pulsed scanned beams [Zankowski and

Podgorsak 1998]. Since the duration of each RP is regularly in the order of ms, and this interval is much longer than the typical ion drift collection time for such chambers [Lin et al. 2015], it is appropriate to consider the raster scanned beam as continuous.

As the HV is increased from its ground value, the resulting electric field begins to separate the ion pairs and the recombination fades. Nonetheless, in the recombination region (cf. Figure 3.19), the current measured by the electrometer does not accurately reflect the energy deposited by the incoming ion-beam. Thereby, experimental acquisitions in this operation zone must be avoided.

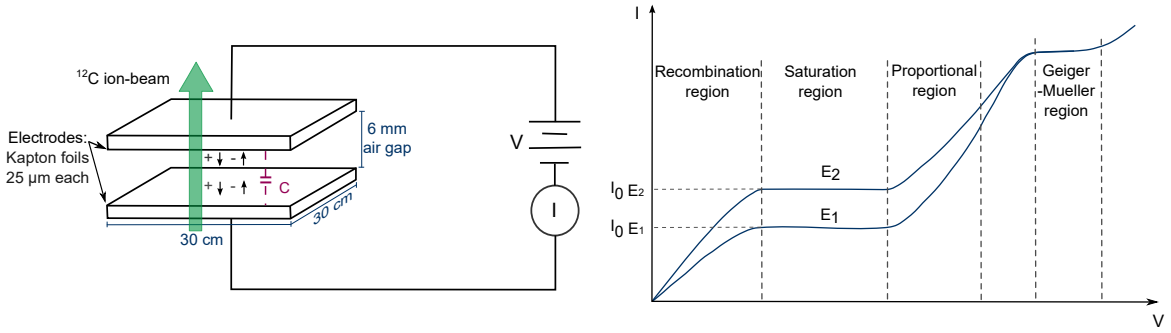

Figure 3.19: (Left panel) Sketch of one of the PPICs of the RRD and operation principle. (Right panel) Typical variation of the integrated current over different operation regimes of gas-filled ICs with respect to the HV. Based on the applied bias-voltage, a PPIC can be operated in various modes, which differ from another by the amount of charges produced and their travel-path within the active volume. The two curves, E1 and E2, correspond to two different beam initial energies. Right image adapted from Syed Naeem Ahmed [2015].

The measured current (I) increases gradually with the increasing voltage, approaching a flat plateau corresponding to the saturation current (I_0), in which a complete collection of the produced charge is expected, and thus the adequate experimental conditions are obtained. Adversely, the increase of the internal HV will inevitably introduce electronic noise during the data acquisition (cf. Section 3.5.3). Hence, the saturation features of the PPICs must be investigated to find the best trade-off between the integrated signal measured and the loaded noise level in the ion-chamber region.

The HV must be also low enough to avoid secondary ion-pair multiplication as it is depicted in the proportional region of Figure 3.19 (right panel). In this zone, electrons liberated by the initial incident beam are accelerated sufficiently to produce further ionization. Higher voltage differences might produce ionization avalanches, reaching a second higher step of steady current level called Geiger-Müller region.

Although all the experiments must be performed at the saturation region (cf. Figure 3.19, right panel), the non-linear working zones might be reached with wrong HV choices. Therefore the applied voltages must be carefully selected according to the specific beam energy, fluence and intensity combination chosen for each experiment, preferably on the same day of acquisition (some discrepancies in the charge detected on different acquisition dates are evident in Figure 3.20).

Normally, the ICs should be operated in the middle of the plateau region of the current-curve to ensure voltage stability. However, due to the severe influence of the noise on the signal, the minimal HV value that appears when the current-curve reaches the saturation plateau is used to minimize the increasing noise level.

A customized and automatized[M] current-voltage protocol, taking approximately 30 minutes, has been designed to be performed previous to each experiment. The protocol consists on homogeneous irradiations of FOVs, without any phantom in between the beam-line nozzle and the RRD, at different drift-HVs varied in steps of 100 V. Due to the energy-dependence on the ionization produced (cf. Figure 3.19, right panel), the beam-energy selected is the one used later on for the image acquisition. According to the BP structural division introduced in Figure 3.16, three mean current-voltage curves are obtained for the plateau, peak and tail, respectively. In addition, the mean SFR (cf. Section 3.4.5) is computed and plotted for each HV merit. The SFR quality-curve is intended to contribute to the HV decision by providing extra information regarding the noise-level of the scans at different voltages. The maximum SFR-point corresponds to the irradiation which is less corrupted by noise. Figure 3.20 shows an exemplary case of the pre-experiment HV analysis-routine for a high-dose 299.94 MeV/u ^{12}C scanned-beam. For these particular scanning settings, the first maximum of the SFR occurs at 400 V, which is in agreement with the starting of the current saturation region on the left panel. Higher voltages (like 900 V) may show comparable SFR values due to charge amplification, however, as it will be demonstrated in Section 3.5.3, increasing the HV also causes severe BC-distortion and should be avoided.

Figure 3.20: Current-voltage analysis produced with a stand-alone pre-experimental protocol. The detector PPICs are irradiated with a centered FOV of 3.0× 3.0 cm^2 (961 RPs for statistical analysis) with a high-dose 299.94 MeV/u ^{12}C-ion beam of intensity equal to 3·10^6 pps. The drift-HVs applied to the PPICs is increased in steps of 100 V, from 0 V to 1000 V. The combined information between the current-voltage curve (left panel) and the SFR behavior (right panel) assists to conclude the optimal bias-voltage for the experimental acquisitions.

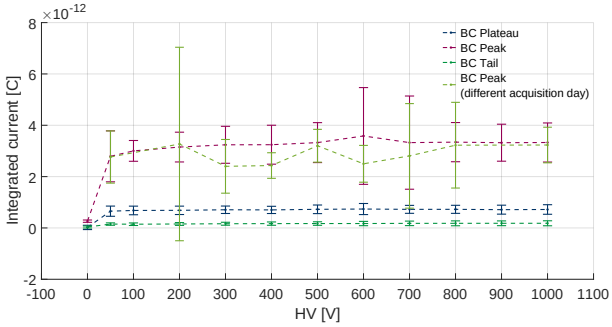

(a) Current-voltage characteristic profiles are obtained for different ionization levels of the BCs (plateau, peak, tail. cf. Figure 3.16).

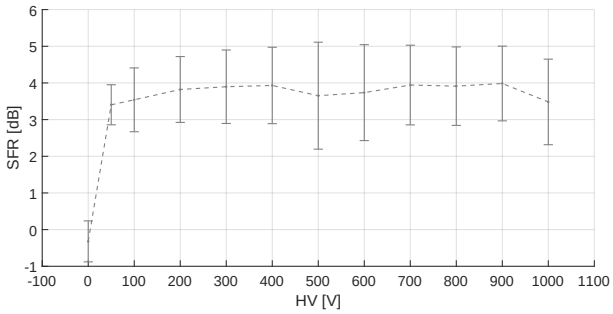

(b) Mean SFR over all the samples of the FOV, concluding a maximum SFR at 400 V, which coincides with the starting of the current saturation region on the left panel.

PPIC response dependence on beam-energy

The energy-dependence of the saturation curve, depicted in Figure 3.19 (right panel), is visible when the current-voltage relation is outlined for the three different LET levels of a single BC. In order to demonstrate the impact of the RRD charge collection capability at different days of operation, the current-voltage curve of the same irradiation parameters obtained on an earlier date is also shown in Figure 3.20a. Nevertheless, when three carbon-ion beams of different energies impinge the detector, the higher their energy, the longer their trajectory and,

[M] Thanks to Benedikt Kopp for his contribution in the automation process.

in consequence, the larger the amount of the RRD-material traversed to lose certain amount of energy, causing a reduced peak-to-plateau ratio (cf. Figure 2.3).

The stopping-power of different-energy beams is directly reflected in the amount of ionization caused in the active volume of the ICs where the BP is encountered. Figure 3.21 confirms such response by showing the current-voltage characteristic profiles of the IC that allocates the BP in various energy-loss scenarios. The lower the beam-energy, the higher the stopping power and thus the ionization at the chamber of the BP.

Figure 3.21: Beam-energy dependence on current-voltage features. The ICs of the RRD are exposed to a FOV of 3.0× 3.0 cm^2 (961 RPs) scanned with three high-dose ^{12}C-ion beams of energies: 187.97 MeV/u, 299.94 MeV/u and 343.46 MeV/u. 11 HVs values are explored.

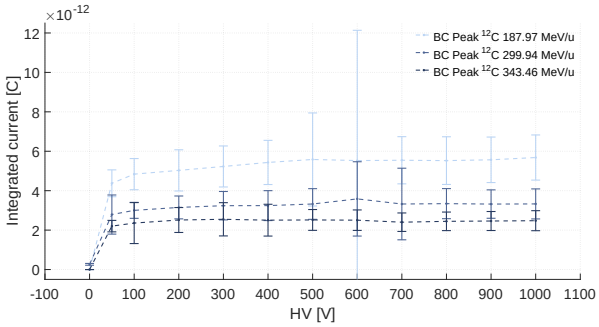

(a) Current-voltage characteristic profiles are obtained for three different beam energies. The three curves show similar minimum saturation threshold $>$ 300 V. This correspondence supports the use of an additional criteria as the SFR to determine an adequate operating drift-voltage.

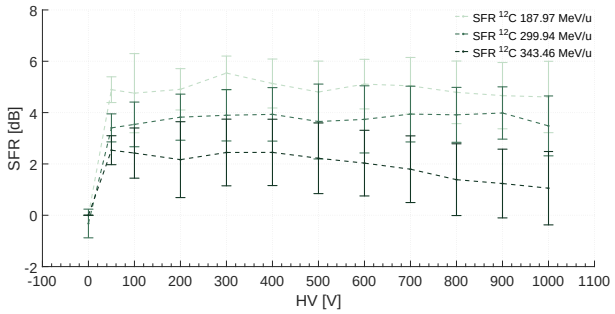

(b) Mean SFR over all the samples of the FOV. This quality curve is intended to contribute to the HV decision by providing extra information regarding the noise-level of the scans at different voltages. The maximum SFR corresponds to the irradiation which is less corrupted by noise. For the three energies presented in this example, the first maximum of the SFR is found between 300 and 400 V.

The fact that the peak-to-plateau difference is reduced while increasing the carbon-beam energy, makes the projections taken with higher energies prone to noise artifacts, which is evident in the trend of Figure 3.21b where the SFR gradually decreases towards higher voltages, being this effect accentuated for the highest energy displayed. This tendency gives grounds on selecting the lowest beam-energy that the thickness of the imaged object allows, as long as it is still covered by the detector dynamic range.

PPIC response dependence on beam-intensity

The current-voltage features of a PPIC are also influenced by the incident beam-intensity as it is shown in Figure 3.22.

The intensity of the incident radiation might change the onset of the plateau region and the output current amplitude as it is outlined in Figure 3.22. The underlying reason of this phenomena in the PPIC is the availability of a larger number of electron-ion pairs at higher beam-intensities. If the rate of production of charge pairs increases, then a higher electric field will be needed to eliminate or to minimize their recombination. On the other hand, with a lower beam-intensity, the ionization density decreases and so the probability of two opposite charge to neutralize. Hence, the saturation point might be reached with a lower HV. Moreover, the output current is proportional to the number of charge pairs in the plateau region, and

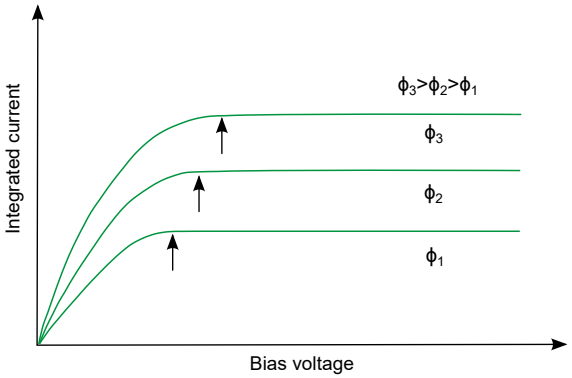

Figure 3.22: Current-voltage characteristic curves of a PPIC at different incident beam-intensities. The output signal as well as the onset of the plateau (indicated on the plot with the crescent arrows) escalate with increasing beam-intensity or flux of delivered ions. Redrawn from Syed Naeem Ahmed [2015].

therefore at higher intensities the plateau current amplitude also varies [Syed Naeem Ahmed 2015].

Figure 3.23: Beam-intensity dependence on current-voltage features and corresponding SFR curves.

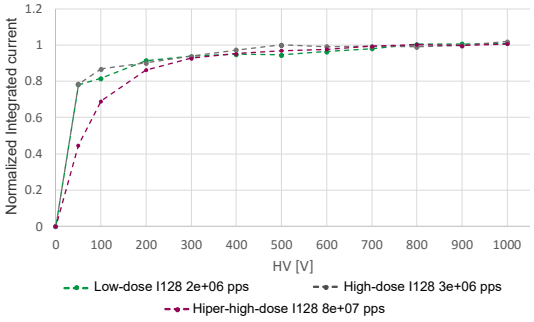

(a) Current-voltage characteristic profiles are obtained for three different beam intensities. A 3.0×3.0 cm^2 FOV was irradiated with a 187.97 MeV/u ^{12}C-ion beam at three different dose-levels (5·10^2 (low), 5·10^3 (high) and 5·10^5 carbon-ions per RP (hyper-high)) with the beam-intensity being selected by the PDG. The mean charges are standardized by the mean value of the measurements obtained with a voltage above 700 V.

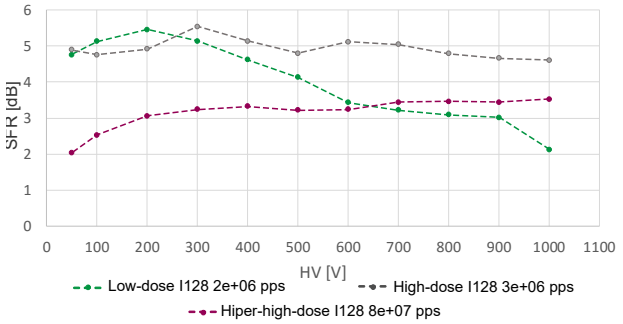

(b) Mean SFR response for three dose and beam-intensity levels. The maximum SFR reveals the irradiation with less signal distortion due to noise. For the low- and high-dose irradiations, 200 V and 300 V are enough to obtain the maximum SFR, respectively.

The dependence of the current-voltage characteristics curve on the beam-intensity and the number of particles requested per RP is shown in Figure 3.23. An extended FOV of 3.0× 3.0 cm^2 was irradiated with a 187.97 MeV/u ^{12}C-ion beam at three different dose-levels. The low- and high-dose schemes used in this work are compared with a *hyper*-high-dose irradiation depositing 5·10^5 carbon-ions per RP, same as used in Rinaldi [2011]. The beam-intensities defined by the PDG are 2·10^6 pps, 3·10^6 pps and 8·10^7 pps from the lowest to the highest-dose, respectively. For a clearer comparison of the saturation curve rising profiles, shown in Figure 3.23a, the mean charges are normalized by the mean value of the corresponding acquisitions taken with a voltage above 700 V.

As expected, the high-intense beam produces the highest ionization density. In consequence, recombination losses remain until a potential difference higher than 700 V is applied between the PPIC electrodes (cf. Figure 3.23a). This *hyper*-high-dose-regime is only shown for reference

comparison of the PPICs working principle, albeit not used in the scope of this work for imaging purposes. When the beam intensity and dose are reduced (to the high-dose level), the charge saturation is evident already from 500 V on. At the low-dose regime, when using the lowest particle-rate, the measurements are more sensitive to non-linearities. In this scenario, low voltages ensure charge saturation from 300 V to 500 V, which is considered as steady IC region of operation.

Figure 3.23b shows the behavior of the SFR relative to the increasing HV for the same samples shown in the left panel, exhibiting the impact of the noise levels at different operating voltages. For the low- and high-dose irradiations, the maximum of the mean SFR appears at 200 V and 300 V, respectively. Although these voltages are lower than the ones indicated in the left panel as the starters of the saturation region, the noise might be considerably reduced. Therefore, a reasonable trade-off between the loaded noise, and the electric field necessary to avoid recombination effects and reach the ionization necessary to produce a recognizable BC might be found one HV step before saturation.

After the SFR reaches is maximum, a declining trend is observed in the low- and high-dose cases. The recombination effects have been overcome, but the noise induced by the voltage is dominating (cf. Section 3.5.3). On the contrary, for *hyper*-high-dose irradiations, the SFR values slowly become larger as the HV rises, only reaching its maximum at the highest available voltage (1000 V).

The RRD throughout characterization described above justifies the importance of deciding on the optimal combination of beam-energy, intensity, dose and HV prior to each experiment in order to assure the highest-quality images.

3.5.2 Charge collection response

Independently of the factors inherent to the imaging experimental-setup that have direct influence in the charge gain per PPIC, such as the beam intensity-fluctuations or signal reliability, the charge collection of some of the PPIC might be also diminished due to environmental conditions (air temperature, humidity and pressure), bad electronics-contact or lack of detector maintenance, causing an under-response effect in the measurements. This might be detrimental especially when the BC falls in one of the under-responsive chambers. Therefore, being aware of the individual performance of each chamber on collecting charge is important to obtain an overall fair-quality discretized BC per RP.

This section aims at using the detailed MC model of the RRD[N], which is comprehensively described in Section 4.0.2, to estimate the charge collection response per chamber and define single-chamber output factors that might be used to compensate the charge gain of acquired data a posteriori.

The collecting volume in the PPIC is modeled in the simulated detector as a 30×30 cm^2 active cross-section × 0.6 cm, which corresponds to the air gap between the two parallel plates of the chamber. The two aluminized electrodes are not considered in the simulated geometry of the detector.

Recalling Equation 3.1, the charge Q_{PPIC} per unit area of the in-silico PPIC is ideally

[N]Thanks to Sebastian Meyer for providing the simulation data-set used for this study.

calculated by:

$$Q_{PPIC}[cm^{-2}] = N_{ions} \cdot \left(\frac{dE}{dx}\right)_{air} d_{PPIC} \cdot \epsilon_{N_{det}} \cdot \frac{e}{W_{air}}[C \cdot cm^{-2}] \tag{3.8}$$

where $e = 1.602 \times 10^{-19}$ C denotes the elementary charge. $W_{air} = 34.1$ eV refers to the mean energy to produce an ion pair within the PPICs, measured by [Brusasco et al. 2000] for the first prototype of the detector used in this work. $\epsilon_{N_{det}}$ is the fraction of initially requested primaries detected. It is determined by the Equation 3.4.4 for each RP of the FOV, in order to make the charge collection estimation independent from the irregular integration times induced by the beam intensity-fluctuations, which have a strong effect on the collected signal.

The MC simulations output is the energy deposited by the ion-beam scored in the active volume of the chamber, i.e., it encodes the first three terms of Equation 3.8, considering an air-density of $\rho_{air} = 0.0012$ g/cm^3. No corrections to the environmental-conditions are applied since they might vary from day to day.

Figure 3.24 shows the expected flat-gain response when a high-energy 430.1 MeV/u ^{12}C-ion beam of two different fluences traverses the detector without stopping within. In general, a good agreement is observed between the experimental and the MC simulated data. In both dose scenarios, the mean deviation is mainly influenced by the under-responsive channels. Additional discrepancies might be caused by the intrinsic beam-intensity fluctuations. Once a benchmark between the experimental and the simulated outputs has been established, it is possible to define an expected efficiency based on the MC-simulations that would allow to assess the performance of individual chambers and potentially correct any systematic under-response.

Figure 3.24: PPIC flat charge-gain response compared to MC simulations. The RRD was irradiated with the highest energy (410.10 MeV/u) carbon-ion beam of high- and low-doses. Ion-beams at this energy have a range in water equal to 30.81 cm, thus the BP does not fall within the detector structure. A flat charge-gain is expected along the 61 channels of the detector.

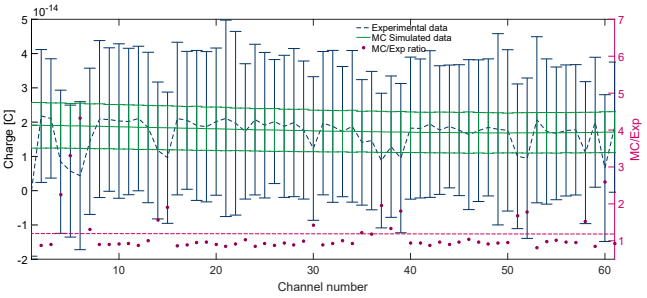

(a) PPIC mean charge-gain response over a FOV of 3.0 × 3.0 cm^2 irradiated with a low-dose 430.1 MeV/u ^{12}C-ion beam. The mean deviation per channel between the charge calculated with the RRD MC-model and the measured charge is depicted with (magenta) dots on the right axis, with a whole channel-array mean deviation equal to 1.20 (dotted magenta line).

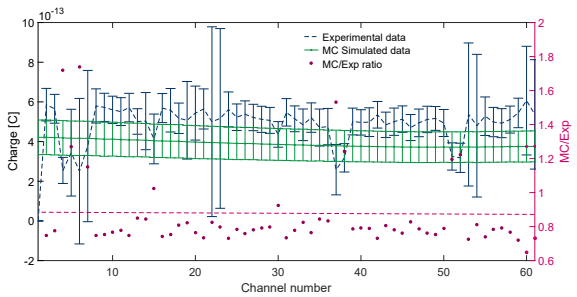

(b) PPIC mean charge-gain response over a FOV of 3.0 × 3.0 cm^2 irradiated with a high-dose 430.1 MeV/u ^{12}C-ion beam. The mean deviation per channel between the charge calculated with the RRD MC-model and the measured charge is depicted with (magenta) dots on the right axis, with a whole channel-array mean deviation equal to 0.86 (dotted magenta line).

Figure 3.25 display how the MC-simulated data match the experimental data for a low-(left panel) and a high-dose (right panel) averaged BC obtained from a scanned irradiation with a 187.97 MeV/u ^{12}C-ion beam. The correspondence is generally as good as in the flat channel-gain case (within ± 10%) shown above. Nonetheless, the quantitative comparison is kept for

the plateau region where the PPICs have a flat charge response. The BP and the tail regions of the curve are subject to signal variations. In the case of the BP, due to the variability of the BP position inside the RRD-channel, as it is evident from the large standard deviations of these data-points; and the tail region is very sensitive to noise fluctuations.

Figure 3.25: PPIC mean charge-gain response compared to MC simulations. The RRD was irradiated with a 187.97 MeV/u ^{12}C-ion beam of low-(left) and high-doses (right).

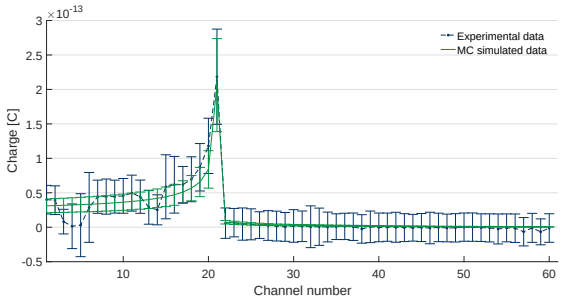

(a) PPIC mean charge-gain response over a FOV of 3.0 × 3.0 cm^2 irradiated with a low-dose 187.97 MeV/u ^{12}C-ion beam.

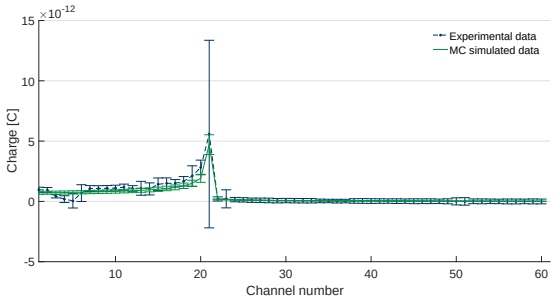

(b) PPIC mean charge-gain response over a FOV of 3.0 × 3.0 cm^2 irradiated with a high-dose 187.97 MeV/u ^{12}C-ion beam.

3.5.3 Transmission-imaging system noise characterization

The dose that a patient would receive when an ion-based image is taken is of major importance. Hence, it is desired to keep about thousand or less ions per RP. As was pointed out in previous sections, the acquisition of these low-dose projections requires an optimized SNR. At this low-dose regime, the BCs measured by the RRD are prone to be dimmed by the broad-band background noise, making it impossible to determine accurately the BP location or to apply post-processing methods based on data modeling, which are especially sensitive to signal fluctuations. Understanding the noise spectrum influencing the experimental setup is crucial to improve the SNR and therefore increase the accuracy of the anatomical retrieval of the phantom/patient ant its corresponding WET. In this section, the underlying causes of the noise affecting the experimental acquisitions are described extensively. Potential technical solutions to overcome their effect are suggested, while a signal processing method to make the signal more robust against the noise is presented in Section 4.1.2.

The principal sources of noise influencing the imaging system are outlined as follows:

- Environmental/electronic noise
- Mechanical vibration
- 25 Hz resonance caused by the vacuum pump transmitted vibration or sound
- 50 Hz and 150 Hz resonances intrinsic to the beam micro-structure
- 50 Hz power-line noise
- Random noise fluctuations induced by the internal HV supply

The next sections explore the experimental evidence and the analysis methods applied to study these noise oscillations.

Discrete Fourier Transform (DFT) methods applied to output signals in the time-domain

Discrete Fourier Transform (DFT)-based methods are used to obtain and analyze the Fourier spectrum of the time-discrete output signals from the I128 electrometer in the time-domain.

The DFT-approach efficiently determines the frequency spectra (periodogram) of periodic distributions, i.e., a complete reconstruction of the original signal from such a discrete spectrum should be possible. If the signal does not contain frequencies higher than F [Hz], it can be completely determined by giving a series of points spaced by $1/2F$ seconds. Analogously, for a sample rate f_s, a full signal-reconstruction is guaranteed for a frequency band-limit $F \leqslant f_s/2$, i.e., the so-called *Nyquist criterion* is satisfied.

However, in case of a non-uniform sampling-frequency, the approximate DFT does not represent exactly the periodogram of the data. If the irregular samples have an underlying distribution, such as a normal spread, there is certainly a similarity between the original signal and its irregular sampled version as it will be demonstrated. Nonetheless, the frequency components might be biased and the frequency resonances will implicitly have an uncertainty in their width and amplitude. In consequence, the inverse DFT will not yield a complete reconstruction of the original signal, which has to be born in mind for the noise interpretation and characterization. The strategy to manage the non-uniform sampling is presented later in this section.

The output signal from the electrometer provides information of the charge collected by the 61 PPICs, simultaneously, in each time-stamp. Generally, this time-stamp would correspond to the sampling time determined by the user-defined integration time. The data-acquisition system allows for two data-streaming modes. The first one acquires data continuously, one integration after the other at the chosen sampling time (t_s), resulting in evenly distributed samples and time-stamps. The second one is the triggered acquisition mode, being used for the generation of ion-based images as explained in Section 3.4.3, which allows an external TTL-signal that announces the arrival of the beam to a new RP and launches the current integration. In this case, the time-stamp varies consistently with the beam intensity-fluctuations, leading to non-uniformly distributed samples. Hence, the time-domain of the signal reflects the irregular sampling of the data acquired.

The signal per channel is the integrated current during the sampling time, i.e., the charge collected by each PPIC. The inherent integration-mode of the RRD limits the fine resolution of the charge signal. This means that high-frequency changes within the signal might be lost during the integration and averaging process. There is no information about the charge dynamics between RP samples in the final output.

Uniformly spaced data acquisition

The regular-sampling case is investigated first to be the comparative reference for the non-uniform sampling scenario, which is presented later. A carbon-ion beam is irradiated continuously at the isocenter; while the beam impinges the RRD, the charge is integrated during a user-defined t_s. By using a proper combination of the ions delivery-rate (beam-intensity) and t_s, the data can be acquired regularly and, at the same time, emulate the RP-based acquisition during the scanned irradiations used to obtain transmitted images.

As an example to illustrate this comparison, a homogeneous PMMA block of $10\times10\times25$ cm^3

was irradiated with a high-dose 350.84 MeV/u ^{12}C-ion beam isocentrically, and then scanned throughout an extended FOV of 10×10 cm^2. For the continuous irradiation, the current-signal was integrated every t_s = 500 μs (cf. Figure 3.26). Recalling, for a high-dose scanned irradiation, the current-signal is usually integrated during 450 μs, hence a fair comparison is expected. The continuous data acquisition allows the data sampling to be uniquely determined by the chosen t_s. Mimicking a radiographic reconstruction by redistributing this data into a scanning grid, each sample would correspond to the charge collected in one RP during the fixed integration time, independently from the beam intensity-fluctuations and would contain approximately the same amount of particles.

For a nominal beam-intensity of 5·10^6 pps, sampled in equally time-spaced data-points every 500 μs, approximately 2500 particles would be registered per RP. This scenario is the closest to the current optimal scanned case in which the integration time does not adapt to the variable t_{RP} and is also not seriously affected by the beam intensity-fluctuations, i.e the reliability of the signal is steadily about 50% (cf. Section 3.4.4). Since the data set is, in this case, uniformly sampled, the DFT can be correctly computed to find the noise frequency spectra present during experimental acquisitions.

The DFT of the charge signal was evaluated and analyzed channel-wise. An exemplary of a 3.5 s portion of the raw signal measured by the channel number 31 and its corresponding frequency spectra are shown in Figure 3.26. Various data-sets acquired on different days, under the same experimental conditions, were analyzed in the same way in order to rule-out any potential day-to-day variation.

The periodogram of the not-scanned signal (cf. Figure 3.26b) shows dominant resonance frequencies at about 25 Hz, 50 Hz, 100 Hz and 150 Hz. As it was previously outlined, the resonance at 25 Hz is caused by the vacuum-pumps transmitted vibration or sound, as the independent investigation in Section 3.5.3 will demonstrate later. The 50 Hz resonance frequency, as well as its higher harmonics at 100 Hz and 150 Hz, are commonly encountered in electronic responses due to the background power-line interference. Furthermore, the ion-beam itself is sensitive to any variation during the irradiation, for instance caused by the ripples of the magnet's power supplies. It has been observed that the ion-beam time-structure at HIT's accelerator has some innate 50 Hz oscillations and corresponding harmonics related to this effect. Additional frequency peaks at 165 and 262 Hz due to minor ripple influence of the synchrotron equipment have been reported by Peters et al. [2008]. All these oscillations add up to a modulation of the beam-current, which is inevitably transported to the experimental data.

Environmental noise

The resonance frequencies listed above are common to most of the channels operated at integration times used for experimental acquisitions. However, due to individual functional sensitivity of the PPICs, each channel might be affected by additional noise frequencies, which is subject for further detailed investigations. In the first instance, to be able to apply noise-removal techniques to whole data-sets (including all the signals acquired simultaneously by the 61 RRD channels), the electronic noise fluctuations that distort all or most of the channels must be characterized. Aiming to efficiently quantify the environmental noise present in the whole system, a

Figure 3.26: An example of a 3.5 s portion of the raw-signal measured in equally distributed samples by the channel number 31 of the RRD and its corresponding frequency spectra obtained by applying a DFT.

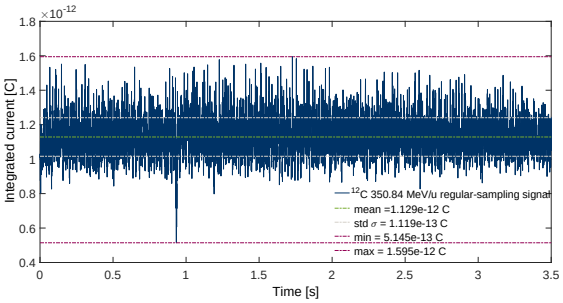

(a) 3.5 seconds signal time-structure measured in 500 μs integrations by the RRD channel number 31 when a high-dose 350.84 MeV/u ^{12}C-ion beam is impinged isocentrically into an homogeneous PMMA block.

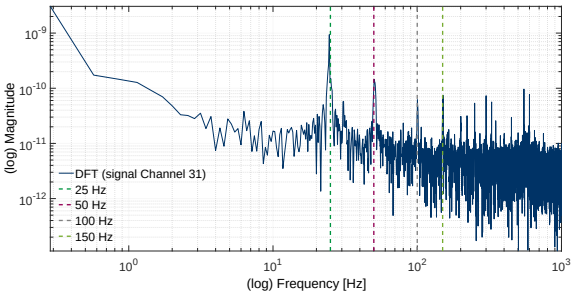

(b) DFT of the signal shown on the left. Frequency spectra of continuous samples taken at t_s= 500 μs. Evident resonance frequencies are at 25 Hz, 50 Hz, 100 Hz and 150 Hz.

pre-experimental noise-analysis protocol provides the resonances with the maximum amplitude encountered per channel. Moreover, it allows to filter the most dominant frequencies to inspect other oscillations that might only affect certain channels. A collection of environmental noise measurements, varying different acquisition parameters such as integration-time and drift-HV, is acquired before each experiment in continuous-mode, hence at evenly separated samples.

For these investigations, the first measured signal is sampled at the shortest time-resolution allowed by the I128 electrometer, t_s = 55 μs, so that the frequency spectra provides the maximum detail. The entire experimental setup (RRD, I128 electrometer, Ether-CAT trigger-signal control unit, internal HV supply and host computer) is connected and, when no beam is present, continuous charge measurements are collected at different integration times and HV values. Figure 3.27 depicts an exemplary output of the noise spectra analysis, the frequencies with the maximum amplitude present in a 0 V raw-signal sampled at 55 μs resolution are displayed for different filtering. The I128 electrometer channels which are not connected to the RRD (i.e., from 62 to 75) are taken as reference of the pure electronic noise.

The utility of these studies is twofold. First, as it was mentioned in Section 3.4.3, when there is a known periodic noise such as the ones appearing in the DFT of the signal, the current can be integrated for a period of time chosen to comprise an integer number of cycles of the periodic noise waveform. Thus, the noise signal integrates to zero and is rejected from the charge collection. And second, bearing in mind the building of the next RRD prototype, it is decisive to know the noise sources affecting the transmission-imaging experimental setup, especially when the low-dose signals fall within the noise level.

Undesired noise pick-up frequencies can affect the overall BC profiles. Although t_s is chosen so that it fulfills the experimental considerations described in Section 3.4.3, random noise can still distort the signal behavior in one of more channels, which might affect the maximum identification in radiography pixels depending on the period of its oscillation. Figure 3.28 shows the effect of noise-interference in individual channel readings at three typical integration times. One of the displayed integration times (t_s=150 μs) captures a resonance, causing a vertical distortion in the detected charge-signal base-line.

As was pointed out earlier, the experimental campaigns accomplished in the framework of this

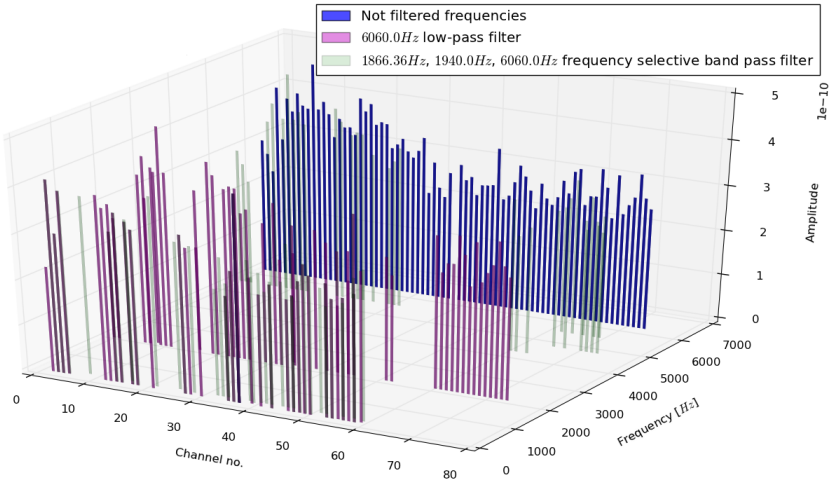

Figure 3.27: Example of the output of the pre-experimental noise-analysis protocol. The 3D-visualization provides information about the predominant resonances in 75 of 128 electrometer-channels (channels 1 to 61 are connected to the RRD) after applying the DFT to the raw-signals. A 6 kHz oscillation affects the whole electrometer, i.e, it is detectable in all the channels independently if they are connected to the RRD or not. A low-pass filter is applied to this resonance in order to reveal other frequencies affecting only the connected channels. The 1.87 kHz resonance predominates after cutting frequencies equal or higher than 6 kHz. Extra filters at are implemented at 1.87 and 1.9 kHz.

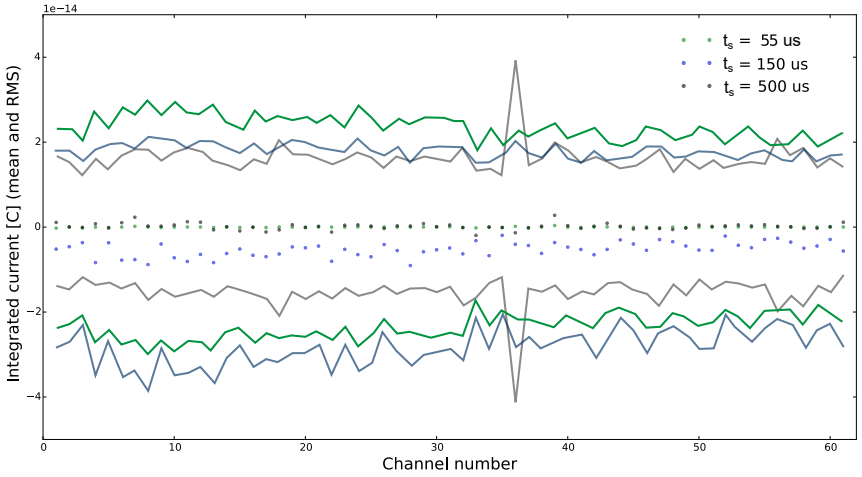

Figure 3.28: Loaded electronic noise (mean and Root-Mean-Square (RMS) (standard deviation)) and the effect of pick-up noise frequencies in individual channel responses, distorting the RP-signal amplitude in all the channels, causing a vertical shift. The electronic noise is acquired continuously at 55 (green), 150 (blue) and 500 μs (gray) separated samples. When the charge is integrated in periods of 55 and 500 μs, the electronic noise mean value remains about the zero-level as expected for random oscillations. However, for t_s=150 μs, a noise resonance is picked-up causing all the charge-collected signals to be shrunk in certain extent. Increasing the signal integration time, reduces the RMS-noise allowing more fluctuations to be averaged to zero.

thesis took place at the HIT's quality assurance/experimental room, where the noise spectra have been characterized. However, envisioning future clinical applications, the noise in one of the horizontal-beam-line treatment rooms was also investigated. Continuous acquisitions were taken under different environmental conditions, by varying controlled factors such as

light, ventilation (air conditioning) and presence of vacuum pumps, in order to distinguish and discard any possible effect on the measured experimental data. In both rooms, the light and air conditioning had no significant effect in terms of noise standard deviation. The main noise contribution to the detected signal in the experimental room is originated by the mechanical vibration due to the vacuum pumps located at ground level, which is not the case in the treatment rooms, where the vacuum pumps are hidden behind the room walls. These noise sources are discussed in the following sections.

Electronic and vibrational noise

In order to diminish the noise due to the mechanical vibration of the floor in the HIT's experimental room, a weight of 40 kg (in lead blocks) was added to the RRD trolley. The electronic noise was measured for 5000 contiguous samples, taken at different fixed integration times ranging from 55 μs to 10 ms. The standard deviation (which is used interchangeably as RMS-noise), normalized by each integration period, was obtained to represent the alternating current. Up to 1 ms, the t_s was increased by direct control of the integrator circuit. Above 1 ms, it was increased by digital averaging of readings (conversions per sample) (cf. Figure 3.29).

Experimental acquisitions require integration times of few hundreds of microseconds, depending on the image-dose and beam delivery-rate. These integration times are located in the left half of the Figures 3.29a and 3.29b. In this region, when no HV is applied (cf. Figure 3.29a), the noise standard deviation is slightly reduced when weights are used to stabilize the experimental setup. However, a significant overall benefit on the use of extra weight is not evident. In both conditions, an unexpected broad peak appears between 1 to 2.5 ms, related to noise frequencies between 1000 to 400 Hz, respectively. The next generation of the PPIC-stack is foreseen to be stable enough to overcome mechanical vibration, moreover it would include vibration isolators to damp the floor vibration and environmental noise. When the internal HV supply is turned on, it causes an increase in the electronic noise, in consequence, high noise current levels are transported to the PPICs as a form of channel-coupling, as it was also demonstrated in Section 3.5.1 and it is visible in Figure 3.16. Figure 3.29b shows the noise standard deviation, acquired and normalized by different integration times when the bias-HV is equal to 500 V. In this case, the advantage of adding extra weight to the experimental system is apparent. On the same right panel, the standard deviation of the electronic noise measured in one of the horizontal beam-line therapy-rooms at HIT is shown. The noise level in this room is in the same order of magnitude as in the experimental room, when extra weight is added to the detector carriage.

The DFT analysis of the electronic/environmental noise in the RRD-channel signals reveals the presence of 50 Hz resonance and its harmonics, which is related to the power-line of the facility. In some of the channels, a 20 to 25 Hz oscillation due to the exposed vacuum pumps is also visible (cf. Figure 3.30), besides a broad region of high-frequency peaks. The exploration of electronic noise frequency spectra is convenient to determine the inherent signal-interference affecting the experimental-system. The effects that are noticeable at this level will occur and enhance in the presence of the beam.

Figure 3.29: Comparison of the noise standard deviation normalized by the acquisition integration times in different experimental scenarios.

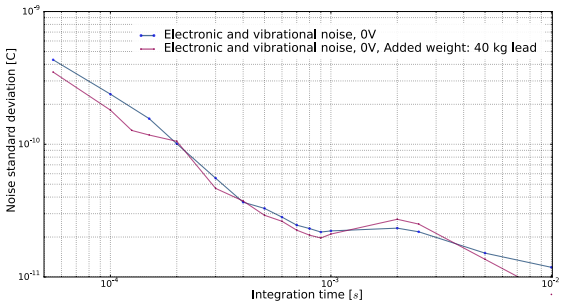

(a) The standard deviation of the electronic and vibrational noise registered in the experimental-setup without applied HV is measured for different integration times with and without added weight to the detector trolley.

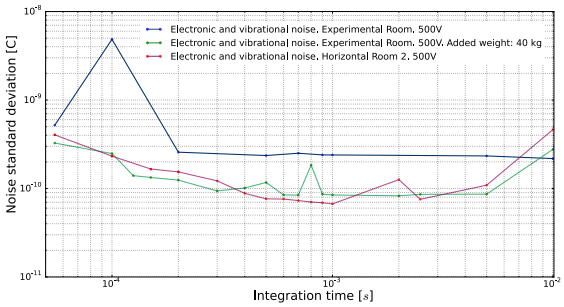

(b) The HV is set to 500 V and the noise standard deviation is measured at different integration times, with and without added weight to the RRD carriage. Furthermore, the RMS-noise is compared to environmental noise acquisitions in one of the horizontal-beam treatment rooms at HIT (magenta). Noise pickups appear at 100 and 800 μs.

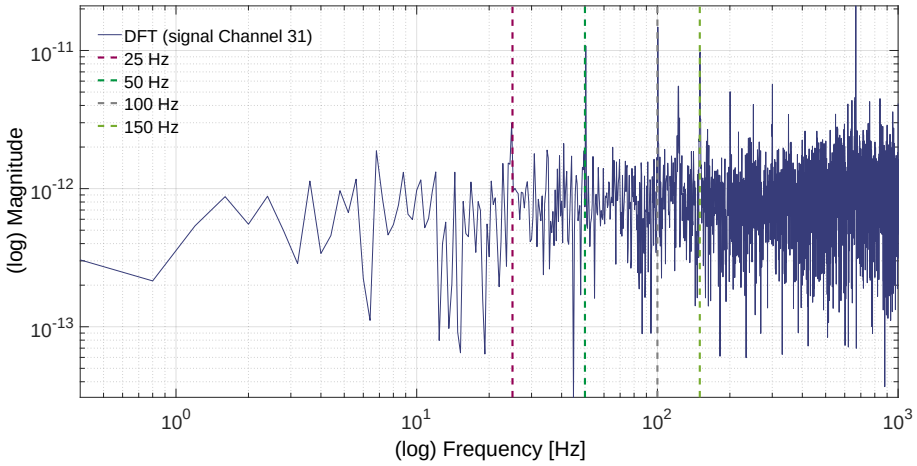

Figure 3.30: DFT of the electronic noise signal acquired continuously at $t_s = 500$ μs in one of the RRD channels when the internal HV supply is tuned to 500 V. The 50 Hz peak related to the power-line and its harmonics, as well as the 20 Hz resonance, caused by the presence of the vacuum pumps, are noticeable in the periodogram and they will be boosted when the irradiations are performed.

Non-uniform-spaced data acquisition

As it was introduced in Section 3.4, the transmitted image formation is possible thanks to the synchronization between the HIT raster-scan technique used during the beam delivery and the RP-triggered charge collection by the electrometer. The PDG defines a nominal RP duration of ∼1.7 ms defined by the integration process of the BAMS. However, beam intensity variations cause this time to fluctuate, too. In consequence, the signals measured by the PPICs of the RRD during the image acquisition are always non-uniformly sampled.

There are few statistical signal processing techniques used to address this issue and/or to interpolate or re-sample the uneven data-points. Nevertheless, when the stochastic sampling process follows a well-defined model, as shown by the normal distribution of t_{RP} (cf. Figure 3.5), it is feasible to calculate the DFT assuming the mean frequency as sampling frequency,

and approximate the inaccuracies introduced by this procedure. The uncertainty on the DFT computation for non-regular sampled signals in the frequency-domain is quantified from the shift in the time-domain ($\Delta\mu = \bar{\mu} - \mu$) between the mean of the Gaussian distribution ($\bar{\mu}$) with respect to the expected RP lapse, μ =1.7 ms. This effect can be perceptible from the displacement of the largest resonace from the 25 Hz green dashed-line in Figure 3.31. Following the exemplary t_{RP} distribution shown in Figure 3.5, $\Delta\mu$ =0.17 ms. This deviation is then translated into the frequency-domain as the difference between the regular sampling frequency normalized to the number of samples, $f_s/N = 0.12$ Hz, minus the irregular sampling frequency including the Gaussian distribution deviation from the expected mean, $f_s + \epsilon_s/N$. Therefore, the shift in the periodogram due to non-uniform sampling is $\Delta f = \epsilon_s/N$ =1.17 Hz relative to frequency spectra obtained with a regular sampling.

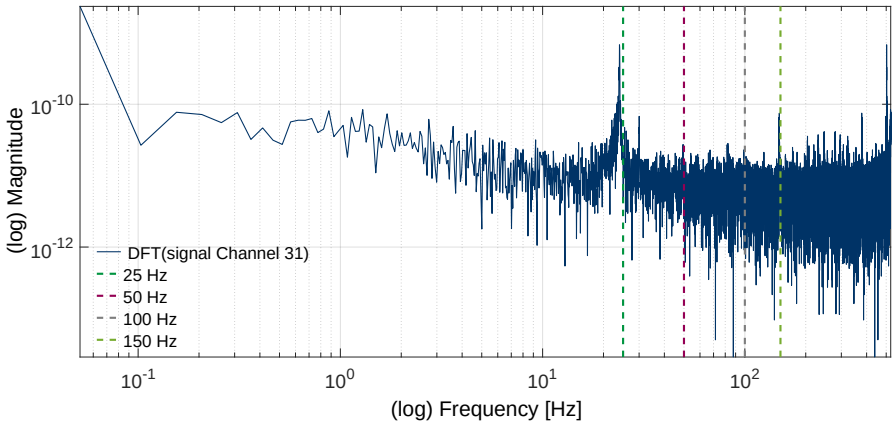

Figure 3.31: Resonance frequency spectra of one-channel signal obtained with a scanned ^{12}C 350.84 MeV/u beam traversing an homogeneous PMMA phantom. The DFT of the raw-signal of the channel 31 is computed with a sampling time equalized to the mean t_{RP}. The assumption of a regular sampling introduces a slight shift (1.16 Hz) of the noise-frequency spectra in respect to the well-defined resonances noticeable in the case of the even sampling time (cf. Figure 3.26).

25 Hz noise resonance

There are three vacuum pumps at the end of the beam-line in the HIT's experimental room that assure a clean path for the ion beam:

- 1. The compact turbo drag pump
- 2. The Kolben pump – Xtra Dry
- 3. The membrane pump

In order to verify if the dominant 25 Hz frequency arises from the influence of the vacuum pumps, two out of three vacuum pumps were turned off. Afterwards, air scanned-projections were acquired and then repeated in the regular experimental conditions for image acquisitions, ensuring a fair comparison.

Except for the first pump operating at ∼800 Hz, which takes several minutes to be completely off, the other two pumps were switched off for approximately 30 minutes to complete these

measurements. Figure 3.32 shows the frequency spectra of the signal measured by one single channel (number 50) with and without the interference caused by two vacuum pumps. The 25 Hz frequency is indicated by the magenta marker in both spectra of Figure 3.32. Some of the channels also reveal a strong 20 Hz resonance. In the right-hand spectrum (cf. Figure 3.32b), both peaks disappear, making evident that the origin of these low-frequencies are the oscillations produced by the vacuum pumps at the end of the beam line in the experimental room.

Figure 3.32: Influence of the vacuum pump noise in the frequency spectrum of the RRD channel-signals, when a 292.84 MeV/u ^{12}C-ion beam is scanned. Comparison of the periodograms of scanned irradiations taken in the usual experimental environment with the vacuum pumps on (left) and the scans with the same beam characteristics acquired when the vacuum pumps 2 and 3 were turned off (right).

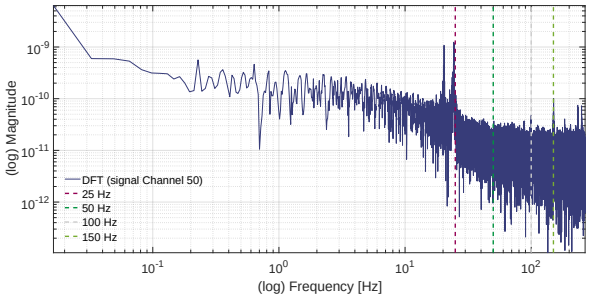

(a) Frequency spectrum of the signal over time measured by the channel 50 of the RRD. Scanned irradiation in usual experimental conditions with the three vacuum pumps turned on.

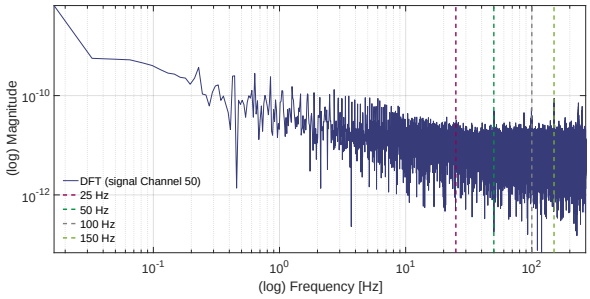

(b) Frequency spectrum of the signal over time measured by the channel 50 of the RRD. Scanned irradiation is performed only with first vacuum pump, while the second and third are turned off.

The 25 Hz noise fluctuation dominates the frequency spectrum in approximately 70% of the RRD channels. Unavoidably, the vacuum pump has a direct influence in the shape of discretized BCs. Generally, the 25 Hz resonance manifests itself in channel-coupling effects, although the signal-distortion results more harmful in channels which are more sensitive to current fluctuations (also induced by the inner HV supply). These scans were acquired with optimized HV, following the current-voltage protocol described in Section 3.5.1. Hence, the influence of the drift-field within the ICs is expected to be minimized.

The interference created by the vacuum pumps causes a BC-signal corruption which is visible in Figure 3.33, when comparing the same RP BCs from the irradiations performed with (dotted lines) and without vacuum pumps (solid lines). These distortions might result in salt-and-pepper noise in the 2D-radiographic-projections if the noise causes abrupt peaks larger than the signal corresponding to the BP. Regardless of the systematic under-response of the already known malfunctioning channels, the channel-coupling issue and random signal fluctuations observed in the dotted curves are mostly overcome when the pumps are off.

Although there is an unambiguous signal distortion due to the vacuum pump noise fluctuations, the pumps can only be switched off for short periods of time no longer than half an hour. Therefore, the possibility of acquiring images under this noise-reduced conditions is experimentally unfeasible.

Generally, the loaded noise (electronic, environmental and vibrational) can be regulated in several ways by experimental means:

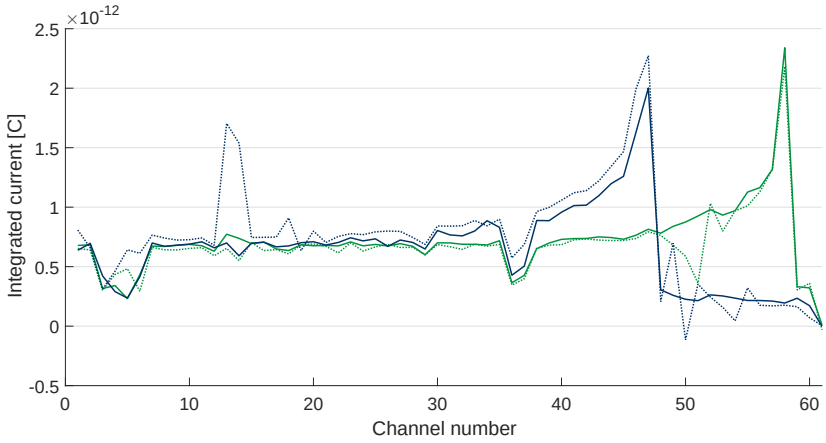

Figure 3.33: Effect of the beam-line vacuum pumps noise on measured BCs. The BCs correspond to a same RP in two different irradiations scenarios: with the vacuum pumps 2 and 3 on (dotted lines) and off (solid lines). Curves obtained with ^{12}C-beams of two different energies (292.84 MeV/u (blue) and 331.83 MeV/u (green)) are displayed, falling in the channels 47 and 58, respectively.

- Electronically, by increasing the integration time. The longer the averaging period, the larger the suppression of RMS noise.
- Digitally avoiding specific noise frequencies (cf. *Noise trade-off* in Section 3.4.3)
- Mechanically, by reducing the cabling distance between the electronics unit and the RRD or actually consider a built-in electronics module plugged directly to the detector channels. Noise-dampeners must be adopted in the constitution of the new RRD prototype, since most of the mechanical-vibration generated by the vacuum pumps comes from the ground. Furthermore, a more stable carriage for the detector is desirable.

3.5.4 Further experimental considerations

The accurate retrieval of the phantom WET from 2D-radiographies or Relative Stopping Power (RSP) from 3D-tomographic reconstructions rely on the uniform constitution of the RRD-channels over the whole active area, i.e., air or homogeneous material projections are expected to yield flat images. This condition, however, can be corrupted due to different factors, including PMMA-slabs inhomogeneities from the manufacturer, electric-field distortion due to environmental conditions (e.g. air temperature and pressure) or moisture effects within the air gap of the PPICs.

Radiographic image inhomogeneities were observed in air-projections, resulting from an unexpected channel-displacement effect at certain regions of the irradiated FOV which was found in most of the detector channels. Clusters of several RPs were recognized with the BP position shifted one channel back than the expected location. For a clearer visualization of an exemplary case, a color-saturated map assigning a contrast-color (green) to the wrongly assigned channel is shown in Figure 3.34a. A high-statistics air-projection ($5{\cdot}10^5$ primaries per RP) is obtained with a 310.58 MeV/u ^{12}C-ion beam. This dose-choice improves the signal-to-noise ratio, allowing to disentangle the study case from the signal quality. In the radiography, green colored RPs indicate wrongly allocated BPs (Channel 49), while the rest of the FOV reflects the expected BP location (Channel 50) according to the defined gray-scale. The correct BP

position is deduced from MC-simulations obtained with the same beam-energy. In the right panel, the reliability of single RP signals, in terms of charge accumulated per RP, is assessed by means of the reliability-index, previously introduced. The RI-map of the same irradiation shows an almost-uniform light-blue shade, which demonstrates no correlation between the performance of the trigger on collecting enough charge and the misplaced BP position shown on the left.

Figure 3.34: Example of image-inhomogeneity effect due to uneven PMMAs absorbers (a) and the reliability-map of the irradiation (b). A high-statistics air-projection ($5{\cdot}10^5$ primaries per RP, to avoid signal disruption by noise) is obtained with a 310.58 MeV/u ^{12}C-ion beam. All the BPs of the projection are expected to fall within the channel number 50, i.e., the pixels are expected to be colored in light-gray. However, the BPs on the upper part of the FOV are allocated one channel before, which is saturated in green for easier identification.

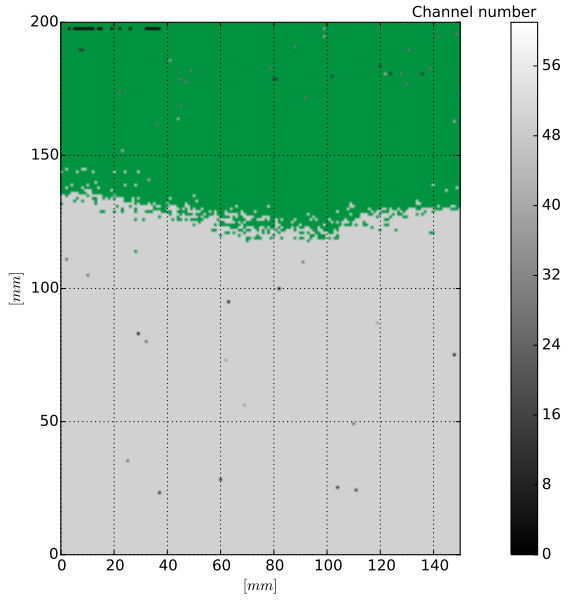

(a) Example of the effect of uneven material distribution of the PMMA absorber(s) of the RRD, causing a discontinuous BP position in the RPs of the upper part of the projection (wrongly assigned BPs are colored in green). In an air projection, all the RPs are expected to be assigned with the same channel/WET value. Dotted lines are drown as visual aid to determine the fraction of the FOV affected.

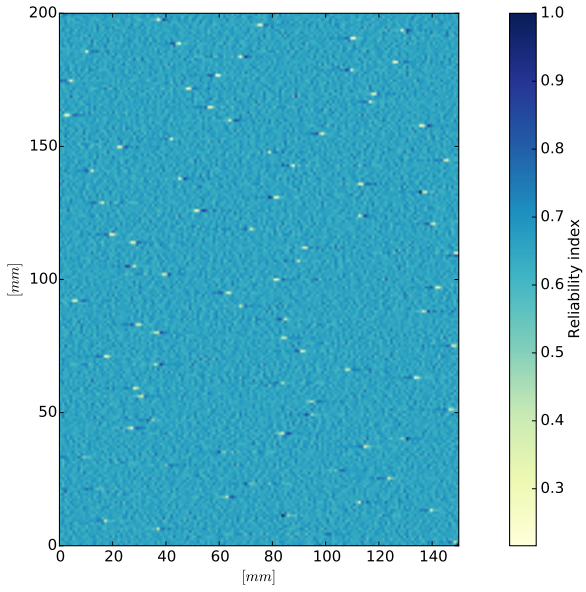

(b) Reliability index map of the air projection shown on the left. The reliability factor goes from 0 to 1. Higher values indicate RPs that integrated more charge in relation to the time that the beam remains on them.

Given the geometrical complexity of the phantoms investigated in this work, the transmitted BPs depth-distribution along the detector channels is equally-complex. Therefore, the impact of the revealed channel-shift in the overall image-accuracy is difficult to be assessed. Especially when the whole experimental setup consists of several components that could have an influence, i.e., the origin of the problem could be beam-line, beam-scanning or detector related. Thus, these variable factors had to be investigated separately.

Exhaustive measurements were conducted to deduce the main cause of the observed displacement. The results of these experiments aid to rule-out a scanning-pattern dependence, a beam-line components dependence, HV-supply influence, day-to-day variation and detection positioning. Temporal radiation-damage of the RRD was also rejected by comparing irradiations performed years ago with actual acquisitions in the same experimental conditions. Besides the signal-reliability (cf. Figure 3.34b), the signal-assessment methods presented in

Section 3.4.5 helped to perceive the behavior of the BCs along the shifted pattern (cf. Figure 3.35). Dose-independence is also supported by the fact that the same patterns appear when hyper-high doses are applied. Consequently, the BP determination in a previous channel than expected is a problem related to individual PPICs, the intrinsic RRD granularity and the maximum-signal identification criteria used in the first instance (without data post-processing (cf. Chapter 4)), to assign the corresponding WET values.

Figure 3.35: SFR (a) and BP-steepness (b) signal-assessment maps to investigate the channel-shift effect shown in Figure 3.34. Both maps show a clear correlation to the original deviation pattern.

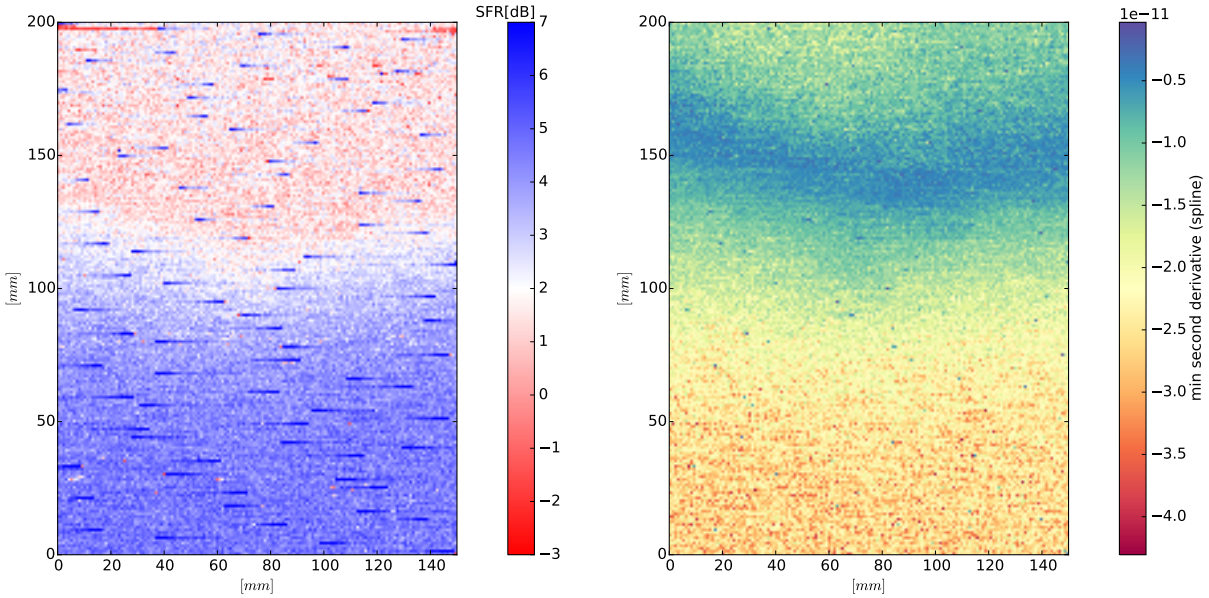

(a) SFR-map

(b) BPS map.

The beam energy is customized according to the phantom's geometry and composition, so that it is guaranteed that all the BCs traversing different densities fall within the RRD and, if possible, avoiding under-responsive or noise-sensitive channels. However, given the single energy-beam used for imaging and the variability in material composition and/or thickness of the imaged phantoms, many BPs might be unfortunately located exactly in between two channels, leading to a channel-discretization issue sketched in Figure 3.36 for three simulated pristine BCs. The stars designate the experimental data-points that discretize the ideal BC. When the BP falls in the frontal-edge of the PMMA-plate, it will be mislead. In case of broader BPs, resulting from range-mixing, the problem is less accentuated, i.e., the air or single-material projections, which lead to sharper BPs are more sensitive to this phenomenon. The examples depicted in Figure 3.36 vary in the skewness and the steepness of the BP fall-off. Thus, a 2D-BPS-map might indicate whether the maximum signal identification criteria is not providing the correct BP-position.

If the detector channels contain rough zones, it is likely that the channel-displacement of the BPs is enhanced according to the accumulated crossed-material by the moment the ion reaches its range.

An additional indirect way to infer the behavior of the BCs over the extended FOV is through signal-assessment metrics maps (cf. Section 3.4.5). Figure 3.35 shows the SFR-map

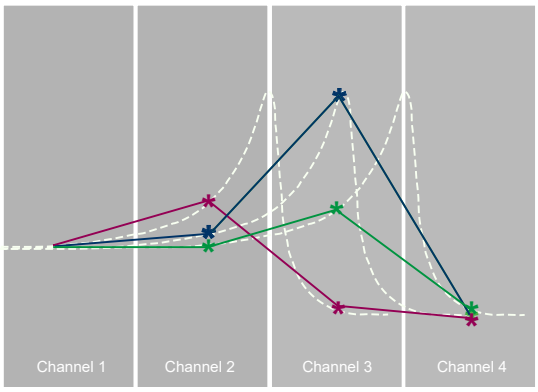

Figure 3.36: Channel discretization sensitivity to maximum-signal identification criteria. By solely finding the maximum-signal, the channel determination can be classified in three main cases. In white dotted-lines three simulated pristine BPs are shown. The stars and colored lines indicate the experimental points in which they are discretized. Other BPs might be shifted within a 1.5 mm range around these samples. For BPs located in a range from the middle towards the distal-edge of the channel (blue discrete curve), the data-point corresponding to the maximum-signal is higher, making the distal-drop of the curve steeper than in the case in which the BP is found at the entrance of the PMMA-slab (magenta discrete curve). For the latter case, the maximum signal will be registered by one channel before than actually should be.

(left panel) and the BP-steepness-map (right panel) suggesting a strong correlation between the channel-deviation and the BC profiles.

The SFR-map (cf. Figure 3.35a) indicates that the BPs in the upper zone of the FOV (in red, poor SFR) are more prone to be misplaced due to lower maximum signal amplitude detected, i.e., small peak-to-plateau difference and large noise fluctuations. This effect is also occurring when the BP is shifted towards the front of the PMMA in which is located (cf. Figure 3.36). Moreover, a smooth transition from red to blue shades reveals that the BP-shift occurs gradually, giving the sign of a decreasing wedge-shaped material distribution from the top to the middle at this particular PMMA-slab or as cumulative effect from the previous ones. Figure 3.35b, supports this hypothesis. Larger absolute values (yellow-orange shades) in the color scale mean a steeper descent, which according to Figure 3.36 refers to BPs falling on the second distal-half of the channel, i.e., that have crossed less material. In contrast, blue-green shaded regions are sign of a shallow spline derivative (cf. Figure 3.18) which, in turn, reflects a shifted BPs falling at the frontal-half of the absorber or one channel before. These BCs are likely to lead to a wrong WET value when only the maximum-signal identification criteria is used (cf. Figure 3.36). A particular blue-colored *ring* is distinguishable in the BP-steepness pattern, which may indicate a subtle layer of extra-material traversed by the beam. These are arguments which reassert the need of further post-processing methods able to increase the system intrinsic depth-resolution as the ones presented in next chapter.

The findings described above suggested a customized channel-wise rectification of the prototype RRD for future experimental acquisitions. A full energy calibration throughout the RRD is suggested to gather information of the FOV zones which are affected in each specific channel. This knowledge would allow to build channel correction-masks to be applied in data post-processing and posterior image formation, although at very-high post-processing cost. Based on precise MC simulations, 88 beam energies were selected from the LIBC so that the BP is allocated in critical positions within the PMMA-slabs, such as the edges (cf. Figure 3.36).

The detector was scanned over a large extended FOV of 20×15 cm^2 in the usual 1 mm RP-step, depositing $5{\cdot}10^4$ carbon-ions per RP. Examples of the shift-patterns appeared in two channels are shown in Figure 3.37. A clear trend is shared by the first 35 channels of the detector in which the BP-shift is located either on the top-left-corner or on the bottom-right-corner of the FOV. On the second half of the detector (after channel 35), the displacement pattern is more symmetrical along the vertical line of the FOV. The impact of this phenomena on the RRD experimental calibration is presented in the next chapter.

Figure 3.37: Example of the channel-displacement effect shown in two different RRD channels. The projections follow the gray-scale tuned by the channel number and the color green is used to saturate the RPs found in a wrong channel.

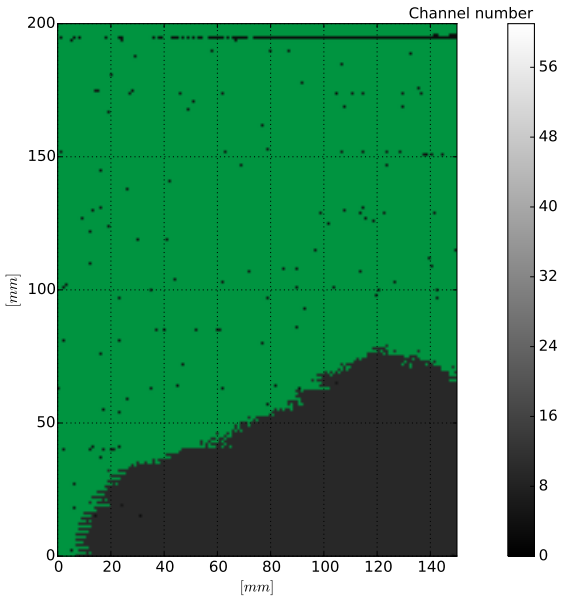

(a) Air projection taken with a carbon-ion beam at 126.11 MeV/u. The BP is expected within the 10th channel according to precise MC simulations, while the green shaded region indicates all the BPs detected one channel before (channel 9). Some salt-and-pepper noise can be observed as well as a pick-up resonance affecting a horizontal sequence of RPs.

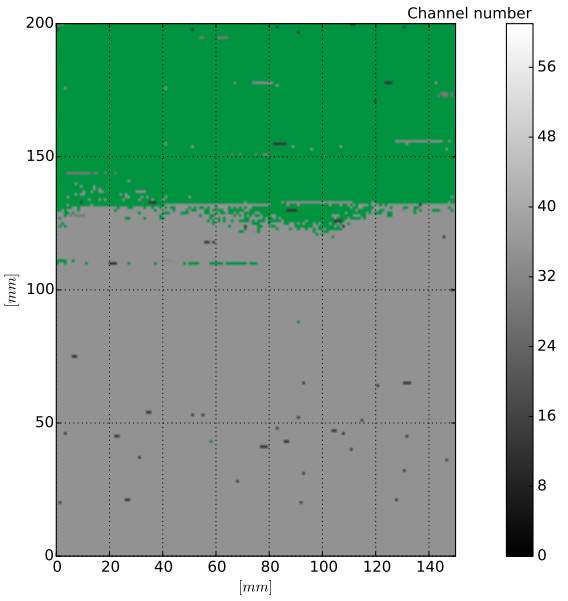

(b) Air projection taken with a carbon-ion beam at 252.40 MeV/u. The BP is expected in the channel 35 according to precise MC simulations, while the green zone represent all the BPs detected one channel before (channel 34). On the channels belonging to the second-half of the RRD the deviation pattern remains mostly horizontal towards the lower part of the FOV, different from the shift patterns found in the first-half of the RRD (left panel), which are oblique.

Further MC-simulations were conducted to investigate the impact on the BC signals in the worse-case scenario, when an uniform ±5% absorber thickness variation is added to all the RRD PMMA absorber plates[O]. The channel-displacement effect is cumulative, therefore the BCs traversing air or light-density materials, falling in farther channels of the RRD are most affected. In such cases, the resulting deviation might be up to 2 channels. Additionally, the RRD discretization (cf. Figure 3.36) might affect differently the channel with the maximum signal according to the exact BP position relative to the adjacent PPIC. Systematically, all the PMMA plates seem thinner in the bottom-part and thicker in the top-part, within the 5% precision limitation claimed by the manufacturer. These studies inquire an accurate quality

[O]Thanks to Sebastian Meyer for performing this study and providing the MC simulated data used for these detector investigations, which are experimentally unfeasible.

assurance on thickness and homogeneity of the PMMA-slabs considered for the new RRD.

3.6 Phantoms

Along the investigations performed in this work, several phantoms of different geometrical designs were imaged to evaluate the imaging-setup performance and to study various image characteristics. In the following, the phantoms are classified in homogeneous and heterogeneous according to their material constituents.

3.6.1 Homogeneous phantoms

Stepped wedge phantom

In order to evaluate the image-quality of radiographic projections, a homogeneous PMMA stepped-wedge phantom was adopted. This type of phantom is commonly used to assess mammographic-images quality. As it is sketched in Figure 3.38, this target consists of equal steps of 20 mm height and 7 mm depth. For later comparison against MC-simulated and true-images, the rWEPL of the PMMA material was obtained from precise (μm) range measurements using the variable water column as it will be described later, yielding $rWEPL_{step}$=1.165.

By placing the stepped phantom in different orientations, downstream the beam-line, it is possible to investigate the step resolution that the transmission-imaging system is able to resolve, as it will be explored in Section 5.1.1 of Chapter 4.

Figure 3.38: Homogeneous PMMA stepped-wedge phantom used for radiographic investigations.

The capability of the transmission-imaging system to resolve various tissue-equivalent materials was assessed through three heterogeneous phantoms, described in the next section. Apart from the radiographic studies, tomographic acquisitions of all the heterogeneous phantoms, with different experimental parameters, were also performed.

3.6.2 Heterogeneous phantoms

Tissue-equivalent slab phantom

The *slab phantom* is a hybrid phantom composed of 6 tissue-equivalent tiles[P]. The slabs arrangement and physical dimension of the phantom are sketched in Figure 3.39, while the Table 3.3 collects the material characteristics such as density and rWEPL[Q]. Further elemental composition of these tissue-equivalent materials is reported in Meyer et al. [2017].

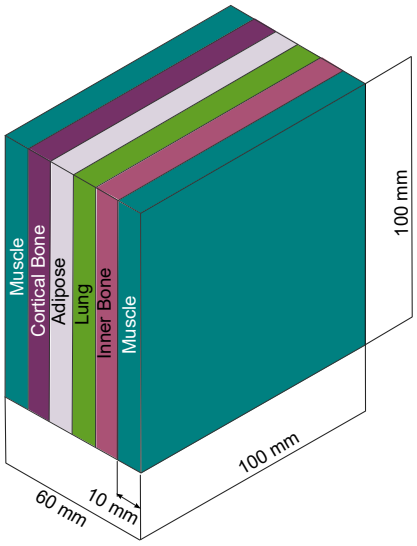

Figure 3.39: Heterogeneous slab phantom composed by five different tissue-equivalent squared plates: muscle, cortical bone, adipose, lung and inner bone. Table 3.3 summarizes the material features such as density and rWEPL.

Material	Density	rWEPL
	$[g/cm^3]$	
Muscle	1.049	1.036
Cortical bone	1.834	1.618
Adipose	0.946	0.948
Lung	0.282	0.284
Inner bone	1.152	1.104

Table 3.3: Features of the slab phantom tissue surrogates: density and rWEPL. The density was measured at HIT using a caliper and a precision balance, while the rWEPL was determined with the adjustable water-column as it will be described in the following chapter.

Cylindrical phantom with tissue-equivalent rods

A cylindrical phantom that emulates some head features was also used for radiographic and tomographic acquisitions. The main material of the cylinder is PMMA and 7 tissue-equivalent rods[R] are inserted therein. As it is depicted in Figure 3.40[S], the rods inserted are made of liver, cortical bone, bone200, breast, muscle, bone400 and adipose surrogates. Table 3.4 summarizes the density and rWEPL of the materials, while further elemental composition is reported in [Hudobivnik et al. 2016].

To perform tomographic acquisitions, the phantoms are placed on a rotating table controlled remotely from outside the experimental room. Laser-guidance supports the whole rotating system positioning in front of the detector and centered along the beam-RRD axis at the isocenter.

[P] Gammex, Middleton, WI, USA
[Q] Thanks to Benjamin Ackermann for providing this information
[R] CIRS, Inc., Norfolk, VA, USA
[S] Thanks to Klaus Wirgler for the technical drawing of the phantom.

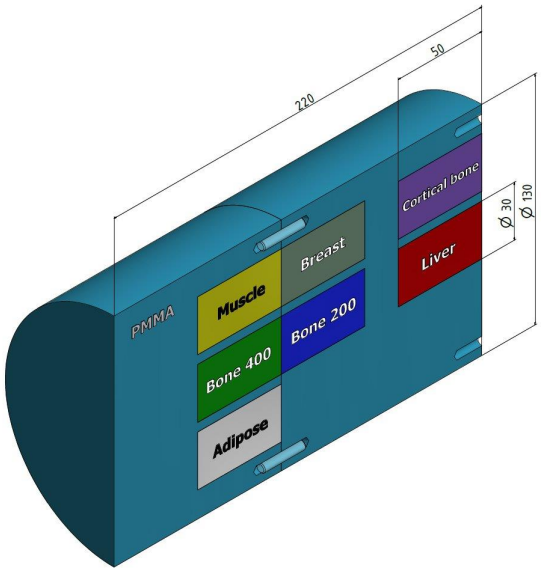

Figure 3.40: Heterogeneous PMMA-cylindrical phantom with seven tissue-equivalent rods: (1) liver, (2) cortical bone, (3) bone200, (4) breast, (5) muscle, (6) bone400, (7) adipose and PMMA. Table 3.4 summarizes the material features and defines the rod's ID

Rod ID	Material	Density	rWEPL
		$[g/cm^3]$	
1	Liver	1.072	1.064
2	Cortical bone	1.910	1.688
3	Bone200	1.161	1.117
4	Breast	0.991	0.989
5	Muscle	1.062	1.057
6	Bone400	1.260	1.216
7	Adipose	0.967	0.970
	PMMA	1.183	1.161

Table 3.4: Features of the rod phantom tissue-equivalent materials: density and rWEPL. The density is provided by the manufacturer and the rWEPL values were measured with the adjustable water-column at HIT.

In physics, the truth is rarely perfectly clear, and that is certainly universally the case in human affairs. Hence, what is not surrounded by uncertainty cannot be the truth.

Richard P. Feynman

4

Data processing methods: Dedicated analysis techniques integrated with Monte Carlo simulations

This chapter describes the analysis methods used to process the transmission-imaging experimental data obtained from the measurements performed in the context of this thesis. Monte Carlo (MC)-simulations strongly support these experimental investigations. The MC imaging-environment used for this purpose has been comprehensively described in Meyer et al. [2017]. This simulated framework, also referred in the following as *in-silico* transmission-imaging system, is being developed as part of an additional PhD thesis (S. Meyer) currently in progress at Ludwig-Maximilians-Universität München, also contributing to the joint project to which this thesis belongs.

The integration of MC-simulations is performed in multiple directions: First of all, as foundation of the image formation process, the channel to WET calibration of the RRD is purely based on simulations (cf. Section 4.1.1). Furthermore, the in-silico transmission-imaging system provides reference projections obtained with extensive acquisition parameters which would be experimentally unnaccesible due to the limited amount of beam-time [Meyer 2015]. This information prior to the experiments serves to assess and decide the imaging variables to be tested. Additionally and most important, the simulated iRADs and iCTs serve as benchmark for comparative quality studies in RP-signal-domain, i.e., the entire discretized BC, and space-domain, which refers to the radiography itself. The image dose evaluation is also MC-based. Simulated images assist to develop and test dedicated processing methods, which are described in Section 4.1.2, to be applied to the experimental data. Last but not least, investigations towards the upgrade of the current imaging prototype are being developed using these simulation tools, as it was mentioned in the previous chapter, namely regarding the reduction of the PMMA-slabs thickness, and the comparison of the RRD performance operated in integration- or list-mode configurations [Meyer et al. 2017].

4.0.1 The FLUKA Monte Carlo code

The FLUKA[A] code is a MC simulation-tool specialized on the representation of the nuclear processes occurring when charged particles propagate and interact with matter, it can determine every radiation process and handles electromagnetic interactions as well, including the ones inherent to ion-beam therapy [Böhlen et al. 2014]. For the latter purpose, FLUKA has a default physics- and transport-settings for hadrontherapy-oriented applications, as activated by the so-called HADROTHErapy input card.

This configuration establishes predefined threshold values for physical processes such as the energy above which explicit δ-rays production occurs, or below which charged particles transport is terminated. Specific applications may be also implemented using suitable user-routines, as it is the case for the complexity of the transmission-imaging system presented in this thesis. Besides providing the simulation core of this investigations, the FLUKA MC-code has been adopted at HIT as computational framework to support the start-up and clinical operation [Parodi et al. 2012b]. Additional applications of this MC-platform in the frame of charged-particle radiotherapy include treatment planning, either as a fully-integrated MC-based TPS [Boehlen et al. 2013; Mairani et al. 2013] or as an assistant tool to provide the ion-beam model to be introduced in the analytic TPS used at HIT [Parodi et al. 2013]. Moreover, FLUKA has found its use in clinically-available range-verification imaging techniques such as PET [Parodi et al. 2012a; Bauer et al. 2013], demonstrating to be a fundamental tool to complement the clinical practice of ion-beam radiotherapy [Bauer et al. 2014].

4.0.2 The in-silico transmission-imaging system

The in-silico transmission-imaging system has been modeled to mimic the experimental setup shown in Figure 3.1 using the FLUKA version 2011.2c.3 with the HADROTHErapy default settings and linked DPMJET and RQMD event generators [Meyer et al. 2017]. The complete simulation environment consists of three main components, as detailed in the following:

Simulation of the primary scanned ion-beam

In order to obtain reliable simulated iRADs and iCTs, an accurate beam model with the same features as the one used experimentally is mandatory. Therefore, the geometry of the beam-line, including the vacuum-window and the BAMS, must be described in detail, since it has a strong influence on the beam shape before it traverses the imaged phantoms. This beam-line information is saved in phase-space files generated for fixed central ion-beams, with 20 million primaries each, positioned at 112.6 cm before the isocenter (phase-space plane, cf. Figure 4.1), right after the *Beam Application and Monitoring System* (BAMS). These files include the beam coordinates (x,y), charge, mass, kinetic energy and the direction cosine of each ion recorded [Tessonnier et al. 2016]. This way, one can make use of the beam features provided by the HIT accelerator without sharing the confidential vendor information about the beam-nozzle.

The phase-spaces can also be used to reproduce the scaning patterns available in the HIT's delivery system. Figure 4.1 represents the simulated irradiation FOV, which is defined as a grid of equally spaced RPs according to the experimental conditions. The irradiation spots at the isocenter (RPs) are achieved by deflecting the simulated beam with origin at the beam

[A] www.fluka.org

scanning syssem, considering that the scanning magnets are located at 650.6 cm before the isocenter, as it is described in Tessonnier et al. [2016] and Meyer et al. [2017].

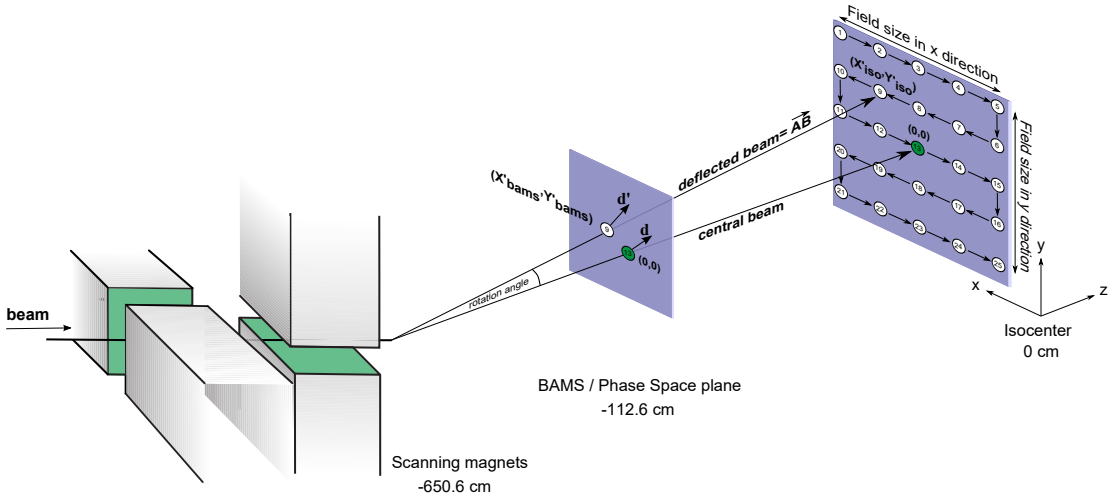

Figure 4.1: The principle of the in-silico active raster scanning at HIT using MC-based phase-space files including the whole beam-line information. Courtesy of Sebastian Meyer in Meyer [2015].

Digitalized phantoms

The phantoms used in this work, described in Section 3.6, were directly modeled in FLUKA according to the known geometry and the manufacturer specifications. This is possible due to the available combinatorial geometry capabilities and the graphical user-interface of the MC-platform, FLAIR[B]. The ionization potential of the compounds, calculated by FLUKA according to the Bragg additive rule, was manually adjusted in order to ensure an agreement with the material rWEPL measurements of better than 0.3% [Meyer et al. 2017].

Multi-channel range telescope simulated implementation

The RRD geometry is modeled by interleaving 3 mm thick homogeneous PMMA absorber plates and 6 mm air gaps. The electrodes of the real PPICs are neglected, however they only constitute a tiny portion of the whole material detector [Meyer et al. 2017]. As it will be detailed later, the density of the PMMA plates is tuned according to the experimentally obtained rWEPL of the RRD.

4.1 Image formation

4.1.1 Radiographic image formation

Imaging system calibration for channel-to-WET conversion

Carbon-ion radiographies are obtained by measuring directly the beam residual-range after traversing the phantom. The RRD-IC with the maximum signal is correlated with the WET value of the imaged object through an appropriate parametrization of the BP position in relation to the beam energy, the target thickness and the RRD-rWEPL determined experimentally. A channel-energy calibration is also necessary prior to the experimental acquisitions in order to select the right beam-energy that takes account of the object dimensions, material density and optimal-functioning channels. As long as the phantom size allows it, using higher energies so

[B] www.fluka.org/flair/

that the BPs fall within distant RRD-channels might favor the reduction of the imaging dose due to the BP remoteness, as it will be exemplified in the following chapter. The retrieval of the phantom WET should be energy independent; therefore, when different energies are used to accommodate various phantom geometries, such calibration is needed.

The channel-WET parametrization is obtained in three steps. First, the energy-channel relation is determined with a series of air-projections at different beam-energies. When no absorbing material is placed between the beam-line nozzle and the RRD, the BP position only depends on the initial beam energy. Higher energies will produce BPs towards the farther side of the RRD. The highest beam energy of the HIT's LIBC whose range falls inside the detector is ∼340 MeV/u; beams with higher energies are not stopped in the RRD anymore. As a second step, the dependence of the BP-position in the RRD channels on the traversed thickness is obtained. Finally, to convert the individual RP information into WET values, the rWEPL of the RRD is required.

The $rWEPL_{RRD}$ can be determined by measuring the residual ranges behind the detector material using a water absorber column of variable thickness and finding the BP position with a movable PPIC, as it is explained in Rietzel [2007]. The rWEPL of the material ($rWEPL_{mat}$) would then be retrieved from the BP shift ($BP_{ref} - BP_{mat}$) resulting from introducing the object of thickness l along the beam-path in front of the detector:

$$rWEPL_{mat} = \frac{BP_{ref} - BP_{mat} + l \cdot rWEPL_{air}}{l}. \tag{4.1}$$

In experimental conditions, the setup is surrounded by air, while vacuum is used as simulation environment. Hence, the term $rWEPL_{air}$ is introduced to account for the replacement of this amount of air when the material of interest is placed. Roughly speaking, 1 m of air produces 1 mm shift in water ($rWEPL_{air} = 0.001$).

In this work, the $rWEPL_{RRD}$, including the entrance and exit windows, PMMA absorbers, electrodes and air gaps therein, has been experimentally determined with the same principle by using an adjustable water column[C], as $rWEPL_{RRD}$ =1.1923. In order to account for this value in the channel-to-WET conversion, the PMMA density of the MC-RRD has been increased from 1.190 g/cm^3 to 1.216 g/cm^3 [Meyer et al. 2017].

The first experimental energy calibration of the RRD was reported by Rinaldi et al. [2013]. The calibration curve was obtained from the mean BP position of 1681 BCs, distributed in 5 mm raster-scan steps over a 200×200 mm^2 FOV, at 19 different beam energies (cf. Figure 4.2)[D]. Recalling the channel-deviation issue reported in Section 3.5.4, the averaged BP location over the whole irradiation-field might not provide the most reliable detector calibration. The individualized channel investigations performed in this work have shown several channel-shift distributions with vertical symmetry about the middle line of the FOV. Therefore, a new experimental energy-calibration has been performed including 88 beam-energies scanned over a 20×15 cm^2 in 1 mm RP-steps. (cf. Section 3.5.4). The FOV has been divided into upper and lower halves to visualize the impact of considering the BPs from one or the other region in the

[C] Peakfinder, PTW, Freiburg, Germany. http://www.ptw.de/peakfinder.html. Thanks to Thomas Tessonnier for his experimental assistance in these measurements.

[D] Thanks to Benedikt Kopp for his contribution to the analysis of this data.

energy calibration (cf. Figure 4.2). This FOV division is only treated as a rough assessment, since the channel-shift patterns might be irregular along the whole RRD.

Furthermore, an energy-channel parametrization obtained with the MC-simulated system [Meyer 2015] is used as the reference which is closest to the expected RRD-calibration. 185 radiographic images at different energies were simulated without additional absorber in front of the RRD, emulating the same irradiation conditions as in the experimental case and reducing the number of primaries per RP to 5000 for computational convenience. The curves are fitted to the semi-empirical Equation 4.2, deduced from typical range-energy curves [Leo 1990], which leads to the fit parameters reported in Table 4.1.

$$BP_0(E) = a \cdot E^{1.75} + b, \tag{4.2}$$

where BP_0 refers to the PPIC that registers the maximum current signal and E is the initial beam-energy.

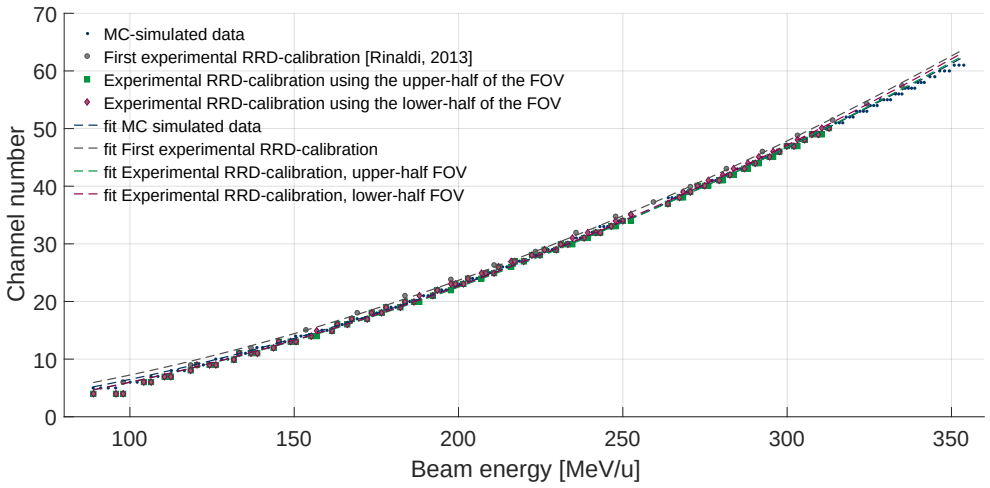

Figure 4.2: Experimental and MC-based RRD energy calibration, showing the BP location within the RRD channels as a function of the initial beam energy. The dots represent the experimental and simulated data while the solid lines correspond to the fitting curve according to the Equation 4.2. The fit-curves accuracy and parameters are reported in Table 4.1. Four different scenarios are shown: a MC-based calibration (blue) is compared to the first experimental calibration obtained by averaging the BP position over the whole FOV (gray), the new experimental calibration considering only the lower- (magenta) and the upper-half (green) of the FOV. The MC-based calibration is selected for use in future channel-to-WET conversions.

Table 4.1: Fitting parameters and goodness of the fit represented by the coefficient of determination R^2 and RMSE values for the four curves in the Figure 4.2, following the fit-function given by Equation 4.2.[E]

Curve to fit	a	b	R^2	RMSE
MC-based	0.0022	-0.408	0.9993	0.4355
First experimental [Rinaldi et al. 2013]	0.0022	0.282	0.9991	0.4783
Experimental, lower-half FOV	0.0022	-1.055	0.9985	0.5315
Experimental, upper-half FOV	0.0022	-1.002	0.9987	0.4975

The parametrization model is in acceptable agreement with the data-sets in the middle of

the curve (150 - 250 MeV/u), which also coincides partially with the energy-range relevant for transmission-imaging purposes. However, extreme energies are not well described by Equation 4.2, especially for the experimental cases. The MC-based calibration is selected for the channel-to-WET conversion of the images produced in the investigations presented in this thesis. This choice is established to avoid the potential uncertainties introduced by the channel inhomogeneities described in Section 3.5.4, and to be consistent in the forthcoming comparative analysis between simulated and experimental images. This decision is also supported by the best RMSE-value of the MC-based energy calibration in Table 4.1. Aiming to improve the quality of the fit along the whole dynamic energy range, the channel containing the BP was also parametrized through a 2nd-degree polynomial function of the form:

$$BP_0(E) = p_1 \cdot E^2 + p_2 \cdot E + p_3, \tag{4.3}$$

with parameters p_1 = 0.0003114 [(MeV/u)$^{-2}$], p_2 = 0.0805 [(MeV/u)$^{-1}$] and p_3 = -5.488.

The polynomial-based calibration slightly improves the goodness of the fit (R^2 = 0.996, RMSE = 0.3216) compared to the exponential approximation and leads to approximately 1% improvement in the channel-to-WET conversion of the tested PMMA stepped-wedge phantom, as it is demonstrated in the Section 5.1.1 for a radiography example acquired with different experimental parameters (cf. Figure 5.1).

As it was mentioned before, the same RRD-calibration procedure has to be performed for the traversed material thickness, i.e. a correlation has to be established between the amount of material penetrated by the beam and the detector channel where the BP is located. The first experimental parametrization was performed by using a PMMA double-wedge. The different thicknesses of the phantom along the wedge-shape were covered in 1 mm steps while the BP-location was obtained from the average of 11 BCs, as it was reported in Rinaldi et al. [2013]. The *in-silico* calibration for the material thickness follows the same principle [Meyer 2015], although considering PMMA slabs instead of a wedge-geometry. The beam energy is fixed to 299.94 MeV/u and 99 mm of absorber PMMA are positioned in 1 mm steps in front of the RRD-model. A linear dependence of the BP position on the PMMA crossed depth is expected and it is parametrized through c and d with a linear fitting equation of the form:

$$BP^{ch}(\Delta x) = c \cdot \Delta x + d, \tag{4.4}$$

where Δx stands for the longitudinal dimension of the PMMA absorber, BP^{ch} is the channel where the BP is located and the fitting parameters $c = -0.3256 \pm 0.0076$ and d = 47.38 are consistently obtained from the MC-based calibration conditions. The accuracy of these fitting parameters is concluded from the known thickness of the RRD inner-slabs (ideally $-c^{-1}$ = 3 mm) and the BP position for the reference beam-energy used for the energy calibration (299.94 MeV/u) when no absorber material is crossed, BP_0 = 47.30, obtained from the fit to Equation 4.2, expressed in terms of channel number [Meyer 2015].

In order to obtain the individual RP information of the raw-projections in WET terms for and arbitrary energy (E), Equations 4.2 or 4.3 and 4.4 must be merged.

The object thickness in terms of RRD material is determined experimentally as:

$$\Delta x = \frac{BP^{ch}(E) - BP_0(E)}{c}, \tag{4.5}$$

where $BP_0(E)$ for any initial beam-energy is given by Equation 4.3.

The WET map of the projected target is finally determined pixel-wise with the aforementioned rWEPL of the RRD, which is obtained experimentally (cf. Section 4.1.1). The RRD-channel that contains the BP is converted into the WET of the target, scanned with a beam of initial energy E, using the empirical exponential approximation 4.2, as:

$$\begin{aligned} WET_{exp} &= rWEPL_{RRD} \cdot \frac{BP^{ch} - a \cdot E^{1.75} - b}{c} \\ &= -1.1923 \cdot 3 \cdot (BP^{ch} - 0.002182 \cdot E^{1.75} + 0.4511), \end{aligned} \tag{4.6}$$

or by using the polynomial approximation 4.3, as:

$$\begin{aligned} WET_{poly} &= rWEPL_{RRD} \cdot \frac{BP^{ch} - p_1 \cdot E^2 - p_2 \cdot E - p_3}{c} \\ &= -1.1923 \cdot 3 \cdot (BP^{ch} - 0.0003157 \cdot E^2 - 0.07883 \cdot E + 5.341). \end{aligned} \tag{4.7}$$

4.1.2 Data post-processing in the signal domain

Bragg peak decomposition

Due to the finite carbon ion-beam spot-size (∼3 - 4 mm FWHM (in air at isocenter) for the beam-energies used in this work), when the beam encounters density interfaces or material inhomogeneities along its path, the BC signal will register multiple BPs that contain mixed WET information [Rinaldi 2011]. The edge between two materials relative to the beam position will determine the measured signal containing two or more BPs, depending on the beam size and proximity of the boundaries. The cause of a biased WET-value towards denser materials is the accumulated signal of the lighter-material BC-plateau, resulting in a larger signal amplitude for the more proximal BP encoding larger WET thicknesses.

Hence, the maximum-identification criteria, relying on the assumption that the highest BP corresponds to the dominant contribution, might assign false WET values to those RPs because this assumption does not always remain valid. Concretely, this issue is specific to integration-mode RRD configurations. This matter will be exemplified for the sharp tissue-interfaces found in the slab phantom images presented in Section 5.2.1.

As solution, the integrated signal can be described as a linear combination of pristine BPs, through the so-called Bragg Peak DecompositionBragg Peak Decomposition (BPD) strategy[F], which disentangles each individual component of the mixed BC and identifies the main WET contribution [Krah et al. 2015]. The decomposed BCs are chosen from a MC-based Look-Up Table (LUT) (cf. Figure 4.3) that contains single BCs organized according to an increasing amount of material traversed in steps of 0.1 mm of PMMA. The weights of the BP components

[F] Processing method developed by S. Meyer

are then derived from the solution of a least-squares Euclidean-distance minimization problem [Meyer et al. 2017].

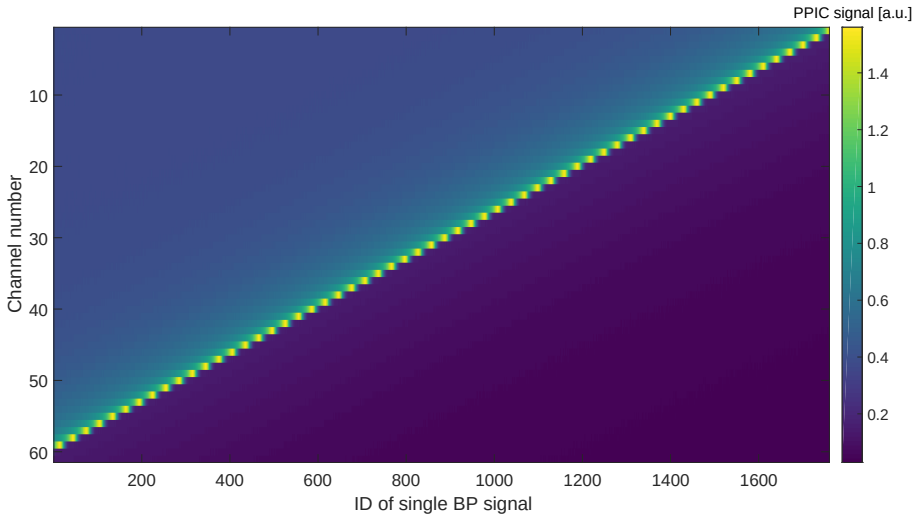

Figure 4.3: Example of the MC-based LUT for the beam-energy equal to 344.94 MeV/u displaying the spectrum of pristine BCs used for the BPD method. Courtesy of Sebastian Meyer.

Figure 4.4a depicts the effect of the BPD processing method on an individual RP experimental signal. In this particular example, the raw signal (magenta) shows a double-peak effect occurring when the beam traverses a material boundary, which would lead to a wrong maximum identification if no BPD is applied.

Monte Carlo-based prior-knowledge for image-quality enhancement

MC prior-information of the same imaged object can be used to enhance the quality of the experimental images by regularizing the signal on a RP-basis[G]. This data processing makes the discretized BC more robust, allowing to overcome noise-related artifacts like channel-coupling and/or under-responsive channels that may yield a wrong BP position determination (cf. Figure 4.4b). The procedure is performed as follows:

1. The simulated iRAD (MC-iRAD) of the image to be enhanced is obtained with the same acquisition parameters used in the experimental configuration.

2. The decomposition of the MC-iRAD using the BPD technique is performed in a RP-basis.

3. For each pixel (RP), the algorithm encompasses a cluster of RPs defined by an adjustable neighborhood (typically 10 pixels = 1 cm) and adds-up the re-binned weight factors generated by the BPD process. Thereby, each RP also contains the decomposition information of its surrounding, enabling a tolerance range for a potential misalignment between the MC-iRAD and the experimental projection (Exp-iRAD).

4. The BPD strategy is applied to the Exp-iRAD. This process is performed based on a weighted-LUT, which is obtained by multiplication of the original LUT and the summed-up weighting-vectors obtained in step number 3. The result is a BP-structure-preserving

[G] idem.

smoothing of the RP-signal, achieved by neglecting the LUT selected solutions that are not present in the MC-iRAD BPD. In consequence, signal spikes due to noise resonances or channel-coupling are discarded by the decomposition procedure, thus revealing a more correct BP identification and optimizing the whole iRAD.

5. The enhanced iRAD is generated by selection of the RRD channel with maximum weight (or single BP ID in the horizontal axis of Figure 4.3), i.e. the principal WET value.

Figure 4.4b shows the incorporation of a MC priori-knowledge to avoid noise-related signal corruption effects such as the channel-coupling occurring after the expected BP, which might yield to a wrong WET-value if only the maximum identification criteria is used.

Figure 4.4: Effect of advanced post-processing methods applied to individual BCs.

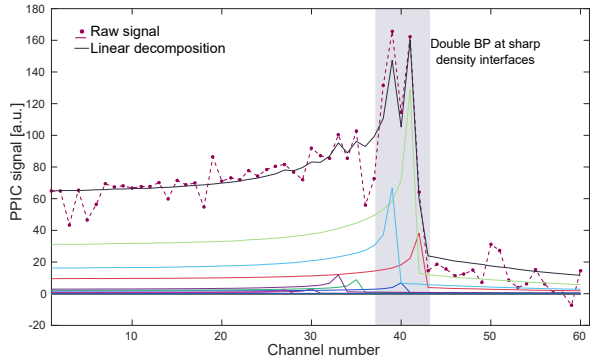

(a) BC after BPD processing to resolve double BPs occurring at sharp-density interfaces.

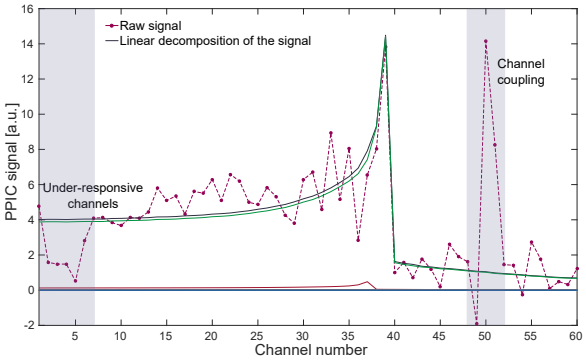

(b) BC after MC-based prior BPD processing to solve noise fluctuations.

4.1.3 Tomographic image reconstruction: Simultaneous Algebraic Reconstruction Technique

The 3D-rWEPL distribution of the imaged objects is reconstructed from a set of different angular projections, using the 2D-Simultaneous Algebraic Reconstruction Technique (SART) proposed by Andersen and Kak [1984], on a slice-by-slice basis.

The CT-Algebraic Reconstruction Technique (ART) is an inverse-problem solution based on the tomography concept that the cross-section of an object, considered as an array of unknowns, can be reconstructed from the projected data. Namely, for a given pixelated image, the value of a single projection line is the sum of all the pixels (containing the rWEPL information) that the beam passes through on its way along the object (cf. Figure 4.5).

Algebraic methods require the knowledge of the beam paths that connect the corresponding source and detector positions [Kak and Slaney 1988]. This condition is fulfilled by carbon-ion beams, due to their minimal MCS inside and outside the imaged object. In principle, one can assume straight carbon-ion trajectories (cf. Section 7.2.2 for an experimental study in this matter). The fraction of the pixels that each projection line crosses in the image is thus described by a system of linear equations which can be solved iteratively (cf. Equations 4.11), as it is detailed below.

This image $f(x, y)$ is divided by a squared grid like the one depicted in Figure 4.5, where f_j refers to the constant value in the jth pixel. The projection lines p_i include the separation

between beams (shaded in green) and contains the integral of the rWEPL along the phantom.

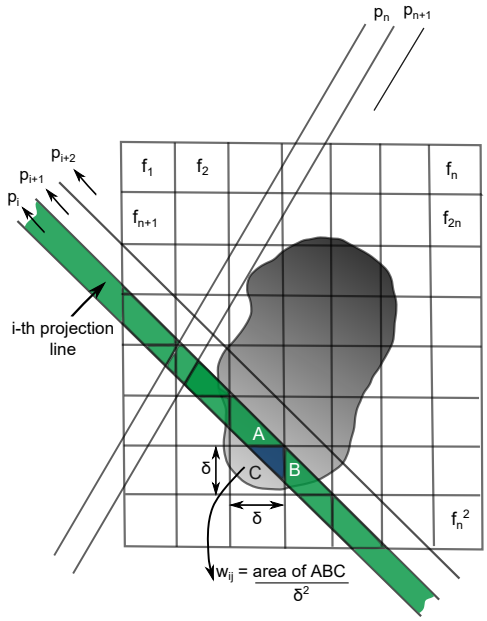

Figure 4.5: Schematic representation of the CT-ART principle. The green shaded area represents one projection line (beam) and the w_{ij} is the weight of the contribution of jth pixel to the ith projection line p_i. Redrawn from Kak and Slaney [1988].

For a M number of beams, the projection lines are expressed in terms of the weighting factors that are equal to the fractional area of the jth pixel intercepted by the ith projection line:

$$p_i = \sum_{j=1}^{N} w_{ij} f_j, \qquad i = 1, 2, ..., M, \tag{4.8}$$

where N is the number of pixels in the image and M is the total number of beams in all the projections. The reconstructed volume is then the solution of this system matrix of M equations:

$$w_{11} f_1 + w_{12} f_2 + \cdots + w_{1N} f_N \quad = p_1 \tag{4.9}$$

$$\ddots \tag{4.10}$$

$$w_{M1} f_1 + w_{M2} f_2 + \cdots + w_{MN} f_N \quad = p_M \tag{4.11}$$

The Kaczmarz method [Kaczmarz 1937] allows to solve algebraic equations by representing each of them as a hyperplane, where the unique solution of the equation set is the intersection of all these hyperplanes in one single point, i.e. the reconstructed image, as it is represented in the Figure 4.6 (left panel) for the case of two unknowns.

Starting from an initialization guess, the vectorial solution $\vec{f}(0)$ is projected onto the first equation, the resulting solution is then projected onto the second equation, continuing the iterations until the convergence is reached. In the final step, when $\vec{f}^{(i-1)}$ is projected on the

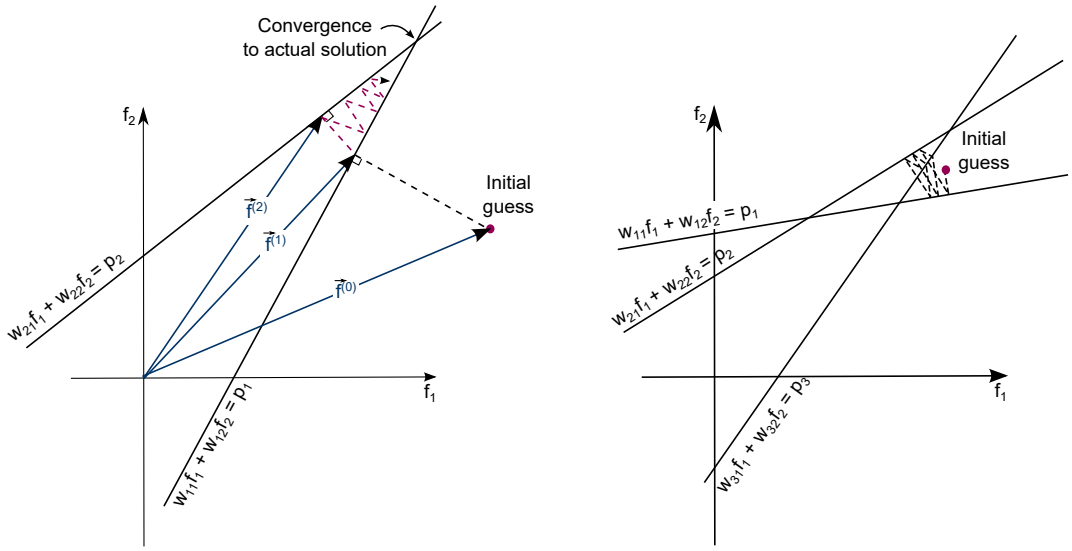

Figure 4.6: Representation of the iterative Kaczmarz method to solve a two-variable system of equations. On the left panel, the initial guess is projected onto the first equation and re-projected onto the second one, successively until the unique solution is found. When the system is affected by noise (right panel), the number of equations is greater than the number of variables to find, i.e. no unique solution (single point) exists. Redrawn from Kak and Slaney [1988].

last hyperplane, the solution $\vec{f}(i)$ can be expressed as:

$$\vec{f}^{(i)} = \vec{f}^{(i-1)} - \frac{\vec{f}^{(i-1)} \cdot \vec{w}_i - p_i}{\vec{w}_i \cdot \vec{w}_i} \vec{w}_i, \tag{4.12}$$

where $\vec{f}^{(i)}$ and p_i contain the information of all pixels and beams, respectively.

The greatest computational challenge of this reconstruction method is the retrieval of the large amount of weighting coefficients w_{ij}. This issue is overcome by transforming Equation 4.12 into another approximation, by means of the following steps:

1. To reduce errors in the approximation of beam integrals of a continous image by finite sums along discrete projection points, the traditional pixel basis is interpreted as combination of bilinear elements:

$$f(x,y) \approx \hat{f}(x,y) = \sum_{j=1}^{N} g_j b_j(x,y), \tag{4.13}$$

where g_i's are the coefficients that describe the image $f(x,y)$ in terms of the basis functions $b_j(x,y)$. The projection line can then be written as:

$$p_i = \sum_{j=1}^{N} g_j R_i b_j(x,y) = \sum_{j=1}^{N} g_j a_{ij}, \tag{4.14}$$

where R_i relates the continuous image with its corresponding discrete projection points, and a_{ij} is the integral of $b_j(x,y)$ along the ith beam. Thus, $R_i b_j(x,y)$ represents the areas of intersection of the beam with the pixels.

2. The former approach still implies a large computational cost, which is reduced by approximating the overall beam integral by a finite sum of equidistant points. For a circular

reconstruction region, zero weights are assigned to the first and last pixels on the individual beams to maintain the original length of the object.

3. Finally, to further reduce the amplitude of the image noise, the correction terms are *simultaneously* applied for all the beams in one projection, instead of sequentially update pixel-corrections on a beam-by-beam basis, as it is performed in the ART. This new approach gives its name to the SART.

   Following this principle, in terms of the redefined SART notation, the reconstructed image yields a special case of Equation 4.12 that can be expressed as:

$$g_j^{(k+1)} = g_j^{(k)} + \frac{\sum_i \left[a_{ij} \frac{p_i - \vec{a}_i^T \vec{g}^{(k)}}{\sum_{j=i}^{N} a_{ij}} \right]}{\sum_i a_{ij}} \tag{4.15}$$

   where the i-summation is over the beams intersecting the jth pixel.

In the presence of noise, as it is the case of the data handled in this work, frequently there is no an unique solution. This is represented as an over-determined equation system in which some of the extra equations are corrupted by noise. As it is shown in the right panel of Figure 4.6, a sole convergence does not exist, the solution rather oscillates in the neighborhood of the hyperplanes intersection [Kak and Slaney 1988]. In such cases, a stopping criteria is necessary to determine the number of iterations. For the reconstructed experimental and simulated iCTs in this thesis, a constrained change of the data fidelity per iteration number n was used, as it is reported in Meyer et al. [2017]. The limiting parameter, ϵ, was adjusted according to the datasets presented in this work. For the iCT reconstruction of the slab phantom, $\epsilon = 0.6 \times 10^{-4}$ was used for both, the raw and post-processed experimental data, whereas the simulated iCTs (with and without BPD) were obtained by stopping the iterations with the parameter $\epsilon = 0.8 \times 10^{-4}$. As for the iCT of the cylindrical phantom, the best image accuracy-noise trade-off was found with $\epsilon = 1 \times 10^{-4}$ for the experimental iCTs (with and without post-processing) and $\epsilon = 4 \times 10^{-4}$ for the simulated iCTs (with and without post-processing).

The number of angular projections needed for the tomographic reconstruction of the imaged phantoms depends on the object dimension to cover (FOV) and the RP step-size (spatial sampling, Δx). The angular sampling $\Delta\phi$ must satisfy the Nyquist theorem to prevent image distortion due to frequency aliasing.

Figure 4.7 represents the relationship between the spatial sampling and the angular sampling necessary to determine the number of projections. The former occurs in the spatial domain and is given by $n_x = {}^{FOV}/_{\Delta_x} + 1$. The latter takes place in the frequency or Fourier domain, where the spatial frequencies are expressed by $\Delta_v = {}^{1}/_{(n_x \Delta_x)}$. The maximum spatial frequency that can be represented discretely is $\Delta_v = {}^{1}/_{(2\Delta_x)}$, hence, following the Figure 4.7, the angular sampling that includes all the frequencies is:

$$\Delta_\phi = \frac{\Delta_v}{1/(2\Delta_x)} = \frac{2}{n_x} = \frac{2\Delta_x}{FOV + \Delta_x}. \tag{4.16}$$

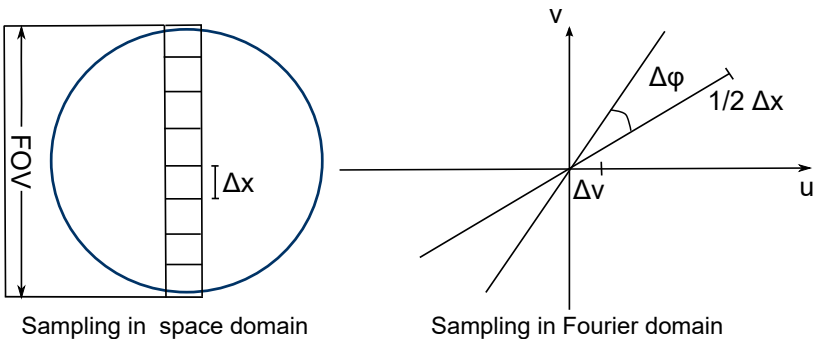

Figure 4.7: Spatial and angular sampling to determine the number of required projections for the tomographic reconstruction.

In consequence, the total number of projections for a 180° coverage is:

$$n_\phi = \frac{\pi}{\Delta_\phi} = \frac{\pi}{2} n_x = \frac{\pi}{2} \cdot \frac{FOV + \Delta_x}{\Delta x}. \tag{4.17}$$

In a typical case of a tomography with a 15 cm FOV length, imaged with RPs spaced by 1 mm, $n_\phi \approx 237$ projections are required, which corresponds to an angular sampling of $\sim 0.8°$. Larger number of projections would be redundant and would increase linearly the image dose. Conversely, a 2 mm RP-separation would require a coarse angular sampling, yielding a further dose reduction, as it will be shown for the middle-dose slab-phantom iCT presented in Chapter 6.

4.2 Overall image-quality and accuracy assessment

4.2.1 Overall image-quality quantification

The Normalized Root Mean Squared Deviation (NRMSD) is used to globally evaluate the quality of the experimental or simulated images, when compared with their ground truth. The true images are obtained from the known geometry and precisely measured rWEPL of the imaged phantom materials (cf. Section 4.1.1). Thus, the NRMSD is derived from the Root Mean Squared Deviation (RMSD):

$$RMSD = \sqrt{\frac{\sum_{i=1}^{n} (y_i^{true} - y_i)^2}{N}}, \tag{4.18}$$

where the mean squared difference is calculated for all the image pixels. w_i^{true} is the expected WET or rWEPL value and y_i is obtained from the experimental or simulated iRAD or iCT. The range of the true WET-values in the image ($y_{max}^{true} - y_{min}^{true}$) is used to normalize the RMSD and make easier the comparison between images with different WET scales:

$$NRMSD = \frac{RMSD}{(y_{max}^{true} - y_{min}^{true})} \tag{4.19}$$

4.2.2 Regional image accuracy assessment

The image accuracy in terms of the retrieval of the WET distributions for the iRADs and the rWEPL for the iCTs is assessed by the ROI-specific Relative Error (RE) and the Interquartile

Range (IQR) (Interquartile Range):

$$RE = \frac{\hat{y} - y_{ROI}^{true}}{y_{ROI}^{true}}, \tag{4.20}$$

where $\hat{y}$ is the median WET or rWEPL value over all the pixels contained in the defined ROI of the projection and y_{ROI}^{true} stands for the expected value within the same area. The median is preferred over the mean simply because the latter might be greatly affected by data outliers. In the spatial domain of the image, outliers are usually noise indicators. The IQR is the difference between the first (25th quantile) and third (75th quantile) quartiles; it measures the width of the interval that contains 50% of the pixels in the ROI. By principle, in homogeneous areas of the image, no variability of the WET is expected, however this is often not the case in experimentally acquired images due to the multi-source noise. The IQR of a ROI will be zero if, at least, the middle 50% of the RPs hold the same WET. These statistical indices represent a robust evaluation of the central tendency of the WE-values in the defined ROIs and the spread or skewness of its distribution.

The impact of the noise and the potential errors introduced by multiple-BPs in the overall image-quality is also reflected in the NRMSD quantification introduced before.

The user-defined ROIs are specifically designed according to the phantom geometry. In the radiography case, two phantoms were evaluated, the PMMA stepped-wedge and the 0°-projection of the tissue-like slab-phantom. The geometry of both phantoms includes sharp material-interfaces, which were avoided in the RE evaluation to evade inaccuracies originated by multi-peak BCs. For each of the levels in the stepped-wedge phantom, 3 mm (3 pixel rows) were cropped form each step transition, i.e. giving a margin of 6 mm in each boundary for the finite beam-size that might be also slightly enlarged due to scattering effects along its trajectory (cf. Section 5.1.1). Two mm were trimmed (2 pixel lines for $\Delta_{RP} = 1$ mm or 1 pixel line for $\Delta_{RP} = 2$ mm) from each side of the interfaces encountered in the slab phantom (cf. Section 5.2.1).

For the tomography case, the image accuracy is characterized by the RE using the median value and the IQR of the obtained rWEPL distributions evaluated in different-shape ROIs. For the slab phantom, rectangular ROIs covering 47.5% of the homogeneous tile were considered; while circular regions covering 64% were used for the cylindrical phantom with tissue-equivalent rods. This method has been implemented for simulated iCTs [Meyer et al. 2017] and applied to the experimental data in this work.

4.3 Image dose exposure assessment

As it was introduced in section 2.1.6, the dose received by the phantom in each RP can be estimated by Equation 2.21. However, it was shown by Marcelos [2014] that using this approach, the dosage is overestimated by up to 5%. Therefore, the imaging dose values presented in this thesis are solely obtained with MC simulations. The local dose deposition within the phantom is scored based on a 3D-cartesian grid with a voxel size of 1 mm^3. The dose deposition is then given by the median value and the IQR for a central slice[H].

The dose might vary slightly due to the different densities traversed by the ion-beam. High-

[H] Values obtained with the MC-framework, courtesy of S. Meyer

density equivalent-tissues, leading to large WET-values, may display dose deposition from the rise of the ionization towards the BP, if the beam-energy is not sufficiently high to cover the imaging target only with the plateau region of the BC. These exceptional cases will be addressed in the results and discussion part (cf. Chapter 5).

Part III.
Results and discussion: Ion-based imaging

I would rather have questions that can't be answered
than answers that can't be questioned.

Richard Feynman

5 Ion-based radiography

As was pointed out in Section 2.4, ion-beam therapy may benefit from the use of iRADs and iCTs at different treatment stages. This chapter focuses on obtaining radiographic images of various phantoms at clinical dose-levels with the current imaging system. iRADs can support the treatment-planning phase, by complementing the HU-rWEPL LUT. Likewise, iRADs at the treatment site can tackle issues related to patient positioning, anatomical changes and ion-range uncertainties in the course of the therapy.

The image-formation process to generate the iRADs has been described in the previous chapter, Section 4.1.1 and the imaged phantoms were introduced in Section 3.6. In all radiographies, each pixel contains the principal WET information of the traversed material by the ion-beam in the corresponding RP.

5.1 Homogeneous phantom

5.1.1 PMMA stepped-wedge

The PMMA stepped-wedge described in Section 3.6.1 has been used in this work for radiography studies. The phantom positioning adopted to obtain the following projections is as sketched in Figure 3.38, with the carbon-ion beam impinging from left to right. This particular arrangement allows to investigate the performance of the RRD on retrieving the wedge WET-map of the well-known phantom-thickness variation in the beam-direction, that might be strongly affected by the innate RRD granularity. In this position, the phantom's longitudinal dimension varies in steps of 7 mm, which might be challenging to be fully resolved due to the intrinsic coarseness of the experimental data, limited by the thickness of the inner PMMA-plates of the RRD. Furthermore, since sharp-edges are present in the phantom geometry, multiple BPs due to the finite beam-width, as it was explained in Section 4.1.2 are also expected. Other experimental factors that might influence the image-quality on the BC-signal or on the spatial domain are also explored in this section.

Aiming at studying the experimental variables that can lead to substantial image artifacts, the iRADs were acquired by varying several parameters (cf. Chapter 3), namely at two different initial beam-energies, two internal HV values and high and medium dose-schemes. The various experimental configurations are summarized in Table 5.1; each experimental acquisition has been labeled with an ID (C1 to C5), and the beam-energy, amount of primaries per RP and HV are listed, too. Additionally, the lower-dose iRAD has been processed with the prior-BPD technique described in the previous chapter. All the exemplary projections of the stepped-wedge phantom presented here were obtained with RP steps of 1 mm and cropped to a FOV of 116×81 mm^2. The nominal dose was evaluated as described in Section 4.3. It is important to place an emphasis on the fact that the dose calculation accounts for all the deposited ions per RP. Nevertheless, due to the actual readout-system poor performance on adapting to the beam-fluctuations, the fraction of detected ions is considerable lower (cf. Section 3.4.4).

Table 5.1: iRADs experimental configurations, dose evaluation and overall quality assessment of the PMMA stepped-wedge phantom. The image formation column refers to the strategy used to retrieve the WET maps: Maximum-signal identification (Max.) or BPD. If a further data post-processing technique is applied it is also stated in the corresponding contiguous column.

ID	Energy [MeV/u]	FWHM [mm]	ions/ RP	Dose [mGy]		HV	Image formation	Processing	NRMSD Poly. fit	NRMSD Exp. fit
				median	IQR					
C1	339.80	3.7	5000	9.430	0.198	200	Max.	-	0.0982	0.1091
C2	330.48	3.7	5000	9.900	0.304	200	Max.	-	0.1353	0.1395
C3	330.48	3.7	5000	9.900	0.304	100	Max.	-	0.1948	0.1990
C4	330.48	3.7	1000	1.984	0.105	200	Max.	-	0.2682	0.2703
C5	330.48	3.7	1000	1.984	0.105	200	BPD	prior-BPD	0.0440	0.0422

In order to quantify the impact of the RRD energy-calibration used to retrieve this phantom's WE-geometry and the ones forthcoming, the WET-maps of the stepped-wedge were obtained with both, exponential and polynomial approximations (cf. Equations 4.6 and 4.7) and compared RP-wise. In general, the exponential calibration, for the considered energies, produces larger WET-values all over the radiography. The last two columns of Table 5.1 show the overall image-quality of the iRADs obtained with both energy-calibrations, supporting that the WE-images retrieved with the exponential parametrization slightly increase the NRMSD in most of the cases. Figure 5.1 displays the percentage NRMSD difference between the iRADs obtained with both channel-to-WET conversions. Except for the post-processed image, on average, the exponential-fit results in ∼0.5% larger discrepancy relative to the polynomial-fit. This effect is pronounced in the high-energy projection (C1), which differs by 1.1%, coinciding with the poor performance of the exponential approach on parametrizing the BP position within the RRD for extreme energies of the therapeutic range (cf. Figure 4.2). In contrast, the middle-dose (1000 ions/RP) iRAD that has been post-processed (C5) and recovered with the exponential calibration decreases the NRMSD to a small extent relative to the polynomial estimation.

Based on these findings, the MC-based polynomial parametrization is favored over the exponential one for the subsequent images produced in this work. The simulated calibration is

chosen for consistency in the comparative analysis between measured and simulated images. The stepped-wedge iRADs (Ground truth and C1 to C5) corresponding to the Table 5.1 are displayed in Figures 5.3 and 5.8.

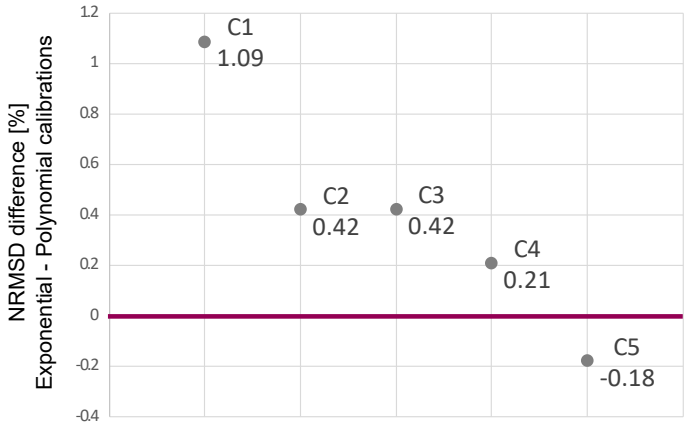

Figure 5.1: NRMSD difference (in percentage) between the iRADs resulting from both exponential and polynomial channel-to-WET calibrations.

The radiography accuracy in terms of WET retrieval is evaluated in a ROI-basis. All the projections of the stepped-wedge are divided in six different levels (L1 to L6) or steps, starting from the top to the bottom of the FOV and avoiding two pixels at each edge of the sharp boundaries. This choice allows to keep inaccuracies due to multiple-BPs or phantom misalignment out of the ROI assessment. The WET RE and IQR with respect to the expected values of the six steps obtained with all the experimental configurations are collected in Figure 5.2. As visual aid of this outcome, selected profiles along the phantom vertical-axis are shown in Figure **??**.

The following sections discuss in detail the effect of different experimental variables on the image-quality and WET recovery accuracy.

Image-quality and -accuracy dependence on initial beam-energy

Figure 5.3 exhibits the homogeneous stepped-wedge phantom iRADs acquired with a 330.48 MeV/u (Figure 5.3c) and a 339.80 MeV/u ^{12}C-ion beam (Figure 5.3b), both of 3.7 mm FWHM, in comparison to the calculated ground truth (Figure 5.9a). Several features can be noticed at a glance: The experimental iRADs highly agree with the ground-truth image in terms of geometry-definition and WET similarity. On one hand, the iRAD acquired with the highest energy (C1) exhibits more random noise, specifically on the top (L1) and bottom (L6) wedge-levels. Consecutive pixels that form horizontal lines of wrongly allocated BPs, typically assigned with a distinct WET than the neighbor pixels, appear in consequence of the pick-up noise frequencies explained in Section 3.5.3. Since they are time-dependent, they follow the beam scanning-sequence and its length is linked to the period of the noise resonance. They have been kept in the raw images only for explanatory purposes. However, a double-constraint algorithm in the space domain, based on the detection of vertical intensity gradients and horizontal number of occurrences, has been applied to detect such artifacts and skip them in a row-basis; particularly for iCTs slice-selection, in order to avoid noise propagation in the reconstructed image (cf. Chapter 6). On the other hand, the projection obtained with the lower energy (C2)

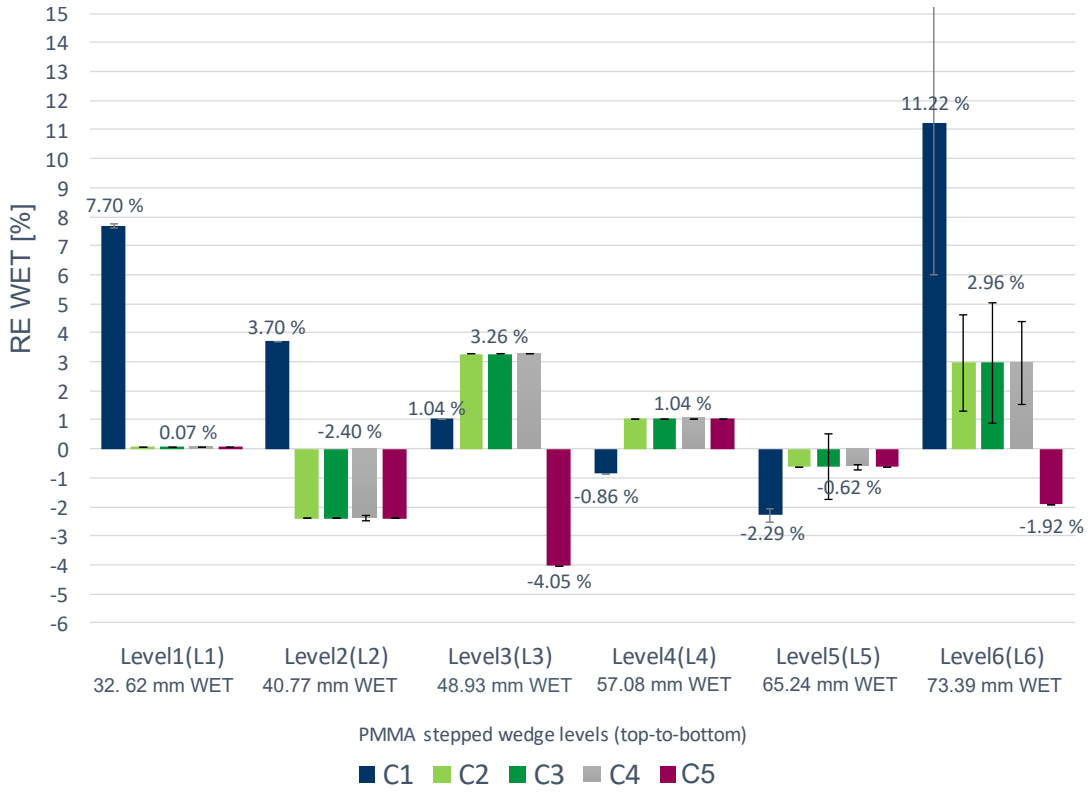

Figure 5.2: Bar plot of the radiography WET-RE of the different depth levels of the PMMA stepped-wedge phantom. The IQR of each configuration is indicated as error bars and serves to represent the spread of the WET-values in case of image-inhomogeneities (cf. Section 4.2.2).

was more affected by pick-up-noise line artifacts than random salt-and-pepper noise visible in C1. The overall image-quality (NRMSD) of these two radiographies, which only vary in the initial beam-energy used, differs by 3.7% (cf. Table 5.1).

For this geometry, some wedge-steps are more prone to WET uncertainties, depending on the initial beam-energy of choice and the resulting BP location. Generally speaking, the configuration C2 has five out of six levels with a RE under $\pm 3\%$, while irradiating the same phantom with a higher energy (configuration C1) increases the WET-RE in four steps of the wedge. For instance, the first and last levels of the higher-energy iRAD reveal the worst WET-RE (cf. Figure 5.2, blue bars of L1 and L6), which is also evident in the vertical profiles compared in Figure 5.4. In such particular stepped geometry, the energy selection might thus improve (or worsen) drastically (up to $\sim 8\%$ in L6) the WET-accuracy of certain ROIs due to the position of the detected BPs within the RRD-channels. As explained in Section 4.2.2, the amount of noise (image inhomogeneity) affecting the ROIs is illustrated by the IQR of the WET distribution, indicated by the error bars in Figure 5.2. Comparing the wedge-levels L1 and L6, one notices that although both ROIs show a significant RE, the latter step is definitely more noisy, showing a larger IQR for both the high- and low-energy configurations (C1, C2 and C3). Furthermore, in the step number 6 of the high-energy iRAD (cf. Figure 5.3b), most of the pixels exhibit a wrong WET value, hence the highest RE-bar. Nonetheless, in the same step of the 330.48 MeV/u ^{12}C iRAD (cf. Figure 5.3c) the IQR increases considerably, reflecting the inhomogeneity of the WET-values within this ROI (cf. Figure 5.2).

Figure 5.3: High-dose PMMA stepped-wedge phantom radiography acquired with two different beam-energies in comparison with the iRAD ground truth.

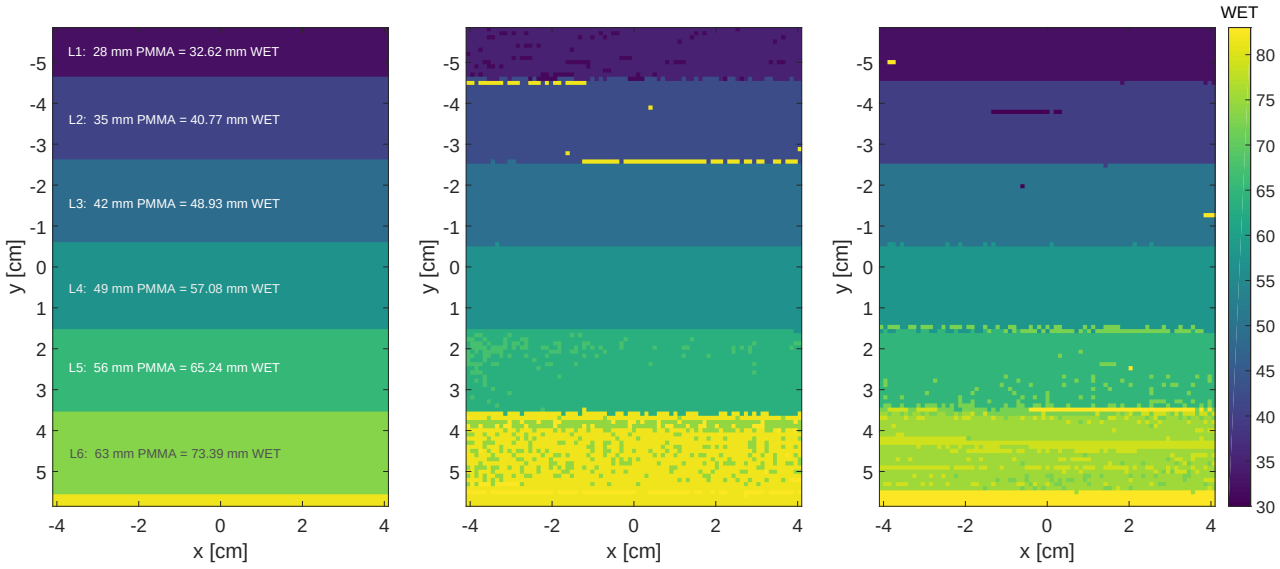

(a) Calculated WE ground truth of the PMMA stepped-wedge phantom.

(b) C1. High-dose radiography obtained with a 3.7 mm FWHM, 339.8 MeV/u ^{12}C-ion beam. HV = 200 V.

(c) C2. High-dose radiography obtained with a 3.7 mm FWHM, 330.48 MeV/u ^{12}C-ion beam. HV = 200 V.

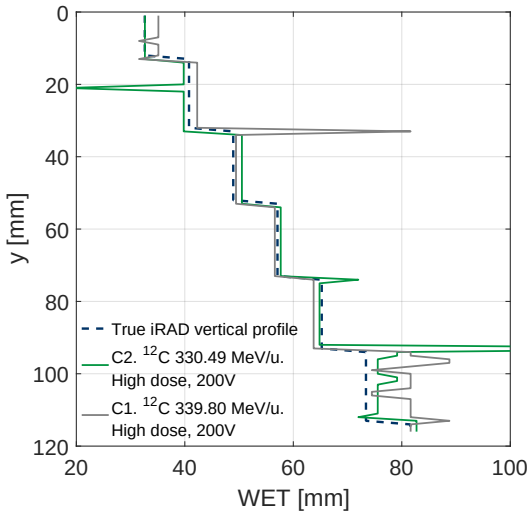

Figure 5.4: Single-RP profiles, along the vertical central axis, obtained with a 3.7 mm FWHM, ^{12}C 330.49 MeV/u and 339.80 MeV/u high-dose iRADs. The expected vertical profile is displayed as reference.

Figure 5.6 exhibits this fact with two comparative pairs of BCs converted to WET by Equation 4.7, extracted from the wedge-steps L1 (cf. Figure 5.6a) and L4 (cf. Figure 5.6b) acquired at 339.8 MeV/u and 330.48 MeV/u. These levels were selected relying upon two ROIs exhibiting the best and worse cases in terms of SFR, for the higher-energy iRADs. The Signal to Fluctuation ratio(SFR) maps displayed in Figures 5.5a and 5.5b illustrate these extreme scenarios with blue and red shades, respectively. As mentioned before, signal quality metrics like the SFR may reveal individual BC features which are not evident in the WE-iRAD.

Inspecting the BCs of the first level (L1) in more detail (cf. Figure 5.6a), it becomes appar-

Figure 5.5: SFR maps. Image-quality dependence on initial beam-energy and dose.

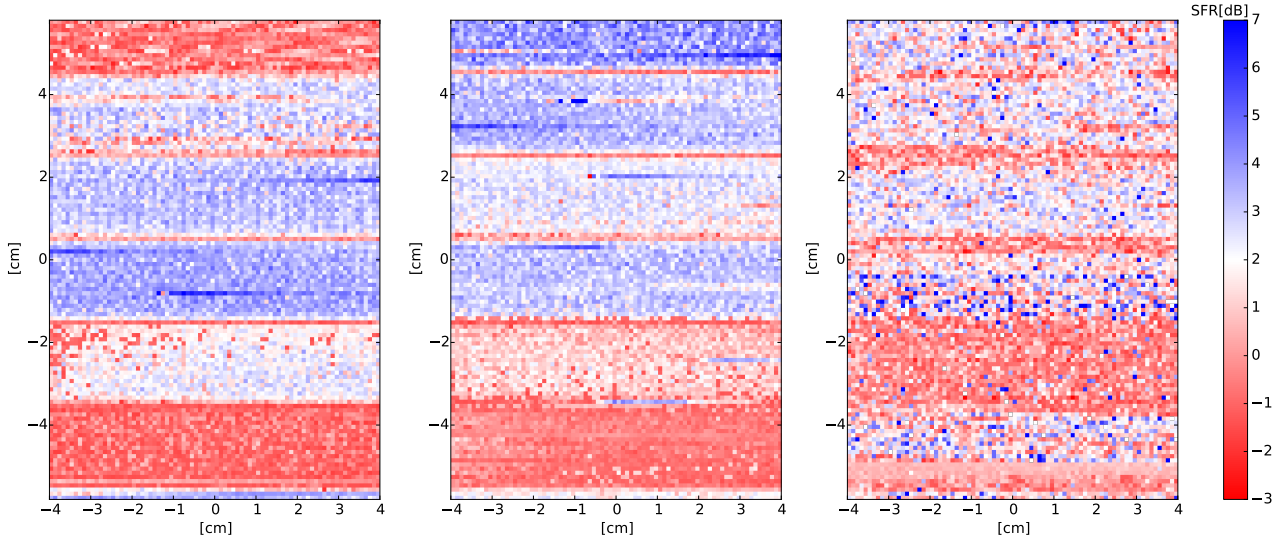

(a) C1. SFR-map of the High-dose iRAD obtained with a 3.7 mm FWHM, 339.80 MeV/u ^{12}C-ion beam. HV = 200 V.

(b) C2. SFR-map of the High-dose iRAD obtained with a 3.7 mm FWHM, 330.48 MeV/u ^{12}C-ion beam. HV = 200 V.

(c) C4. SFR-map of the Middle-dose iRAD obtained with a 3.7 mm FWHM, 330.48 MeV/u ^{12}C-ion beam. HV = 200 V.

ent that the BP of higher energy falls exactly in the middle of two channels, leading to the simplified case given in the Figure 3.36. In fact, the actual BP position is missed and instead, a rising point is identified as a maximum in a previous channel. This particular issue is unavoidable when relying on simple maximum identification approaches, since it has its origin in the detector granularity and beam-energy selection. The discretized BC also have a reduced peak-to-plateau ratio, which increases the sensitivity to inaccuracies due to signal-corruption by noise fluctuations.

On the other hand, a couple of BCs of the fourth step (L4) are selected to examine two ROIs, from different energy irradiations, that share similar SFR-values. From the blue-shaded SFR-scale, one can rely on a stable BP-location and minimal-distortion BC-shapes to correctly determine the channel with the maximum signal, as figure 5.6b illustrates.

Figure 5.6: Single-RP BCs of the stepped-wedge iRAD obtained with two different energies and extracted from two levels of the imaged phantom: L1 (worst-case scenario, left panel) and L4 (best-case scenario, right panel).

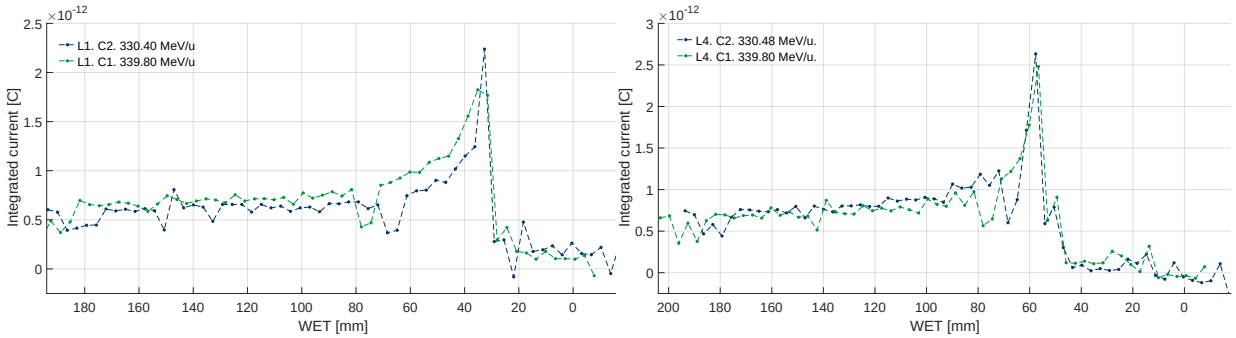

(a) BCs taken form the first level (L1) of the stepped-wedge iRAD aquired with 330.48 MeV/u (blue) and 339.8 MeV/u (green) ^{12}C-ion beams.

(b) BCs taken form the fourth level (L4) of the stepped-wedge iRAD aquired with 330.48 MeV/u (blue) and 339.8 MeV/u (green) ^{12}C-ion beams.

Unfortunately, given the complexity of the WET variability in the phantoms investigated and in real-anatomy cases, there will be always certain material combinations yielding BPs pinpointed in the middle of two RRD-channels. Such cases strongly support the need of a finer RRD granularity to increase the longitudinal resolution of the BCs (cf. Section 8.2.1) and improved post-processing techniques.

Another important aspect to consider when selecting the beam-energy is the imaging dose. In principle, transmission-imaging requires that the beam travels completely through the object, i.e., that the target-coverage is confined to the plateau-region of the BCs. In contrast, when a thick body or a high-density material is imaged with a relatively low-energy beam, it is likely that the object is reached by the increasing stopping-power part of the BC, hence receiving a slightly higher dose. Table 5.1 shows how only a 40 MeV/u difference in the initial beam-energy (between the first (C1) and second (C2) experimental configurations) might reduce the iRAD median-dose by half mGy in the same scanning conditions.

Image-quality and -accuracy dependence on internal HV supply

The RRD-ICs operating HV can corrupt the BC signals to a large extent. Ideally, the drift HV should be chosen such that the PPICs function in the saturation region, thus avoiding non-linear recombination effects (cf. Section 3.5.1). Nevertheless, the RRD noise-characterization has shown that increasing the internal HV increments the noise fluctuations. Noise resonances may distort the BC signal in two main ways: (1) affecting the gain of single/independent channels, which results in charge-readings with lower (notches) and/or higher (spikes) values, or (2) causing signal-coupling between two or three consecutive channels, as it is exemplified in Figure 5.7. Most of the noise outcomes can be resolved by the dedicated post-processing techniques described in Section 4.1.2 (cf. Figure 4.1.2). Small signal fluctuations among the RRD-channels are irrelevant to the final image as long as the BC-structure is not severely distorted and its maximum is recognizable. For instance, a 100 V HV-difference did not cause significant differences between the iRAD 5.3c acquired with a HV = 200 V and the iRAD 5.8a obtained with HV = 100 V, since it only produces a minor distortion on a BC-signal basis. In consequence, the ROI's WET-RE remains unchanged and the WET-IQR slightly increases in L5 and L6, as it is shown in the dark-green bars in Figure 5.2. The overall image-quality, however, might vary up to $\sim 6\%$ when two different voltage configurations are used (cf. Table 5.1, C2 versus C3). However, since no more voltage settings were tested in this experimental campaign, the difference in NRMSD can be also attributed to reproducibility effects between both acquisitions. Lower voltages may be affected by ion-recombination effects, which would cause an amplitude reduction of the signal, while higher voltages may cause a spiky BC. This is a relevant consideration when considering large HVs-values (~ 1000 V) (cf. Figure 5.7b). Thus, it is highly advisable to perform a prior current-voltage characterization for each experimental scenario, in order to assure an optimal RRD performance during the image acquisition.

Image-quality and -accuracy dependence on image dose

The beam-delivery technical challenges related to the reduction of imaging dose exposure were introduced in Section 3.3. By decreasing the number of primaries per RP, we proportionally degrade the BC signal-amplitude and the multi-source noise affecting the imaging setup be-

Figure 5.7: Effect of the HV-induced noise in single-RP BCs acquired at the same energy (330.48 MeV/u) but different voltages. In both panels the same pixel was considered for the two profiles.

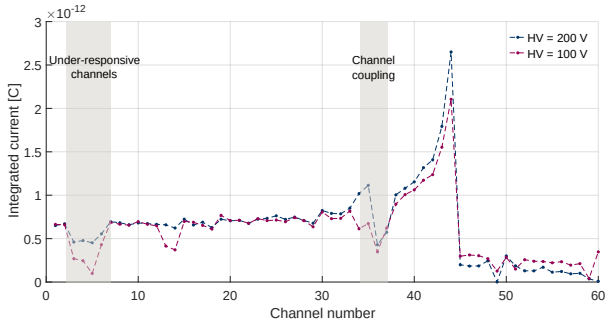

(a) BCs acquired with a 330.48 MeV/u ^{12}C-ion beam at two different HVs (HV = 200 V (blue) and HV = 100 V (magenta)). These voltages set the threshold to operate the RRD PPICs in the saturation region. These BCs were obtained with the stepped-wedge placed in front of the detector.

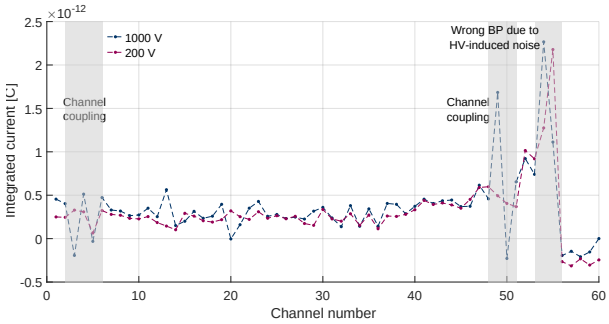

(b) BCs acquired with a 330.48 MeV/u ^{12}C-ion beam at two different HVs (HV = 1000 V (blue) and HV = 200 V (magenta)) for voltage-characterization purposes, before the experiment. No target was placed before the detector.

Figure 5.8: PMMA stepped-wedge phantom radiography (HV and middle-dose experimental configurations).

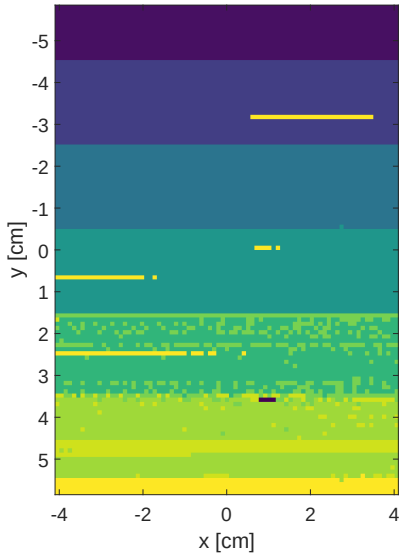

(a) C3. High-dose radiography obtained with a 3.7 mm FWHM, 330.48 MeV/u ^{12}C-ion beam. HV = 100 V.

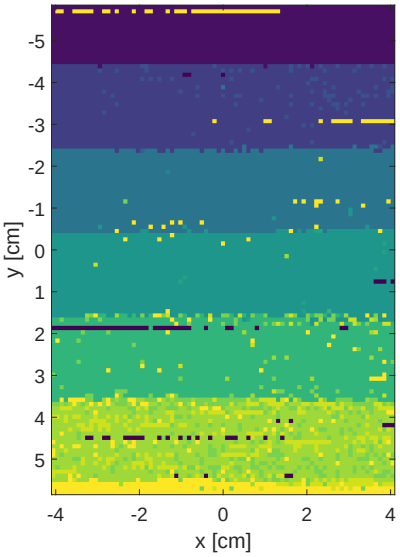

(b) C4. Middle-dose radiography obtained with a 3.7 mm FWHM, 330.48 MeV/u ^{12}C-ion beam. HV = 200 V.

comes a major issue. The signal response to the different dose-schemes in the BC-domain has been shown in Section 3.2. To illustrate this fact in the spatial-domain, the iRADs 5.3c (C2) and 5.8b (C4) were acquired with the same beam-energy of 330.48 MeV/u and HV = 200 V but the dose was reduced by a factor of five, one with respect to the other. When 1000 ^{12}C-ions are deposited per RP instead of 5000, the median dose calculated in a middle slice of the phantom is reduced down to 1.984 mGy (from 9.900 mGy); while the NRMSD is approximately doubled (changing from 13.53% to 26.82%) (cf. Table 5.1). The instability of the BC-signal at these low-dose levels is noticeable from the reddish tendency of the corresponding SFR-map (cf. Figure 5.5c). As in the high-energy experimental configuration (C2), the accuracy of the WET is

quantified through the median value of the RE and the IQR. The WET-RE does not vary in any phantom level when the imaging-dose is reduced (cf. Figure 5.2 and Table 5.2), however when comparing the configurations C2 versus C4, the IQR increases in L2 and L5, while the steps L1, L3 and L4 maintain the same IQR of the high-dose scheme. Contrarily, L6 appears more homogeneous than its high-dose analogue, since less noise-resonances were picked up in continuous rows in this specific ROI, yielding a reduced IQR.

Table 5.2: Global absolute mean WET-RE ($\overline{RE}$) and IQR ($\overline{IQR}$) including the six levels of the stepped-wedge phantom, obtained with all the different experimental configurations.

C1		C2		C3		C4		C5	
$\overline{RE}$ [%]	$\overline{IQR}$	$\overline{RE}$ [%]	$\overline{IQR}$	$\overline{RE}$ [%]	$\overline{IQR}$	$\overline{RE}$ [%]	$\overline{IQR}$	$\overline{RE}$ [%]	$\overline{IQR}$
4.47	0.92	1.72	0.28	1.72	0.54	1.72	0.27	1.68	0.00

Image-quality effect of post-processing methods

One of the main goals of these investigations is attaining low-dose images without compromising their quality. This aim can be achieved either by noise-removal methods that reject some of the most dominating resonances encountered in the experimental setup or by applying the dedicating post-processing strategies described previously in Section 4.1.2. Figure 5.9b displays the enhanced version of the iRAD shown in Figure 5.8b after the prior-BPD method has been applied. The post-processing results in a notable improvement, especially by reducing the salt-and-pepper noise in expected homogeneous regions of the phantom. The noise-lines caused by pick-up resonances during the acquisition are also overcome. Moreover, the sharp edges in the transitions from one step to the next one are redefined and the geometry is better recovered as one can notice by comparing with the calculated ground truth on the left. The raised overall iRAD quality is confirmed by the reduction of the NRMSD by ∼22% (cf. Table 5.1). However, the prior-BPD post-processing method still introduces some fluctuations at the step-edges, which is evident in the (magenta) vertical profile depicted in Figure 5.10.

The vertical profiles of the PMMA-stairs (cf. Figure 5.10) show clearly, for this central line of single-pixels, that the prior BPD strategy (magenta) reduces the erroneous identification of peaks due to the noise in the original iRAD (gray), bringing it closer to the true value (dashed blue).

The reliability of the WET recovered after the post-processing was also inspected in a ROI-basis, yielding to an 1% improvement in the absolute RE of the last level of the stepped-wedge (L6), while the WET-RE in the rest of the steps remained the same. The most significant change is visible in the drastic reduction of the IQR to zero.

Summarizing, the RE evaluation centers the attention on the prevailing WET value per ROI and the IQR accounts for the image homogeneity (or noise) (cf. Section 4.2.2). Therefore, configurations C2 and C4 obtained with the same beam-energy lead to the same RE regardless on the noise level, when no post-processing is applied (cf. Figure 5.2, green (C2) and gray (C4) bars).

Table 5.2 brings together the global mean absolute WET-RE ($\overline{RE}$) and IQR ($\overline{IQR}$) encompassing the six steps of the wedge-phantom. As expected, the fifth configuration (C5), in which

Figure 5.9: Comparison between the true iRAD of the stepped-wedge phantom and the post-processed middle-dose one.

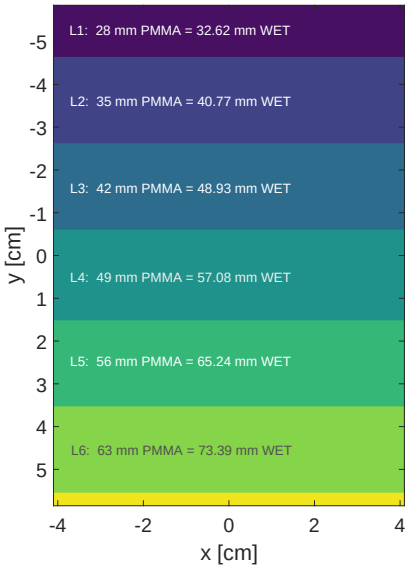

(a) Calculated WE ground truth of the PMMA stepped-wedge phantom.

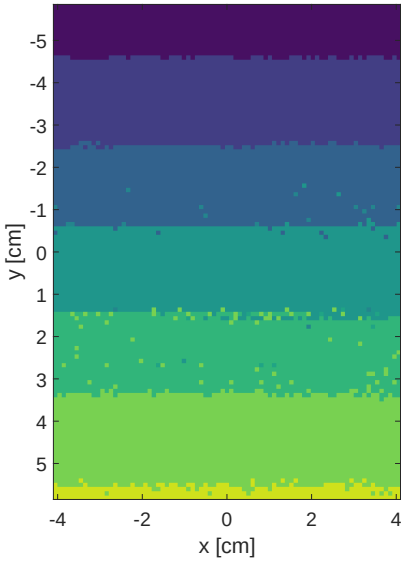

(b) C5. Middle-dose radiography obtained with a 3.7 mm FWHM, 330.48 MeV/u ^{12}C-ion beam. HV = 200 V. The MC-based prior-BPD post-processing technique was applied.

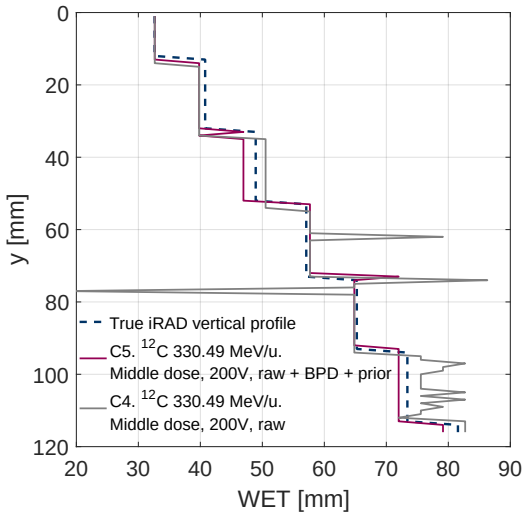

Figure 5.10: Single-RP profiles, along the vertical central axis, obtained with a 3.7 mm FWHM, ^{12}C 330.49 MeV/u middle-dose raw iRAD before and after the application of the prior-BPD post-processing method.

the prior-BPD has been applied, reveals the lowest global RE and no major WET variability.

The iRAD of a PMMA stepped-wedge phantom has served to investigate the capability of the RRD to resolve sharp phantom edges (of 7 mm) found along the beam direction, while exploring different experimental conditions. The factors varied in this study, together with the intrinsic resolution defined by the thickness of the RRD inner-absorbers may result in major WET uncertainties that must be reduced with the envisioned prototype which is under construction.

5.2 Heterogeneous phantoms

5.2.1 Slab phantom

Once the WET retrieval accuracy and precision of the RRD has been obtained with the RRD has been assessed for a PMMA homogeneous-target of different thickness, the WET of tissue-equivalent materials must be quantified in the same detail. To this aim, the slab phantom described in Section 3.6.2 was used. This geometry allows to investigate five different surrogates, namely: muscle, inner bone, adipose, lung and cortical bone tissue-like slabs. Furthermore, the chosen configuration also aids to represent some of the major challenges faced in the image formation and tomographic reconstruction, such as prominent density interfaces which cause multiple BPs due to the finite beam-width, as it was explained in Section 4.1.2. This effect inherently occurs at the transitions from one level to the other of the previously analyzed stepped-wedge phantom, albeit in minor scale since the traversed material remains the same.

Figure 5.11a shows the calculated true iRAD of the slab phantom studied in this section, which has been experimentally assessed in terms of slab rWEPL. It is also referred as the 0°-radiography, since it is the starting projection of the tomographic acquisition presented in the next chapter. Right below, Figure 5.11b displays the corresponding MC-simulated iRAD[A]. Visually comparing these two images, geometrical discrepancies can be noticed, those are caused by double BPs at density transitions in the phantom. In the interface region between the muscle and inner-bone slabs, the integrated BC signal encloses a WET-mixed information of both tissues. Being the muscle lighter than the bone, it allows the ion-beam to travel further in the detector. Therefore, the plateau information of the muscle-BCs is integrated into the inner-bone-BCs, thus magnifying the original signal amplitude. In consequence, the inner-bone BPs are dominant and the corresponding slabs appear thicker. The same effect is visible between the densest cortical-bone tile (yellow) and the last muscle-material on the right. This issue will be properly approached with the aforementioned BPD strategy. The nominal dose was evaluated as described in Section 4.3. As previously stated, the dose calculation considers all the deposited ions per RP. Since only a minor fraction is actually detected (cf. Section 3.4.4), there is a great room for dose reduction when the RRD-electronics is updated.

The slab phantom was also imaged under different experimental scenarios, namely varying the initial beam-energy, the dose and the scanning step-size. The experimental configurations investigated are summarized in Table 5.3 and examined in detail in the next sections. The effect of the BPD on the high- and middle-dose acquisition was evaluated, too. Moreover, for the low dose irradiations, the prior-BPD post-processing technique was applied. Analogously to the analysis performed for the previous phantom, the overall image-quality was defined in terms of the NRMSD, while the WET retrieval of the imaged tissues was quantified ROI-wise using the median-RE and IQR.

Image-quality and -accuracy dependence on initial beam-energy, before and after post-processing methods

The slab phantom iRADs were acquired with two different ^{12}C-ion beams of 3.9 mm FWHM, 299.94 MeV/u and 3.7 mm FWHM, 344.94 MeV/u. Geometrically speaking, the 0°-iRAD of this

[A]The simulated images were obtained with the MC-simulated environment, courtesy of S. Meyer

Figure 5.11: Slab phantom 0° WE-radiography ground truth and simulation. The images of this phantom were acquired with a FOV of 160 × 30 mm^2.

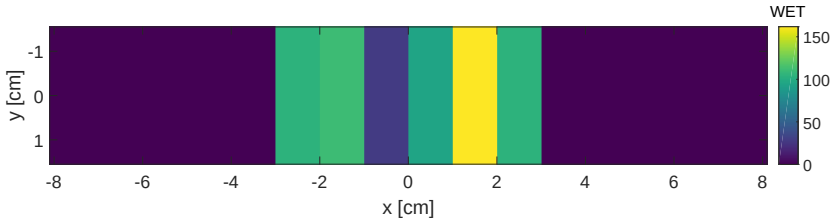

(a) True slab phantom 0° iRAD calculated according to the experimentally measured rWEPL of the tissue-equivalent slabs. From left to right, the tissue-equivalent tiles correspond to muscle, inner bone, lung, adipose, cortical bone and muscle.

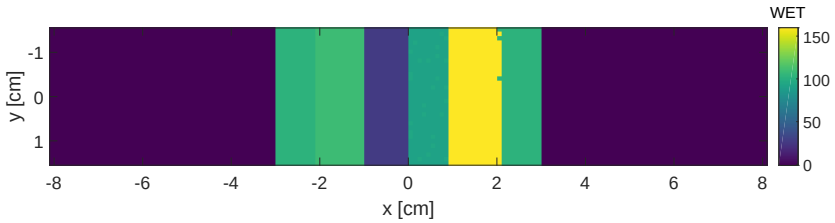

(b) Simulated slab phantom 0° radiography, obtained with a 3.9 mm FWHM, high-dose 299.94 MeV/u ^{12}C-ion beam scanned in 1 mm RP steps with the supportive MC-environment.

Table 5.3: iRADs configurations, dose evaluation and overall quality assessment of the tissue-equivalent slab phantom. The image formation column refers to the strategy used to retrieve the WET maps: Maximum-signal identification (Max.) or BPD. If a further data post-processing technique is applied it is also stated in the corresponding contiguous column.

ID	Energy [MeV/u]	ions /RP	RP-step [mm]	Dose [mGy]		Image formation	Processing	NRMSD
				median	IQR			
S1 (MC)	299.94	5000	1	10.165	0.439	BPD	-	0.0418
S2	299.94	5000	1	10.165	0.439	Max.	-	0.1153
S2.1	299.94	5000	1	10.165	0.439	Max.	BPD	0.1097
S3	344.94	5000	1	9.032	0.668	Max.	-	0.1122
S3.1	344.94	5000	1	9.032	0.668	Max.	BPD	0.1138
S4	299.94	1000	2	0.501	0.051	Max.	-	0.1261
S4.1	299.94	1000	2	0.501	0.051	Max.	BPD	0.1393
S5 (MC)	299.94	500	1	1.019	0.068	BPD	-	0.0433
S6	299.94	500	1	1.019	0.068	Max.	-	0.3130
S6.1	299.94	500	1	1.019	0.068	Max.	BPD + prior	0.1096

phantom does not contain sharp edges along the beam direction (as in the case of the PMMA stepped-wedge). Nonetheless, the change of material in terms of WET can be seen analogous to the (less drastic) step-thickness variation along the beam direction. Two additional features can be distinguished between these two phantoms: (1) the homogeneous-material regions differ in size, the tissue-slabs are thinner than the PMMA steps, which has to be considered for the beam lateral-dimension. Moreover, (2) the WET difference between levels is ∼8 mm in the

step phantom whereas the WET might have changes up to 82 mm (WE) in extreme-density interfaces such as the the one between lung and inner-bone. The overall radiography quality of the two experimental high-dose iRADs without applied post-processing only differs in 0.3% (cf. S2 and S3 in Table 5.3). In contrast, as expected, the MC-simulated iRAD has a ∼7% reduced NRMSD relative to the experimental projections. Important to mention is that for this particular phantom-geometry, any positioning errors with respect to the ground truth, which by construction do not occur in the in-silico iRADs, can extremely magnify the NRMSD, which considers all the image-pixels and not only the ones contained in the selected ROI.

In term of dose exposure, irradiating with higher beam energies has an advantage. It allows the BPs to be allocated farther in the RRD, keeping the phantom in a safe dose plateau-region. This becomes evident in the dose-evaluation of the configurations S2 (lower energy) and S3 (higher energy), which is reduced by 1.13 mGy in the latter case.

The effect of the BPD post-processing technique on retrieving the slabs thickness can be seen in Figure 5.12 for the low-energy iRAD and in Figure 5.13 for the high-energy iRAD. At such high-dose levels, the imaging-setup is more noise-resistant, therefore the raw-iRADs quality is expected to be high even without the application of extra processing after acquisition.

Figure 5.12: High-dose slab phantom 0°-projection obtained with a 3.9 mm FWHM, 299.94 MeV/u ^{12}C-ion beam scanned in 1 mm RP steps, before and after the BPD-technique was applied. From left to right, the tissue-equivalent tiles correspond to muscle, inner bone, lung, adipose, cortical bone and muscle.

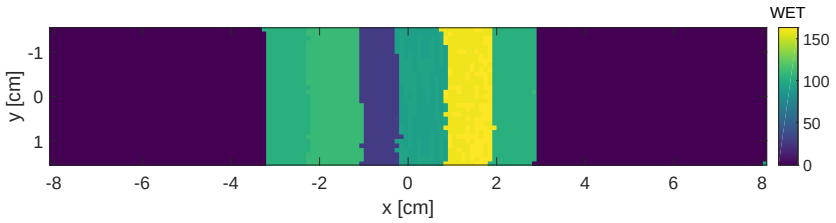

(a) Experimental radiography.

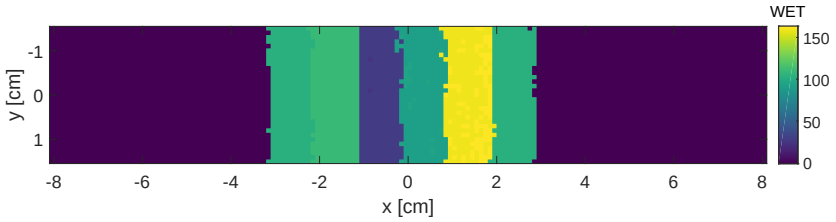

(b) Experimental radiography after BPD processing.

The same broadening-effect observed in the tissue-equivalent slabs of the MC-simulated iRAD 5.11b is evident in the experimental acquisitions (cf. Figures 5.12a and 5.13a). However, ambivalent WET-values occur more often in sharp tissue transitions of the experimental iRADs. In order to disentangle this source of error which is already considered in the NRMSD evaluation, the image accuracy is quantified in a trimmed ROI-basis as explained previously.

As it was introduced before, the BPD-method aims at breaking-up the different tissue contributions of the integrated BCs. Its achievement is already visible in the rectified width and better delimitation of the lightest material (lung, blue tile in Figures 5.12b and 5.13b). Moreover, the NRMSD of the configuration S2.1 is reduced by 0.56%, while the NRMSD of the

Figure 5.13: High-dose slab phantom 0°-projection obtained with a 3.7 mm FWHM, 344.94 MeV/u ^{12}C-ion beam scanned in 1 mm RP steps, before and after the BPD-technique was applied. From left to right, the tissue-equivalent tiles correspond to muscle, inner bone, lung, adipose, cortical bone and muscle.

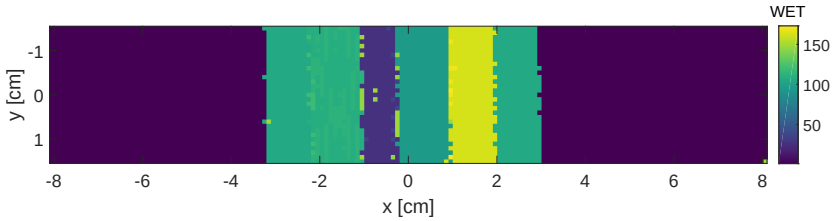

(a) Experimental radiography.

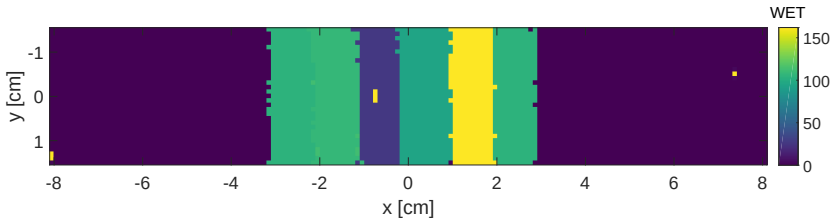

(b) Experimental radiography after BPD processing.

configuration S3.1 reports a small 0.16% increment (from11.22% to 11.38%), likely due to the random couple of pixels with clearly visible WET outliers (colored in yellow). In such cases, the BPD-algorithm does not converge and fails assigning the correct WET-value during the BPD-process (cf. Table 5.3)). The correct WET value of these arbitrary wrong pixels might be identified in the initial original iRAD and retrieved from neighboring pixels.

Some degree of inhomogeneity in certain tissue-ROIs is visible in both iRADs acquired with different beam-energies. This is particularly pronounced in the adipose and cortical-bone tissue-surrogates of the 299.94 MeV/u ^{12}C projection and the inner-bone band of the 344.94 MeV/u ^{12}C projection. This ROI-specific image-noise is due to the unfavorable BP location in between two RRD-channels. The discretized BCs in these areas usually present a *flattened* top, caused by the coarseness of the data points and the effect seen in Figure 3.36, which inevitably increases the probability to detect a rising section of the BP rather than the actual peak due to the presence of uncontrollable signal-noise. The purple and light-green BCs in Figure 5.14a, which represent the RRD signal after penetrating the adipose surrogate and the densest material (cortical-bone), as well as the orange BC in Figure 5.14b, corresponding to the inner-bone stripe, are shown as examples. The BPD also helps to smooth this image artifact, as it is evident at first sight from Figures 5.12b and 5.13b. Inherently, the projection of the lung equivalent-tissue is highly sensitive to WET-ambiguities due to its porosity, which makes the ion-beam traveling simultaneously through air and low-density material. Furthermore, one can notice in Figure 5.14b that the ascending part of the BC corresponding to the lung equivalent-tissue (yellow BC) is very prone to uncertainties in the BP position due to a malfunctioning channel located right before the peak, which is sensitive to signal noise-fluctuations. This unfortunate experimental condition and a lower peak-to-plateau ratio featured by the BCs that traverse a larger amount of detector material, may lead to considerable image-distortion, which is also reflected in a very large WET-RE (cf. Figure 5.15).

Figure 5.14: Experimental BCs extracted from the slab phantom 0°-projection obtained at two different beam-energies. The bottom-x-axis shows the BP-location in the RRD channels while the top-x-axis expresses these BP-positions in the corresponding WET-value.

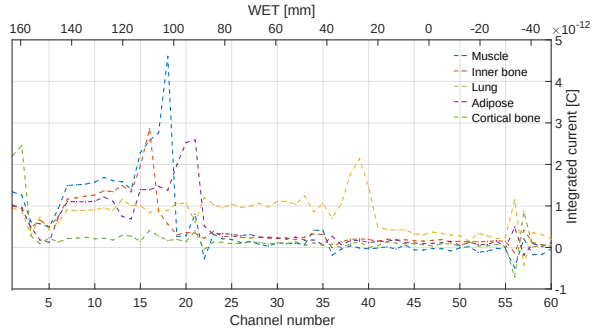

(a) Exemplary of BCs of the various tissue-ROIs, extracted from the slab phantom iRAD. The projection was obtained with a high-dose 299.94 MeV/u ^{12}C-ion beam.

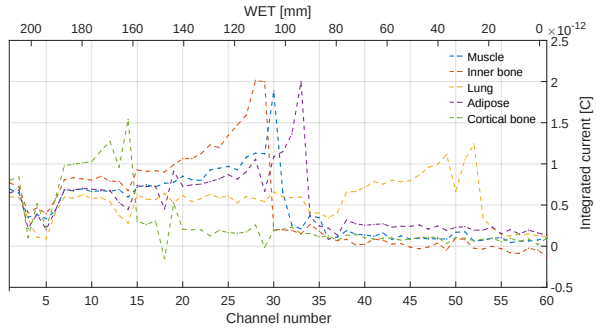

(b) Exemplary of BCs of the various tissue-ROIs, extracted from the slab phantom iRAD. The projection was obtained with a high-dose 344.94 MeV/u ^{12}C-ion beam.

Figure 5.15 gathers the WET-RE results of the imaged materials that constitute the slab phantom, acquired with two experimental configurations (S2 (gray bar) and S3 (green bar) in Table 5.3) and the effect of applying the BPD post-processing to the raw images (S2.1 (magenta bar) and S3.1 (blue bar) in Table 5.3).

The BPD-method is intended to solve the WET ambiguity at density-boundaries. Thus, since the WET-RE evaluation is done in a ROI-basis, with no material transitions included, the WET-accuracy is expected to be the same after decomposing the BC. The IQR, however, is a measure of the WET variability within the selected ROIs (cf. Section 4.2.2). The IQR of a ROI will be zero if, at least, the middle 50% of the RPs achieve the same WET-value. Thus, a consequence of the BPD-technique applied to certain ROI affected by noise is making it uniform in terms of local WET. Hence, usually the RE-IQR is reduced (most of the times to zero).

Recalling, in the 299.94 MeV/u radiography (S2), the adipose and cortical-bone tissues are more likely to mislead the BP location, which is clearly reflected by their larger IQRs, which are reduced after the BPD is implemented (S2.1). In this projection, most of the tissues result in a RE below 1.3% with respect to the expected WET-values, except from the adipose and lung which slightly exceed the 3%.

On the contrary, the higher-energy iRAD (cf. S3 in Table 5.3 and green bar in Figure 5.15) reduces the WET-RE for the adipose and cortical-bone tissues. Excluding the lung slab, the highest RE corresponds to the inner-bone ROI, being equal to 1.73%, which is related to the unfavorable BP position in the middle of two RRD-channels (cf. Figure 5.14b). The absolute WET-RE-value of the muscle material is only increased in 0.26%.

Figure 5.16 exhibits exemplary horizontal profiles extracted from the same pixel-row of the experimental iRADs configurations S2, S2.1, S3 and S3.1 described in Table 5.3. The ground truth profile is shown with the blue dashed line. The vertical shift of the experimental profiles with respect to the true baseline indicates the slight error introduced by the RRD-channel to WET calibration, which assigns a WET-value different from 0 when only air is traversed. Edges shifts result from double peaks in the transitions from one material to the other and/or millimetric phantom misalignment during the experimental acquisition. Since the profiles out-

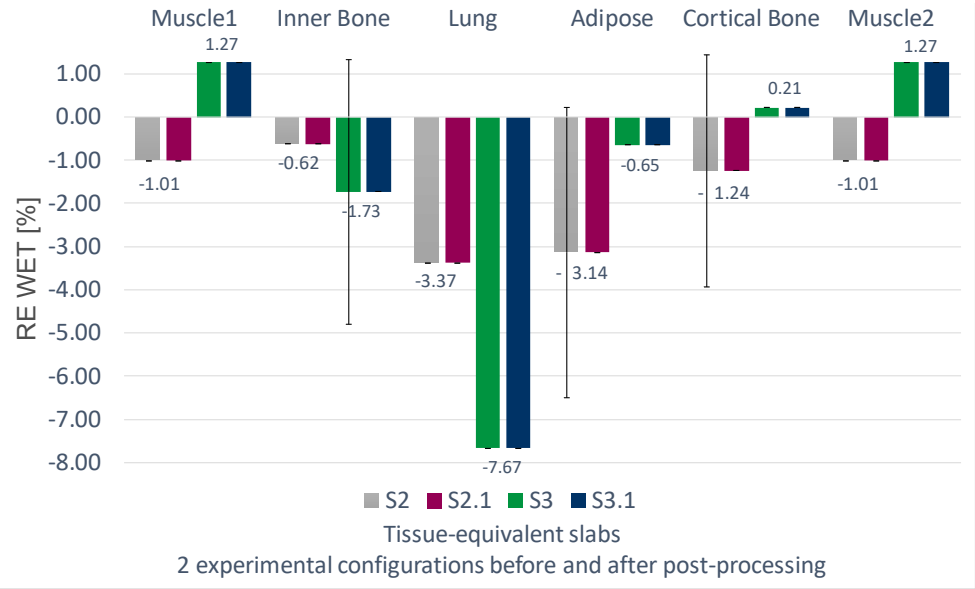

Figure 5.15: Radiography RE and fluctuation (IQR) in the WET of different tissue-equivalent materials acquired with high dose at two different beam energies: 299.94 MeV/u (S2) and 344.94 MeV/u (S3), before and after applying the post-processing BPD technique (cf. S2.1 and S3.1 in Table 5.3).

lined in Figure 5.16 correspond to single rows of pixels along the horizontal dimension of the slab-phantom, the boundaries between tissues might be affected by WET ambiguities, leading to an apparent shift of the profile with respect to the others if a different WET-value is picked. The comparison also illustrates clearly the smoothness effect of the BPD by flattening the profiles of the ROIs that show some rippling.

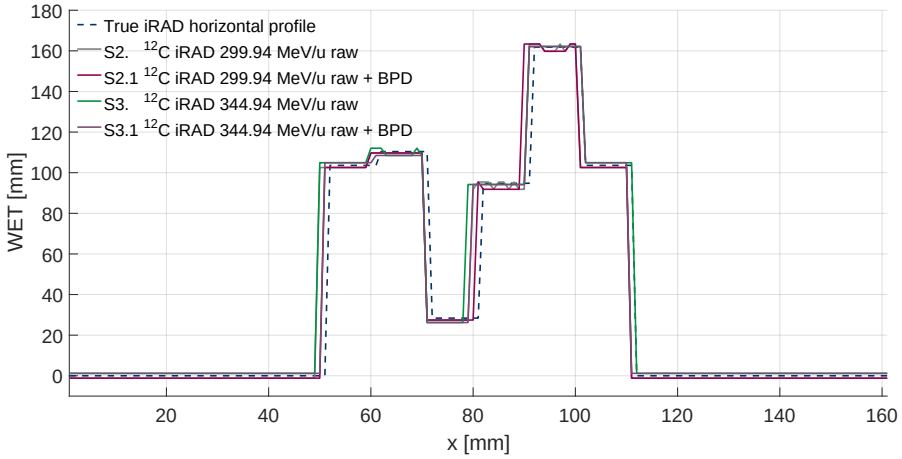

Figure 5.16: Comparison of horizontal profiles of the high-dose iRAD of the tissue-equivalent slab phantom obtained with two different energies and optimized with the BPD post-processing technique (cf. configurations S2, S2.1, S3 and S3.1 in Table 5.3). The true profile is also shown. As reference, the tissue-equivalent slabs disposition follows the following order from left to right: muscle, inner bone, lung, adipose, cortical bone and muscle.

Image-quality and -accuracy dependence on image dose, before and after post-processing methods

In order to further reduce the image dose, the slab phantom 0°-iRAD was obtained under the middle- and low-dose schemes and varying the beam-scanning step size.

Figure 5.17: Middle-dose slab phantom 0°-degree projection obtained by varying experimental acquisition parameters such as RP step-size and deposited ions per RP, before and after the BPD strategy has been applied.

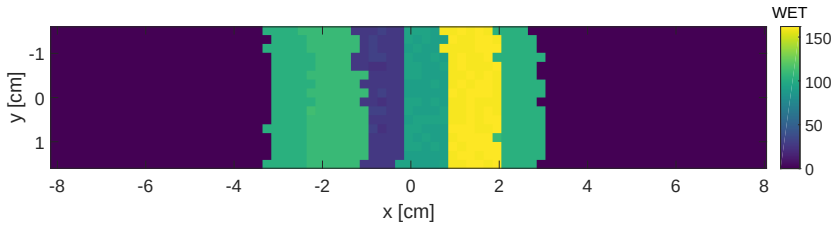

(a) Experimental 0°-degree radiography of the slab phantom performed with a middle-dose, 3.9 mm FWHM, 299.94 MeV/u ^{12}C-ion beam in 2 mm RP steps.

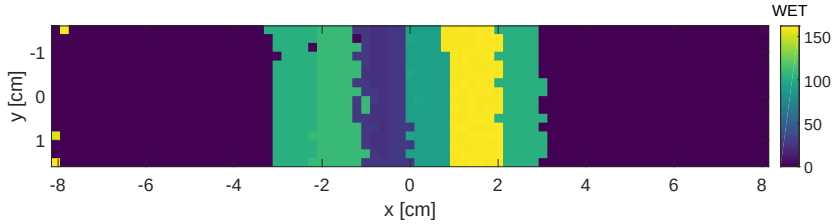

(b) Experimental 0°-degree radiography of the slab phantom performed with a middle-dose, 3.9 mm FWHM, 299.94 MeV/u ^{12}C-ion beam in 2 mm RP steps after applying the BPD post-processing technique.

Figure 5.18: Simulated (a), experimental (b) and post-processed (c) low-dose slab phantom 0°-degree projection.

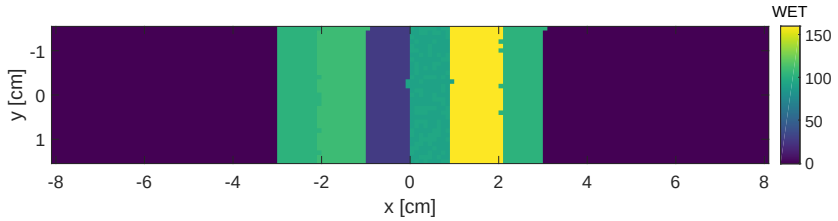

(a) Simulated 0°-degree radiography of the slab phantom acquired with a low-dose, 3.9 mm FWHM, 299.94 MeV/u ^{12}C-ion beam in 1 mm RP steps.

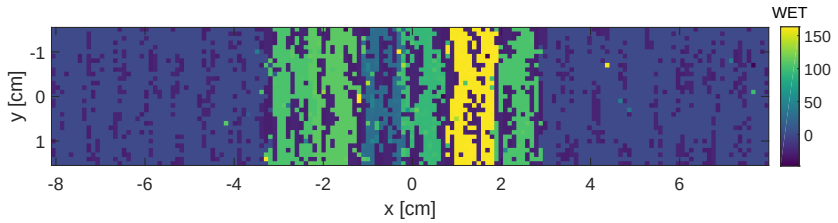

(b) Experimental 0°-degree radiography of the slab phantom acquired with a low-dose, 3.9 mm FWHM, 299.94 MeV/u ^{12}C-ion beam in 1 mm RP steps.

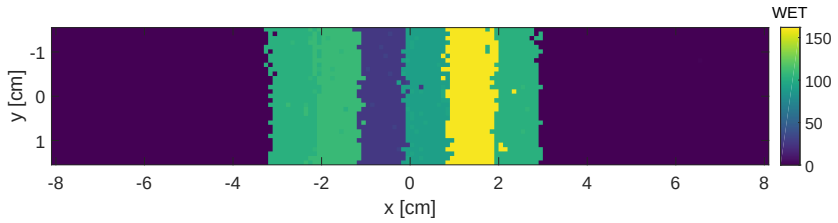

(c) Experimental 0°-degree radiography of the slab phantom acquired with a low-dose, 3.9 mm FWHM, 299.94 MeV/u ^{12}C-ion beam in 1 mm RP steps after applying the prior-BPD strategy.

Figure 5.17a corresponds to the iRAD obtained with the 3.9 mm FWHM, 299.94 MeV/u ^{12}C-ion beam, depositing 1000 carbon-ions per RP, which are now separated by 2 mm. This

irradiation configuration then reduces the image dose by a factor of 20, as it is reported in Table 5.3, from 10.16 mGy to 0.50 mGy. The overall image-quality is only slightly affected by increasing the NRMSD in 1.08% (from 11.53% to 12.56%) relative to the analogue high-dose iRAD. This experimental layout represents a major trade-off between significant dose-reduction and preservation of image-quality. It is also convenient when considering that the middle-dose scheme does not require complex technical adjustments in the HIT's dose delivery system, as it does the low-dose scenario. Moreover, the reduced number of RP by one fourth allows to complete the irradiation of the same FOV much faster. One drawback of lowering the dose by increasing the space between RPs would be a slight degradation of the iRAD spatial resolution. This consideration has not been investigated in experimental radiographies within the scope of this work; however, it was explored in the simulated framework by Meyer [2015]. Nonetheless, the overlapped beam-spot information in between two RPs can be exploited to compensate the expected reduction in iRAD spatial-resolution as suggested by Gianoli et al. [2016].

The median WET-RE of the different tissue-surrogates in the middle-dose iRAD (S4) remains almost unaltered in relation to the high-dose projection acquired with the 1 mm scanning step (S2) (cf. Figures 5.12a and 5.17a, respectively). The only tissue that revealed a change in WET-RE was the cortical-bone-equivalent ROI, being decreased by 1.1% (cf. Figure 5.19). This error reduction appears as a statistical consequence of cutting-down the number of analyzed RPs in the corresponding ROI of the S4 configuration to about one fourth of the RPs covered with the ROI used for the S2 scheme. As indicated previously, the cortical-bone ROI is sensitive to WET uncertainties due to the unfavorable BP location in the foremost RRD channels. In both configurations, the WET value assigned to this tissue fluctuates between 159.79 mm and 163.36 mm. In the S2 irradiation, the smaller WET occurs in 70% of the total number of pixels, therefore the median WET-value coincides with it. On the other hand, the cortical-bone ROI in the S4 setting contains 64 pixels, out of which only 44% were assigned with the smaller WET. Since the latter WET distribution is clearly not skewed towards one dominant value, the median WET of the cortical-bone ROI results to be the mean between the two most common WETs, i.e., 161.58 mm, which is actually quite close to the true WET of the cortical bone (161.80 mm), leading to an extremely reduced RE. The statistical behavior featured in this particular ROI suggests to apply larger areas for WET-RE evaluation in order to have fairly comparable statistics, when double-spacing between RP is used.

Although the application of the BPD technique to the middle-dose iRAD with sparser steps benefits the recovery of the real thickness of the lighter slabs (especially the lung one), it also increases the NRMSD by 1.32% (from 12.61% to 13.93%) (cf. Figure 5.17b). The ROI-based WE-RE analysis also reveals the problematic slabs that worsen the overall image-quality. The RE of the lung-tissue is increased by 12%, while its IQR conserved the same extent (cf. Table 5.4). The cause of this error-enhancement is the underlying principle of the BPD-algorithm which strongly relies in a recognizable BC-structure. When the RRD-signals are so severely misshaped by noise that they do not resemble a BC, the BPD is likely to fail finding the most suitable WET-contribution.

On the other hand, the cortical-bone tile, which it is known to be particularly sensitive to WET-uncertainties with this beam-energy, increased the WE-RE by 0.55%, whereas its IQR

Table 5.4: Median iRAD WET values of the various tissue-equivalent slabs obtained with the experimental configurations summarized in Table 5.3 and evaluated in terms of the RE and IQR in Figures 5.15 and 5.19.

ID	Muscle1		Inner Bone		Lung		Adipose		Cortical Bone		Muscle 2	
	WET [mm]	IQR	WET [mm]	IQR	WET [mm]	IQR	WET [mm]	IQR	WET [mm]	IQR	WET [mm]	IQR
True	103.60	-	110.40	-	28.40	-	94.80	-	161.80	-	103.60	-
S1	102.56	0.00	109.71	0.00	27.44	0.00	91.83	0.00	159.79	0.00	102.56	0.00
S2	102.56	0.00	109.71	0.00	27.44	0.00	91.83	3.35	159.79	2.68	102.56	0.00
S2.1	102.56	0.00	109.71	0.00	27.44	0.00	91.83	0.00	159.79	0.00	102.56	0.00
S3	104.91	0.00	108.49	3.07	26.22	0.00	94.18	0.00	162.15	0.00	104.91	0.00
S3.1	104.91	0.00	108.49	0.00	26.22	0.00	94.18	0.00	162.15	0.00	104.91	0.00
S4	102.56	0.00	109.71	0.00	27.44	1.19	91.83	2.38	161.58	2.68	102.56	0.00
S4.1	102.56	0.00	109.71	0.00	23.86	1.19	91.83	0.00	160.68	3.58	102.56	0.00
S5	102.56	0.00	109.71	0.00	27.44	0.00	91.83	0.00	159.79	0.00	102.56	0.00
S6	102.56	96.58	109.71	82.16	0.62	44.35	91.83	79.84	159.79	95.68	102.56	96.58
S6.1	102.56	0.00	109.71	0.89	27.44	0.00	91.83	0.51	159.79	0.00	102.56	0.00

was reduced (cf. Figure 5.19). The adipose slab, whose BPs are located, unluckily, between two RRD channels, maintained the same WET-RE, however its IQR was reduced to the minimum.

The horizontal profile of the S4 and S4.1 iRADs shown in Figure 5.20a exhibits that the WET-uncertainty increases according to the scanning step length, either at sharp material interfaces or due phantom misalignment. With longer scanning step-size, RPs with a wrong WET value will affect larger areas in the image spatial-domain.

The iRAD 5.18b was generated with the lowest ion-fluence achievable at HIT. At a glance, the image-quality of the raw projection is severely affected by noise and/or beam-intensity fluctuations, making the expected geometry of the slab phantom scarcely visible. As it was introduced in Sections 3.2 and 3.5.3, for such low number of particles deposited per RP, the integrated signal falls beyond the system-noise level, making it very hard to discern the correct BPs among the signal noise-fluctuations. Nonetheless, most of the pixels assigned with a wrong WET contain, systematically, the same values (dark blue in the color-scale). This behavior indicates that there is a pair of malfunctioning RRD channels (54 and 55), which are particularly sensitive to noise-fluctuations, causing a strong signal-coupling in the tail of the BC. This signal spike is misinterpreted as the BP when using the standard BP maximum identification. The horizontal profile corresponding to this iRAD (cf. Figure 5.20b, gray line) also makes it evident when the WET leaps down below its base-line, always towards the same value.

The raw-image is shown only for illustrative purposes. However, in the iRAD-formation process, knowing that the initial beam-energy used for this irradiation (299.94 MeV/u) produces the farthest BPs (traversing only air) within the channel number 47, one can dismiss the channel-signals afterwards, thus forcing the maximum identification algorithm to recognize the second highest peak.

Without applying any post-processing technique, the NRMSD of the iRAD 5.18b increased by a factor of 3 (11.22% to 31.31%) with respect to the high-dose iRAD obtained with the same beam-energy, while the dose is reduced to one tenth (cf. Table 5.3). As reference, the

expected projection simulated with the imaging MC-platform is shown in Figure 5.18a.

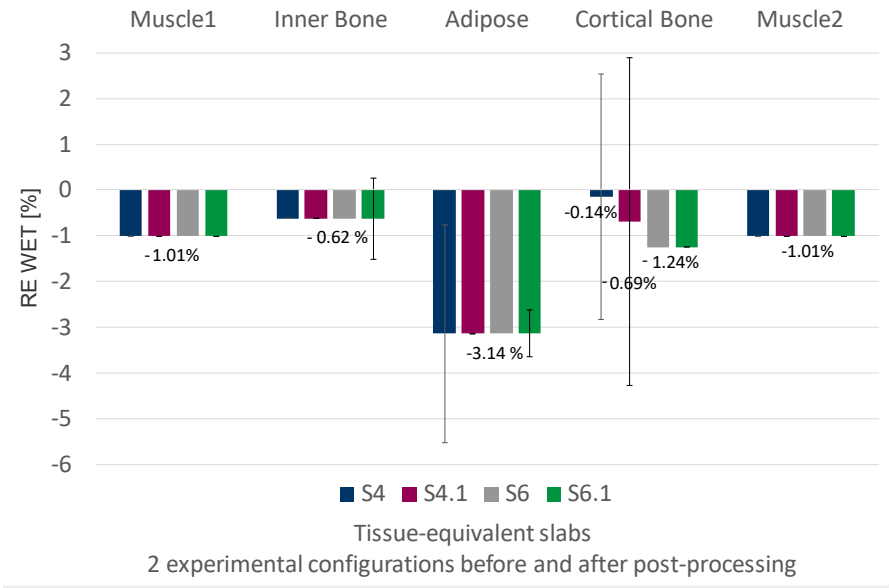

Figure 5.19: iRAD RE in the WET of different tissue-equivalent materials acquired with a 299.94 MeV/u ^{12}C-ion beam in two dose scenarios: S4: middle-dose projection with 2 mm RP steps (blue bars) and S6: low-dose projection with 1 mm RP steps (gray bars). The bars represent the median RE-WET value whereas the error whiskers show the IQR of the WET distribution. The REs of the raw experimental images after applying the BPD and the BPD-prior technique are also displayed (cf. S4.1 (magenta bars) and S6.1 (green bars) in Table 5.3). The lung-equivalent tissue evaluation as well as the IQRs of the raw experimental low-dose iRAD are not shown because it is evident from the inhomogeneity of the iRAD 5.18b and Table 5.4 that their values fall far beyond the scale of the graphics.

In terms of individual tissues, excluding the lung equivalent-tissue which exhibits an extreme WET discrepancy, the rest of the surrogates in the low-dose iRAD maintain the same disparity as in the high- and middle-dose projections (median RE muscle = -1.01%, inner-bone = -0.62%, adipose = -3.14%, cortical-bone = -1.24%) (cf. Figures 5.18b and 5.19). This indicates that, although the overall image-quality is distorted due to the noise caused by the low-dose irradiation technical limitations, the iRAD WET-accuracy is unaffected and it stays within reasonable RE percentages. A negative RE indicates, in general, an underestimated WET, as it is the case for all the tissues and most of the experimental configurations used to image the slab phantom.

The low-dose iRAD was post-processed with the prior-BPD strategy introduced in the previous chapter (cf. Figure 5.18c). In this case, the prior information considers a 5 mm (5 pixels) misalignment relative to the MC-simulated iRAD, which falls within the uncertainties faced on a daily-basis in the clinical environment. The prior-BPD procedure gets rid of the noise-related image artifacts, disclosing a radiography in which the tissue-equivalent slabs are clearly distinguishable. A significant 20.3% reduction of the NRMSD (from 31.30% to 10.96%) with respect to the raw-image results in an overall image-quality comparable to the post-processed (only with BPD) high-dose radiography (cf. S2.1 in Table 5.3) but with one order of magnitude reduced dose (1.02 mGy). As it could be foreseen, the WET-IQR is extremely reduced, in most of the surrogates, down to the minimum, as it is listed in Table 5.4 and represented with the error-whiskers of the green bars in Figure 5.19.

Table 5.4 brings together the WET results obtained with all the explored schemes reported in Table 5.3, and Table 5.5 summarizes the group mean absolute WET-RE ($\overline{RE}$) and corre-

Figure 5.20: Comparison of horizontal profiles of the middle- and low-dose iRADs of the tissue-equivalent slab phantom. The former (cf. configurations S4 and S4.1 in Table 5.3) was post-processed with the BPD-technique and the latter (cf. configurations S6 and S6.1 in Table 5.3) was furthermore optimized with the prior-BPD-method. The true slab phantom horizontal-profile is also shown.

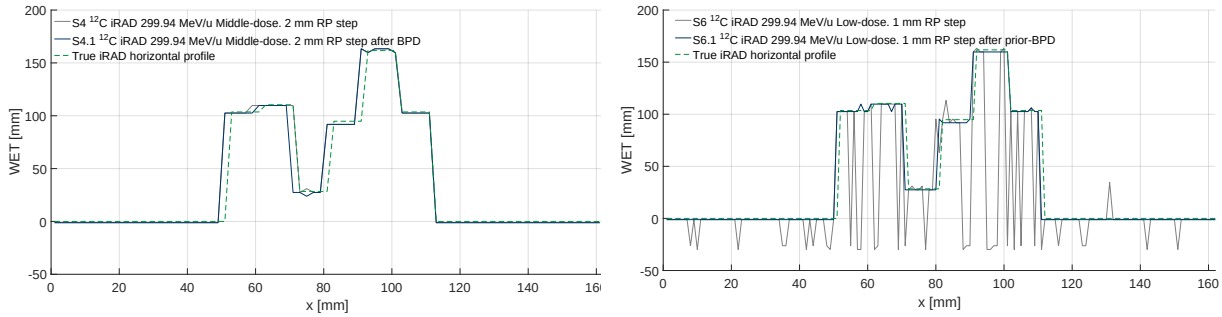

(a) True, experimental and post-processed horizontal profiles extracted from the middle-dose iRAD acquired with 2 mm RP step-size.

(b) True, experimental and post-processed horizontal profiles extracted from the low-dose iRAD acquired with 1 mm RP step-size.

sponding $\overline{IQR}$ including all the tissue-equivalent components of the slab phantom. All in all, configurations S2, S3 (high-dose but different beam energy) and S6 (low-dose), which share the same RP size, display similar mean absolute RE-WET, while they significantly vary in their IQRs according to the individual irradiation conditions that may introduce severe image-artifacts reflected in the spread of the WET distribution. The iRAD acquired with the S4 characteristics shows the best image results in terms of image-quality based on its WET-RE, IQR and dose trade-off. However, it is important to bear in mind that this is a pixel-based assessment and the number of evaluated pixels has a statistical influence in the image-quality results. When the RP step-size is doubled, the number of pixels in the FOV is reduced by a factor of 0.25. In consequence, if there are less pixels affected at sharp density-interfaces, the overall image-quality metric (NRMSD) might appear enhanced. Generally, the presence of sharp-edges or boundary zones in the imaged phantom has a strong influence in the radiography NRMSD, as it will be seen in the reduction of the NRMSD-values of the cylindrical phantom analyzed in the following section.

Table 5.5: Global absolute mean WET-$\overline{RE}$ and $\overline{IQR}$ comprising all the tissue-equivalent ROIs of the slab phantom. The iRADs were obtained experimentally in four different configurations (cf. Table 5.3). The lung-slab is not included in this evaluation for the low- and middle-dose experimental scenario (S4, S4.1, S6 and S6.1).

S2		S3		S4		S6	
$\overline{RE}$ [%]	$\overline{IQR}$	$\overline{RE}$ [%]	$\overline{IQR}$	$\overline{RE}$ [%]	$\overline{IQR}$	$\overline{RE}$ [%]	$\overline{IQR}$
1.73	1.01	2.13	0.51	1.18	1.01	1.40	87.19
S2.1		**S3.1**		**S4.1**		**S6.1**	
$\overline{RE}$ [%]	$\overline{IQR}$	$\overline{RE}$ [%]	$\overline{IQR}$	$\overline{RE}$ [%]	$\overline{IQR}$	$\overline{RE}$ [%]	$\overline{IQR}$
1.73	0.00	2.13	0.00	1.29	0.71	1.40	0.28

5.2.2 Cylindrical phantom with tissue-equivalent rods

The phantom with tissue-equivalent cylindrical surrogates represents a more-realistic scenario of a clinical-case target to be imaged, thus allowing the radiography assessment of a geometry

that contains curved shapes. It was especially designed to study anatomical changes in head and neck cases [Landry et al. 2014].

Due to the cylindrical geometry of the phantom with rods, a calculated true iRAD, which is not accurately interpolated at the round borders, is not convenient for a pixel-based evaluation of iRADs, as it was for the previously studied phantoms. Hence, based on the already benchmarked MC-simulated imaging setup, the *in-silico* high-dose iRAD of the rod-inserts phantom (cf. Figure 5.21a) was considered as a ground-truth WET-map for the NRMSD evaluation of the experimental iRADs.

Image-quality and -accuracy dependence on image dose, before and after post-processing methods

Table 5.6 itemizes the different simulated and experimental configurations used for the cylindrical phantom investigated. As before, the overall image-quality was assessed through the NRMSD for the experimental iRADs acquired with the three dose-schemes (R2, R4 and R6 in Table 5.6). The NRMSD obtained for MC-simulated projections under the same irradiation conditions is also shown (R1, R3 and R5 in Table 5.6). As expected, the NRMSD of the experimental projections is significantly larger and increases according to the dose reduction: the high-dose experimental iRAD presents a NRMSD equal to 6.78% compared to the NRMSD of 0.17% of the iRAD simulated by emulating the same experimental conditions (cf. Figures 5.21a and 5.21b), whereas the low-dose experimental radiography is deviating by ∼24% NRMSD from the *in silico* iRAD (cf. Figures 5.23a and 5.23b).

Table 5.6: Radiography quality assessment of the tissue-equivalent rods cylindrical phantom. The high-dose simulated iRAD is used as ground truth to assess the overall quality of the rest of the radiographic images.

ID	Energy [MeV/u]	ions/RP	RP step [mm]	Dose [mGy]		Image formation	Processing	NRMSD
				median	IQR			
R1(MC)	310.58	5000	1	10.072	0.362	BPD	-	0.0017
R2	310.58	5000	1	10.072	0.362	Max.	-	0.0678
R2.1	310.58	5000	1	10.072	0.362	Max.	BPD	0.0599
R3(MC)	310.58	1000	1	2.016	0.128	BPD	-	0.0091
R4	310.58	1000	1	2.016	0.128	Max.	-	0.1089
R4.1	310.58	1000	1	2.016	0.128	Max.	Prior-BPD	0.0505
R5(MC)	310.58	500	1	1.01	0.082	BPD	-	0.0141
R6	310.58	500	1	1.01	0.082	Max.	-	0.2414
R6.1	310.58	500	1	1.01	0.082	Max.	Prior-BPD	0.0545

The BPD post-processing technique was applied to the experimental high-dose iRAD (R2.1 in Table 5.6), reducing the overall image-quality metric only in 0.8%. The raw image is already quite accurate in most of the pixels, with the exception of the continuous rows which are strongly affected by pick-up noise frequencies. The enhancement is perceivable when visually comparing Figures 5.21b and 5.21c, the BPD-method is also able to eliminate a pick-up noise stripe appearing on the top of the FOV and defines better the plastic fastener (middle-top of

the FOV) and an air gap on the bottom of one of the rods (upper-left quadrant of the FOV) that incidentally happened during the experimental acquisition of this projection. By contrast, a second noise-line found almost in the middle of the FOV was not detected, nor corrected. Some pepper-and-salt noise is introduced in the image when certain BCs are severely affected by signal-noise and the BPD technique is unable to select the most relevant WET contribution. As it was pointed-out before for the low-dose slab phantom iRAD, in certain radiographies, when a specific channel is recognized to be systematically affected by a noise resonance or coupling, the affected channel signal may be adjusted before the decomposition process so that the BPD-algorithm does not converge into a wrong weighting value. Generally, these particular cases can be identified and corrected according to the original radiography and/or by means of interpolation from the neighbor pixels. Some unevenness is noticeable at the lateral borders of the phantom; in these regions the boundary is not as sharp as in the slab phantom, i.e., those BPs can have comparable heights. In consequence, depending on the noise level, sometimes one or the other is chosen as dominant component.

Figure 5.21: Tissue-equivalent rod-inserts phantom high-dose iRAD. 0°-projection acquired with a 310.58 MeV/u ^{12}C-ion beam at 1 mm RP step-size.

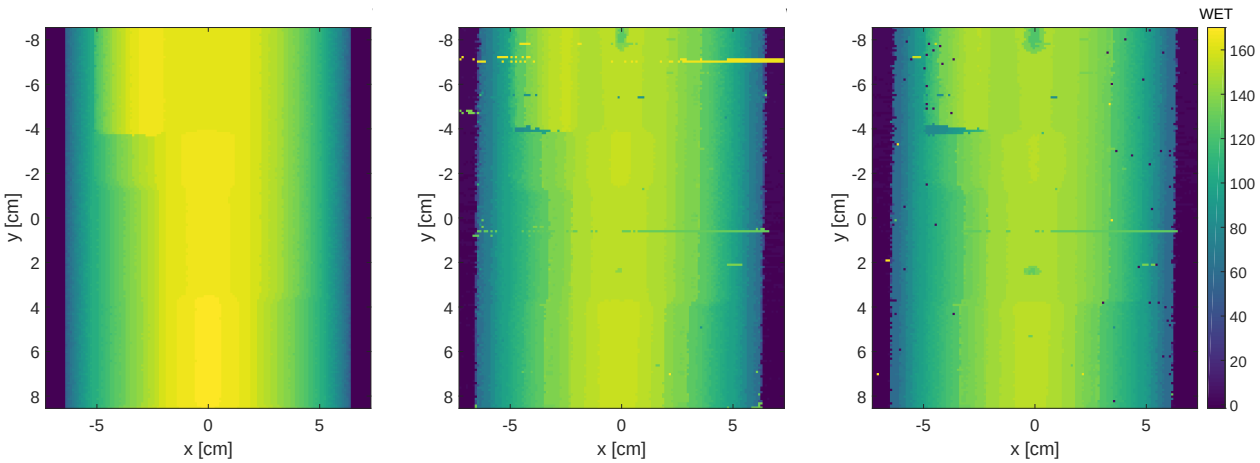

(a) MC-simulated high-dose iRAD of the rod insert phantom

(b) Experimental high-dose iRAD of the rod insert phantom

(c) Experimental high-dose iRAD of the rod insert phantom after applying the BPD post-processing technique.

In the high-dose projection cases, only the BPD post-processing method is applied. At this dose level, the BC signal is not highly distorted by noise, therefore the BPD is enough to correctly recover most of the phantom features. When the number of deposited ions per RP is reduced to 1000, the image-quality declines considerably (cf. Figure 5.22b). Only the outline of the phantom region that contains more material is distinguishable, whereas the thinner areas towards the vertical borders are deteriorated by noise. In order to recover most of the expected WET distribution, the prior-BPD technique was applied. 5 mm displacement in the MC-simulated iRAD were considered as prior information, resulting in the improved radiography shown in Figure 5.22c. The overall image-quality resulted in 5.45% NRMSD, which is comparable to the quality of the post-processed high-dose iRAD of NRMSD = 5.99% but with significantly less dose (cf. Table 5.6). The post-processing algorithm was able to overcome all the noise-related issues and recover the expected WET map yielding an even

higher quality than the highest-dose raw irradiation.

Figure 5.22: Tissue-equivalent rod-inserts phantom middle-dose iRAD. 0°-projection acquired with a 310.58 MeV/u ^{12}C-ion beam at 1 mm RP step-size.

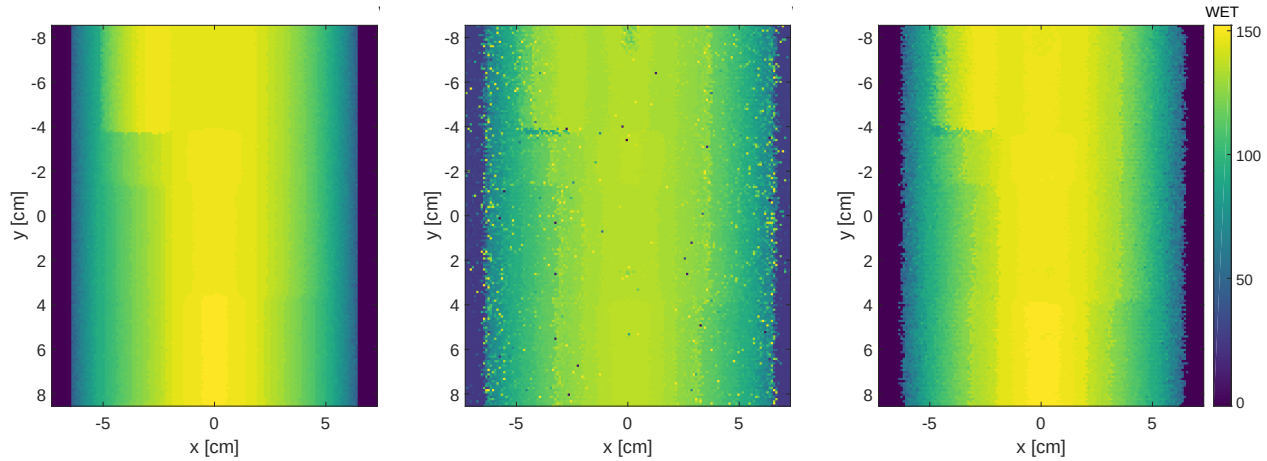

(a) MC-simulated middle-dose iRAD of the rod insert phantom

(b) Experimental middle-dose iRAD of the rod insert phantom.

(c) Experimental middle-dose iRAD of the rod-inserts phantom after applying the prior-BPD post-processing technique.

In order to decrease the physical dose even further, the cylindrical rod phantom was imaged under the low-dose scheme. The produced iRAD is shown in Figure 5.23b. Visibly, although no pick-up noise lines affected this projection, random noise dispersed over the whole FOV severely distorts the expected image. Nevertheless, by applying once again the 5 mm shift prior-BPD strategy, the phantom geometry is revealed with no major distortions and a quality-image comparable to the ones resulting from the higher doses (NRMSD $\sim 5-6\%$). This radiography-quality enhancement represents a distinct gain, given the fact that the imaging dose is reduced by a factor of 10 with respect to the highest-dose acquisition (cf. Table 5.6). In the radiographic images, the rWEPL of the different materials is integrated along the beam-path, hence, a ROI evaluation per individual tissue is reserved after performing the iCT reconstruction in the following chapter.

Generally, it should be noticed that the image-quality assessment using the NRMSD might be highly influenced by the phantom geometry, especially when it contains strong material boundaries as it is the case of the stepped-wedge and slab phantoms. This results in considerable larger NRMSD-values in comparison to a phantom with smoother density transitions like the cylindrical phantom and most of the real clinical cases.

Figure 5.23: Tissue-equivalent rod-inserts phantom low-dose iRAD before and after prior-BPD post-processing. 0°-projection acquired with a 310.58 MeV/u ^{12}C-ion beam at 1 mm RP step-size.

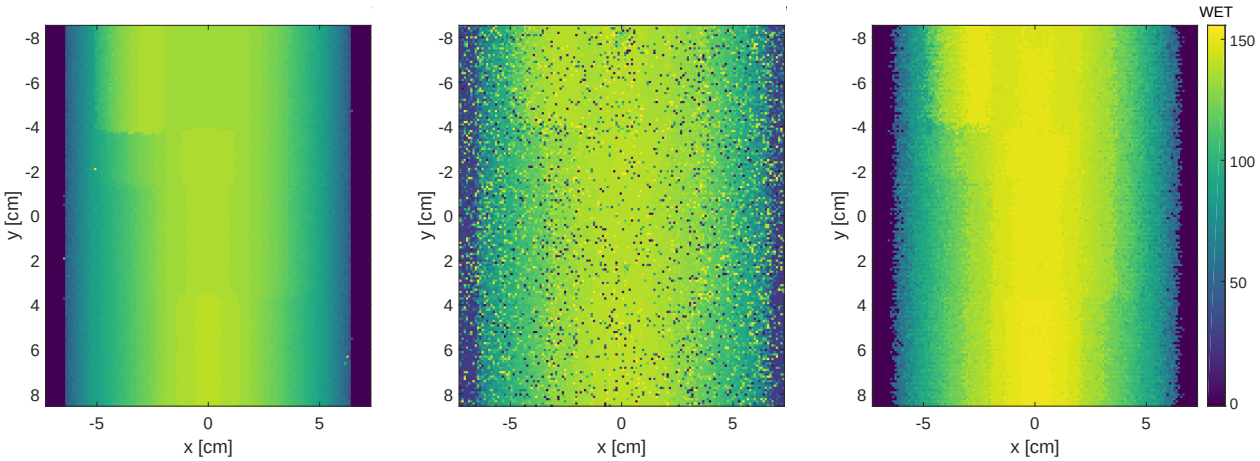

(a) MC-simulated low-dose iRAD of the rod insert phantom

(b) Experimental low-dose iRAD of the rod insert phantom.

(c) Experimental low-dose iRAD of the rod-inserts phantom after applying the prior-BPD post-processing technique.

While there is irony in the award, there is also hope that even in these days of increasing specialization there is a unity in the human experience, a unity clearly known to Alfred Nobel by the broad spectrum of his awards. I think that he would have been pleased to know that an engineer and a physicist, each in his own way, have contributed just a little to the advancement of medicine.

Allan M. Cormack's speech at the Nobel Banquet, December 10, 1979 [Cormack 1979]

6

Ion-based computed tomography

This chapter is dedicated to the evaluation of the reconstructed iCTs of the tissue-equivalent slab phantom and the cylindrical phantom with rod inserts. The slice-based tomographic reconstruction of both phantoms was implemented with the SART algorithm presented in Section 4.1.3. The phantoms' 3D-data was obtained from a 360° coverage in 0.9° angular steps according to the sampling Nyquist's theorem (cf. Section 4.1.3). In principle, the complete phantom reconstruction is possible with only half of the projections (180° coverage), as it has been shown for noise-free simulated data in Meyer et al. [2017]. In this case, the projections of the additional half coverage would add unnecessary dose and redundant rWEPL information without providing a significant image-quality improvement. However, in our specific case, the quality of the measured data is diminished by the presence of electronic and environmental noise, hence the full data-set (400 projections) has been considered to accomplish a better iCT-quality. Similar to the evaluation of the iRADs (cf. Chapter 5), the iCT accuracy assessment is based on the RE of the rWEPL in comparison to the true values for each of the tissue-equivalent surrogates (cf. Section 4.2.2). Experimental and simulated iCTs are compared in these terms and the effect of the application of post-processing techniques is investigated in both phantoms. In this regard, two approaches were considered: (1) Applying the BPD strategy to the simulated data and (2) using BPD with additional prior-simulated information to regularize noisy experimental BCs and enhance the accuracy of the experimental images. As for the first step (1), since the almost noise-free simulated imaging setup produces non-distorted BCs, the BPD strategy is sufficient to overcome the multi-BP issue (cf. Section 4.1.2) at material interfaces and retrieve a more precise WET-values in the projection domain. On the other step (2), the non-negligible noise present in the experimental acquisitions might mislead the correct BP identification if the noise signal-amplitude exceeds the actual maximum of the BC. Therefore, the prior-BPD post-processing (described in detail in Section 4.1.2), is necessary to suppress severely corrupted signals due to coupling, under- or over-response of certain RRD

channels. Depending on the noise location within the channel domain, this signal-misbehavior might not be solved by the plain BPD, since noise-spikes can be misinterpreted as BPs.

6.1 Tissue-equivalent slab phantom

Each radiographic image was obtained with a 299.94 MeV/u ^{12}C-ion beam actively scanned through a 16 × 3 cm^2 FOV, in 1 mm RP steps and depositing 5000 ions per RP. Before the iCT-slice reconstruction process, some major systematic noise-issues were identified in the RRD-channel domain, which might cause BP misleading in the WET maps. The signal manipulation was constrained to the RRD channels that caused severe signal distortions in more than one projections. Namely, channels 12, 13, 14, 26 and 34 to 37, which were observed to strongly corrupt the BCs. To fairly preserve the inherently increasing shape of the discretized BC in each of the modified pixels, the affected channel signals were overwritten using the signal of the preceding adjacent PPIC. For instance, if a corrupted signal was found in channel 26, the signal corresponding to channel 25 was taken. In case of channel coupling or distortion in two contiguous channels, the signal of one RRD channel before and one after were respectively used for substitution. This choice was based on the well-known BC-shape, which raises after the plateau-region and falls-off abruptly after the BP. Given the scarcity of data points, interpolation might not provide a substitute value fitting to the expected BC. The reconstructed iCT slice number 9 (y = 9 mm in the phantom dimensions, cf. Figure 6.1) through the 6 tissue-equivalent slabs was the least affected by noise-fluctuations and therefore chosen for the presented analysis.

The slab phantom iCT was reconstructed as detailed in the introduction of this chapter. The only variable that differs in the iCT reconstruction of the different data sets presented in this thesis is the stopping parameter ϵ (cf. Section 4.1.3). The choice of ϵ is data-set-specific, i.e., it depends on the chosen experimental parameters and it will be determined by the signal-quality over the different imaged materials, so that a proper convergence is ensured before noise breakup. The one used for the raw and post-processed experimental data was $\epsilon = 0.6 \times 10^{-4}$. On the other hand, for the simulated iCT data (with and without BPD), $\epsilon = 0.8 \times 10^{-4}$ was adopted.

Overall, the slab phantom represents an extremely challenging geometry to be reconstructed owing to the sharp material-interfaces that the ion-beam traverses during the imaging process. This leads to a high-sensitivity to rWEPL-uncertainties due to the multiple-BPs described previously (cf. Section 4.1.2). Furthermore, this particular geometry is characterized by a high spatial frequency along one specific direction [Meyer et al. 2017]. In consequence, there is a significant accuracy degradation in comparison to the cylindrical phantom that will be presented in the following section. In spite of this drawback, experimental and simulated results reproduce the expected geometry of the tissue-equivalent slabs, as can be seen from the exemplary iCT slices shown in Figure 6.1 and the trans-axial middle line profiles through the phantom depicted in Figure 6.2 for all the investigated configurations.

Figure 6.1: Reconstructed experimental and *in-silico* iCT slice of the tissue-equivalent slab phantom (left column). The experimental and simulated images after the post-processing methods are shown on the right column.

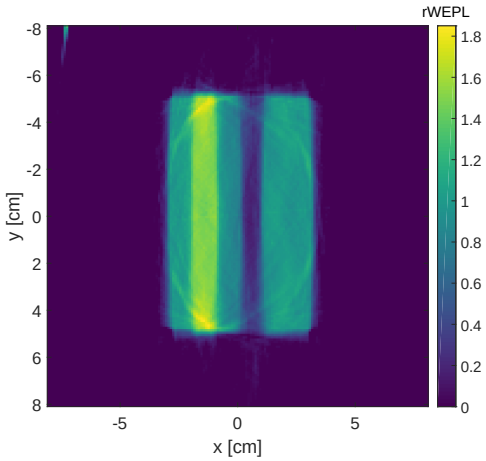

(a) Experimental iCT-slice.

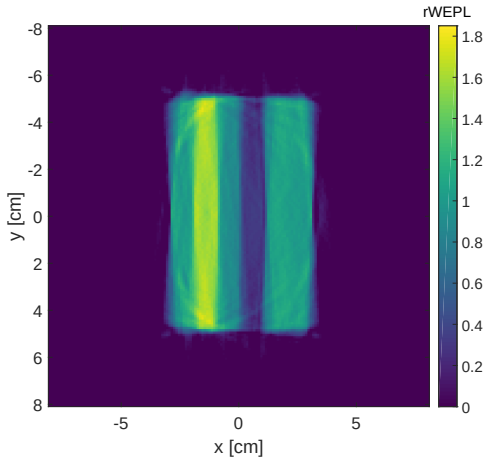

(b) Experimental iCT-slice after prior-BPD post-processing method.

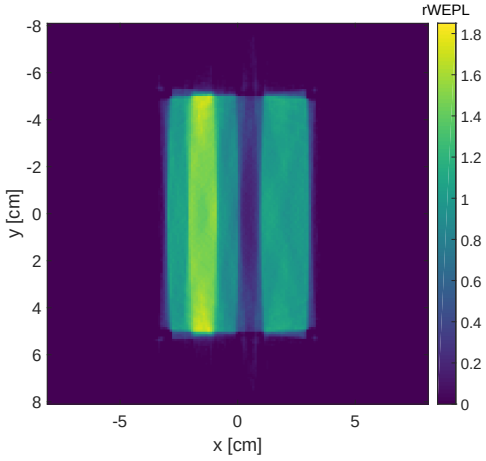

(c) MC-simulated iCT-slice.

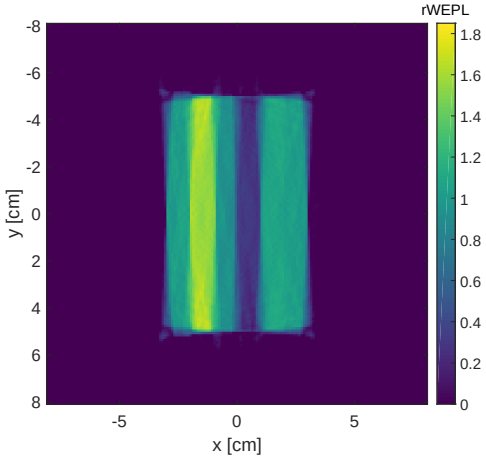

(d) MC-simulated iCT-slice after BPD post-processing method.

Experimental and simulated image accuracy comparison without post-processing methods

This section focuses on the comparative analysis of the data-sets which have not been post-processed. The iCT accuracy was assessed in the same manner as it was performed in the radiographic case, i.e., the median rWEPL was obtained ROI-wise and was compared to the true rWEPL values to calculate the percentage RE (cf. Section 4.2.2). Table 6.1 lists the rWEPL-RE results obtained from the raw experimental and simulated iCTs for all the tissue-equivalent materials. On a first comparison between the raw experimental and simulation data, the latter clearly shows a better image-quality judged as the global absolute mean rWEPL-RE of 4.14% compared to the 6.34% of the analogous experimental data. The IQR also reflects this behavior, being 0.07 and 0.08 in terms of rWEPL, for the simulated and experimental iCT, respectively (cf. Figure 6.4 and Table 6.3), which is expected given the fact that the experimental data is inherently more noisy. However, what mostly affects the rWEPL accuracy of non-processed

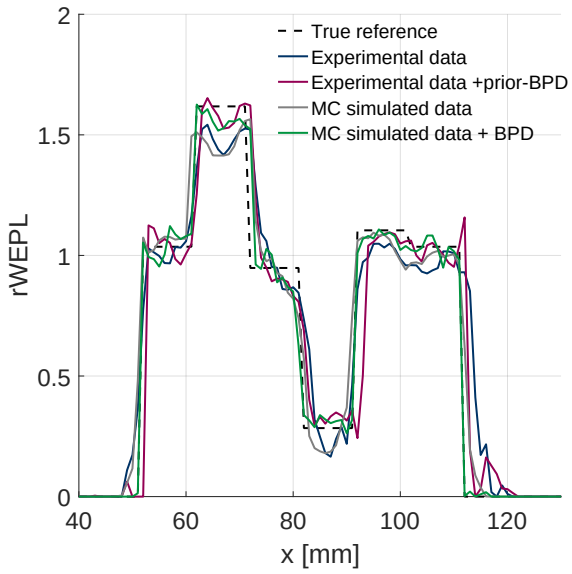

Figure 6.2: Comparison of middle-line profile of a trans-axial slice of the tissue-equivalent slab phantom iCT obtained with experimental and simulated data, before and after post-processing. The true rWEPL values are shown as reference.

Figure 6.3: Experimental and simulated sinogram of the tissue-equivalent slab phantom slice, before (upper row) and after applying post-processing strategies (lower row).

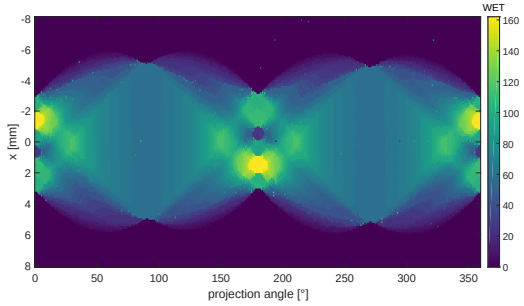

(a) Experimental sinogram.

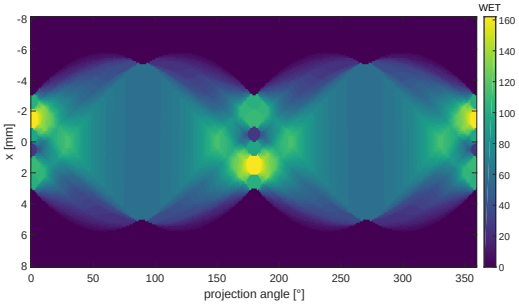

(b) MC-simulated sinogram.

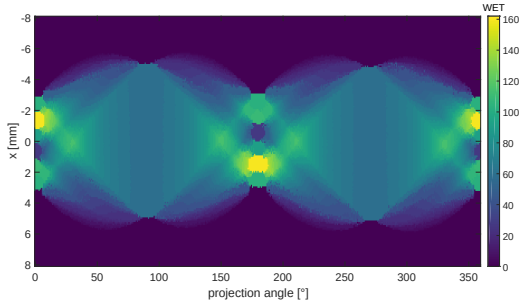

(c) Experimental sinogram after prior-BPD post-processing method.

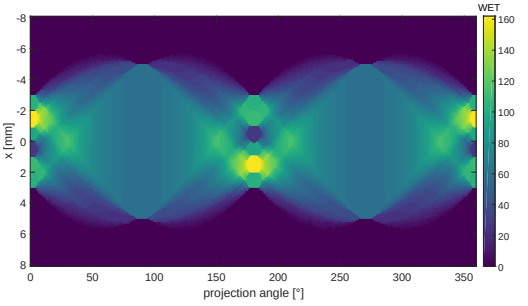

(d) MC-simulated sinogram after BPD post-processing method.

images are the BP ambiguities at sharp material-transitions. The main inconsistencies in the raw experimental image come from the extreme-density materials, namely cortical-bone and lung, and phantom edges where air-material transitions occur. In both, measured and simulated data-sets, the reconstructed cortical-bone slab presents clear rWEPL inhomogeneities at the

upper and lower parts of the tile. These outliers can be visualized as dots out of the whiskers in the corresponding cortical-bone box in Figure 6.4. A drop in rWEPL is evident in the central-line profiles shown in Figure 6.2, as well as the tendency to widen the higher-rWEPL tiles. The large variability of the lung-rWEPL is reflected in the elongated corresponding box in Figure 6.4 and its notable absolute RE reaching 9.51% (cf. Table 6.1). Thus, due to wrong BP assignment when pixels with multiple-peaks are encountered, since the lung-rWEPL is the lowest of all materials, a shrinkage in the thickness of the lung slab is expected if no post-processing is applied (cf. Section 6.1). However, this effect is evidently enhanced in the raw-experimental image compared with the image resulting from non-processed simulated data (cf. Figure 6.1a and Figure 6.1c).

Table 6.1: rWEPL-RE results for the tissue-equivalent materials which compose the slab phantom obtained from the iCT reconstruction of the experimental and simulated data without post-processing.

Tissue surrogate	rWEPL True	rWEPL Exp.	rWEPL-IQR Exp.	rWEPL-RE Exp. [%]	rWEPL Sim.	rWEPL-IQR Sim.	rWEPL-RE Sim. [%]
Muscle 1	1.036	1.019	0.059	-1.64	1.035	0.055	-0.10
Cortical bone	1.618	1.518	0.083	-6.18	1.489	0.093	-7.97
Adipose	0.948	0.886	0.080	-6.54	0.899	0.053	-5.17
Lung	0.284	0.257	0.120	-9.51	0.280	0.105	-1.41
Inner bone	1.104	1.000	0.065	-9.42	1.032	0.064	-6.52
Muscle 2	1.036	0.987	0.057	-4.73	0.998	0.029	-3.67

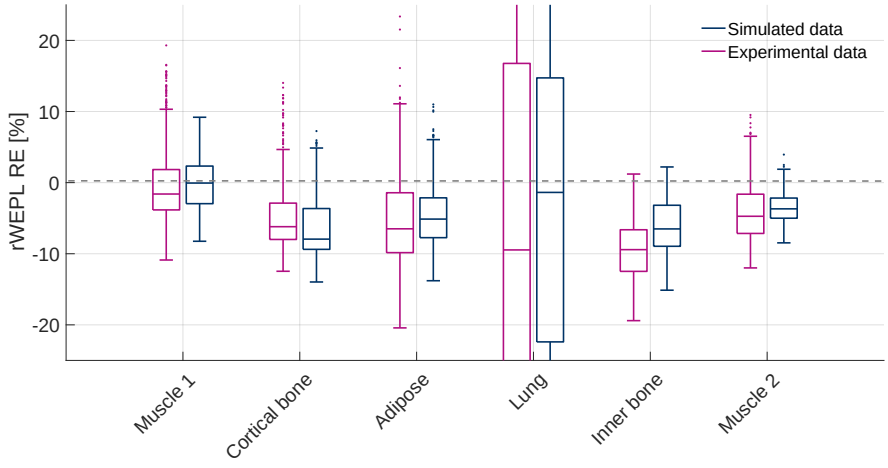

Figure 6.4: Comparison of the rWEPL-REs per tissue-equivalent tile of the slab phantom obtained with raw experimental (magenta) and simulated data (blue). The RE distribution of each material is represented with a box, where the median value is indicated with the central-horizontal line and the extreme edges of the box are the 25^{th} and 75^{th} percentiles of the distribution, respectively. The visualization of the RE spreading is limited by the whisker length, which specifies 1.5 times the interquartile range; the data points found beyond this interval are considered as outliers and are displayed with dot markers.

Figure 6.3 shows the 2D-array of data containing the full-coverage angular projections, organized per projection angle, the so-called *sinogram*. In general, the experimental sinogram (cf.

Figure 6.3a) shows only few randomly spread salt-and-pepper noise spots, owed to the aforementioned pre-processing of noise corrupted channels. Nonetheless, multiple ring-artifacts due to the propagation of pixels with wrong WET values in the projection domain, and a small strip artifact in the upper left corner are visible in the reconstructed iCT from measurements (6.1a). The visible artifacts in the reconstructed iCT from simulated data occur predominantly at the edges of the geometry due to the local inconsistencies of the projections at the air-material interface and to the tendency of other projection inconsistencies to move towards the edges during the tomographic image reconstruction.

The most noticeable disparity in the 2D projection-domain is the widespread experimental sinogram (cf. Figure 6.3a) in the x-direction, caused by the well-known multiple-BP issue. All the phantom slabs have the same thickness (10 mm), therefore no difference in size of each WET region is expected. However, a clear geometrical distortion is visible at the lateral extremes and the middle of the sinogram, corresponding to the 0°, 180° and 359.1° projections, where the tissue-equivalent slabs are arranged parallel (0° and 180°) or quasi-parallel (359.1°) to the beam direction. This is also reflected in the blurred transitions from one WET value to the other along the sinogram. The raw-simulated sinogram (cf. Figure 6.3b) also undergoes the aforementioned image distortion at material boundaries, although in a smaller scale.

Experimental and simulated image accuracy assessment after post-processing methods

Applying the corresponding post-processing techniques was highly beneficial to determine the most dominant WET-weight in the radiography domain, thus ameliorating the image correctness of both, experimental and simulated data. As it was pointed out in the introduction of this chapter, the simulated data was processed with the BPD technique (cf. Section 4.1.2); whereas for the experimental data, besides the BPD, a simulated prior information (cf. Section 4.1.2) was used to improve the image-quality. Table 6.2 collects the rWEPL-RE results of the different tissue surrogates that constitute the slab phantom, obtained after processing the measurements and simulations data. The boxplots 6.5 and 6.6 in turn aid for a visual comparison of the rWEPL accuracy obtained after applying the post-processing techniques to experimental and simulated images.

Table 6.2: rWEPL-RE results for the tissue-equivalent materials which compose the slab phantom as obtained from the iCT reconstruction of the experimental and simulated data after post-processing.

Tissue surrogate	rWEPL True	rWEPL Exp. +prior-BPD	rWEPL-IQR Exp. +prior-BPD	rWEPL-RE Exp. +prior-BPD [%]	rWEPL Sim. +BPD	rWEPL-IQR Sim. +BPD	rWEPL-RE Sim. +BPD [%]
Muscle 1	1.036	1.041	0.103	0.48	1.033	0.049	-0.29
Cortical bone	1.618	1.604	0.051	-0.87	1.582	0.067	-2.22
Adipose	0.948	0.902	0.054	-4.85	0.934	0.039	-1.48
Lung	0.284	0.301	0.049	5.99	0.286	0.049	0.70
Inner bone	1.104	1.068	0.047	-3.26	1.087	0.032	-1.54
Muscle 2	1.036	1.034	0.061	-0.19	1.027	0.035	-0.87

The global absolute mean rWEPL accuracy of the experimentally acquired iCT is improved by 3.73% (cf. Table 6.3) with the prior-BPD strategy. The IQR was 0.08 for the raw-experimental data and was slightly reduced down to 0.06 after the post-processing. Visually, the aforementioned strip artifact disappears after applying the prior-BPD technique (cf. Figures 6.1a and 6.1b). The ring artifacts, however, result from the propagation of certain WET inconsistencies in the projection domain and are not fully corrected with the post-processing. In addition to the improved rWEPL results, the correct thickness of the most influenced slabs is recovered (cf. Figure 6.1b), potentially also resulting in a better spatial resolution. Looking at the green cross-sectional profile in Figure 6.2, which corresponds to the post-processed simulated data, it is clear that the expected true geometry is mostly retrieved.

After applying the prior-BPD to the experimental data, the sinogram gets closer to the true one and the different WET-zones are better defined (cf. Figure 6.3c). This effect is also visible, although in a smaller scale, in the post-processed simulated sinogram, where the BPD overcomes inconsistencies due to wrongly allocated WET values between material interfaces (cf. Figure 6.3d).

Table 6.3: Global absolute mean rWEPL-$\overline{RE}$ and $\overline{IQR}$ considering all the tissue-equivalent materials of the slab phantom. The iCTs were obtained and evaluated under four different configurations: Experimental, experimental + prior-BPD, simulated and simulated + BPD

Experimental		Experimental + prior+BPD		Simulated		Simulated + BPD	
$\overline{RE}$ [%]	$\overline{IQR}$	$\overline{RE}$ [%]	$\overline{IQR}$	$\overline{RE}$ [%]	$\overline{IQR}$	$\overline{RE}$ [%]	$\overline{IQR}$
6.34	0.08	2.61	0.06	4.14	0.07	1.18	0.05

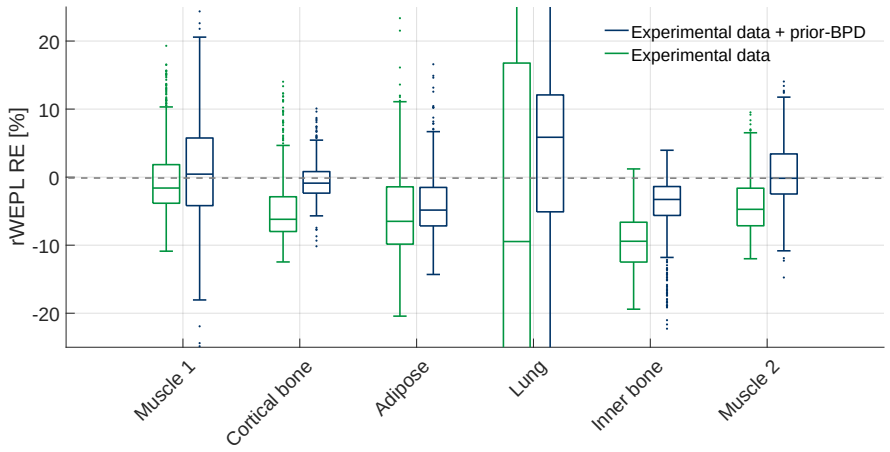

Figure 6.5: Comparison of the rWEPL-REs per tissue-equivalent tile of the slab phantom obtained with experimental data before (green) and after post-processing (blue). The RE distribution of each material is represented with a box, where the median value is indicated with the central-horizontal line and the extreme edges of the box are the 25^{th} and 75^{th} percentiles of the distribution, respectively. The visualization of the RE spreading is limited by the whisker length, which specifies 1.5 times the interquartile range; the data points found beyond this interval are considered as outliers and are displayed with dot markers.

The reduced rWEPL-RE is strongly influenced by the lung region. Since this ROI has the lowest rWEPL compared to the adjacent regions, the double-BP issue in the projection-domain

causes the iCT reconstruction to be highly sensitive to the chosen number of iterations. Thus, specifically varying the parameter ϵ used for the stopping criteria (cf. Section 4.1.3) of this material might further improve the results. However, for consistency in the analysis presented in this work, the stopping criteria has been standardized.

Figures 6.1b and 6.1d render the results of Table 6.2, confirming a rWEPL-RE reduction of 3.73 % and 2.96 % for the processed experimental and simulation data, respectively. The effect in the experimental iCT is also apparent in Figure 6.5, as the blue boxes corresponding to the post-processed data get closer to the 0 dashed-line, meaning that the rWEPL-RE has been reduced.

Finally, Figure 6.6 shows the remarkable improvement of the rWEPL statistics for all the tissues when the BPD method is performed with and without the support of prior information.

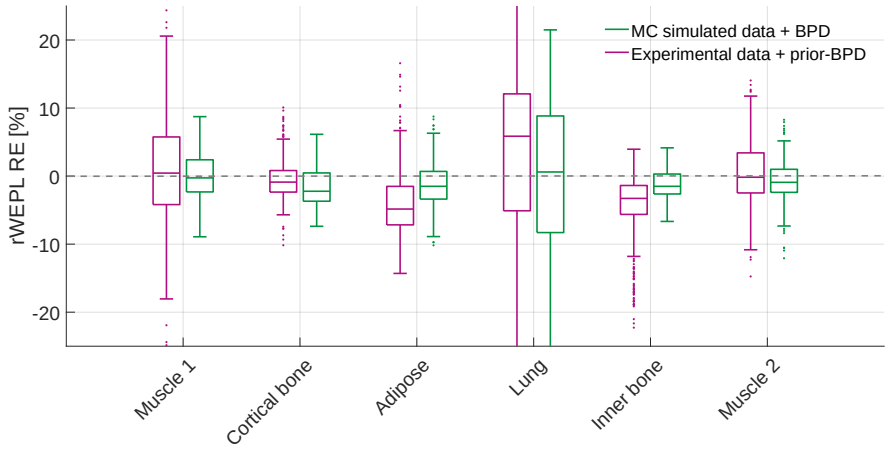

Figure 6.6: Comparison of the rWEPL-REs per tissue-equivalent tile of the slab phantom obtained with post-processed experimental (magenta) and simulated data (green). The RE distribution of each material is represented with a box, where the median value is indicated with the central-horizontal line and the extreme edges of the box are the 25^{th} and 75^{th} percentiles of the distribution, respectively. The visualization of the RE spreading is limited by the whisker length, which specifies 1.5 times the interquartile range; the data points found beyond this interval are considered as outliers and are displayed with dot markers.

6.2 Cylindrical phantom with tissue-equivalent rods

The tomographic projections were acquired with a 310.58 MeV/u ^{12}C-ion beam actively scanned through a 14.5 × 17 cm^2 FOV, in 1 mm RP steps. 5000 ions were allocated in each RP. Without traversing any material before the detector, ion-beams at this specific energy are stopped within the channel 50 of the RRD, where the BP is expected. Thus, the signals from the 11 subsequent PPICs were omitted in order to avoid unnecessary noise-corrupted data points at the BC level. Given the phantom rod-inserts distribution, three iCT slices were selected for the analysis presented in this thesis, to be able to investigate all the tissue-equivalent materials. The first slice includes the muscle-, bone400- and adipose-equivalent inserts. The second slice comprises the breast and bone200 surrogates and the third slice includes the cortical-bone and liver tissue-equivalent rods. Within the analyzed slices, 8 pixels which were obviously affected by noise, showing distinctively wrong WET-values in the radiography-domain, were manually manipulated. By individual inspection of these RPs on the channel level, the corrupted signals were found in the PPICs 49 and 50 due to noise-coupling between both channels and were

substituted with the signal corresponding to the neighbor channel 48.

The cross-sectional rWEPL reconstruction analysis of the cylindrical phantom was also performed on a slice-basis using the SART algorithm (cf. Section 4.1.3). The stopping criteria to determine the number of iterations was $\epsilon = 1 \times 10^{-4}$ for the experimental iCTs (with and without post-processing) and $\epsilon = 4 \times 10^{-4}$ for the simulated iCTs (with and without post-processing).

Exemplary reconstructed first and third iCT slices are presented in Figures 6.7 and 6.8 in the same four configurations analyzed with the previous phantom: raw experimental, raw simulated, experimental with prior-BPD and simulated with BPD. In general, the experimentally obtained images retrieve the phantom geometry and correspond to the simulated iCT slices, as can be observed in the previously mentioned figures and with the traversal profiles shown in Figure 6.9. In the sections below a comparative analysis between the different outcome from the studied configurations is discussed.

Figure 6.7: Reconstructed experimental 1st iCT slice of the cylindrical phantom including muscle, bone400 and adipose tissue-equivalent rods. Experimental and simulated images before and after post-processing methods are shown.

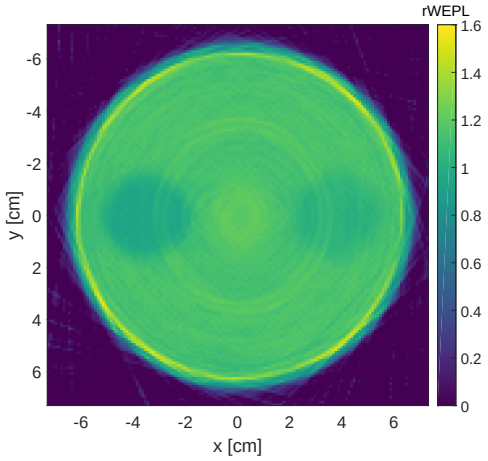

(a) Experimental iCT-slice.

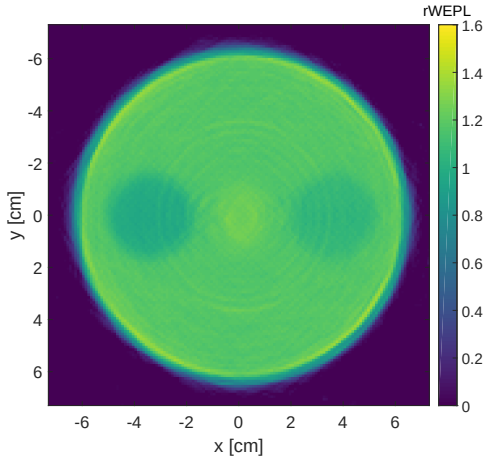

(b) Experimental iCT-slice after prior-BPD post-processing method.

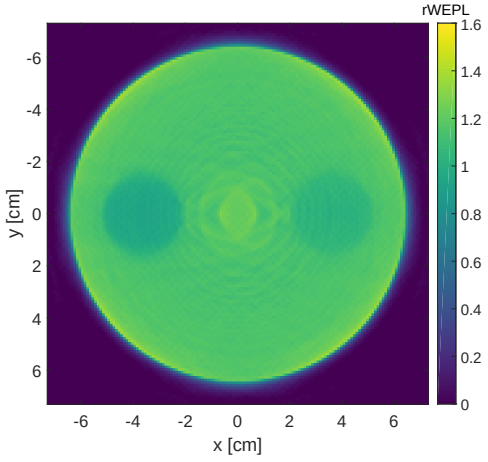

(c) MC simulated iCT-slice.

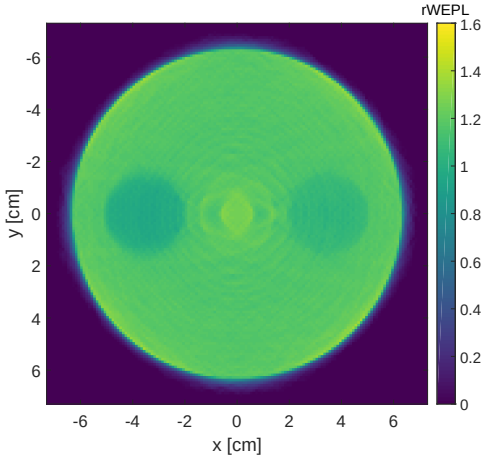

(d) Simulated iCT-slice after BPD post-processing method.

Figure 6.8: Reconstructed experimental 3rd iCT slice including cortical-bone and liver tissue-equivalent inserts. Experimental and simulated images before and after post-processing methods are shown.

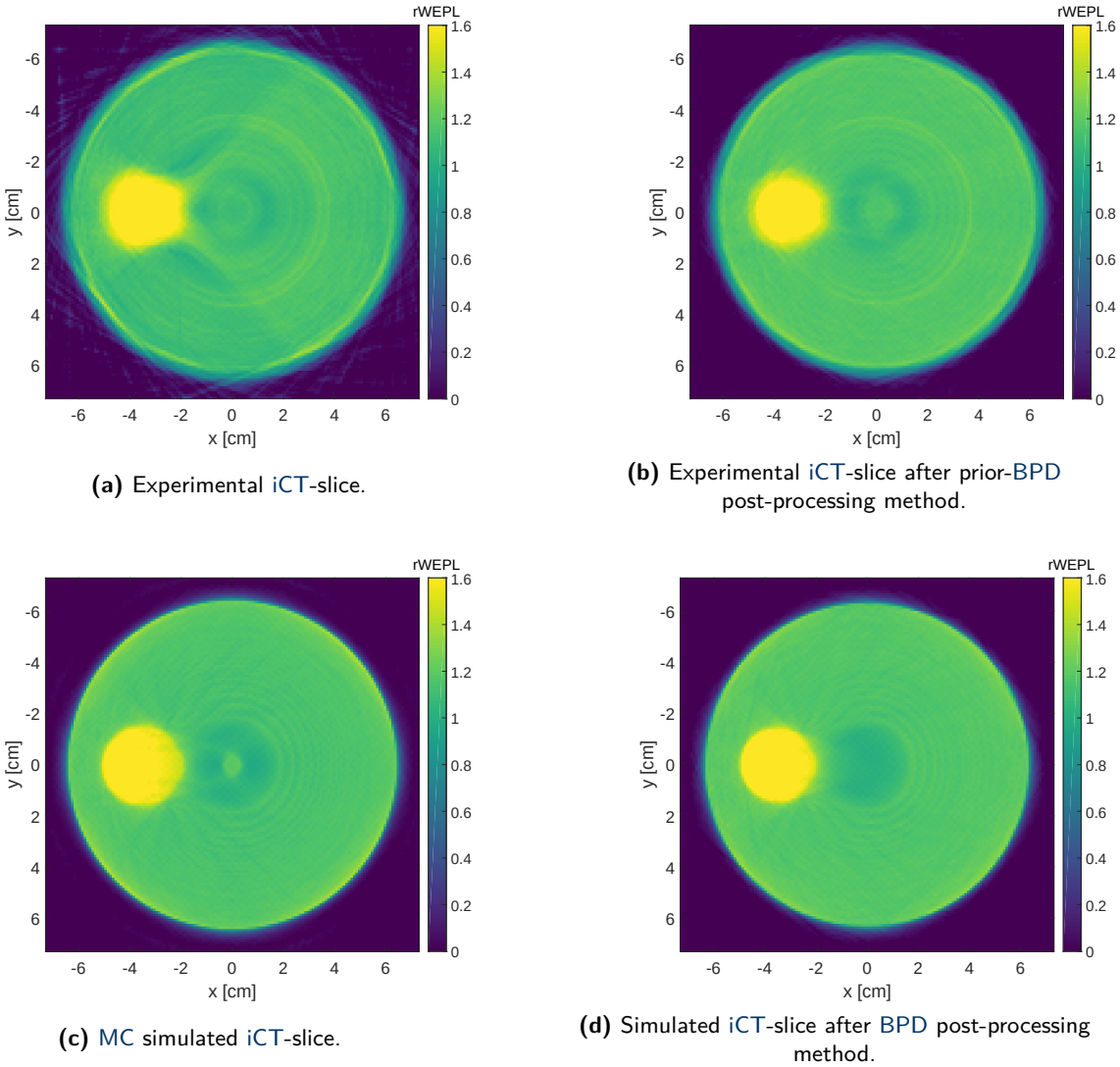

(a) Experimental iCT-slice.

(b) Experimental iCT-slice after prior-BPD post-processing method.

(c) MC simulated iCT-slice.

(d) Simulated iCT-slice after BPD post-processing method.

Experimental and simulated image accuracy comparison without post-processing methods

As expected, the raw simulated data leads to a lower global mean rWEPL-RE than the experimental data (including all the tissue-equivalent inserts), yielding 1.83%, whereas the rWEPL-RE obtained from the measurements is increased by 0.24% respect to the MC-simulated iCTs (i.e., 2.07%). The global rWEPL-IQR however remains the same for both configurations. Tables 6.4 and 6.5 collect these results and Figure 6.10 graphically represents the measured and simulated rWEPL-RE statistical distributions of each tissue surrogate. The first experimental iCT-slice (cf. Figure 6.7a) truthfully recovers the phantom geometry and the three inserted rods, as the simulated one does, too (cf. Figure 6.7c). The middle bone400 insert has a true rWEPL of 1.216, which is very close to the one of the PMMA container (cf. Table 6.4), thus appearing hidden with a similar color as the surrounding material. Few ring artifacts are visible, which likely arise from WET inconsistencies at the projection level. More severe strip artifacts

Figure 6.9: Comparison of the experimental and MC-simulated cross-sectional rWEPL profiles corresponding to the 1st (a) and 3rd (b) reconstructed slices of the cylindrical phantom iCT, before and after applying post-processing methods. The true expected profile is also shown as reference.

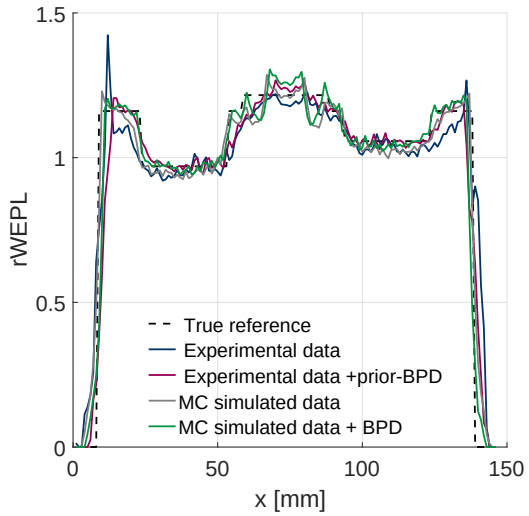

(a) Cross-sectional rWEPL profiles along the x-dimension of the 1st reconstructed slice of the cylindrical phantom iCT. From left to right, the muscle, bone 400 and adipose rWEPL are distinguished within the PMMA cylinder container.

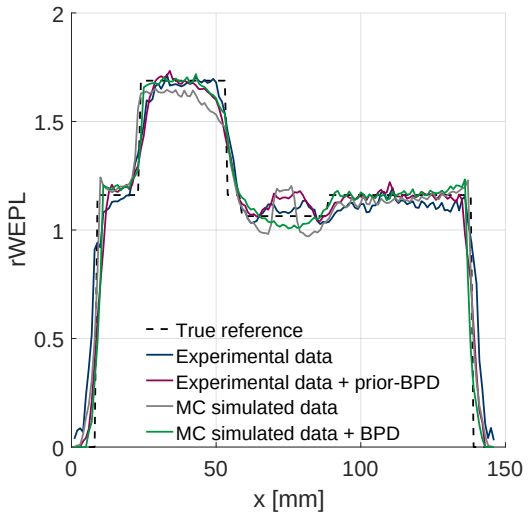

(b) Cross-sectional rWEPL profiles along the x-dimension of the 3rd reconstructed slice of the cylindrical phantom iCT. From left to right, the cortical-bone and liver rWEPL are distinguished within the PMMA cylinder container.

occur on the phantom contour, which have their origin in the double-BP ambiguity commonly occurring at material interfaces. Moreover, this issue leads to clear rWEPL-inconsistencies in the denser materials: bone200, bone400 and cortical-bone, causing a visible augmentation effect of the original geometry.

On the other hand, the MC-simulated 1st iCT-slice exhibits a reduced image-noise and strip/ring artifacts (cf. Figures 6.7c and 6.8c) than the experimentally obtained iCTs (cf. Figures 6.7a and 6.8a), especially at the circumference of the phantom.

In particular, the third iCT-slice of the experimental tomography shows the highest rWEPL discrepancy (cf. Table 6.5). The reason of this increased inaccuracy is a large rWEPL-RE arising from the cortical-bone and liver tissue-equivalent inserts, yielding 2.01% and 4.23% RE, respectively (cf. magenta boxes in Figure 6.10), which is not observed in the simulated tomography (cf. Figure 6.8c). It is worth noticing that the observed discrepancies are also function of the stopping criteria, therefore, tuning the ϵ parameter might yield different outcomes. In the former surrogate, this behavior in the experimental image is owed to the strong geometrical distortion of the cortical-bone tissue (cf. Figure 6.8a). The central part of the measured sinogram (cf. Figure 6.11a) reveals the projections with the deformed WET-region, caused by an over-response of the second RRD channel on these WET-maps. The true maximum is expected around channel 4. This issue also influences the liver ROI accuracy because the beam traverses the two materials and the projection includes the integrated WET information of both. Moreover, its unfavorably location in the center of the slice and next to a high-rWEPL material (dominant BP) can cause the visible ring-artifacts, which cannot be easily corrected without dedicated image manipulation.

Table 6.4: Experimental rWEPL results and RE assessment of the tissue-equivalent rods inserted in the cylindrical phantom, in comparison to the expected true values and the ones obtained with simulated data without post-processing.

Tissue surrogate	rWEPL True	rWEPL Exp.	rWEPL-IQR Exp.	rWEPL-RE Exp. [%]	rWEPL Sim.	rWEPL-IQR Sim.	rWEPL-RE Sim. [%]
Adipose	0.97	0.953	0.028	-1.75	0.954	0.02	-1.65
Bone400	1.216	1.19	0.025	-2.14	1.198	0.061	-1.48
Muscle	1.057	1.038	0.029	-1.80	1.037	0.018	-1.89
Breast	0.989	0.975	0.029	-1.42	0.977	0.022	-1.21
Bone200	1.117	1.092	0.026	-2.24	1.115	0.034	-0.18
Cortical bone	1.688	1.722	0.067	2.01	1.618	0.042	-4.15
Liver	1.064	1.109	0.035	4.23	1.039	0.046	-2.35
Top PMMA	1.161	1.144	0.031	-1.46	1.141	0.019	-1.72
Bottom PMMA	1.161	1.143	0.037	-1.55	1.14	0.018	-1.81

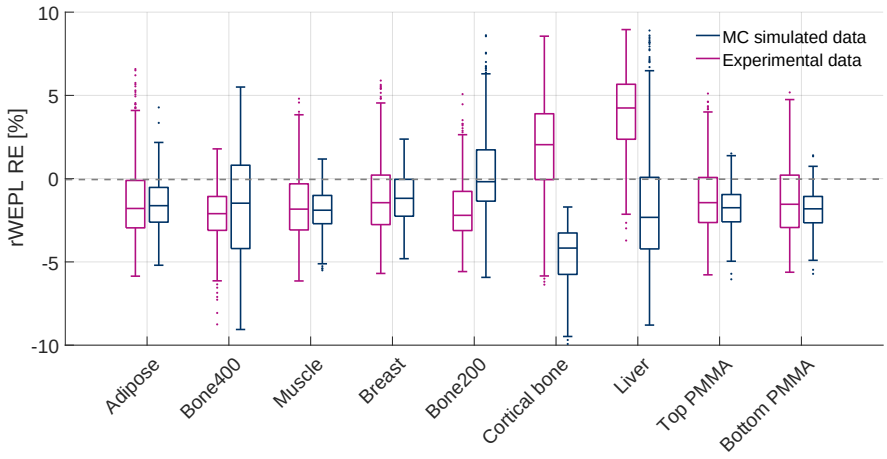

Figure 6.10: Comparison of the rWEPL-REs per tissue-equivalent insert of the cylindrical phantom obtained with raw experimental (magenta) and simulated data (blue). The RE distribution of each material is represented with a box, where the median value is indicated with the central-horizontal line and the extreme edges of the box are the 25^{th} and 75^{th} percentiles of the distribution, respectively. The visualization of the RE spreading is limited by the whisker length, which specifies 1.5 times the interquartile range; the data points found beyond this interval are considered as outliers and are displayed with dot markers.

Table 6.5: Global absolute mean rWEPL-$\overline{RE}$ and $\overline{IQR}$ comprising all the tissue-equivalent rods of the cylindrical phantom. The iCTs were obtained and evaluated for four different configurations: Experimental, experimental + prior-BPD, simulated and simulated + BPD (cf. Tables 6.4 and 6.2)

Experimental		Experimental + prior+BPD		Simulated		Simulated + BPD	
$\overline{RE}$ [%]	$\overline{IQR}$	$\overline{RE}$ [%]	$\overline{IQR}$	$\overline{RE}$ [%]	$\overline{IQR}$	$\overline{RE}$ [%]	$\overline{IQR}$
2.07	0.03	0.91	0.03	1.83	0.03	0.92	0.03

Experimental and simulated image accuracy assessment after post-processing methods

The experimental iCT-slices were enhanced with prior information at the radiography level. As it was explained in Section 4.1.2, the prior-BPD post-processing strategy allows to use

Figure 6.11: Experimental and simulated sinogram of the cylindrical phantom 3rd slice containing the cortical-bone and liver rods, before and after applying post-processing strategies.

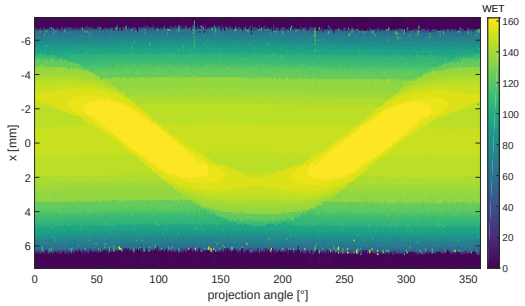

(a) Experimental sinogram.

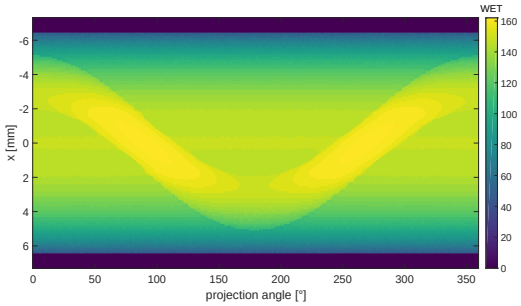

(b) MC-simulated sinogram.

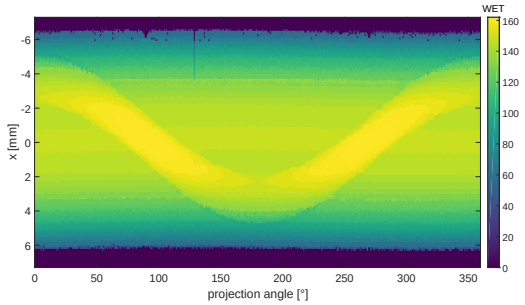

(c) Experimental sinogram after prior-BPD post-processing method.

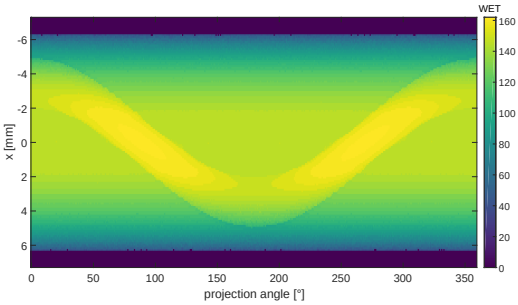

(d) MC-simulated sinogram after BPD post-processing method.

a modified simulated projection of the imaged object which contains additional information of adjacent pixels in each RP. In this case, a 5 mm (5 pixels) neighborhood was considered to include a conservatively large misalignment likely to occur on a daily basis in the clinical practice. In the simulated case, only the BPD method was performed.

The performance of the prior-BPD on the experimental data leads to a 1.16% improvement in the global mean rWEPL-accuracy (Table 6.5). Table 6.6 lists individually the median rWEPL obtained for each of the tissue-equivalent inserts after post-processing. Figure 6.13 focuses on the statistical distributions of the rWEPL-RE improved when the prior-BPD technique is applied to experimental acquisitions. Except from the cortical-bone and liver rods, the rest of the materials feature a negative rWEPL-RE, indicating an underestimation of the expected rWEPL. After post-processing the raw data, almost all the surrogates (but the liver one) reduce their absolute rWEPL-RE under 1%.

Figure 6.14 in turn compares the two post-processed data-sets. The obtained rWEPL-accuracy is very similar in both cases, which is expected given the fact that prior-BPD method uses the information of the corresponding simulation data, as it was explained in Section 4.1.2. On average, the enhanced experimental data has a slightly reduced rWEPL-RE of 0.91% in comparison to the one resulting from processed simulations (0.92%) (cf. Table 6.5). The decomposed MC-simulation data exhibits a smaller IQR in the cortical-bone and liver cases, although the global mean IQR remains the same in both improved configurations (cf. Tables 6.5 and 6.6). Once again, the main rWEPL-disparity emerges from the cortical-bone regions. This can be also affected by the choice of the ϵ stopping parameter and/or convergence performance of the SART algorithm.

Table 6.6: Experimental and simulated rWEPL results and RE assessment after post-processing of the tissue-equivalent rods inserted in the cylindrical phantom, in comparison to the expected true values.

Tissue surrogate	rWEPL True	rWEPL Exp. + prior-BPD	rWEPL-IQR Exp. + prior-BPD	rWEPL-RE Exp. + prior-BPD [%]	rWEPL Sim. + BPD	rWEPL-IQR Sim. + BPD	rWEPL-RE Sim. + BPD [%]
Adipose	0.970	0.977	0.023	0.72	0.974	0.023	0.41
Bone400	1.216	1.224	0.037	0.66	1.210	0.069	-0.49
Muscle	1.057	1.059	0.021	0.19	1.058	0.021	0.09
Breast	0.989	0.993	0.029	0.40	0.997	0.032	0.81
Bone200	1.117	1.122	0.022	0.45	1.137	0.031	1.79
Cortical bone	1.688	1.687	0.058	-0.06	1.667	0.034	-1.24
Liver	1.064	1.106	0.052	3.95	1.030	0.024	-3.20
Top PMMA	1.161	1.172	0.021	0.95	1.163	0.020	0.17
Bottom PMMA	1.161	1.170	0.022	0.78	1.162	0.020	0.09

In order to identify the phantom regions in the experimental image which are more prone to uncertainties, rWEPL absolute-difference maps between the best and worse scenarios according to the global rWEPL-REs reported in Table 6.5 are presented in Figure 6.12 for the three iCT-slices studied. The largest rWEPL-accuracy enhancement is achieved after applying the prior-BPD post-processing technique to the experimentally acquired iCT.

Figure 6.12: rWEPL-difference maps between the experimental IC-slices before and after post-processing.

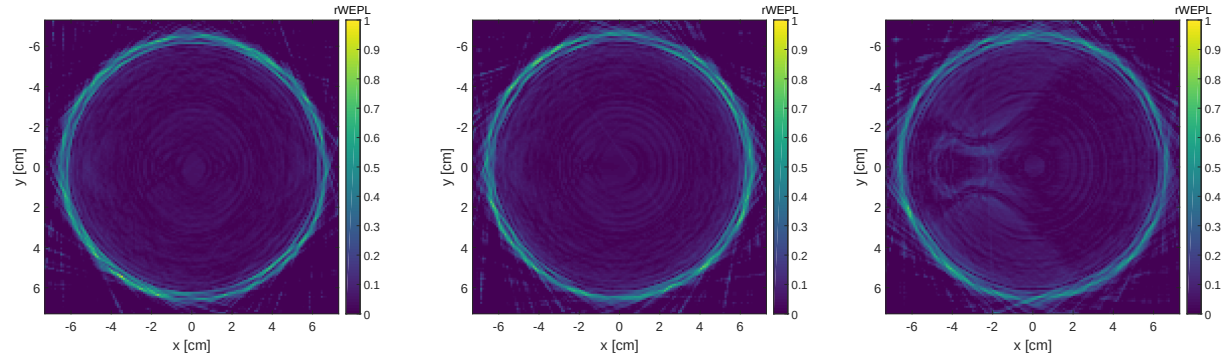

(a) 1st iCT-slice including muscle, bone400 and adipose inserts.

(b) 2nd iCT-slice including breast and bone200 inserts.

(c) 3rd iCT-slice including cortical-bone and liver inserts.

In comparison to the raw-image, the post-processing technique aids to remove the aforementioned strip artifacts (cf. Figure 6.12) caused by wrong WET-values assigned at the phantom borders in the projection domain. Furthermore, it is evident by comparing Figure 6.7a with Figure 6.7b and Figure 6.8a with Figure 6.8b that by decomposing the BC and assigning the dominant WET at material density-interfaces in the radiography domain, the phantom and inserts circumferences are better defined and shrunk toward their expected dimensions, resulting in an overall experimental image-quality comparable to that obtained by MC-simulations. This correction also occurs in the post-processed simulated iCT-slices 6.7d and 6.8d.

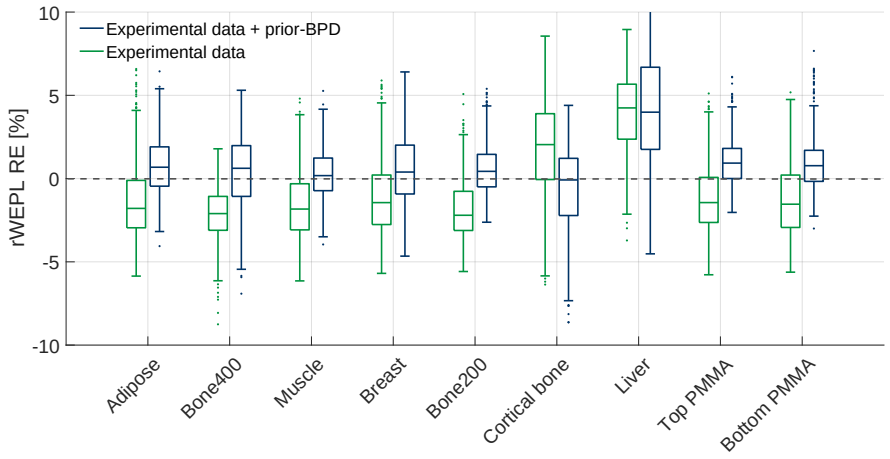

Figure 6.13: Comparison of the rWEPL-REs per tissue-equivalent insert of the cylindrical phantom obtained with experimental data before (green) and after post-processing (blue). The box-plot indicates the same statistics as in Figure 6.10.

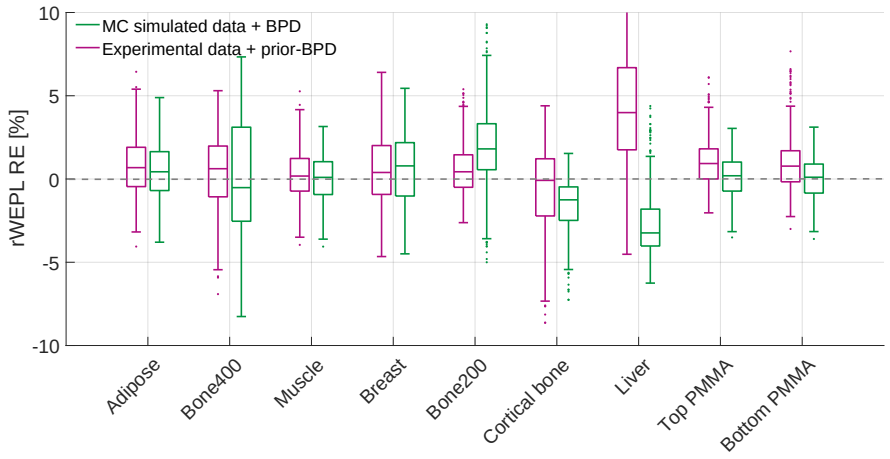

Figure 6.14: Comparison of the rWEPL-REs per tissue-equivalent insert of the cylindrical phantom obtained with post-processed experimental (magenta) and simulated data (green). The box-plot indicates the same statistics as in Figure 6.10.

6.3 Tomographic imaging dose

As it was explained before, at the radiography level, the physical-dose received by the imaged target is determined by the primaries deposited per pixel (beam-fluence), the separation between RPs and the beam-energy (cf. Section 4.3), particularly in cases where high-density materials are involved and the BP is stopped very close to the RRD entrance.

To facilitate the experimental acquisition of all the necessary projections for the iCTs reconstruction, both tomographies presented in this thesis were acquired under the high-dose scenario, which does not require additional technical adjustments in the synchrotron standard functionality. This scheme consists on depositing 5000 ions per RP, separated in 1 mm steps. For the tomographic acquisitions, the angular-sampling also influences the received dose; both phantoms investigated were rotated in angular steps of 0.9°, which results in 400 projections to cover 360° (cf. Section 4.1.3). The full tomography dose is thus obtained by multiplication

of the single projection dose with the number of projections used for the iCT reconstruction.

Recalling the radiographic doses presented in last chapter, in this high-dose configuration, the slab and the rod-inserts cylindrical phantom received 10.165 mGy and 10.072 mGy per projection, respectively (cf. Tables 5.3 and 5.6). Consequently, the full tomography acquisition yields a physical-dose equal to 4.07 Gy for the slab phantom and 4.09 Gy for the rods one. The dose can be reduced to the half when only 180°-coverage projections are used, in case the noise-level of the measurements are not extreme. These dose-levels are still very high for a desired ion-based transmission-imaging framework to be used clinically. However, considering the image-quality achieved with the post-processed low-dose iRADs (500 ions/RP in 1 mm steps) of these phantoms, iCTs (using only 200 projections) can be achieved with a dose to the target up to ∼0.20 Gy for both phantoms. Additionally, by increasing the separation of the scanning steps to 2 mm and depositing 1000 ions in each RP, as it was also presented for the slab phantom before, tomographic acquisitions of 0.10 Gy can be performed. It is worth to bear in mind that the dosimetric results shown in these studies were obtained from the simulation of iCTs obtained with the nominal number of ions (5000 carbon-ions/RP) in the high-dose regime; however the measured signal represents only a small fraction (under 50%) of this initially irradiated particles, due to the poor performance of the current electronics system (cf. Section 3.4.4). This means that the dose could be significantly reduced when the DAQ system is improved.

Part IV.
Wrapping up

If we knew what it was we were doing, it would not be called research, would it?

Albert Einstein

7

Preliminary investigations towards combining the integration-mode residual-range detector with a floating-strip Micromegas tracking system

Lighter ions inherently undergo larger MCS effects than heavier ones, statistically resulting in a deviation from their initial trajectory, as it was introduced in Chapter 2, Section 2.1.3. The MCS process underlying the transmission-imaging principle (cf. Figure 2.5) and the spatial-resolution limitation affecting especially proton based-imaging was also discussed. This shortcoming motivates the search for a hybrid detection solution that allows single-ion tracking in combination to the integrated ionization signal obtained from the RRD. Exploiting single particle position and angle data provided by tracking detectors located before and after the imaged object, together with a range telescope capable to render individual-particle information, might be useful to estimate the ions-MLP used for the reconstruction. This was found to increase the image spatial resolution [Li et al. 2006]. In the case of the integration-mode RRD used in this work, another promising application is to merge the output of both detector systems (beam spot-size from the Micromegas and integrated signal from the RRD) to add information about the amount of particles in certain defined ROIs or at material-interfaces, thus potentially enhance the spatial resolution of the projections acquired with the RRD.

This chapter is intended to establish the transition from the carbon-ion-based imaging, which is the core study of this thesis, towards the potential use of the RRD to produce iRADs and iCTs with lighter particles, such as protons and helium-ions. By complementing the integrated beam information per known RP with individual-ion information from tracking detectors, it might be feasible to enhance the image-quality. For instance, at extreme material-transitions, it would be possible to determine which fraction of the beam spot-size (in terms of single events) actually passed through each material, simplifying the distinction of the correct BPs,

whenever multiple peaks appear. The preliminary results presented in the following were obtained from independent experimental measurements performed with a position-sensitive Micromegas system alone, and coupled with the RRD described before. Further investigations on proton and helium imaging using the latter experimental setup will be found in Kopp [2017]. The measurements presented in this chapter were part of a combined series of experiments performed at HIT to investigate the potential of Micromegas tracking detectors coupled to a scintillator-based range detector for transmission-radiography [Bortfeldt et al. 2016]. Besides the originally intended experiments, additional irradiations were designated to pursue the MCS studies presented here, aiming at measuring the beam-spreading undergone by the proton and carbon-ion beams after traversing the phantom and before the RRD entrance. In the case of carbon-ion imaging, straight ion-paths have been assumed so far, relying on their reduced MCS. However, when the ion-beam crosses dense materials non-negligible beam spreading is expected.

In order to measure the entrance, exit and deviation angle of individual ions, a tracking-system consisting of four low-material budget Micromegas with one-dimensional strip readout and two Micromegas with two-dimensional strip readout has been used. As it will be detailed in the coming sections, different experimental configurations were explored to investigate the energy- and material-dependence on the beam-scattering of both, protons and carbon-ion beams, when traversing the homogeneous PMMA stepped phantom and the tissue-equivalent slab-phantom. The information about the beam lateral-broadening can be also used for the beam-spot model required by the advanced post-processing methods being developed to deconvolve the redundant information of the integrated BCs between the RPs [Gianoli et al. 2016], which would improve the image spatial-resolution.

7.1 Materials and Methods

7.1.1 The Micromegas detectors

The Micromegas detectors and their potential in transmission ion-based imaging were briefly described in Section 2.4.3. Nonetheless, a throughout characterization of their development and performance can be found in Bortfeldt [2014]. The functional principle of this type of detectors is outlined in Figure 7.1a and a traversal cut through a Micromegas doublet used for the presented experiments is shown in Figure 7.1b.

The Micromegas detectors, following the principle of any gas-filled detector, measure the charge created by the ionization process of traversing charged particles within their active volume. What differentiates the Micromegas from typical ionization chambers is the metallic *micro-mesh* located in between the gas-gap delimited by the readout electrodes. Therefore, these detectors have a two-stage parallel-plate gap: a drift gap of 6 mm between the cathode and the micro-mesh and a small amplification gap of 150 μm. The ionizing particles produce electron-ion-pairs in the wider drift-zone, then the electrons travel towards the amplification region between the mesh and the copper anode-strips, where they are amplified due to an avalanche effect (cf. Figure 7.1a). This band-like structure of the anode gives the *floating-strip* attribution to this type of detectors. The copper anode-strips are individually connected to the HV via high ohm resistors. In this way, during a discharge, the potential difference can *float* and each strip can quickly recover. The floating-strip Micromegas used for these acquisitions

Figure 7.1: Micromegas functional principle (left panel) and combined doublet (right panel).

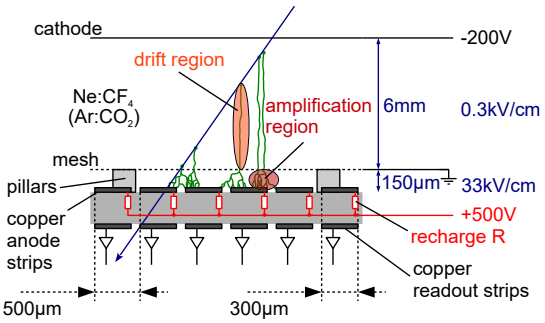

(a) Scheme of a one-dimensional floating strip Micromegas. Courtesy of F. Klitzner in Klitzner et al. [2016]

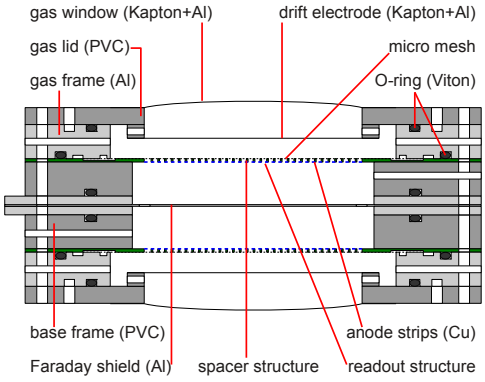

(b) Traversal view of a floating strip Micromegas doublet composed of two single detectors mounted together, either with a one- or with a two-dimensional readout structure. Courtesy of J. Bortfeld in Bortfeldt [2014].

have an active area of $64 \times 64\,\mathrm{mm}^2$, which is subdivided into 128 strips that enable single-particle position determination in one dimension [Bortfeldt 2014]. The overall WET of a single Micromegas layer is on the order of $(200 \pm 50)\,\mu\mathrm{m}$.

For the beam-scattering experiments performed at HIT, two Micromegas detectors were attached in one single unit called *doublet*, as it is shown in Figure 7.1b. Three of these doublets are positioned in the dedicated experimental setup. Figure 7.2 represents the information at different stages of the beam-trajectory which is required to reconstruct single-particle straight paths: x and y ion-coordinates before and after the phantom and the scattering angle.

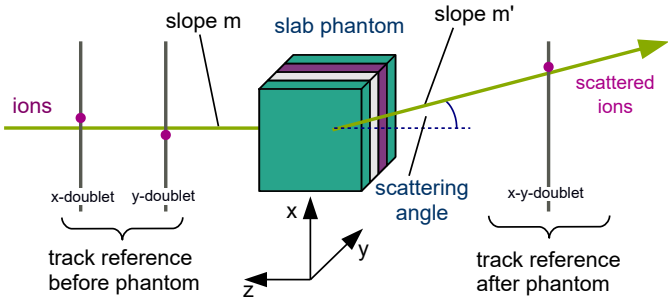

Figure 7.2: Schematic representation of the information needed for single-ion tracking before and after the traversed object. The tracking system before the phantom is represented by the two track reference-planes x and y, each corresponding to one Micromegas one-dimensional (1D)-doublet. Analogously, individual particles are tracked after the phantom with a 2D-doublet represented with a single track reference plane which contains 2D information. Courtesy of F. Klitzner.

7.1.2 Experimental setup

The beam-scattering studies were carried out with the setup shown in Figure 7.3. The RRD was simultaneously set for data acquisition since the individual ion-tracking information was intended to be combined with a iRADs. The readout system of the Micromegas tracking detectors thus requires a single-particle trigger signal. This was derived from a coincident signal in two off-axis placed finger-structure scintillators for the carbon-ion irradiations. In the case of the proton-beam acquisitions, the triggering signal was obtained from a signal detected in a

100 mm×90 mm wide scintillator of 10 mm thickness, placed directly in the beam-path before reaching the RRD. The latter configuration was mandatory since the number of scattered secondary particles used for triggering is significantly smaller than the ones produced with carbon-ion beams.

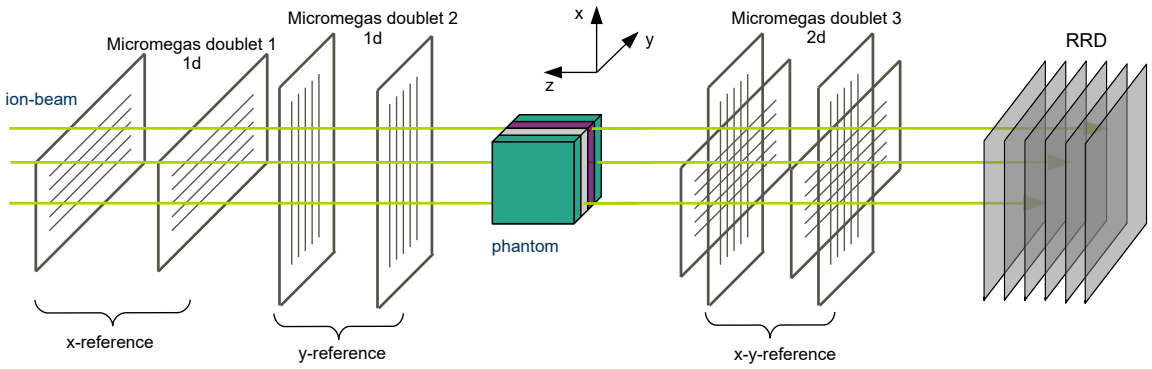

Figure 7.3: Experimental setup for the beam-scattering investigations performed with the Micromegas tracking system and the RRD.

The 2D-information of the beam position between the nozzle and the phantom location is measured by two 90° rotated (around the beam-direction -z) 1D-Micromegas doublets, corresponding to x and y coordinates, respectively. The beam spots after traversing the phantom volume are then recorded by a one 2D-Micromegas doublet. The output of each of the up- and down-stream coupled-trackers is combined into *reference* virtual planes (cf. Figure 7.4) that collect the hits clusters at each doublet for further analysis. Proton and carbon ionization signals are inherently different owing to their different stopping power. Hence, the definition of the reference planes for data analysis differs from one ion-type to the other, according to the signal characteristics or limitations, as it will be detailed in the following section.

7.1.3 Analysis methods: Stand-alone identification of RPs and beam-spot shape of proton and carbon-ion beams

Figure 7.4 schematically shows the reference planes used to reconstruct the scanning pattern of both proton and carbon-ion beams and discern the RPs.

In the case of proton beams, from left to right in Figure 7.3, the first Micromegas doublet (1) provides the combined spot information for the x-reference plane before the phantom. The second Micromegas doublet (2) gives the y-reference before the phantom and the third Micromegas doublet (3) determines only the y-reference after the phantom, since the x-stripes did not yield the sufficient statistics to afford the 2D retrieving of all the beam-hits (cf. Figure 7.4, upper panel). Either due to an unexpected disconnection or mistake, no drift HV was applied to the Micromegas during these measurements, which made it impossible to track the protons individually. Nonetheless, only simultaneous hits on two detectors are required to reconstruct a beam-spot before and after the phantom, which considerably increases the number of particles registered for each RP. The combined hits constitute a *tracklet* of two detectors, using an extrapolated hit in the middle of both detectors. For carbon-ions tracking, only two reference-planes were necessary to obtain the 2D information before and after the phantom (cf. Figure 7.4, lower panel), owed to their larger stopping power.

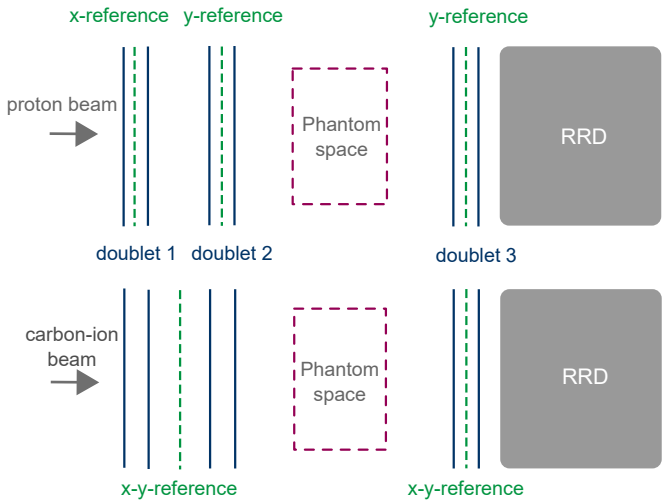

Figure 7.4: Sketch of the virtual-planes defined to analyze automatically the data extracted from combined Micromegas-doublets according to Figure 7.3. The reference-panels used for the proton acquisitions are shown in the upper panel, whereas the lower panel outlines the arrangement of the virtual-planes used for the carbon-ion data analysis.

The next challenging task in the analysis procedure, before the identification of single-particles or beam-spots, is to determine the scanning pattern followed by the ion-beam and extract the information corresponding to each RP. For this purpose, an automatized ROOT[A] script was developed[B]. The methodology consists of recognizing high-quality tracks with customized thresholds and differentiating the RP sequence followed by the ion-beam. Figure 7.5 displays exemplary Micromegas data of the reconstructed x- and y-position of a proton-beam before crossing the phantom. The ion-beam moves originally in a horizontal zig-zagged pattern to cover the FOV. Thus, this trajectory is translated in short beam-steps in y (cf. Figure 7.5b) with the beam staying for a longer time in one x-position (cf. Figure 7.5a). A so-called *sliding-window technique* automatically splits this sequence in the scanned RPs. The underlying principle of the average running-window consists of calculating and comparing the mean position in two different windows, before and after an optimized number of recognized events in the windows, and look for the maximum difference (within a given threshold), which indicates that a transition to a new RP has occurred.

Once the RPs have been identified, the hits belonging to each event fill single-RP histograms, that are fit either to two 1D-Gaussian, one in each direction (protons) (cf. Figure 7.6) or to a 2D-Gaussian (carbon-ions) (cf. Figure 7.7). In the following, the x- and y- mean-position and width (σ) of the beam-spot are then individually extracted from the Gaussian parametrization.

The Micromegas detector single particle tracking capability is determined by three main factors[C]:

1. Readout electronics: The APV25-based electronics used for data-acquisition in these measurements has a maximum readout rate of about 1 kHz. Therefore, although the Micromegas detectors have a higher detection rate, the readout system is bounded to the

[A] https://root.cern.ch/

[B] Thanks to F. Klitzner (LMU) and J. Bortfeld (CERN) for developing the analysis strategy to be applied on the Micromegas experimental data.

[C] Private communication with J. Bortfeld, December, 2016

Figure 7.5: Reconstructed two-dimensional beam-position (scanning pattern) of a proton beam in the Micromegas active area before the image target. Data provided by F. Klitzner.

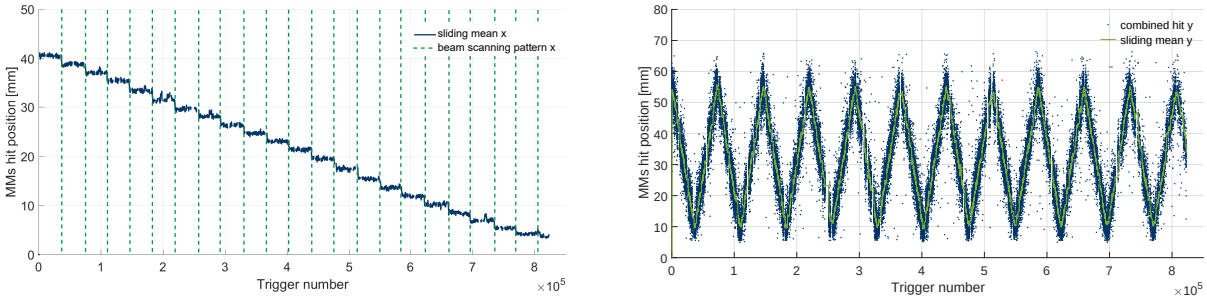

(a) Reconstructed beam hit position in the Micromegas x-direction.

(b) Reconstructed beam hit position in the Micromegas y-direction.

Figure 7.6: Exemplary x- and y-beam-spot distributions of a 157.43 MeV/u proton beam fitted to a Gaussian curve. The beam has a 10.7 mm FWHM at isocenter, which corresponds to a $\sigma \sim 4.54$ mm. This RP characteristics were extracted from a 5×5 FOV scanned in 2 mm steps detected with the Micromegas-doublet placed in front of the phantom. Since the detection point is located before the isocenter, a smaller beam-size than the one reported in the HIT's LIBC is expected. Figures courtesy of F. Klitzner.

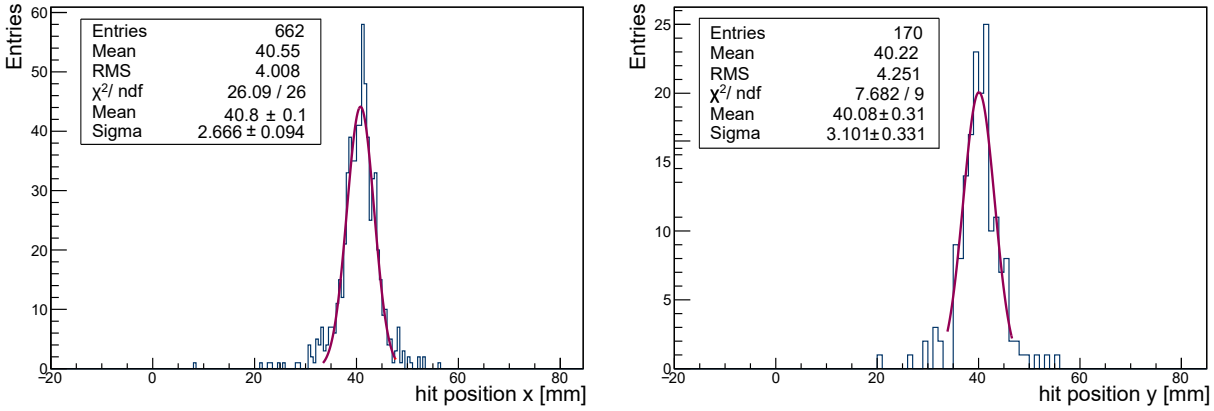

(a) Exemplary spot-distribution in x-direction of a proton beam corresponding to the RP number 5 and corresponding Gaussian fit parameters.

(b) Exemplary spot-distribution in y-direction of a proton beam corresponding to the RP number 5 and corresponding Gaussian fit parameters.

electronics limit. In order to increase this rate to around 1 MHz a different electronics, based on the so-called VMM3 chips (cf. Section 8.2.3), must be considered.

2. Detector rate capability: The maximum particle flux, that any strip detector can handle (in the sense that coincident particle hits are reconstructed as individual hits), is determined by the strip pitch and the signal duration. These floating-strip Micromegas are able to separate all particle hits up to particle rates of 10 MHz. This corresponds to a particle flux of about 7 MHz$\times cm^{-2}$ [Bortfeldt et al. 2015]. If the rate becomes larger, individual particle hits are merged into clusters. Nevertheless, up to a rate of 80 MHz individual particles can still be registered, although with reduced efficiency.

3. Drift field: The drift field produced by the HV considerably improves the collection of charge in the the detector and thus greatly enhances the signal behavior. Due to the high ionization of carbon ions, the detectors were working well with the carbon-ion beams and

Figure 7.7: Detected carbon-ion beam spots using the sliding-window technique. Two RPs extracted from a 5×5 cm^2 FOV actively scanned with a 299.94 MeV/u carbon-ion beam are shown. Figures courtesy of J. Bortfeld.

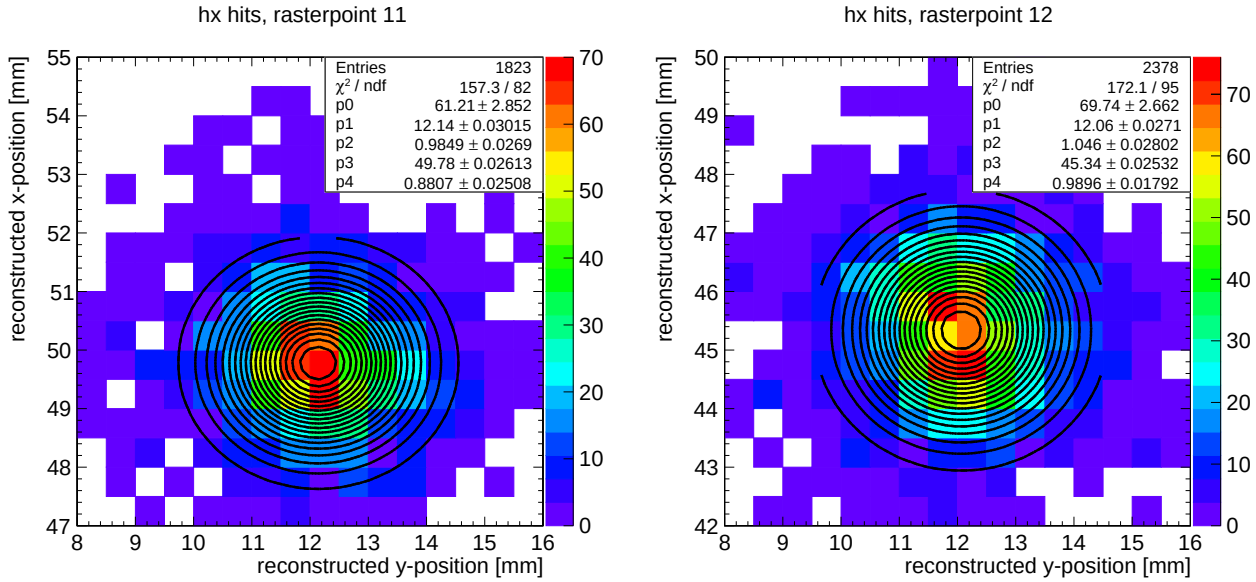

(a) RP number 11

(b) RP number 12

were able to track all single ions. For the protons on the other hand, the drift field would have been necessary.

Proton beam irradiation

In order to avoid the overflow of the trigger and readout systems due to high particle-rate, all the acquisitions were taken in the synchrotron research mode, that allows to irradiate low-fluence beams necessary for lower-dose scenarios (cf. Section 3.3) than the levels typically used in the clinical practice. The beam-intensity has been reduced to 1% of the lowest nominal intensity (8×10^7 pps) by decreasing the current threshold allowed by the first IC of the BAMS (cf. Section 2.1). The irradiated plans covered a FOV of $5\times5\,\mathrm{cm}^2$ in 2 mm scanning-steps. Three different irradiations were conducted in this study:

1. Air-projection (no phantom) with a 157.43 MeV proton-beam of the smallest focus (10.7 mm FWHM at isocenter, corresponding to a $\sim$ 4.5 mm σ), allocating 8×10^5 primaries per RP (cf. Figure 7.8a and 7.8b).

2. Slab-phantom projection with a proton beam of the smallest focus at 157.43 MeV and 8×10^5 primaries per RP (cf. Figure 7.8).

3. PMMA stepped-wedge-phantom projection with a proton beam of the smallest focus (8.1 mm FWHM at isocenter $\sim$ 3.4 mm σ) at the highest beam-energy 221.06 MeV and 8×10^5 primaries per RP (cf. Figure 7.10).

Carbon-ion beam irradiation

Carbon-ion beams at 299.94 MeV/u with the smallest focus (3.9 mm FWHM at isocenter, corresponding to a $\sim$1.66 mm) and the lowest beam-intensity available (2×10^6 pps) were used to scan a $5\times5\,\mathrm{cm}^2$ extended-field in 5 mm RP-steps to image the following configurations:

1. Air-projection (no phantom between the tracking system).
2. Slab-phantom projection (cf. Figure 7.11).
3. PMMA stepped-wedge-phantom projection (cf. Figure 7.13).

7.2 Results and discussion

Since the RRD operates in a integration-mode, individual-particle information is not available for the transmitted-images obtained with carbon-ion beams in this thesis, nonetheless the image-quality is acceptable under the assumption that the beam-spread of heavy-ions is minimal. However, the same premise does not hold for lighter ions. In order to evaluate the effects of MCS on the detected beam, the change ion-beam spot-size is investigated before and after traversing air and various phantom materials in the aforementioned irradiation configurations for protons and carbon-ions.

7.2.1 Proton beam scattering

Figures 7.8a and 7.8b show the RPs detected by using the sliding-window strategy (cf. Section 7.1.3) before and after the phantom position, respectively. The color-scale represents the spot-size width in y-direction, given in mm, i.e., the σ_y of the Gaussian fit. In this first comparison, no target is placed. As it was mentioned above, the x-stripes of the third reference plane corresponding to the 2D-Micromegas doublet did not provide position information after the phantom space. Therefore, the x-data-points of each RP were always defined by the first Micromegas doublet.

In principle, a homogeneous grid of RPs is expected. However, some dead-strips in the second and third Micromegas-doublets were identified, thus being likely the cause of the observed irregularities in some regions of the FOV. On the other hand, several RPs are also missing due to the overloaded readout system that was explained before.

Nevertheless, keeping in mind that in the optimal detector functioning conditions of the Micromegas listed above, the detectors are capable to track individual particles, the inhomogeneities can be resolved by implementing this single-ion additional information. As it is expected, the 157.43 MeV proton beam is scattered and undergoes beam-divergence even in a short air-distance. The mean beam-width registered by the first measurement plane was $\sigma_{0y} = 2.7$ mm, corresponding to a ∼6.4 mm FWHM. After the beam traversed about half a meter of air, the second Micromegas-doublet measured a mean beam-width of $\sigma_{2y} = 3.6$ mm, i.e., ∼8.4 mm FWHM, which is consistent with the fact that the second Micromegas-doublet was positioned shortly before the iso-center, where a beam-FWHM = 10.7 mm is expected according to the HIT's LIBC.

Figure 7.8c depicts the relative augmentation in the proton beam lateral profiles due to MCS within the different tissue-equivalent materials. As the form of the Highland's formula suggests (cf. Equation 2.11 in Section 2.1.3), the βpc term in the denominator, which includes the projectile mass, velocity and beam-energy information, greatly influences the extent of the final beam-spread. This implies what it was shown already in Figure 2.5 when only air is crossed: lighter ions as protons will experience more scattering than the heavier ones and the angular scattering significantly increases towards low beam-energies. However, when the

Figure 7.8: Identified proton beam-spots by the Micromegas doublets positioned before and after the phantom location, according to the experimental setup. Different RPs throughout the irradiated FOV of 5×5 cm^2 are recognized. Measurements with and without the presence of a phantom are presented. The width (σ) of each RP is indicated by the color scale in mm and the marker size is arbitrarily chosen.

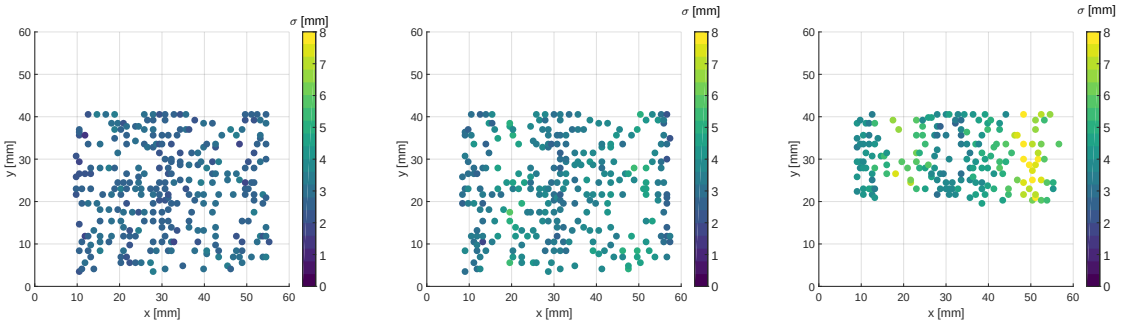

(a) Identified RPs in the irradiated FOV by the Micromegas doublet located before the phantom position.

(b) Identified RPs in the irradiated FOV by the Micromegas doublet located after the phantom position, without phantom.

(c) Identified RPs in the irradiated FOV by the Micromegas doublet located after the slab-phantom.

slab phantom is positioned in between the Micromegas-doublets 1 and 2, the beam-spread dependency on the traversed materials also becomes evident (cf. Figure 7.8c). Recalling the geometrical arrangement of the tissue-equivalent tiles in the slab-phantom: muscle, inner bone, lung, adipose, cortical bone and muscle, it is visible that the scattering effects are enhanced at the inner-bone (at around $15 < x < 25$ mm) and the cortical-bone regions (approximately at $45 < x < 55$). The target material in Equation 2.11 is described by its thickness (L) and its radiation length (L_{rad}). The latter term gets smaller for dense or high-Z materials. In consequence, targets with these characteristics cause a larger angular spread than targets of light elements with the same thickness [Schardt and Elsässer 2010], as it is clearly shown in Figure 7.9. In this graphics, histograms of the beam-σ detected in the third Micromegas-double, after traversing the different tissues of the slab-phantom, are superimposed. The mean σ per material distribution is also indicated with dashed lines. The cortical- and inner-bone surrogates are the materials that cause the largest beam-scattering, being the Gaussian standard deviation (σ) increased after the phantom approximately by a factor of 2.6 and 2.1 times, respectively, relative to the mean initial beam-width $\sigma_0 = 2.7$ mm.

Besides the slab phantom, the PMMA stepped-wedge phantom has been placed in the center of the tracking system and irradiated with the highest proton-beam energy available at HIT (221.06 MeV/u). Figure 7.10 shows the detected RPs on the first (left panel) and on the second (right panel) Micromegas-doublets. As expected from the Highland formula, before traversing any material, the RP spot-size of higher-energy beams is reduced compared to the one corresponding to the lower beam energy presented above (157.43 MeV, cf. Figure 7.8). A 221.06 MeV/u proton-beam yields an averaged σ_y of 2.2 mm corresponding to 5.2 mm FWHM before impinging the phantom and a mean $\sigma_y = 3.4$ mm equivalent to 8.0 mm FWHM after traversing a stepped homogeneous target. The σ_y-values detected by the third Micromegas-doublet are normally distributed allover the FOV, meaning that there is no beam-width position dependence after the high-energetic beam passes through the homogeneous phantom, although the geometry has a slight thickness variability in steps of 7 mm. The step phantom geometry

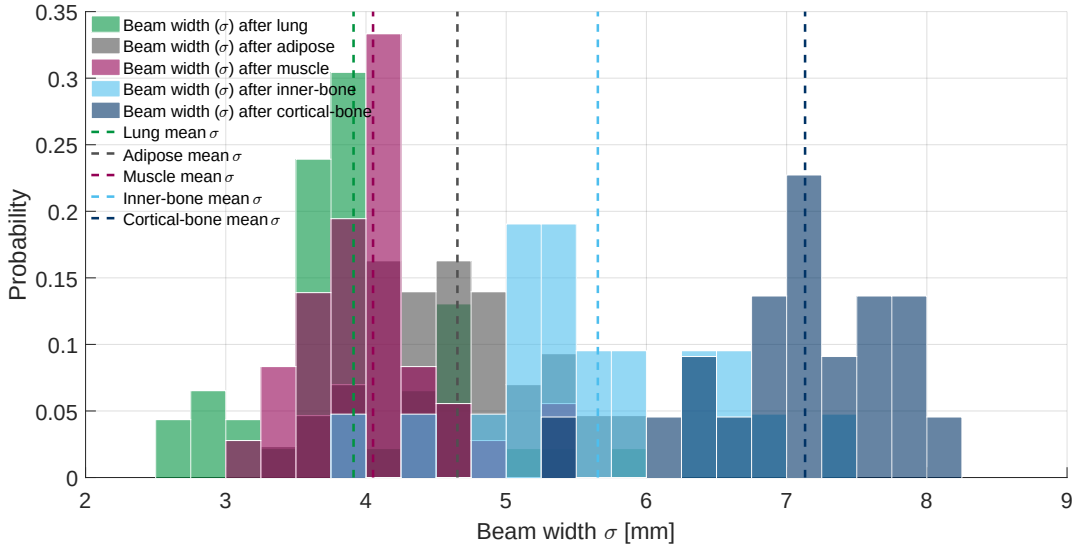

Figure 7.9: Histograms of the beam-spot width (σ) of a 157.43 MeV proton beam after traversing the different tissue-equivalent materials of the slab-phantom. The mean lateral beam-spreading (σ) is indicated with dashed lines for each tissue distribution.

is not recognized, which is an indication that for this energy and imaged objects in the order of ten of centimeters size, the scattering effects are only material dependent with no observable influence of such small target thickness changes. In fact, for the same proton-beam energy traveling only through air, a beam-focus of 8.1 mm FWHM at isocenter is expected according to the HIT's LIBC, therefore no significant scattering effects can be concluded.

Figure 7.10: Identified RPs by the Micromegas doublets positioned before and after the homogeneous stepped-wedge phantom irradiated with the highest proton beam-energy available at HIT, 221.06 MeV/u. The FOV of 5×5 cm^2 was scanned in steps of 2 mm. Using this beam-energy, the BP falls beyond the phantom. The width (σ) of each RP is indicated by the color scale in mm and the marker size is arbitrary.

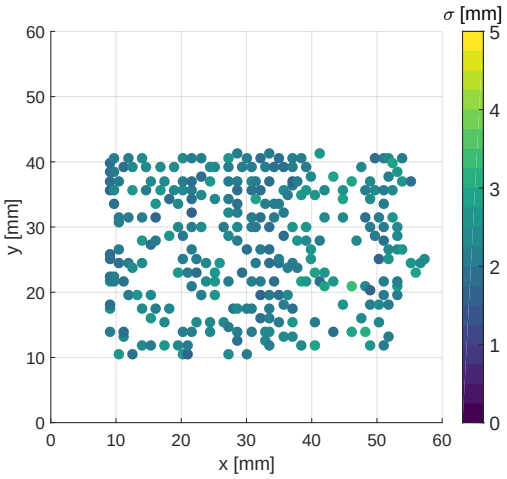

(a) Identified RPs in the irradiated FOV detected with the Micromegas doublet placed before the stepped-wedge phantom.

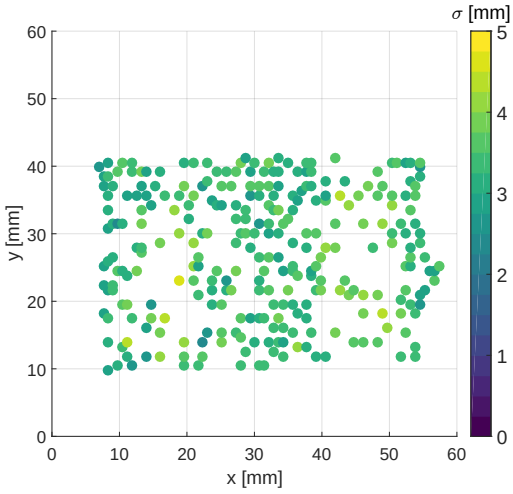

(b) Identified RPs in the irradiated FOV detected with the Micromegas doublet placed after the stepped-wedge phantom.

7.2.2 Carbon-ion beam scattering

As it was explained before, the higher stopping power featured by carbon-ion beams allows a better signal quality detected by the Micromegas, even when no drift voltage was applied. This is immediately reflected on the improvement of the individual RP detection and position determination. Before proceeding to examine the MCS of carbon-ion beams in the tissue-equivalent materials of the two phantoms, the little beam spread in air deserves few comments. An air-projection with a 299.94 MeV/u carbon-ion beam of the smallest focus (3.9 mm FWHM at isocenter) was performed. Bearing in mind the reference two planes used to combine the Micromegas-doublets (cf. Figure 7.4, lower panel) the mean beam-spot is fitted to a 2D-Gaussian (cf. Figure 7.6), thus the σ information is available in x- and y-directions. When no phantom is positioned in between the tracking system, a mean $\sigma_x = \sigma_y = 1.0$ mm was measured by the first reference plane, which corresponds to a beam focus of ∼2.4 mm FWHM. The second reference plane registered a mean of $\sigma_x = 1.4$ and a $\sigma_y = 1.5$ mm, i.e., approximately 3.4 mm and 3.6 mm FWHM, respectively, confirming the foreseeable minimal scattering effects of heavy-ion beams in air.

Figures 7.11 and 7.13 show the MCS aftereffect of carbon-ion beams when traversing the slab and stepped-wedge phantoms, respectively. Regarding the slab phantom, the spot-size of the carbon-ion beams measured by the second reference plane is shown in Figure 7.11b. It depicts a dominant MCS dependence on the material crossed approximately at the coordinates $45 < x < 55$ of the FOV, where the cortical-bone is projected. Therefore, contrary to the straight carbon-ion beam-trajectory assumed in this work so far, a non-negligible beam spread occurs when the carbon-ion beam travels through dense materials like bone structures. This suggests that also carbon-ion-based images might benefit from the additional positioning and angular deviation information provided by the trackers, for future post-processing methods that currently rely on beam-sizes obtained theoretically.

The carbon-ion beam spread due to different material composition is assessed in Figure 7.12 using tissue-specific histograms of the σ_y of the 2D-Gaussian fit applied to the identified RPs after the phantom. The sigma in y direction is an arbitrary choice, since it does not differ significantly from σ_x. The most extreme beam-spread is observed when the carbon-ion beam crosses the cortical-bone tissue-equivalent slab, which causes the beam-width to be enlarged almost 6 times compared to the beam-width before entering the phantom. In contrast to the proton case (cf. Figure 7.9), the adipose-equivalent material seems to cause a larger mean scattering of the carbon-beam. However, one can observe in Figure 7.11 that the FOV region where the adipose surrogate is imaged ($\sim 35 < x < 44$) contains two distinct outliers (colored in light blue and yellow) detected in the frontal and distal reference panels, which might indicate a failure of the Micromegas tracking or the parametrization algorithm in this specific RP that can negatively influence the averaged Gaussian standard deviation (σ).

Analogous to the proton-beam case presented above, the stepped-wedge phantom was also placed in the middle of the Micromegas tracking system. The carbon-ion beam detected on the second 2D-measurement-plane (cf. lower panel of Figure 7.4), confirmed the MCS phantom-thickness independence for the presented phantom geometry configuration. A mean beam-width featured by $\sigma_x = \sigma_y = 2.2$ mm, both centered in a normal-distribution over all the

Figure 7.11: Identified RPs by the Micromegas doublets located before and after the slab phantom irradiated with a scanned 299.9 MeV/u carbon-ion beam of the smallest focus (3.9 mm FWHM at isocenter). The FOV was 5×5 cm^2 covered in 5 mm scanning steps and depositing 2×10^6 primaries per RP. The marker color represents the standard deviation (σ [mm]) of the y-direction 2D-Gaussian fit and the marker size is arbitrary.

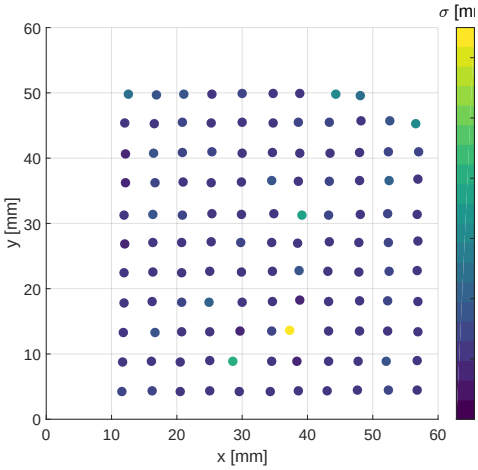

(a) Identified RPs in the irradiated FOV detected with the Micromegas doublet placed before the slab phantom.

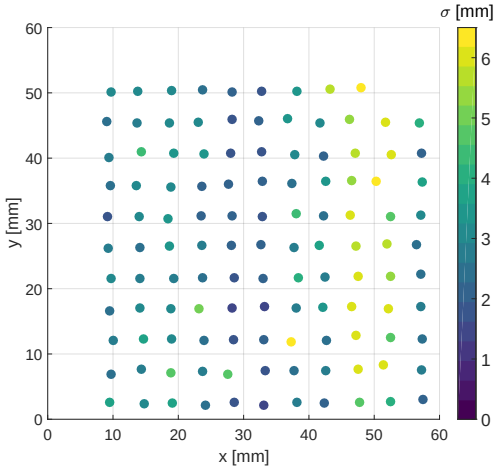

(b) Identified RPs in the irradiated FOV detected with the Micromegas doublet placed after the slab phantom.

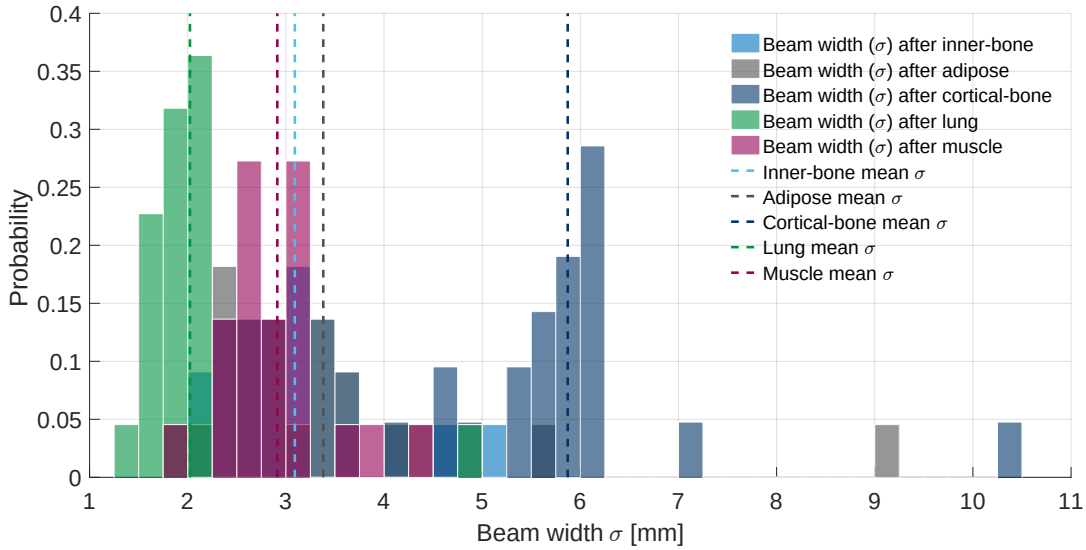

Figure 7.12: Histogram of the beam-spot width (σ) of a 299.94 MeV/u carbon-ion beam when traversing the different tissue-equivalent materials of the slab-phantom. The mean lateral beam-spreading (σ_y) is indicated with dashed lines for each tissue distribution.

RP in the FOV was found. Comparing this value with the averaged beam σ_x = 0.9 mm and σ_y =1.1 mm obtained with the Micromegas doublets before the phantom, the homogeneous PMMA causes a fairly constant beam-dispersion throughout the irradiated field of about 2.8 mm in FWHM, which is consistently slightly higher than the scattering effects observed due to air.

The findings from these preliminary studies suggest that even heavy-ion beams might present non-negligible scattering effects in dense and high-Z materials before being detected by the

Figure 7.13: Identified RPs by the Micromegas doublets located before and after the stepped-wedge phantom irradiated with a scanned 299.9 MeV/u carbon-ion beam of the smallest focus (3.9 mm FWHM at isocenter). The FOV was 5×5 cm^2 covered in 5 mm scanning steps and depositing 2×10^6 primaries per RP. The color scale indicates the beam-width (σ) in mm and the marker size is arbitrarily chosen.

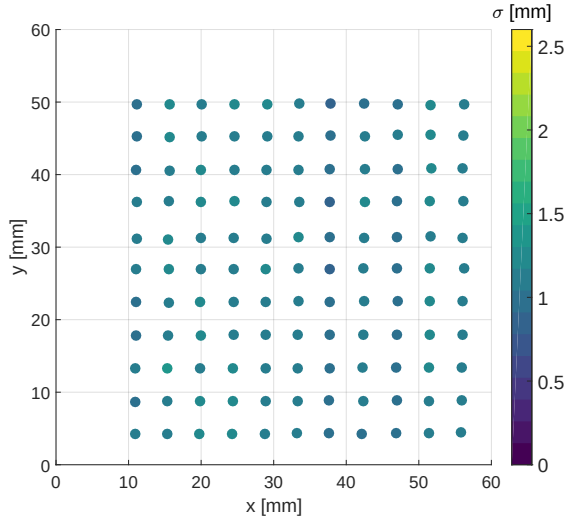

(a) Identified RPs in the irradiated FOV detected with the Micromegas doublet placed before the stepped-wedge phantom.

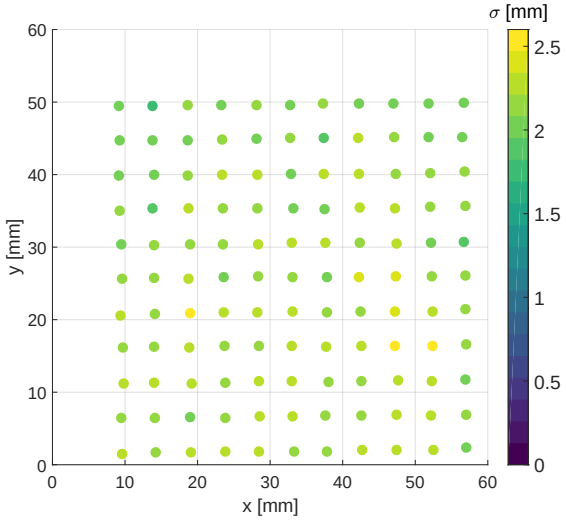

(b) Identified RPs in the irradiated FOV detected with the Micromegas doublet placed after the stepped-wedge phantom.

imaging system. However, it is important to bear in mind that the Micromegas detection setup might contain high-Z materials also contributing to the final beam spread. Therefore, there is a definite need of a careful characterization of the beam behavior traversing different materials combination, supported with single-particle information and the *in-silico* model of the experimental setup. Further envisioned investigations about the merged imaging detector system are commented in the outlook section of this work.

Focus on the journey not the destination. Joy is found not in finishing an activity but in doing it.

Greg Anderson

8 Conclusion and outlook

8.1 Conclusion

Ion-beam therapy has already a history of more than half of a century, since the first cancer patient was treated with proton-beams. From then onward, its incessant development has not stopped, following several research directions that aim to understand and wholly exploit the physical and biological capabilities of charged-particles to battle tumors. The current clinical practice of particle therapy follows well defined procedures and is routinely applied in several facilities worldwide. However, there is still a large room for improvement and progress; namely in two aspects that are significant within the context of this thesis: the accuracy of the treatment planning and the implementation of beam-range verification strategies during the treatment delivery. The investigations presented in this work pursue to minimize the uncertainties arising at these stages of the therapy.

It is well-known that charged-particle treatments feature a precise and confined dose deposition in the tumor volume, due to the so-called Bragg-peak. This also enables to maximize the protection of healthy surrounding tissue from unnecessary dose. However, these high-dose gradients inherent to ion-beams might also lead to detrimental over- or under-dosage of the tumor if the ion-beam does not stop in the intended position inside the patient. The main cause of beam-range uncertainties during treatment planning arise from the X-ray planning CT-HU conversion to the corresponding tissue-rWEPL. On the other hand, during treatment delivery, positioning and anatomical changes of the patient might introduce considerable inaccuracies. Nowadays these range-errors are typically overcome in the daily clinical-practice by expanding the margins of the treated volume, at the cost of extra dose deposited in (some cases) up to 1 cm of healthy tissue and/or using robust treatment plans. Ion-based imaging techniques support the mitigation of this major drawback. During the planning phase, they can provide direct rWEPL information of the tissue to be treated, and at the treatment site, they might serve

as in-vivo range verification/monitoring strategy, allowing to assure that the irradiation-dose is deposited only in the prescribed volume. This thesis was developed in the context of the joint DFG project: *A novel imaging technique for ion-beam therapy: Ion Computed Tomography* between the Lüdwid-Maximilians Universität, München, the Heidelberg Uniklinik through the Heidelberger Ionenstrahl-Therapiezentrum and the GSI Helmholtzzentrum für Schwerionenforschung, Darmstadt, Germany. The investigations accomplished in this work propose *ion-based transmission images* as a promising method to eliminate the aforementioned sources of uncertainty in the current practice of ion-beam therapy. The experimental research presented here was performed in the operating HIT facility in Heidelberg, Germany, and it focused on the development and characterization of the optimal experimental environment necessary for the generation of low-dose carbon- iRADs and iCTs using an integration-mode RRD as a range telescope.

An ion-based imaging system must fulfill minimal but crucial requirements towards its application in the clinical practice: assuring the minimal dose received by the patient and providing reliable anatomical information in terms of WET for planar projections (iRADs) or rWEPL for volumetric images (iCTs) of the imaged object. Bearing these demands in mind, the studies carried-out in this work can be divided in three major categories of investigations related to: facility, detection-system and image-formation.

- Facility investigations: The HIT synchrotron functionality at lower fluences than the therapeutic ones has been explored. Based on these studies, the lowest limit of ions that can be deposited per image-pixel of the acquired iRADs has been determined. Furthermore, the accuracy of the BAMS which control the beam-positioning and ion-delivery was compared to an external dosimeter in order to assess the monitoring-system behavior in the low-dose regime.

- Detection-system investigations: The experimental setup has been characterized and optimized for low-doses in terms of the SNR and current-voltage necessary for the best performance of the RRD-PPICs, since these factors have a great influence on the signal-quality that will be reflected in the subsequent image formation. The synchronization between the readout and the HIT active delivery systems has been improved, too, by modifying the trigger signal which links them together. Moreover, a new electronics module with a larger buffering and transmission-rate capabilities has been integrated to the RRD, allowing for simultaneous data-streaming with no delay.

- Imaging investigations: In order to gradually approach the anatomical complexities encountered in the human body, homogeneous and heterogeneous phantoms of different geometries and tissue-equivalent materials were imaged. An exhaustive quantitative and qualitative analysis of the images obtained was made in comparison to the ground-truth and simulated data. Data processing methods were applied at channel-, projection- and tomographic-domains, as well as dedicated MC-based post-processing methods were tested and implemented to accomplish the optimal trade-off between imaging dose and quality. All the images presented in this work were evaluated in terms of physical-dose to the object [Gy], accuracy [% of RE] and overall quality [NRMSD].

iRADs of a PMMA stepped-wedge homogeneous phantom and two heterogeneous (tissue-equivalent slab and rod) phantoms were acquired, exploring different experimental configurations such as initial beam-energy, ions per RP and RP-step size. The quality enhancement achieved after applying the prior-BPD method to the measured data was evaluated and compared to the results obtained from simulated images. All the radiographies resulted in a reliable representation of the irradiated geometries. The irradiation configurations that achieved the lowest doses for the tissue-equivalent slab phantom after post-processing were (1) a 0.501 mGy iRAD, with an overall image-quality of 13.93% NRMSD and an absolute global WET-RE of 1.29%; and (2) a radiography yielding 1.019 mGy dose, overall image-quality of 10.96% NRMSD and an absolute global WET-RE of 1.40%. The findings of this projection study indicate that, applying the dedicated post-processing methods, the imaging dose can be reduced to the minimum while maintaining its quality relatively stable. As for the rod-insert cylindrical phantom, it was possible to produce a 1.010 mGy iRAD with an overall image-quality of 5.45% NRMSD. The difference in NRMSD between the slab and rod phantoms is explained by the challenging geometry of the former one, and it reflects the frequent occurrence of multi-BP at sharp density-boundaries. The water-equivalence assessment of the cylindrical phantom tissue-surrogates was addressed from its tomographic reconstruction.

iCT of both heterogeneous phantoms were performed under the high-dose scheme. This configuration was merely chosen to facilitate the data acquisition without time-consuming technical adjustments needed by the accelerator to reach the lowest dose-levels. Nevertheless, with the encouraging low-dose projections previously obtained, it is possible to extrapolate conclusions about the dose received by the phantom due to a low-dose iCT. As mentioned above, the accuracy of the reconstructed iCTs was evaluated via the rWEPL-RE, before and after post-processing the measured data. As for the slab phantom, the overall absolute rWEPL-RE (including all the tissue-equivalent tiles) of the raw experimental tomography yielded 6.34%, which was greatly reduced down to 2.61% after implementing the prior+BPD method. This improvement indicates that decomposing the multi-BP encountered at material-interfaces and finding the most dominant rWEPL values successfully contributes to retrieving the expected stopping power properties of the imaged object. Concerning the rod-inserts cylindrical phantom, the absolute mean rWEPL-RE was reduced by 1.16% (from 2.07% to 0.91%) after the prior+BPD was used. Both high-dose full-coverage iCTs produced a $\sim$4.1 Gy imaging dose, which is still very high for the required clinical standards. However, by using low-dose projections and doubled RP step-size, full reconstructed iCTs can be produced with $\sim$0.2 Gy dose deposition. The dose evaluation was based on the nominal deposited dose to the phantom. However bearing in mind the low detection efficiency (in average about 50% for high-dose irradiations) of the current system due to fix-integration electronics, and the results based on these outcomes, one can optimistically foresee a significant dose reduction when the DAQ system is updated.

Furthermore, a transition towards the possibility to integrate the RRD with Micromegas detectors has been established. The Micromegas single-particle tracking capabilities are en-

visioned to extend the application of the RRD to proton- or helium-ions imaging, in which the MCS badly influences the image spatial resolution at both radiography- and tomography-level. Additionally, individual-ion information would definitely enhance the image-quality in the projection domain, since it would allow a more correct determination of the WET at each pixel, especially at sharp-density boundaries, regardless of the beam spot-size. Thereby, the preliminary beam-scattering studies carried-out might establish the grounding for post-processing techniques dedicated to exploit the redundant information between RPs due to the finite beam-size.

Taken together, the present investigation reinforces the application of ion-based transmission imaging to the ion-therapy clinical practice. The lowest-dose experimental limits have been attained and the major limitations of the investigated setup have been identified. Notwithstanding the shortcomings, the MC-based dedicated post-processing strategies have demonstrated being able to accurately retrieve the original water-equivalent geometry within an acceptable relative-error. In consequence, iRADs and iCTs could overcome two of the major sources of uncertainties faced in the daily application of ion-beam therapy, derived from the treatment planning and delivery processes. In the following, based on the results obtained so far, some considerations are introduced as future possibilities to continue the path from the research environment to clinical application.

8.2 Outlook

The envisioned near-future investigations considered to follow the research-line of this work are three-fold:

8.2.1 Upgrade of the ion-based imaging detector prototype

The upgrade version of the current transmission-imaging prototype is being developed at the GSI Detector Laboratory. In order increase the nominal depth resolution by a factor of three, which is currently limited by the thickness of the PMMA slabs (3 mm), the new RRD system will have 1 mm thick PMMA tiles to complete a 128-channel array, as it is illustrated in figure 8.1. The beam stoppers might be passive or active absorber plates for single particle tracking. The kapton electrodes also have a reduced thickness, from 25 to 20 μm.

The novel detector-design is accompanied with a comprehensive simulation investigation in two main directions: The first one, developed in FLUKA [Meyer et al. 2017] (cf. Section 4.0.1 for further details), emulates the whole image-formation principle including the active raster-scanning system and beam-line at HIT. These simulations serve as important reference for the exploration of plenty of experimental acquisition parameters with direct influence on image-quality. The in-silico imaging system, detailed in Section 4.0.2, already includes the increased resolution improvement planned for the upgraded detector (although the simulations used in this work are consistently based on a 3 mm absorber RRD model).

The second line of simulations research explores the physical response of the new geometry and material implemented in the RRD setup. Along with the design, the performance of the new detector generation has been simulated using GEometry ANd Tracking (GEANT4) [Agostinelli et al. 2003] and Garfield++[A] [Takechi et al. 2014]. For instance, the energy and

[A] http://garfieldpp.web.cern.ch/garfieldpp/

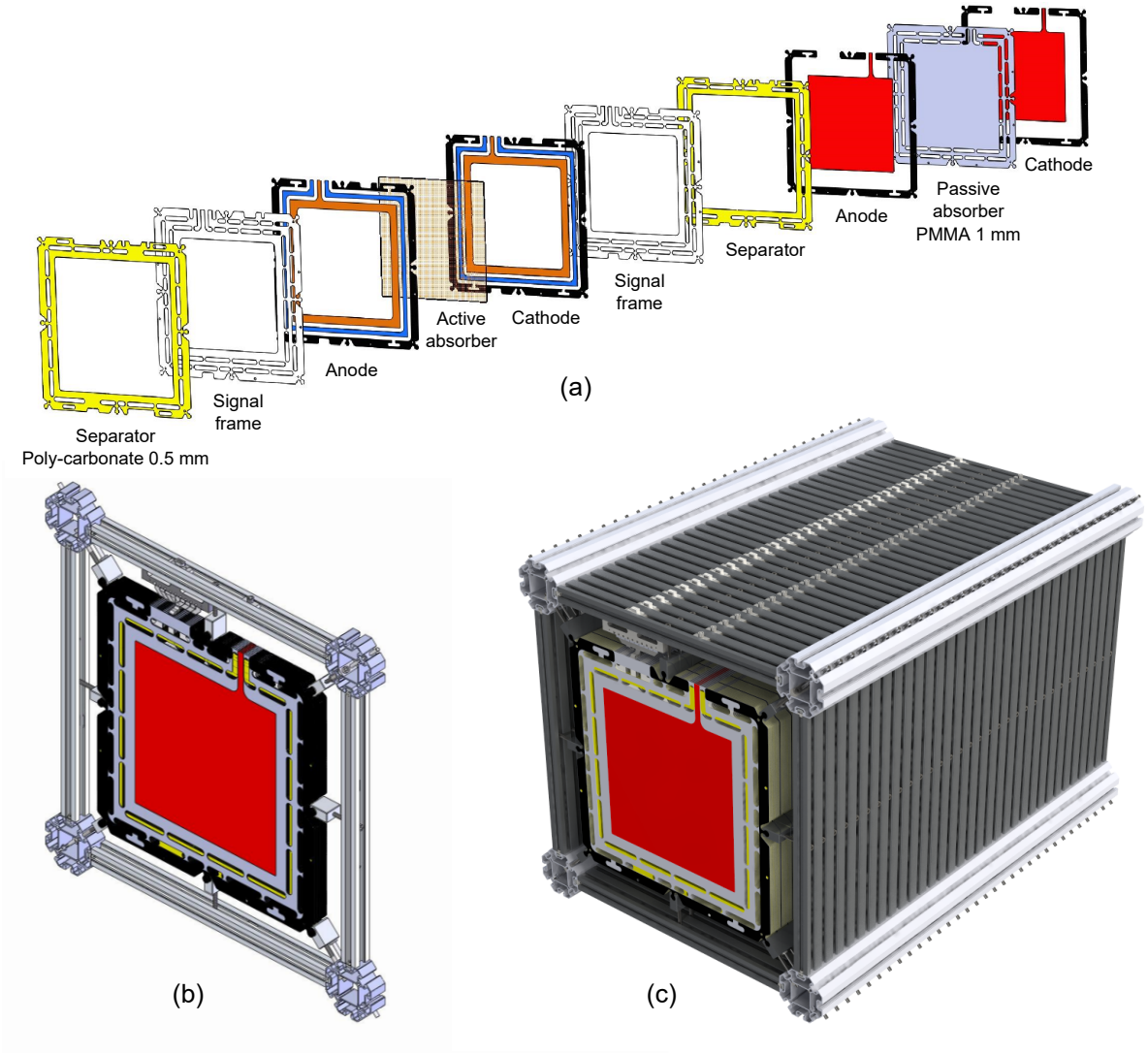

Figure 8.1: Upgrade of the ion-based imaging detector prototype. The major changes in the new design of the transmission-imaging detector are the reduced thickness of the PMMA absorbers from 3 mm to 1 mm and the potential inclusion of active absorber plates (a). For stability reasons, a modular assembly of electrodes and absorbers is necessary (b) to constitute the full-scale 128-channel PPIC stack structure (c). Isometric drawings courtesy of Bernd Voss.

angular straggling of the ^{12}C-ion beam in each PMMA slab was calculated by GEANT4. Additionally, the secondary electrons, their drift tracks and induced currents in the PPICs were calculated by Garfield++. The effect of the light fragments from the primary carbon-ion beam produced in the RRD absorbers on the spectrum of the BC is also being studied as can be seen in Figure 8.2.

8.2.2 Improved readout electronics system

A natural evolution of the current readout electronics points towards the implementation of an adaptive triggering signal that allows to increase the detection efficiency of the RRD. This possibility, as it was preliminary tested in this work, would enable larger integration times adapted to the variable RP duration, according to the inherent beam-intensity fluctuations. Consequently, an increased number of measured ions per iRAD pixel and considerable enhancement of the SNR is expected.

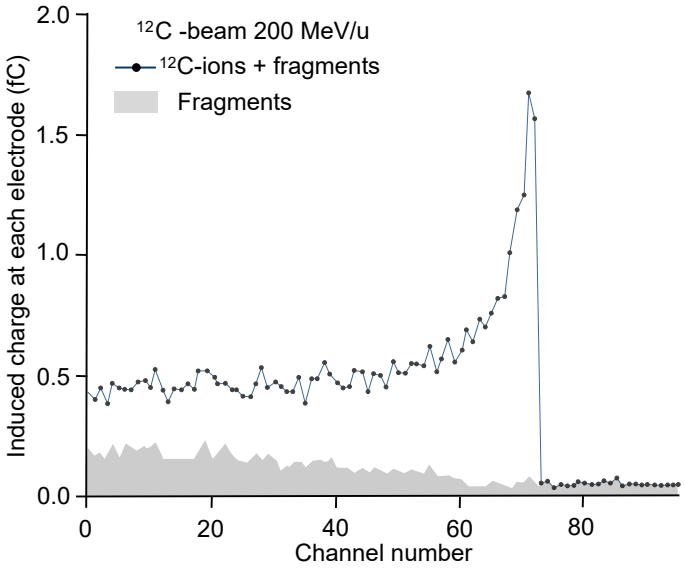

Figure 8.2: Simulated PPIC charge induced by a 200 MeV/u ^{12}C-beam and light fragments produced along the material traversed. Simulations are performed using Garfield++ and GEANT4 [Takechi et al. 2014].

8.2.3 Integration of single-particle tracker detectors with the RRD transmission imaging system

It has been shown that the Micromegas tracking detectors can provide integrated measurements of the beam spot shape as well as individual-ion position and angular scattering information. Hence, merging the data obtained from both detection systems (RRD and Micromegas) would assist the correct determination of the correct BP position, especially at sensitive regions that contain sharp-density boundaries, where multiple-BPs appear as a consequence of the integration-nature of the sole RRD.

Future studies in this direction have been put forward. For instance, new high-rate capable chips for the Micromegas detectors are being developed at CERN for the ATLAS experiment, and their use might be translated to medical imaging applications. Furthermore, two dimensional floating-strip Micromegas with a larger active area of 192×192 mm^2 are being investigated at the Ludwig-Maximilians Universität (LMU) [Klitzner et al. 2016].

Overall, this thesis strengthens the motivation to bring ion-based transmission imaging to the clinical practice. Given its potentiality to generate accurate low-dose transmission-images of the patient at the treatment site, the treatment planning and delivery might benefit directly to a great degree. As a *ripple-effect*, this novel imaging modality may also be suitable for Image Guided Radiotherapy (IGRT), ART (by refining the HU-rWEPL calibration curve in between the prescribed fractions) or for the integration with other available imaging techniques to provide all possible information necessary to comprehensively optimize the quality of ion-beam therapy.

Acknowledgments

Undertaking and concluding this PhD challenge has been a truly life-changing experience for me. It would not have been possible to complete it without many people who gave me the precise supportive hand in the most needed moments along this journey. There would never be enough space, nor words to express my gratitude to all of you who contributed in certain extent to this endeavor. However, I will try my best to fairly include all of you who helped with the best feedback, advice, support or hug necessary to bring this work till the end.

First of all, I would like to express my special appreciation and thanks to my main advisor Professor Dr. Katia Parodi, you have surpassed the attribute of mentor with your great commitment. The way you have encouraged my research and gave me the right guidance allowed me to grow as a becoming-scientist. Although I consider this career as a continuous and never ending learning process, the knowledge and experience that you have shared with me during these years is invaluable.

I also would like to thank the support of my second supervisor Professor Dr. Oliver Jäkel, you were always understanding on the difficulties faced along this way and your eagerness was crucial for me to go through. I also appreciate the different perspectives that you gave to my research, with your pertinent suggestions and expertise.

I am also grateful for the opportunity to share this project with Dr. Bernd Voss from GSI. Besides developing the main device which made possible these investigations, you always provided fruitful insights and discussions to guide the path of this work. Moreover, I admire your equanimity and good judgment whenever we faced difficult challenges.

I gratefully acknowledge the funding dedicated to my PhD, received from the DFG through the joint project: *A novel imaging technique for ion beam therapy: Ion Computed Tomography.* This financial aid gave me the opportunity to spend these years working at HIT, which definitely enriched my academic experience being close to the daily clinical environment. Furthermore, I feel fortunate for having the possibility to attend very important national and international conferences that contributed to my formation and kept me updated with the current state-of-the-art.

Thanks to my graduation committee members, Professor Dr. Andreas Burkert, Professor Dr. Jochen Weller , Professor Dr. Otmar Biebel and Professor Dr. Dieter Braun for accepting to be part of my committee and making a gap in your agendas for a close review of my thesis and attending to my defense in the following weeks.

Special and enormous thanks go to my dear LMU team, Chiara Gianoli, Basti Meyer, Ben Kopp and Max Goeppel. Your immeasurable support, not only in the academic-related issues but generally throughout this undergoing was crucial for me to strive towards my goal. I can not take all the credits of this work, it has been definitely a shared accomplishment. I would be always grateful for getting along so nicely with you. This allowed us to develop not only our research but our friendship, too. Without your help in endless beam-time nights, rich discussions remotely and proof-reading, this thesis would have been never become true. Grazie Chiara for sharing your expertise in imaging and teaching me the tools to create and interpret the most challenging data. Danke Basti for your simulations, which endorsed this experimental work in a great extent, giving scientific perspectives that would never be possible to reach otherwise. Your precise comments and suggestions always helped to enrich every single piece of this work. And finally Danke Ben for being an inquisitive student; accompanying your

work from the beginning allowed me to have an integral overview of our research and learn together as a team.

I spent this PhD time in two different offices in Heidelberg, where I am sure that I made life-lasting friends. First, I arrived to the Kopfklinik, where I had the opportunity to meet Antoni, Vania, Daniel and Martin, thank you for the nice discussions and valuable advice along this shared professional path. I also spent a very nice time in my office at HIT together with Thomas, Julia, Josefine, Wenjing and lately with Sodai, Steward and Manuel. I appreciate that you always created a friendly working environment. Thank you very much for that. Outside the the office, at HIT, I was also surrounded by very valuable people who always offer their unconditional help whenever it was needed. I would like to say special thanks to Stephan Brons for your sincere willingness to share all your experience. Likewise, I express my gratitude to Ralf Panse, Benjamin Ackermann, Christian Schömers, Rosi Van-Meyer, Andrea Mairani, Marcus Winter, Timo Strecker, Julian Horn and the accelerator team. Experimental Physics always has certain unpredictability, during the experimental campaigns of this work, there were sometimes minor and major trouble that I would not have been able to solve without your help.

I also thank Ilaria Rinaldi for all your support on the very beginning of this journey, her research represented the baseline of these investigations and the opportunity to delve into the topic. It was definitely necessary to deeply understand the capabilities and limitations of the current setup towards a the success development of the next generation. Even at hardship, the means of education and teaching do not compromise the final learning.

I also would like to express my thankfulness to John Gordon for facilitating the loan of the read-out system for the detector used during all the measurements, as well as for your always friendly collaboration and insights into any issue related to this device. I have learned a lot from our fruitful discussions in conferences and beam-times spent together.

My thanks also go out to Dr. Reinhard Schulte because he indirectly accompanied the last phase of this work with his always cordial stimulus and empathy. He definitely motivated me to keep going, knowing that a next step in my career was waiting for me to start. We see each other soon.

For the non-scientific side of my thesis, but not less important, I would like to thank my friends in Heidelberg who definitely made it an ever better place with their presence. I also maintained a strong connection with the people I met in Bonn, many of them also witnessed and supported this process from far away, I will be always more than grateful for that. I know that names are not necessary for you to know who you are.

Ana, siguiendo tu naturaleza, te corresponde la transición entre Alemania y México. Nuestras idas y venidas entre Köln y Heidelberg le inyectaron vitalidad esta etapa. Gracias por tu apoyo sin límites siempre y por la empatía de compartir la travesía del doctorado. Nunca olvidaré tu mano ayudándome a conquistar la Himmelsleiter, que puso en un gesto todo lo que tu amistad significa para mí.

Finalmente, parte de mis agradecimientos viajan de regreso a México: a mis papás que ante todo han depositado toda su confianza en mí y me han dejado llegar hasta aquí sin límites desde que decidí comenzar esta travesía, por soportar la lejanía que nos ha restado experiencias juntos cada día, pero que pronto sabremos recompensar. A mis hermanos Mona y Alan por siempre hacerse presentes de las maneras más inesperadas y en los momentos precisos. A todos y cada uno de mis amigos (que no me alcanzarían estas páginas para nombrarlos) y el resto de mi familia por haber creido en mí siempre, por el continuo flujo de buenas vibras que hicieron llegar constantemente hasta aquí. A mis profesores y maestros que indirectamente con su ejemplo me hicieron muchas veces retomar el camino. Estoy convencida de que todas sus palabras, pensamientos y buenas intenciones atravesaron el Atlántico cuando más los he necesitado para no dejarme vencer por ninguna dificultad. Gracias inmensas. Siempre estuvimos unidos a pesar de los kilómetros. A veces hay que viajar muy lejos para encontrar el camino propio. Nos abrazaremos pronto.

Bibliography

http://www.niu.edu/nicadd/research/medical, 2016. URL http://www.niu.edu/nicadd/research/medical/.

A .M. Koehler and V. W. Steward. Proton radiographic detection of strokes. *Nature*, 245: 38–40, 1973. ISSN 0028-0836. doi: 10.1038/245038a0.

S. Abe, K. Nishimura, H. Sato, H. Muraishi, T. Inada, T. Tomida, and F. Tatsuya. Heavy ion CT system based on measurement of residual range distribution. *Jpn. J. Med. Phys*, 22 (1), 2002.

S. Agostinelli, J. Allison, K. Amako, J. Apostolakis, H. Araujo, P. Arce, and ... GEANT4 - A simulation toolkit. *Nuclear Instruments and Methods in Physics Research, Section A: Accelerators, Spectrometers, Detectors and Associated Equipment*, 506(3):250–303, 2003. ISSN 01689002. doi: 10.1016/S0168-9002(03)01368-8.

U. Amaldi and G. Kraft. Radiotherapy with beams of carbon ions. *Reports on Progress in Physics*, 68(8):1861–1882, 2005. ISSN 0034-4885. doi: 10.1088/0034-4885/68/8/R04.

U. Amaldi, A. Bianchi, Y. H. Chang, A. Go, W. Hajdas, N. Malakhov, J. Samarati, F. Sauli, and D. Watts. Construction, test and operation of a proton range radiography system. *Nuclear Instruments and Methods in Physics Research, Section A: Accelerators, Spectrometers, Detectors and Associated Equipment*, 629(1):337–344, 2011. ISSN 01689002. doi: 10.1016/j.nima.2010.11.096.

American Cancer Society. Global Cancer Facts & Figures 3rd Edition. *American Cancer Society*, (800):1–64, 2015. ISSN 1097-0215. doi: 10.1002/ijc.27711. URL http://www.ncbi.nlm.nih.gov/pubmed/22019360.

A. Andersen and A. Kak. Simultaneous Algebraic Reconstruction Technique (SART): A superior implementation of the ART algorithm. *Ultrasonic Imaging*, 6(1):81–94, 1984. ISSN 01617346. doi: 10.1016/0161-7346(84)90008-7.

K. Ando and Y. Kase. Biological characteristics of carbon ion therapy. *International Journal for Radiation Biology*, 85(9):715–728, 2009.

K. Ando, S. Koike, K. Nojima, Y. J. Chen, C. Ohira, S. Ando, N. Kobayashi, T. Ohbuchi, W. Shimizu, and T. Kanai. Mouse skin reactions following fractionated irradiation with carbon ions. *International journal of radiation biology*, 74(1):129–138, jul 1998. ISSN 0955-3002 (Print).

P. Andreo, D. T. Burns, K. Hohlfeld, S. H. M, T. Kanai, F. Laitano, V. Smyth, N. Zealand, and S. Vynckier. Absorbed Dose Determination in External Beam Radiotherapy : An International Code of Practice for Dosimetry based on Standards of Absorbed Dose to Water. 2001(May), 2001.

W. Assmann, S. Kellnberger, S. Reinhardt, S. Lehrack, a. Edlich, P. G. Thirolf, M. Moser, G. Dollinger, M. Omar, V. Ntziachristos, and K. Parodi. Ionoacoustic characterization of

the proton Bragg peak with submillimeter accuracy. *Medical Physics*, 42(2):567–574, 2015. ISSN 0094-2405. doi: 10.1118/1.4905047. URL http://scitation.aip.org/content/aapm/journal/medphys/42/2/10.1118/1.4905047.

F. H. Attix. *Introduction to Radiological Physics and Radiation Dosimetry*. WILEY-VCH Verlag GmbH & Co. KGaA, Weinheim, 1986. ISBN 3527617140.

H. W. Barkas. Nuclear Research Emulsions. *Academic Press*, 1, 1963.

J. F. Barrett and N. Keat. Artifacts in CT: recognition and avoidance. *Radiographics*, 24(6):1679–91, 2004. ISSN 1527-1323. doi: 10.1148/rg.246045065. URL http://www.ncbi.nlm.nih.gov/pubmed/15537976{%}5Cnhttp://www.ncbi.nlm.nih.gov/pubmed?term=artifactsinCT:regonitionandavoidance.

V. A. Bashkirov, R. W. Schulte, and R. F. Hurley. Novel scintillation detector design and performance for proton radiography and computed tomography. *Medical Physics*, 43:664–74, 2016. ISSN 0094-2405. doi: 10.1118/1.4939255. URL http://dx.doi.org/10.1118/1.4939255.

J. Bauer, D. Unholtz, F. Sommerer, C. Kurz, T. Haberer, K. Herfarth, T. Welzel, S. E. Combs, J. Debus, and K. Parodi. Implementation and initial clinical experience of offline PET/CT-based verification of scanned carbon ion treatment. *Radiotherapy and oncology : journal of the European Society for Therapeutic Radiology and Oncology*, 107(2):218–26, may 2013. ISSN 1879-0887. doi: 10.1016/j.radonc.2013.02.018. URL http://www.ncbi.nlm.nih.gov/pubmed/23647759.

J. Bauer, F. Sommerer, A. Mairani, D. Unholtz, R. Farook, J. Handrack, K. Frey, T. Marcelos, T. Tessonnier, S. Ecker, B. Ackermann, M. Ellerbrock, J. Debus, and K. Parodi. Integration and evaluation of automated Monte Carlo simulations in the clinical practice of scanned proton and carbon ion beam therapy. *Physics in Medicine and Biology*, 59(16):4635, 2014. URL http://stacks.iop.org/0031-9155/59/i=16/a=4635.

E. Benton, R. Henke, C. Tobias, and M. Crutry. Radiography with heavy particles. Technical report, Donner Laboratory. Lawrence Berkeley Laboratory Report LBL-2887, 1975.

M. J. Berger and S. M. Seltzer. Tables of Energy Losses and Ranges of Electrons and Positrons. *Nasa Sp-3012*, pages 1–134, 1964.

J. Bernier, E. J. Hall, and A. Giaccia. Radiation oncology: a century of achievements. *Nat Rev Cancer*, 4(9):737–747, sep 2004. ISSN 1474-175X. URL http://dx.doi.org/10.1038/nrc1451.

C. Bert and E. Rietzel. 4D treatment planning for scanned ion beams. *Radiation Oncology*, 2(1):1–10, 2007. ISSN 1748-717X. doi: 10.1186/1748-717X-2-24. URL http://dx.doi.org/10.1186/1748-717X-2-24.

H. Bethe. Zur Theorie des Durchgangs schneller Korpuskularstrahlen durch Materie. *Ann. Phys.*, 397(3), 1930.

A. K. Biegun, J. Visser, T. Klaver, N. Ghazanfari, M.-J. van Goethem, E. Koffeman, M. van Beuzekom, and S. Brandenburg. Proton Radiography With Timepix Based Time Projection Chambers. *IEEE Transactions on Medical Imaging*, 35(4):1099–1105, 2016. ISSN 0278-0062. doi: 10.1109/TMI.2015.2509175. URL http://ieeexplore.ieee.org/lpdocs/epic03/wrapper.htm?arnumber=7360190.

F. Bloch. Zur Bremsung rasch bewegter Teilchen beim Durchgang durch Materie. *Annalen der Physik*, 5(16), 1933.

T. T. Boehlen, J. Bauer, M. Dosanjh, A. Ferrari, T. Haberer, K. Parodi, V. Patera, and A. Mairani. A Monte Carlo-based treatment-planning tool for ion beam therapy. *Journal of Radiation Research*, 54(SUPPL.1):77–81, 2013. ISSN 04493060. doi: 10.1093/jrr/rrt050.

T. T. Böhlen, F. Cerutti, M. P. W. Chin, A. Fassò, A. Ferrari, P. G. Ortega, A. Mairani, P. R. Sala, G. Smirnov, and V. Vlachoudis. The FLUKA Code: Developments and challenges for high energy and medical applications. *Nuclear Data Sheets*, 120:211–214, 2014. ISSN 00903752. doi: 10.1016/j.nds.2014.07.049.

N. Bohr. Scattering and Stopping of Fission Fragments. *Physical Review*, 58(7):654–655, oct 1940. URL http://link.aps.org/doi/10.1103/PhysRev.58.654.

T. Bortfeld. An analytical approximation of the Bragg curve for therapeutic proton beams. *Medical Physics*, 24(12):2024, 1997. ISSN 0094-2405. doi: 10.1118/1.598116. URL http://www.ncbi.nlm.nih.gov/pubmed/9434986{%}5Cnhttp://scitation.aip.org/content/aapm/journal/medphys/24/12/10.1118/1.598116.

J. Bortfeldt. Development of Floating Strip Micromegas Detectors. 2014.

J. Bortfeldt, M. Bender, O. Biebel, H. Danger, B. Flierl, R. Hertenberger, P. Lösel, S. Moll, K. Parodi, I. Rinaldi, A. Ruschke, and A. Zibell. High-Rate Capable Floating Strip Micromegas. 00:1–7, 2015. URL http://arxiv.org/abs/1508.00802.

J. Bortfeldt, O. Biebel, B. Flierl, R. Hertenberger, F. Klitzner, P. Lösel, L. Magallanes, R. Müller, K. Parodi, T. Schlüter, B. Voss, and A. Zibell. Low material budget floating strip Micromegas for ion transmission radiography. *Nuclear Instruments and Methods in Physics Research Section A: Accelerators, Spectrometers, Detectors and Associated Equipment*, pages 1–5, 2016. ISSN 01689002. doi: 10.1016/j.nima.2016.05.003. URL http://dx.doi.org/10.1016/j.nima.2016.05.003.

W. H. Bragg and R. Kleeman. On the α particles of radium, and their loss of range in passing through various atoms and molecules. *Philosophical Magazine Series 6*, 10(57):318–340, 1905. doi: 10.1080/14786440509463378. URL http://dx.doi.org/10.1080/14786440509463378.

A. Brown and H. Suit. The centenary of the discovery of the Bragg peak. *Radiotherapy and Oncology*, 73(3):265–268, 2004. ISSN 01678140. doi: 10.1016/j.radonc.2004.09.008.

C. Brusasco, B. Voss, and D. Schardt. A dosimetry system for fast measurement of 3D depth–dose profiles in charged-particle tumor therapy with scanning techniques. *… Instruments and Methods …*, 168:578–592, 2000. ISSN 0168583X. doi: 10.1016/S0168-583X(00)00058-6. URL http://www.sciencedirect.com/science/article/pii/S0168583X00000586.

M. Bucciantonio, U. Amaldi, R. Kieffer, N. Malakhov, F. Sauli, and D. Watts. Fast readout of GEM detectors for medical imaging. *Nuclear Instruments and Methods in Physics Research, Section A: Accelerators, Spectrometers, Detectors and Associated Equipment*, 718:160–163, 2013. ISSN 01689002. doi: 10.1016/j.nima.2012.10.046. URL http://dx.doi.org/10.1016/j.nima.2012.10.046.

A. Carabe, M. Moteabbed, N. Depauw, J. Schuemann, and H. Paganetti. Range uncertainty in proton therapy due to variable biological effectiveness. *Phys. Med. Biol*, 57:1159–1172, 2012. ISSN 1361-6560. doi: 10.1088/0031-9155/57/5/1159.

G. T. Chen, R. P. Singh, J. R. Castro, J. T. Lyman, and J. M. Quivey. Treatment planning for heavy ion radiotherapy. *International Journal of Radiation Oncology*Biology*Physics*, 5 (10):1809–1819, oct 1979. ISSN 03603016. doi: 10.1016/0360-3016(79)90564-9. URL http://www.redjournal.org/article/0360301679905649/fulltext.

W. T. Chu. Instrumentation for treatment of cancer using proton and light ion beams. *Review of Scientific Instruments*, 64(January):2055–2122, 1993. doi: 10.1063/1.1143946.

S. E. Combs, M. Ellerbrock, T. Haberer, D. Habermehl, A. Hoess, O. Jäkel, A. Jensen, S. Klemm, M. Münter, J. Naumann, A. Nikoghosyan, S. Oertel, K. Parodi, S. Rieken, and J. Debus. Heidelberg Ion Therapy Center (HIT): Initial clinical experience in the first 80 patients. *Acta oncologica (Stockholm, Sweden)*, 49(7):1132–1140, 2010. ISSN 0284-186X. doi: 10.3109/0284186X.2010.498432.

S. E. Combs, J. Bauer, D. Unholtz, C. Kurz, T. Welzel, D. Habermehl, T. Haberer, J. Debus, and K. Parodi. Monitoring of patients treated with particle therapy using positron-emission-tomography (PET): the MIRANDA study. *BMC Cancer*, 12(1):133, 2012a. ISSN 1471-2407. doi: 10.1186/1471-2407-12-133. URL http://www.biomedcentral.com/1471-2407/12/133.

S. E. Combs, K. A. Kessel, K. Herfarth, A. Jensen, S. Oertel, C. Blattmann, S. Ecker, A. Hoess, E. Martin, O. Witt, O. Jäkel, A. E. Kulozik, and J. Debus. Treatment of pediatric patients and young adults with particle therapy at the Heidelberg Ion Therapy Center (HIT): establishment of workflow and initial clinical data. *Radiation Oncology (London, England)*, 7:170, oct 2012b. ISSN 1748-717X. doi: 10.1186/1748-717X-7-170. URL http://www.ncbi.nlm.nih.gov/pmc/articles/PMC3504515/.

A. M. Cormack. Representation of a function by its line integrals, with some radiological applications. II. *Journal of Applied Physics*, 35(10):2908–2913, 1964. ISSN 00218979. doi: 10.1063/1.1713127.

A. M. Cormack. Banquet Speech, 1979. URL http://www.nobelprize.org/nobel{_}prizes/medicine/laureates/1979/cormack-speech.html.

A. M. Cormack. Nobel Lecture: Early two-dimensional reconstruction and recent topics stemming from it. Technical report, World Scientific Publishing Co., Singapore, 1992, 1980.

A. M. Cormack and A. M. Koehler. Quantitative proton tomography: preliminary experiments. *Physics in Medicine and Biology*, 21(4):560, 1976. ISSN 0031-9155. doi: 10.1088/0031-9155/21/4/007. URL http://stacks.iop.org/0031-9155/21/i=4/a=007.

K. M. Crowe, T. F. Budinger, J. L. Cahoon, V. P. Elischer, R. H. Huesman, and L. L. Kanstein. Axial scanning with 900 MeV alpha particles. 1975.

D. Cussol, B. Braunn, J. Colin, C. Courtois, J. M. Fontbonne, and M. Labalme. Nuclear physics and Hadron therapy. In *AIP Conference Proceedings*, volume 1412, pages 303–310, 2011. ISBN 9780735409866. doi: 10.1063/1.3665328.

Depauw. Ion Radiography as a Tool for Patient Set-up & Image Guided Particle Therapy: A Monte Carlo Study. *Technology in Cancer Research and Treatment*, 13(1), 2013. ISSN 15330346. doi: 10.7785/tcrt.2012.500357. URL http://tct.sagepub.com/lookup/doi/10.7785/tcrt.2012.500357.

N. Depauw and J. Seco. Sensitivity study of proton radiography and comparison with kV and MV x-ray imaging using GEANT4 Monte Carlo simulations. *Physics in medicine and biology*, 56(8):2407–2421, 2011. ISSN 0031-9155. doi: 10.1088/0031-9155/56/8/006.

D. Dolney, C. Ainsley, R. Hollebeek, and R. Maughan. Monte Carlo simulations of a novel Micromegas 2D array for proton dosimetry. *Physics in Medicine and Biology*, 61(4):1563–1572, 2016. ISSN 0031-9155. doi: 10.1088/0031-9155/61/4/1563. URL http://stacks.iop.org/0031-9155/61/i=4/a=1563?key=crossref.635077a07f4ce6fe57d04a95f45e5ad7.

P. J. Doolan, G. Royle, A. Gibson, H.-M. Lu, D. Prieels, and E. H. Bentefour. Dose ratio proton radiography using the proximal side of the Bragg peak. *Medical physics*, 42(4):1871–83, 2015. ISSN 0094-2405. doi: 10.1118/1.4915492. URL http://www.ncbi.nlm.nih.gov/pubmed/25832077.

M. Durante and J. S. Loeffler. Charged particles in radiation oncology. *Nature Reviews Clinical Oncology*, 7(1):37–43, 2009. ISSN 1759-4774. doi: 10.1038/nrclinonc.2009.183. URL http://dx.doi.org/10.1038/nrclinonc.2009.183.

W. Enghardt, P. Crespo, F. Fiedler, R. Hinz, K. Parodi, J. Pawelke, and F. Pönisch. Charged hadron tumour therapy monitoring by means of PET. *Nuclear Instruments and Methods in Physics Research Section A: Accelerators, Spectrometers, Detectors and Associated Equipment*, 525(1-2):284–288, 2004. ISSN 01689002. doi: 10.1016/j.nima.2004.03.128. URL http://linkinghub.elsevier.com/retrieve/pii/S0168900204004218.

U. Fano. Penetration of protons, alpha particles and mesons. *National Bureau of Standards*, 1963.

T. Fleck, R. Bär, and J. Mosthaf. Status of the Accelerator Control System (Acs) for the Therapy Facility HIT. In *PCaPAC08*, pages 215–217, Ljubljana, Slovenia, 2008. URL http://accelconf.web.cern.ch/Accelconf/pc08/papers/wep021.pdf.

M. F. Gensheimer, T. I. Yock, N. J. Liebsch, G. C. Sharp, H. Paganetti, N. Madan, P. E. Grant, and T. Bortfeld. In vivo proton beam range verification using spine MRI changes. *International journal of radiation oncology, biology, physics*, 78(1):268–275, sep 2010. ISSN 1879-355X (Electronic). doi: 10.1016/j.ijrobp.2009.11.060.

C. Gianoli, S. Meyer, L. Magallanes, G. Dedes, G. Landry, R. Nijhuis, U. Ganswindt, C. Thieke, C. Belka, and K. Parodi. Spatial Resolution Enhancement in Integration-Mode Detectors for Proton Radiography and Tomography. *Radiotherapy and Oncology*, 118:S46–S47, 2016. ISSN 01678140. doi: 10.1016/S0167-8140(16)30096-2. URL http://linkinghub.elsevier.com/retrieve/pii/S0167814016300962.

A. Giebeler, J. Fontenot, P. Balter, G. Ciangaru, R. Zhu, and W. Newhauser. Dose perturbations from implanted helical gold markers in proton therapy of prostate cancer. *Journal of applied clinical medical physics / American College of Medical Physics*, 10(1):2875, jan 2009. ISSN 1526-9914. URL http://www.ncbi.nlm.nih.gov/pmc/articles/PMC2949274/.

M. Goitein. Three-dimensional density reconstruction from a series of two-dimensional projections. *Nuclear Instruments and Methods*, 101(3):509–518, 1972. ISSN 0029554X. doi: 10.1016/0029-554X(72)90039-0.

J. Gordon. Private communication. Technical report, Heidelberg, 2015.

B. Gottschalk. Physics of proton interactions in matter. In H. Paganetti, editor, *Proton therapy physics*, chapter 2, pages 19–60. Taylor and Francis Group, Boca Raton, FL, 2012.

J. J. Griffin. Statistical Model of Intermediate Structure. *Physical Review Letters*, 17(9): 478–481, aug 1966. URL http://link.aps.org/doi/10.1103/PhysRevLett.17.478.

E. H. Grubbé. Priority in the Therapeutic Use of X-rays. *Radiology*, 21(2):156–162, aug 1933. ISSN 0033-8419. doi: 10.1148/21.2.156. URL http://dx.doi.org/10.1148/21.2.156.

R. Grün, T. Friedrich, T. Elsässer, and M. Krämer. Impact of enhancements in the local effect model (LEM) on the predicted RBE-weighted target dose distribution in carbon ion therapy. *Phys. Med. Biol.*, 2012. URL stacks.iop.org/PMB/57/7261.

K. Gwosch, B. Hartmann, J. Jakubek, C. Granja, P. Soukup, O. Jäkel, and M. Martišíková. Non-invasive monitoring of therapeutic carbon ion beams in a homogeneous phantom by tracking of secondary ions. *Physics in Medicine and Biology*, 58(11):3755, 2013. ISSN 0031-9155. URL http://stacks.iop.org/0031-9155/58/i=11/a=3755.

T. Haberer, W. Becher, D. Schardt, and G. Kraft. Magnetic scanning system for heavy ion therapy. *Nuclear Instruments and Methods in Physics Research Section A: Accelerators, Spectrometers, Detectors and Associated Equipment*, 330(1-2):296–305, jun 1993. ISSN 01689002. doi: 10.1016/0168-9002(93)91335-K. URL http://www.sciencedirect.com/science/article/pii/016890029391335K.

T. Haberer, J. Debus, H. Eickhoff, O. Jäkel, D. Schulz-Ertner, and U. Weber. The heidelberg ion therapy center. *Radiotherapy and Oncology*, 73:S186–S190, dec 2004. ISSN 01678140. doi: 10.1016/S0167-8140(04)80046-X. URL http://www.thegreenjournal.com/article/S016781400480046X/fulltext.

E. J. Hall and A. Giaccia. *Radiobiology for the Radiologist*. Lippincott Williams & Wilkins, Philadelphia, USA, 7th edition, 2012.

D. C. Hansen, N. Bassler, T. S. Sørensen, and J. Seco. The image quality of ion computed tomography at clinical imaging dose levels. *Medical Physics*, 41(11):111908, 2014a. ISSN 0094-2405. doi: 10.1118/1.4897614. URL http://search.ebscohost.com/login.aspx?direct=true{&}db=mnh{&}AN=25370641{&}lang=pt-br{&}site=eds-live{&}scope=site.

D. C. Hansen, J. B. B. Petersen, N. Bassler, and T. S. Sørensen. Improved proton computed tomography by dual modality image reconstruction. *Medical Physics*, 41(3):031904, mar 2014b. ISSN 0094-2405. doi: 10.1118/1.4864239. URL http://scitation.aip.org/content/aapm/journal/medphys/41/3/10.1118/1.4864239.

K. M. Hanson, J. N. Bradbury, T. M. Cannon, R. L. Hutson, D. B. Laubacher, R. Macek, M. A. Paciotti, and C. A. Taylor. The application of protons to computed tomography. *IEEE Transactions on Nuclear Science*, 25(1):657–660, 1978. ISSN 15581578. doi: 10.1109/TNS.1978.4329389.

K. M. Hanson, J. N. Bradbury, T. M. Cannon, R. L. Hutson, D. B. Laubacher, R. J. Macek, M. A. Paciotti, and C. A. Taylor. Computed tomography using proton energy loss. *Physics in Medicine and Biology*, 26(6):965, 1981. ISSN 0031-9155. doi: 10.1088/0031-9155/26/6/001. URL http://stacks.iop.org/0031-9155/26/i=6/a=001.

K. M. Hanson, J. N. Bradbury, R. a. Koeppe, R. J. Macek, D. R. Machen, R. Morgado, M. a. Paciotti, S. a. Sandford, and V. W. Steward. Proton computed tomography of human specimens. *Physics in medicine and biology*, 27(1):25–36, 1982. ISSN 0363-8715. doi: 10.1097/00004728-198208000-00062.

P. Henriquet, E. Testa, M. Chevallier, D. Dauvergne, G. Dedes, N. Freud, J. Krimmer, J. M. Létang, C. Ray, M. Richard, and F. Sauli. Interaction vertex imaging (IVI) for carbon ion therapy monitoring: a feasibility study. *Physics in medicine and biology*, 57(14):4655–69, jul 2012. ISSN 1361-6560. doi: 10.1088/0031-9155/57/14/4655. URL http://www.ncbi.nlm.nih.gov/pubmed/22750688.

V. L. Highland. Some practical remarks on multiple scattering. *Nuclear Instruments and Methods*, 129(2):497–499, nov 1975. ISSN 0029554X. doi: 10.1016/0029-554X(75)90743-0. URL http://www.sciencedirect.com/science/article/pii/0029554X75907430.

J. L. Hintze and R. D. Nelson. Violin Plots: A Box Plot-Density Trace Synergism. *The American Statistician*, 52(2):181–184, 1998.

HIT. Heidelberg Ion beam Therapy Center. URL https://www.klinikum.uni-heidelberg.de/About-us.124447.0.html?{&}L=1.

R. Hollebeek, M. Newcomer, G. Mayers, B. Delgado, G. Shukla, R. Maughan, and D. Dolney. A new technology for fast two-dimensional detection of proton therapy beams. *Physics Research International*, 2012(i), 2012. ISSN 1687689X. doi: 10.1155/2012/714782.

L. Huber, J. Telsemeyer, M. Martišíková, and O. Jäkel. Patient position verification in ion-beam therapy using ion-beam radiography and fiducial markers. *Journal of Instrumentation*, 6(11):C11008–C11008, 2011. ISSN 1748-0221. doi: 10.1088/1748-0221/6/11/C11008. URL http://stacks.iop.org/1748-0221/6/i=11/a=C11008?key=crossref.28257cbc4c6f08f665a4cb6b8b468e5d.

N. Hudobivnik, F. Schwarz, T. Johnson, L. Agolli, G. Dedes, T. Tessonnier, F. Verhaegen, C. Thieke, C. Belka, W. H. Sommer, K. Parodi, and G. Landry. Comparison of proton therapy treatment planning for head tumors with a pencil beam algorithm on dual and single energy CT images. *Medical Physics*, 43(1):495–504, 2016. ISSN 0094-2405. doi: 10.1118/1.4939106. URL http://scitation.aip.org/content/aapm/journal/medphys/43/1/10.1118/1.4939106.

F. Hueso-González, F. Fiedler, C. Golnik, T. Kormoll, G. Pausch, J. Petzoldt, K. E. Römer, and W. Enghardt. Compton Camera and Prompt Gamma Ray Timing: Two Methods for In Vivo Range Assessment in Proton Therapy. *Frontiers in oncology*, 6(April):80, 2016. ISSN 2234-943X. doi: 10.3389/fonc.2016.00080. URL http://www.ncbi.nlm.nih.gov/pubmed/27148473{%}5Cnhttp://www.pubmedcentral.nih.gov/articlerender.fcgi?artid=PMC4829070.

N. Hünemohr. *Dual energy CT as an alternative for ion radiotherapy treatment planning*. PhD thesis, Heidelberg University, 2014.

N. Hünemohr, H. Paganetti, S. Greilich, O. Jäkel, and J. Seco. Tissue decomposition from dual energy CT data for MC based dose calculation in particle therapy. *Medical physics*, 41(6):061714, 2014. ISSN 0094-2405. doi: 10.1118/1.4875976. URL http://scitation.aip.org/content/aapm/journal/medphys/41/6/10.1118/1.4875976.

R. Hurley, R. W. Schulte, V. Bashkirov, G. Coutrakon, H.-W. Sadrozinski, and B. Patyal. The Phase I Proton CT Scanner and Test Beam Results at LLUMC. *Trans Am Nucl Soc.*, (106):63–66, 2012. doi: 10.1126/scisignal.2001449.Engineering.

IAEA and ICRU. Relative Biological Effectiveness in Ion Beam Therapy. *IAEA Technical Reports*, (461):1–165, 2008. doi: TechnicalReportsSeriesNo.461. URL http://www-pub.iaea.org/MTCD/publications/PDF/trs461{_}web.pdf.

ICRU78. *Prescribing, recording, and reporting proton-beam therapy*, volume 7. ICRU, Bethesda, MD, 2007. URL http://cds.cern.ch/record/1177350.

ICRU85. ICRU Report 85a - Fundamental Quantities And Units For Ionizing Radiation. *Journal of the ICRU*, 11(1):1–35, 2011.

O. Jäkel and P. Reiss. The influence of metal artefacts on the range of ion beams. *Physics in medicine and biology*, 52(3):635–644, feb 2007. ISSN 0031-9155 (Print). doi: 10.1088/0031-9155/52/3/007.

O. Jäkel, G. H. Hartmann, C. P. Karger, P. Heeg, and S. Vatnitsky. A calibration procedure for beam monitors in a scanned beam of heavy charged particles. *Medical physics*, 31(5):1009–1013, 2004. ISSN 00942405. doi: 10.1118/1.1689011.

O. Jäkel, C. Jacob, D. Schardt, C. P. Karger, and G. H. Hartmann. Relation between carbon ion ranges and x-ray CT numbers. *Medical Physics*, 28(4):701, 2001. ISSN 00942405. doi: 10.1118/1.1357455. URL http://link.aip.org/link/MPHYA6/v28/i4/p701/s1{&}Agg=doi.

M. Jermann. Particle Therapy Statistics in 2014. *International Journal of Particle Therapy*, 2(1):50–54, 2015. ISSN 2331-5180. doi: 10.14338/IJPT-15-00013. URL http://theijpt.org/doi/10.14338/IJPT-15-00013.

R. P. Johnson, V. Bashkirov, L. Dewitt, V. Giacometti, R. F. Hurley, P. Piersimoni, T. E. Plautz, H. F. Sadrozinski, S. Member, K. Schubert, S. Member, R. Schulte, B. Schultze, and A. Zatserklyaniy. A Fast Experimental Scanner for Proton CT : Technical Performance and First Experience With Phantom Scans. *IEEE Transactions on Nuclear Science*, 63(1):52–60, 2016.

B. Jones. A Simpler Energy Transfer Efficiency Model to Predict Relative Biological Effect for Protons and Heavier Ions. *Frontiers in oncology*, 5:184, 2015. ISSN 2234-943X. doi: 10.3389/fonc.2015.00184. URL http://www.pubmedcentral.nih.gov/articlerender.fcgi?artid=4531328{&}tool=pmcentrez{&}rendertype=abstract.

S. Kaczmarz. Angenäherte Auflösung von Systemen linearer Gleichungen. *Bull. Acad. Pol. Sci. Lett. A*, 6-8(A):335–357, 1937.

K. Kagawa, M. Murakami, Y. Hishikawa, M. Abe, T. Akagi, T. Yanou, G. Kagiya, Y. Furusawa, K. Ando, K. Nojima, M. Aoki, and T. Kanai. Preclinical biological assessment of proton and carbon ion beams at Hyogo Ion Beam Medical Center. *International journal of radiation oncology, biology, physics*, 54(3):928–938, nov 2002. ISSN 0360-3016 (Print).

A. Kak and M. Slaney. *Principles of Computarized Tomographic Imaging*. IEEE Press, 1988.

F. Klitzner, O. Biebel, B. Flierl, B. Gillich, and R. Hertenberger. Novel Two-Dimensional Floating Strip Micromegas Detectors. *Proceedings of Science*, (August):3–6, 2016.

A. Knopf and A. Lomax. In vivo proton range verification: a review. *Phys. Med. Biol.*, 58, 2013. doi: 10.1088/0031-9155/58/15/R131.

A. M. Koehler. Proton Radiography. *Science*, 160(3825), 1968.

B. Kopp. *Master thesis. LMU. In preparation.* Munich, Germany, 2017.

A. C. Kraan. Range Verification Methods in Particle Therapy: Underlying Physics and Monte Carlo Modeling. *Frontiers in Oncology*, 5(July):150, 2015. ISSN 2234-943X. doi: 10.3389/fonc.2015.00150. URL http://journal.frontiersin.org/Article/10.3389/fonc.2015.00150/abstract.

G. Kraft. RBE and its interpretation. *Strahlentherapie und Onkologie : Organ der Deutschen Röntgengesellschaft*, 175 Suppl:44–47, 1999. ISSN 0179-7158. doi: 10.1007/BF03038887.

N. Krah, M. Testa, S. Brons, O. Jäkel, K. Parodi, B. Voss, and I. Rinaldi. An advanced image processing method to improve the spatial resolution of ion radiographies. *Physics in medicine and biology*, 60(21):8525–8547, 2015. ISSN 1361-6560. doi: 10.1088/0031-9155/60/21/8525. URL http://iopscience.iop.org/article/10.1088/0031-9155/60/21/8525.

M. Krämer. Swift ions in radiotherapy – Treatment planning with TRiP98. *Nuclear Instruments and Methods in Physics Research Section B: Beam Interactions with Materials and Atoms*, 267(6):989–992, mar 2009. ISSN 0168583X. doi: 10.1016/j.nimb.2009.02.015. URL http://www.sciencedirect.com/science/article/pii/S0168583X09002456.

M. Krämer and M. Durante. Ion beam transport calculations and treatment plans in particle therapy. *European Physical Journal D*, 60(1):195–202, 2010. ISSN 14346060. doi: 10.1140/epjd/e2010-00077-8.

M. Krämer, O. Jäkel, T. Haberer, G. Kraft, D. Schardt, and U. Weber. Treatment planning for heavy-ion radiotherapy : physical beam model and dose optimization. 3299, 2000. URL http://iopscience.iop.org/0031-9155/45/11/313/pdf/0031-9155{_}45{_}11{_}313.pdf.

S. L. Krämer, D. R. Moffett, R. L. Martin, E. P. Colton, and V. W. Steward. Proton imaging for medical applications. *Radiology*, 135(2):485–494, 1980. doi: 10.1148/radiology.135.2.6245430. URL http://dx.doi.org/10.1148/radiology.135.2.6245430.

S. C. Krejcarek, P. E. Grant, J. W. Henson, N. J. Tarbell, and T. I. Yock. Physiologic and Radiographic Evidence of the Distal Edge of the Proton Beam in Craniospinal Irradiation. *International journal of radiation oncology, biology, physics*, 68(3):646–649, jul 2007. ISSN 0360-3016. doi: 10.1016/j.ijrobp.2007.02.021. URL http://www.ncbi.nlm.nih.gov/pmc/articles/PMC1955224/.

C. Kurz. *4D offline PET-based treatment verification in ion beam therapy: experimental and clinical evaluation*. PhD thesis, Ludwig-Maximilians-Universität München, 2014.

G. Laczko, V. Dangendorf, M. Krämer, D. Schardt, and K. Tittelmeier. High-resolution heavy ion track structure imaging. *Nuclear Instruments and Methods in Physics Research Section A: Accelerators, Spectrometers, Detectors and Associated Equipment*, 535(1-2):216–220, dec 2004. ISSN 01689002. doi: 10.1016/j.nima.2004.07.125. URL http://www.sciencedirect.com/science/article/pii/S0168900204016067.

G. Landry, K. Parodi, J. E. Wildberger, and F. Verhaegen. Deriving concentrations of oxygen and carbon in human tissues using single- and dual-energy CT for ion therapy applications. *Phys. Med. Biol.*, 58:5029–5048, 2013.

G. Landry, G. Dedes, C. Zöllner, J. Handrack, G. Janssens, J. Orban de Xivry, M. Reiner, C. Paganelli, M. Riboldi, F. Kamp, M. Söhn, J. J. Wilkens, G. Baroni, C. Belka, and K. Parodi. Phantom based evaluation of CT to CBCT image registration for proton therapy dose recalculation. *Physics in medicine and biology*, 60(2):595–613, 2014. ISSN 0031-9155. doi: 10.1088/0031-9155/60/2/595. URL http://stacks.iop.org/0031-9155/60/i=2/a=595?key=crossref.67d675928de6c7001f2da3c872381148{%}5Cnhttp://www.ncbi.nlm.nih.gov/pubmed/25548912.

W. R. Leo. *Techniques for Nuclear and Particle Physics Experiments*. Springer-Verlag, 2nd editio edition, 1990. ISBN 978-3-540-57280-0. doi: 10.1007/978-3-642-57920-2. URL http://tocs.ulb.tu-darmstadt.de/27968561.pdf.

W. P. Levin, H. Kooy, J. S. Loeffler, and T. F. Delaney. Proton beam therapy. *British Journal of Cancer*, 93:849–854, 2005. doi: 10.1038/sj.bjc.6602754.

H. W. Lewis. Range Straggling of a Nonrelativistic Charged Particle. *Physical Review*, 85(1):20–24, jan 1952. URL http://link.aps.org/doi/10.1103/PhysRev.85.20.

T. Li, Z. Liang, J. V. Singanallur, T. J. Satogata, D. C. Williams, and R. W. Schulte. Reconstruction for proton computed tomography by tracing proton trajectories – A Monte Carlo study. *Medical physics*, 33(3):699–706, mar 2006. ISSN 0094-2405. URL http://www.ncbi.nlm.nih.gov/pmc/articles/PMC1550979/.

L. Lin, M. Kang, T. D. Solberg, T. Mertens, C. Baumer, C. G. Ainsley, and J. E. Mcdonough. Use of a novel two-dimensional ionization chamber array for pencil beam scanning proton therapy beam quality assurance. 16(3):270–276, 2015.

D. Lo Presti, D. L. Bonanno, F. Longhitano, C. Pugliatti, S. Aiello, G. A. P. Cirrone, V. Giordano, E. Leonora, N. Randazzo, S. Reito, F. Romano, G. V. Russo, M. Russo, V. Sipala, C. Stancampiano, and C. Ventura. Development of a real-time, large area, high spatial resolution particle tracker based on scintillating fibers. *Advances in High Energy Physics*, 2014, 2014. ISSN 16877365. doi: 10.1155/2014/692908.

J. S. Loeffler and M. Durante. Charged particle therapy- optimization, challenges and future directions. *Nature Publishing Group*, pages 1–14, 2013. ISSN 1759-4774. doi: 10.1038/nrclinonc.2013.79. URL http://dx.doi.org/10.1038/nrclinonc.2013.79.

A. J. Lomax. Intensity modulated proton therapy and its sensitivity to treatment uncertainties 2: the potential effects of inter-fraction and inter-field motions. *Physics in medicine and biology*, 53(4):1043–1056, feb 2008. ISSN 0031-9155 (Print). doi: 10.1088/0031-9155/53/4/015.

M. E. Lomax, L. K. Folkes, and P. O'Neill. Biological consequences of radiation-induced DNA damage: Relevance to radiotherapy. *Clinical Oncology*, 25(10):578–585, 2013. ISSN 09366555. doi: 10.1016/j.clon.2013.06.007. URL http://dx.doi.org/10.1016/j.clon.2013.06.007.

L. Magallanes, V. Bernd, S. Brons, O. Jäkel, K. Parodi, I. Rinaldi, and M. Takechi. Ongoing investigations on ion-based radiography and tomography. *Radiotherapy and Oncology*, 110:S61, 2014a. ISSN 01678140. doi: 10.1016/S0167-8140(15)34145-1. URL http://linkinghub.elsevier.com/retrieve/pii/S0167814015341451.

L. Magallanes, S. Brons, T. Marcelos, M. Takechi, B. Voss, O. Jäkel, I. Rinaldi, and K. Parodi. On the role of ion-based imaging methods in modern ion beam therapy. pages 142–146, 2014b. doi: 10.1063/1.4901379. URL http://scitation.aip.org/content/aip/proceeding/aipcp/10.1063/1.4901379.

A. Mairani, T. T. Böhlen, A. Schiavi, T. Tessonnier, S. Molinelli, S. Brons, G. Battistoni, K. Parodi, and V. Patera. A Monte Carlo-based treatment planning tool for proton therapy. *Physics in Medicine and Biology*, 58(8):2471, 2013. URL http://stacks.iop.org/0031-9155/58/i=8/a=2471.

T. Marcelos. *Carbon ion radiography and tomography : a Monte Carlo study. Master Thesis.* Ludwig-Maximillians Universität München, Munich, Germany, 2014.

Medipix. https://medipix.web.cern.ch/medipix/. URL https://medipix.web.cern.ch/medipix/.

S. Meyer. *A systematic Monte Carlo study of the influence of different acquisition and detector parameters on the image quality of carbon ion radiography and tomography using a range telescope. Master Thesis.* Munich, Germany, 2015.

S. Meyer, C. Gianoli, L. Magallanes, B. Kopp, T. Tessonnier, G. Landry, G. Dedes, B. Voss, and K. Parodi. Comparative Monte Carlo study on the performance of integration- and list-mode detector configurations for carbon ion computed tomography. *Phys. Med. Biol.*, 62(3), 2017.

S. Minohara, T. Kanai, M. Endo, and K. Kawachi. Effects of object size on a function to convert x-ray CT numbers into the water equivalent path length of charged particle beam. *Third Workshop on Physical and Biological Research with Heavy Ions*, pages 14–15, 1993. URL http://inis.iaea.org/Search/search.aspx?orig{_}q=RN:26033105.

G. Moliere. Theorie der Streuung schneller geladener Teilchen.I. Einzelstreuung am abgeschirmten Coulomb-Feld. II. Mehrfach- und Vielfachstreuung. *Z. Naturforsch. A*, 2: 133–145, 1947. URL http://cds.cern.ch/record/425612.

C. Morris, J. Hopson, and P. Goldstone. Proton radiography. *Los Alamos Science*, 5(30), 2006. ISSN 00291021. doi: 10.1016/0029-1021(72)90085-0.

J. M. Mosthaf, A. Peters, S. Hanke, S. Scheloske, S. Vollmer, H. Ion, T. Centre, and T. Fleck. OVERVIEW OF THE COMMUNICATION STRUCTURE OF THE HIT ACCELERATOR CONTROL SYSTEM. In *PCaPAC08*, pages 168–170, Ljubljana, Slovenia, 2008. WEP002.

M. F. Moyers, M. Sardesai, S. Sun, and D. W. Miller. Ion stopping powers and CT numbers. *Medical dosimetry : official journal of the American Association of Medical Dosimetrists*, 35(3):179–94, jan 2010. ISSN 1873-4022. doi: 10.1016/j.meddos.2009.05.004. URL http://www.meddos.org/article/S095839470900051X/fulltext.

H. Muraishi, K. Nishimura, S. Abe, H. Satoh, S. Hara, H. Hara, Y. Takahashi, T. Mogaki, R. Kawai, K. Yokoyama, N. Yasuda, T. Tomida, Y. Ohno, and T. Kanai. Evaluation of Spatial Resolution for Heavy Ion CT System Based on the Measurement of Residual Range Distribution With HIMAC. *IEEE Transactions on Nuclear Science*, 56(5):2714–2721, oct 2009. ISSN 0018-9499. doi: 10.1109/TNS.2009.2023520. URL http://ieeexplore.ieee.org/lpdocs/epic03/wrapper.htm?arnumber=5280521.

M. Muramatsu and A. Kitagawa. A review of ion sources for medical accelerators (invited). *The Review of scientific instruments*, 83(2):02B909, feb 2012. ISSN 1089-7623. doi: 10.1063/1.3671744. URL http://www.ncbi.nlm.nih.gov/pubmed/22380341.

A. A. Mustafa and F. D. Jackson. The relation between x-ray CT numbers and charged particle stopping powers and its significance for radiotherapy treatment planning. *Physics in Medicine and Biology*, 28(2):169, 1983. ISSN 0031-9155. URL http://stacks.iop.org/0031-9155/28/i=2/a=006.

O. Nairz, M. Winter, P. Heeg, and O. Jäkel. Accuracy of robotic patient positioners used in ion beam therapy. *Radiation Oncology (London, England)*, 8:124, may 2013. ISSN 1748-717X. doi: 10.1186/1748-717X-8-124. URL http://www.ncbi.nlm.nih.gov/pmc/articles/PMC3749753/.

F. Nensa, K. Beiderwellen, P. Heusch, and A. Wetter. Clinical applications of PET/MRI: Current status and future perspectives. *Diagnostic and Interventional Radiology*, 20(5):438–447, 2014. ISSN 13053612. doi: 10.5152/dir.2014.14008.

W. D. Newhauser and R. Zhang. The physics of proton therapy. *Physics in Medicine and Biology*, 60(8):R155, 2015. ISSN 0031-9155. doi: 10.1088/0031-9155/60/8/R155. URL http://iopscience.iop.org/0031-9155/60/8/R155{%}5Cnhttp://iopscience.iop.org/0031-9155/60/8/R155/pdf/0031-9155{_}60{_}8{_}R155.pdf{%}5Cnhttps://iopscience.iop.org/0031-9155/60/8/R155/.

K. Noda, T. Furukawa, S. Shibuya, T. Uesugi, M. Muramatsu, M. Kanazawa, E. Takada, and S. Yamada. Advanced RF-KO slow-extraction method for the reduction of spill ripple. *Nuclear Instruments and Methods in Physics Research Section A: Accelerators, Spectrometers, Detectors and Associated Equipment*, 492(1-2):253–263, oct 2002. ISSN 01689002. doi: 10.1016/S0168-9002(02)01319-0. URL http://www.sciencedirect.com/science/article/pii/S0168900202013190.

H. Paganetti. Range uncertainties in proton therapy and the role of Monte Carlo simulations. *Physics in Medicine and Biology*, 57(11), 2012. doi: 10.1088/0031-9155/57/11/R99.

H. Paganetti. Relative biological effectiveness (RBE) values for proton beam therapy. Variations as a function of biological endpoint, dose, and linear energy transfer. *Phys. Med. Biol.*, 59, 2014.

H. Paganetti, A. Niemierko, M. Ancukiewicz, L. E. Gerweck, M. Goitein, J. S. Loeffler, and H. D. Suit. Relative biological effectiveness (RBE) values for proton beam therapy. *International Journal of Radiation Oncology*Biology*Physics*, 53(2):407–421, jun 2002. ISSN 03603016. doi: 10.1016/S0360-3016(02)02754-2. URL http://www.sciencedirect.com/science/article/pii/S0360301602027542.

K. Parodi. PET monitoring of hadrontherapy. *Nuclear Medicine Review*, 15(Supp. C):37–42, 2012.

K. Parodi. Heavy ion radiography and tomography. *Physica medica : PM : an international journal devoted to the applications of physics to medicine and biology : official journal of the Italian Association of Biomedical Physics (AIFB)*, pages 1–5, mar 2014. ISSN 1724-191X. doi: 10.1016/j.ejmp.2014.02.004. URL http://www.ncbi.nlm.nih.gov/pubmed/24685181.

K. Parodi, A. Ferrari, F. Sommerer, and H. Paganetti. Clinical CT-based calculations of dose and positron emitter distributions in proton therapy using the FLUKA Monte Carlo code. *Phys. Med. Biol.*, 100(2):130–134, 2012a. doi: 10.1016/j.pestbp.2011.02.012.Investigations.

K. Parodi, A. Mairani, S. Brons, B. G. Hasch, F. Sommerer, J. Naumann, O. Jäkel, T. Haberer, and J. Debus. Monte Carlo simulations to support start-up and treatment planning of scanned proton and carbon ion therapy at a synchrotron-based facility. *Physics in medicine and biology*, 57(12):3759–84, 2012b. ISSN 1361-6560. doi: 10.1088/0031-9155/57/12/3759. URL http://www.ncbi.nlm.nih.gov/pubmed/22617050.

K. Parodi, A. Mairani, and F. Sommerer. Monte Carlo-based parametrization of the lateral dose spread for clinical treatment planning of scanned proton and carbon ion beams. *Journal of radiation research*, 54 Suppl 1(suppl_1):i91–6, jul 2013. ISSN 1349-9157. doi: 10.1093/jrr/rrt051. URL http://jrr.oxfordjournals.org/cgi/content/long/54/suppl{_}1/i91.

P. Pemler, J. Besserer, J. de Boer, M. Dellert, C. Gahn, M. Moosburger, U. Schneider, E. Pedroni, and H. Stäuble. A detector system for proton radiography on the gantry of the Paul-Scherrer-Institute. *Nuclear Instruments and Methods in Physics Research Section A: Accelerators, Spectrometers, Detectors and Associated Equipment*, 432 (2-3):483–495, aug 1999. ISSN 01689002. doi: 10.1016/S0168-9002(99)00284-3. URL http://www.sciencedirect.com/science/article/pii/S0168900299002843.

A. Peters. *The accelerator facility of the Heidelberg Ion-Beam Therapy Centre (HIT)*, chapter 42, pages 801–812. O. Brüning, S.Myers, 2016. doi: 10.1142/9789814436403_0042. URL http://www.worldscientific.com/doi/abs/10.1142/9789814436403{_}0042.

A. Peters, R. Cee, T. Haberer, and T. Winkelmann. Spill Structure Measurements Heidelberg Ion Therapy Centre. In *11th European Particle Accelerator Conference, Genoa, Italy, 23 - 27 Jun 2008*, pages 1824–1826, 2008.

T. Plautz, V. Bashkirov, V. Feng, F. Hurley, R. P. Johnson, C. Leary, S. Macafee, A. Plumb, V. Rykalin, H. F. W. Sadrozinski, K. Schubert, R. Schulte, B. Schultze, D. Steinberg, M. Witt, and A. Zatserklyaniy. 200 MeV proton radiography studies with a hand phantom using a prototype proton CT scanner. *IEEE Transactions on Medical Imaging*, 33(4):875–881, 2014. ISSN 02780062. doi: 10.1109/TMI.2013.2297278.

J. C. Polf, S. Peterson, M. McCleskey, B. T. Roeder, A. Spiridon, S. Beddar, and L. Trache. Measurement and calculation of characteristic prompt gamma ray spectra emitted during proton irradiation. *Physics in Medicine and Biology*, 54(22):N519, 2009. URL http://stacks.iop.org/0031-9155/54/i=22/a=N02.

G. Poludniowski, N. M. Allinson, T. Anaxagoras, M. Esposito, and S. Green. Proton-counting radiography for proton therapy : a proof of principle using CMOS APS technology. 59(11): 2569–2581, 2014. doi: 10.1088/0031-9155/59/11/2569.Proton-counting.

G. Poludniowski, N. M. Allinson, and P. M. Evans. Proton radiography and tomography with application to proton therapy. *British Journal of Radiology*, 88(1053):1–14, 2015. ISSN 00071285. doi: 10.1259/bjr.20150134.

PTCOG. Particle Therapy Co-Operative Group. URL http://www.ptcog.ch/.

Pyramid Technical Co. I128 Ionization Chamber Controller User Manual, 2012. URL www.ptcusa.com.

M. R. Raju and S. G. Carpenter. A heavy particle comparative study. Part IV: acute and late reactions. *The British Journal of Radiology*, 51(609):720–727, sep 1978. ISSN 0007-1285. doi: 10.1259/0007-1285-51-609-720. URL http://dx.doi.org/10.1259/0007-1285-51-609-720.

M. H. Richard, M. Chevallier, D. Dauvergne, N. Freud, P. Henriquet, F. Le Foulher, J. M. Letang, G. Montarou, C. Ray, F. Roellinghoff, E. Testa, M. Testa, and A. H. Walenta. Design Guidelines for a Double Scattering Compton Camera for Prompt-gamma Imaging During Ion Beam Therapy: A Monte Carlo Simulation Study. *IEEE Transactions on Nuclear Science*, 58(1, Part 1):87–94, 2011. ISSN 0018-9499.

E. Rietzel. Range accuracy in carbon ion treatment planning based on CT-calibration with real tissue samples. *Radiation oncology*, 2(14), 2007.

I. Rinaldi. *Investigation of novel imaging methods using therapeutic ion beams. PhD Thesis.* University of Heidelberg, Heidelberg, Germany, 2011.

I. Rinaldi, S. Brons, J. Gordon, R. Panse, and B. Voss. Experimental characterization of a prototype detector system for carbon ion radiography and tomography. 413, 2013. doi: 10.1088/0031-9155/58/3/413.

I. Rinaldi, S. Brons, O. Jäkel, B. Voss, and K. Parodi. Experimental investigations on carbon ion scanning radiography using a range telescope. *Physics in medicine and biology*, 59(12): 3041–57, 2014. ISSN 1361-6560. doi: 10.1088/0031-9155/59/12/3041. URL http://stacks.iop.org/0031-9155/59/i=12/a=3041.

W. C. Roentgen. On a new kind of ray (first report). *Munchener medizinische Wochenschrift (1950)*, 101:1237–1239, jul 1959. ISSN 0027-2973 (Print).

H. Rohdjeß. New medical carbon accelerators in Kiel, Marburg and Heidelberg. In *EuCARD 2nd annual meeting*, Paris, France, 2011. URL {\char"00A9\relax}SiemensAG2011, HealthcareSector,ParticleTherapy.

B. Rossi. *High-Energy Particles*. Englewood Cliffs, NJ, 1952.

H. Ryu, E. Song, J. Lee, and J. Kim. Density and spatial resolutions of proton radiography using a range modulation technique. *Physics in Medicine and Biology*, 53(19):5461–5468, 2008. ISSN 0031-9155. doi: 10.1088/0031-9155/53/19/012.

D. Sánchez Parcerisa. *Experimental and computational investigations on the water-to-air stopping power ratio for ion chamber dosimetry in carbon ion radiotherapy.* PhD thesis, Heidelberg University, 2012.

M. Scaringella, M. Bruzzi, M. Bucciolini, M. Carpinelli, G. A. P. Cirrone, C. Civinini, G. Cuttone, D. L. Presti, S. Pallotta, C. Pugliatti, N. Randazzo, F. Romano, V. Sipala, C. Stancampiano, C. Talamonti, M. Tesi, E. Vanzi, and M. Zani. A proton Computed Tomography system for medical applications. *Journal of Instrumentation*, 8(02):C02021, 2013. ISSN 1748-0221. doi: 10.1088/1748-0221/8/02/C02021. URL http://stacks.iop.org/1748-0221/8/i=02/a=C02021.

B. Schaffner and E. Pedroni. The precision of proton range calculations in proton radiotherapy treatment planning: experimental verification of the relation between CT-HU and proton stopping power. *Physics in Medicine and Biology*, 43(6):1579–1592, 1998. URL http://www.ncbi.nlm.nih.gov/pubmed/9651027.

D. Schardt and T. Elsässer. Heavy-ion tumor therapy: Physical and radiobiological benefits. *Reviews of Modern Physics*, 82(1):383–425, 2010. ISSN 00346861. doi: 10.1103/RevModPhys.82.383. URL http://link.aps.org/doi/10.1103/RevModPhys.82.383.

S. Scheloske, S. Hanke, J. Mosthaf, and T. Knoch. OVERVIEW OF THE PERSONNEL SAFETY SYSTEM AT THE HEIDELBERG ION THERAPY FACILITY. In TUP005, editor, *PCaPAC08*, pages 88–90, Ljubljana, Slovenia, 2008.

C. Schiepers and M. Dahlbom. Molecular imaging in oncology: the acceptance of PET/CT and the emergence of MR/PET imaging. *European Radiology*, 21(3):548–554, mar 2011. ISSN 0938-7994. doi: 10.1007/s00330-010-2033-y. URL http://www.ncbi.nlm.nih.gov/pmc/articles/PMC3032196/.

U. Schneider and E. Pedroni. Proton radiography as a tool for quality control in proton therapy. *Medical physics*, 22(4):353–363, 1995. ISSN 00942405. doi: 10.1118/1.597470.

U. Schneider, P. Pemler, J. Besserer, E. Pedroni, A. Lomax, and B. Kaser-Hotz. Patient specific optimization of the relation between CT-Hounsfield units and proton stopping power with proton radiography. *Medical Physics*, 32(1):195, 2005. ISSN 00942405. doi: 10.1118/1.1833041. URL http://link.aip.org/link/MPHYA6/v32/i1/p195/s1{&}Agg=doi.

U. Schneider, E. Pedroni, M. Hartmann, J. Besserer, and T. Lomax. Spatial resolution of proton tomography: Methods, initial phase space and object thickness. *Zeitschrift für Medizinische Physik*, 22(2):100–108, 2012. ISSN 09393889. doi: 10.1016/j.zemedi.2011.06.001.

W. Schneider, T. Bortfeld, and W. Schlegel. Correlation between CT numbers and tissue parameters needed for Monte Carlo simulations of clinical dose distributions. *Physics in Medicine and Biology*, 45(2):459, 2000. URL http://stacks.iop.org/0031-9155/45/i=2/a=314.

C. Schoemers, E. Feldmeier, J. Naumann, R. Panse, A. Peters, and T. Haberer. The intensity feedback system at Heidelberg Ion-Beam Therapy Centre. *Nuclear Instruments and Methods in Physics Research Section A: Accelerators, Spectrometers, Detectors and Associated Equipment*, 795:92–99, 2015. ISSN 01689002. doi: 10.1016/j.nima.2015.05.054. URL http://linkinghub.elsevier.com/retrieve/pii/S0168900215007135.

M. Scholz and G. Kraft. Calculation of Heavy Ion Inactivation Probabilities Based on Track Structure, X Ray Sensitivity and Target Size. *Radiation Protection Dosimetry*, 52(1-4):29–33, apr 1994. URL http://rpd.oxfordjournals.org/content/52/1-4/29.abstract.

M. Scholz and G. Kraft. Track structure and the calculation of biological effects of heavy charged particles. *Advances in Space Research*, 18(1-2):5–14, jan 1996. ISSN 02731177. doi: 10.1016/0273-1177(95)00784-C. URL http://www.sciencedirect.com/science/article/pii/027311779500784C.

R. Schulte and T. Ling. Early and late responses on ion irradiation. In U. Linz, editor, *Ion Beam Therapy: Fundamentals, Technology, Clinical Applications*, chapter 5. Springer-Verlag Berlin Heidelberg, Heidelberg, 2012.

R. Schulte, V. Bashkirov, T. Li, Z. Liang, K. Mueller, J. Heimann, L. R. Johnson, B. Keeney, H. F. W. Sadrozinski, A. Seiden, D. C. Williams, L. Zhang, Z. Li, S. Peggs, T. Satogata, and C. Woody. Conceptual design of a proton computed tomography system for applications in proton radiation therapy. *IEEE Transactions on Nuclear Science*, 51(3 III):866–872, 2004. ISSN 00189499. doi: 10.1109/TNS.2004.829392.

R. W. Schulte and S. N. Penfold. Proton CT for Improved Stopping Power Determination in Proton Therapy, invited. *Trans Am Nucl Soc*, 106:55–58, 2012. ISSN 0003018X. URL http://www.ncbi.nlm.nih.gov/pubmed/24771877.

R. W. Schulte and A. J. Wroe. New developments in treatment planning and verification of particle beam therapy. *Translational cancer research*, 1(3):184–195, 2012. ISSN 2218-676X. doi: 10.3978/j.issn.2218-676X.2012.10.07. URL http://www.pubmedcentral.nih.gov/articlerender.fcgi?artid=4266163{&}tool=pmcentrez{&}rendertype=abstract.

R. W. Schulte, V. Bashkirov, M. C. L. Klock, T. Li, A. J. Wroe, I. Evseev, D. C. Williams, and T. Satogata. Density resolution of proton computed tomography. *Medical physics*, 32(4): 1035–1046, 2005. ISSN 00942405. doi: 10.1118/1.1884906.

R. W. Schulte, V. Bashkirov, R. Johnson, H.-W. Sadrozinski, and K. Schubert. Overview of the LLUMC/UCSC/CSUSB Phase 2 Proton CT Project. *Trans Am Nucl Soc. 2012*, pages 59–62, 2012. ISSN 0003018X.

D. W. Scott. On optimal and data-based histograms. *Biometrika*, 66(3):605–610, dec 1979. doi: 10.1093/biomet/66.3.605. URL http://biomet.oxfordjournals.org/content/66/3/605.abstract.

J. Seco and N. Depauw. Proof of principle study of the use of a CMOS active pixel sensor for proton radiography. *Medical Physics*, 38(2):622, 2011. ISSN 00942405. doi: 10.1118/1.3496327. URL http://scitation.aip.org/content/aapm/journal/medphys/38/2/10.1118/1.3496327.

J. Seco and M. F. Spadea. Imaging in particle therapy: State of the art and future perspective. *Acta Oncologica*, 54(9):1254–1258, 2015. ISSN 0284-186X. doi: 10.3109/0284186X.2015.1075665. URL http://www.tandfonline.com/doi/full/10.3109/0284186X.2015.1075665.

J. Seco, M. Oumano, N. Depauw, M. F. Dias, R. P. Teixeira, and M. F. Spadea. Characterizing the modulation transfer function (MTF) of proton/carbon radiography using Monte Carlo simulations. *Med Phys.*, 40(9):091717, 2013. ISSN 0094-2405. doi: 10.1118/1.4819816. URL http://www.ncbi.nlm.nih.gov/pubmed/24007150{%}5Cnhttp://scitation.aip.org/content/aapm/journal/medphys/40/9/10.1118/1.4819816.

R. Serber. Nuclear Reactions at High Energies. *Physical Review*, 72(11), 1974.

V. Sipala, M. Brianzi, M. Bruzzi, M. Bucciolini, G. A. P. Cirrone, C. Civinini, G. Cuttone, D. Lo Presti, S. Pallotta, N. Randazzo, F. Romano, C. Stancampiano, M. Scaringella, C. Talamonti, and M. Tesi. PRIMA: An apparatus for medical application. *Nuclear Instruments and Methods in Physics Research, Section A: Accelerators, Spectrometers, Detectors and Associated Equipment*, 658(1):73–77, 2011. ISSN 01689002. doi: 10.1016/j.nima.2011.05.025. URL http://dx.doi.org/10.1016/j.nima.2011.05.025.

J. Smeets, F. Roellinghoff, D. Prieels, F. Stichelbaut, A. Benilov, P. Busca, C. Fiorini, R. Peloso, M. Basilavecchia, T. Frizzi, J. C. Dehaes, and A. Dubus. Prompt gamma imaging with a slit camera for real-time range control in proton therapy. *Physics in medicine and biology*, 57(11):3371–405, jun 2012. ISSN 1361-6560. doi: 10.1088/0031-9155/57/11/3371. URL http://www.ncbi.nlm.nih.gov/pubmed/22572603.

F. G. Sommer, C. A. Tobias, E. V. Benton, K. H. Woodruff, R. P. Henke, W. Holly, and H. K. Genant. Heavy-ion radiography: density resolution and specimen radiography. *Invest Radiol.*, 13(2):163–170, 1978. ISSN 00209996. doi: 10.1097/00004424-197803000-00012. URL http://www.ncbi.nlm.nih.gov/pubmed/207658.

M. F. Spadea, A. Fassi, P. Zaffino, M. Riboldi, G. Baroni, N. Depauw, and J. Seco. Contrast-enhanced proton radiography for patient set-up by using x-ray CT prior knowledge. *International Journal of Radiation Oncology Biology Physics*, 90(3):628–636, 2014. ISSN 1879355X. doi: 10.1016/j.ijrobp.2014.06.057. URL http://dx.doi.org/10.1016/j.ijrobp.2014.06.057.

V. W. Steward. Proton (Heavy Ion) Radiography in Medical Diagnosis. *IEEE Transactions on Nuclear Science*, 26(2):2257–2261, 1979. ISSN 0018-9499. doi: 10.1109/TNS.1979.4329851. URL http://ieeexplore.ieee.org/lpdocs/epic03/wrapper.htm?arnumber=4329851.

V. W. Steward and a. M. Koehler. Proton beam radiography in tumor detection. *Science (New York, N.Y.)*, 179(76):913–914, 1973. ISSN 0036-8075. doi: 10.1126/science.179.4076.913.

B. Stewart and C. Wild. World Cancer Report 2014. *Clin Cancer Res*, 20(1), 2014.

Syed Naeem Ahmed. *Physics and Engineering of Radiation Detection*. Elsevier, 2nd edition, 2015.

J. Takatsu, E. R. Van der Graff, M.-J. Van Goethem, M. Van Beuzekom, T. Klaver, J. Visser, S. Brandenburg, and A. Biegun. Proton radiography imaging tool to improve a proton therapy treatment. *Physica Medica*, 30(December), 2014. ISSN 11201797. doi: 10.1016/j.ejmp.2014.07.088. URL http://www.sciencedirect.com/science/article/pii/S112017971400252X.

M. Takechi, J. Kunkel, H. Risch, L. Magallanes, S. Brons, O. Jaekel, and K. Parodi. A Detector setup for Heavy Ion Computed Tomography ∗. Technical Report 2013, GSI Scientific Report, 2014.

O. Taksuahiro, N. Atsuko, and O. Noruyuki. Visualization of complex DNA double-strand breaks in a tumor treated with carbon ion radiotherapy. *Scientific Reports*, 2016.

S. Tanaka, T. Nishio, K. Matsushita, M. Tsuneda, S. Kabuki, and M. Uesaka. Development of proton CT imaging system using plastic scintillator and CCD camera. *Physics in Medicine and Biology*, 61(11):4156–4167, 2016. ISSN 0031-9155. doi: 10.1088/0031-9155/61/11/4156. URL http://stacks.iop.org/0031-9155/61/i=11/a=4156?key=crossref.af9722beb43d647dbc1531dcffa31380.

J. Taylor, P. Allport, G. Casse, N. Smith, I. Tsurin, N. Allinson, M. Esposito, a. Kacperek, J. Nieto-Camero, T. Price, and C. Waltham. Proton tracking for medical imaging and dosimetry. *Journal of Instrumentation*, 10(April 2016):C02015–C02015, 2015. ISSN 1748-0221. doi: 10.1088/1748-0221/10/02/C02015. URL http://stacks.iop.org/1748-0221/10/i=02/a=C02015?key=crossref.9aba03f949b463920287190a3984ccdb.

J. T. Taylor, C. Waltham, T. Price, N. M. Allinson, P. P. Allport, G. L. Casse, A. Kacperek, S. Manger, N. A. Smith, and I. Tsurin. A new silicon tracker for proton imaging and

dosimetry. *Nuclear Instruments and Methods in Physics Research, Section A: Accelerators, Spectrometers, Detectors and Associated Equipment*, pages 1–5, 2016. ISSN 01689002. doi: 10.1016/j.nima.2016.02.013. URL http://dx.doi.org/10.1016/j.nima.2016.02.013.

J. Telsemeyer, O. Jäkel, and M. Martišíková. Quantitative carbon ion beam radiography and tomography with a flat-panel detector. *Physics in medicine and biology*, 57(23):7957–71, 2012. ISSN 1361-6560. doi: 10.1088/0031-9155/57/23/7957. URL http://www.ncbi.nlm.nih.gov/pubmed/23154641.

J. Telsemeyer, B. Ackermann, S. Ecker, O. Jäkel, and M. Martišíková. Experimental verification of ion range calculation in a treatment planning system using a flat-panel detector. *Physics in Medicine and Biology*, 59(14):3737, 2014. URL http://stacks.iop.org/0031-9155/59/i=14/a=3737.

T. Tessonnier, T. Marcelos, A. Mairani, S. Brons, and K. Parodi. Phase space generation for Proton and carbon ion Beams for external Users' applications at the heidelberg ion Therapy center. *Front. Oncol*, 5(5):2973389–297, 2016. ISSN 2234-943X. doi: 10.3389/fonc.2015.00297.

E. Testa, M. Bajard, M. Chevallier, D. Dauvergne, F. Le Foulher, N. Freud, J.-M. Létang, J.-C. Poizat, C. Ray, and M. Testa. Dose profile monitoring with carbon ions by means of prompt-gamma measurements E. *Nuclear Instruments and Methods in Physics Research B*, 267:993–996, 2009.

J. Thariat, J.-M. Hannoun-Levi, A. Sun Myint, T. Vuong, and J.-P. Gérard. Past, present, and future of radiotherapy for the benefit of patients. *Nature Reviews Clinical Oncology*, 10(1):52–60, 2012. ISSN 1759-4774. doi: 10.1038/nrclinonc.2012.203. URL http://www.ncbi.nlm.nih.gov/pubmed/23183635{%}5Cnhttp://www.nature.com/doifinder/10.1038/nrclinonc.2012.203.

C. Tobias, E. Benton, M. Capp, A. Chatterjee, M. Crutry, and R. Henke. Particle radiography and autoactivation. *International Journal for Radiation Biology*, 3:35–44, 1977.

C. A. Tobias. Pituitary Irradiation with High-Energy Proton Beams A Preliminary Report Pituitary Irradiation with High-Energy Proton Beams A Preliminary Report *. 18(February): 121–134, 1958.

C. A. Tobias, H. O. Anger, and J. H. Lawrence. Radiological use of high energy deuterons and alpha particles. *The American journal of roentgenology, radium therapy, and nuclear medicine*, 67(1):1–27, jan 1952. ISSN 0002-9580 (Print).

S. A. Uzunyan, G. Blazey, S. Boi, G. Coutrakon, A. Dyshkant, B. Erdelyi, D. Hedin, E. Johnson, J. Krider, V. Rykalin, V. Zutshi, R. Fordt, G. Sellberg, J. . E. Rauch, M. Roman, P. Rubinov, P. Wilson, and M. Naimuddin. A New Proton CT Scanner. In *23rd Conference on Application of Accelerators in Research and Industry, CAARI*, pages 1–6, San Antonio, TX, 2014. ISBN 9781629938288. URL http://arxiv.org/abs/1409.0049.

E. Vanzi, M. Bruzzi, M. Bucciolini, G. A. P. Cirrone, C. Civinini, G. Cuttone, D. Lo Presti, S. Pallotta, C. Pugliatti, N. Randazzo, F. Romano, M. Scaringella, V. Sipala, C. Stancampiano, C. Talamonti, and M. Zani. The PRIMA collaboration: Preliminary results in FBP reconstruction of pCT data. *Nuclear Instruments and Methods in Physics Research, Section A: Accelerators, Spectrometers, Detectors and Associated Equipment*, 730:184–190, 2013. ISSN 01689002. doi: 10.1016/j.nima.2013.05.193. URL http://dx.doi.org/10.1016/j.nima.2013.05.193.

J. M. Verburg and J. Seco. Proton range verification through prompt gamma-ray spectroscopy. *Phys. Med. Biol.*, 59:7089–7106, 2014.

B. Voss, I. Rinaldi, S. Brons, O. Jäkel, R. Panse, and K. Parodi. Heavy-Ion Computed Tomography applying a stack of ionization chambers. *GSI Scientific Report 2010*, Volume 201:484, 2010.

D. R. Warren, M. Partridge, M. A. Hill, and K. Peach. Improved calibration of mass stopping power in low density tissue for a proton pencil beam algorithm. *Phys. Med. Biol*, 60:4243, 2015. ISSN 0031-9155. doi: 10.1088/0031-9155/60/11/4243. URL http://iopscience.iop.org/0031-9155/60/11/4243.

U. Weber and G. Kraft. Comparison of carbon ions versus protons. *Cancer journal (Sudbury, Mass.)*, 15(4):325–32, 2009. ISSN 1528-9117. doi: 10.1097/PPO.0b013e3181b01935. URL http://www.ncbi.nlm.nih.gov/pubmed/19672150.

R. R. Wilson. Radiological use of fast protons. *Radiology*, 47(5):487–491, nov 1946. ISSN 0033-8419 (Print). doi: 10.1148/47.5.487.

Y. Yuan, O. C. Andronesi, T. R. Bortfeld, C. Richter, R. Wolf, A. R. Guimaraes, T. S. Hong, and J. Seco. Feasibility study of in vivo MRI based dosimetric verification of proton end-of-range for liver cancer patients. *Radiotherapy and oncology : journal of the European Society for Therapeutic Radiology and Oncology*, 106(3):378–382, mar 2013. ISSN 1879-0887 (Electronic). doi: 10.1016/j.radonc.2013.01.016.

T. Zacharias, W. Dorr, W. Enghardt, T. Haberer, M. Kramer, R. Kumpf, H. Rothig, M. Scholz, U. Weber, G. Kraft, and T. Herrmann. Acute response of pig skin to irradiation with 12C-ions or 200 kV X-rays. *Acta oncologica (Stockholm, Sweden)*, 36(6):637–642, 1997. ISSN 0284-186X (Print).

C. Zankowski and E. B. Podgorsak. Determination of saturation charge and collection efficiency for ionization chambers in continuous beams. *Medical physics*, 25(6):908–15, 1998. ISSN 0094-2405. doi: 10.1118/1.598269. URL http://www.ncbi.nlm.nih.gov/pubmed/9650181.

R. Zhang and W. D. Newhauser. Calculation of water equivalent thickness of materials of arbitrary density, elemental composition and thickness in proton beam irradiation. *Physics in medicine and biology*, 54(6):1383–95, 2009. ISSN 0031-9155. doi: 10.1088/0031-9155/54/6/001. URL http://www.ncbi.nlm.nih.gov/pubmed/19218739.

R. Zhang, P. J. Taddei, M. M. Fitzek, and W. D. Newhauser. Water equivalent thickness values of materials used in beams of protons, helium, carbon and iron ions. *NIH Public Access*, 55(9):2481–2493, 2010. ISSN 0031-9155. doi: 10.1088/0031-9155/55/9/004.Water.

J. F. Ziegler. The Stopping of Energetic Light Ions in Elemental Matter. *J.Appl.Phys/Rev.Appl.Phys.*, 85(1999):1249–1272, 1999. ISSN 00218979. doi: 10.1063/1.369844.

P. Zygmanski, K. P. Gall, M. S. Rabin, and S. J. Rosenthal. The measurement of proton stopping power using proton-cone-beam computed tomography. *Physics in medicine and biology*, 45(2):511–28, 2000. ISSN 0031-9155. doi: 10.1088/0031-9155/45/2/317. URL http://www.ncbi.nlm.nih.gov/pubmed/10701518.